Fabrication and investigation of ultrahigh vacuum compatible interfaces of topological insulators and superconductors

Von der Fakultät für Mathematik, Informatik und Naturwissenschaften der

RWTH Aachen University

zur Erlangung des akademischen Grades eines Doktors der Naturwissenschaften genehmigte Dissertation

vorgelegt von

Priyamvada Bhaskar

aus Bangalore

Berichter: Univ.-Prof. Dr. rer. nat. Markus Morgenstern
Univ.-Prof. Dr. Markus Ternes

Tag der mündlichen Prüfung: 23.08.2023

Zusammenfassung

Die Konstruktion der lateralen Grenzfläche zwischen einem dreidimensionalen topologischen Isolator und einem Supraleiter zur Untersuchung von Proximity-Effekten wird auf zwei Arten angegangen.

Zunächst wird die Herstellung von strukturierten Proben mit Hilfe eines Ultrahochvakuum Mask Aligners demonstriert. Der durch Piezomotoren angetriebene Mask Aligner verwendet eine Siliziumnitrid-Schattenmaske mit kapazitiven Sensoren zum Auslesen des Abstands zwischen Maske und Probe. Der Herstellungsprozess solcher Masken für den Mask Aligner wird hier etabliert. Mithilfe dieser Maske können aufeinanderfolgende Aufdampfungen durchgeführt werden, wobei zwischen den einzelnen Aufdampfungen eine horizontale Verschiebung der Probe erfolgt. Auf diese Weise wird eine supraleitende Schicht mit vordefinierten Löchern auf einem topologischen Isolator hergestellt, woraufhin die laterale Grenzfläche mit einem Rastertunnelmikroskop (STM) untersucht werden kann. Eine Demonstration für die Verwendung der Schattenmasken mit dem Mask Aligner beim Aufdampfen von Au auf Si(111) und Pb auf Si(111) zeigt scharfe Kanten mit einem Halbschatten kleiner als 100 nm und teilweise bis zu 10 nm, bei Abständen zwischen Maske und Probe unter 1 μm ohne direkten Kontakt dazwischen.

Weiterhin wird der Einfluss von Nb auf $(Bi_xSb_{1-x})_2Te_3$ mittels winkelaufgelöster Photoemissionsspektroskopie (ARPES) und STM untersucht. Vorläufige ARPES-Messungen deuten auf eine Verschiebung der $(Bi_xSb_{1-x})_2Te_3$-Bandstruktur von 50 meV – 200 meV zu niedrigeren Energien nach der Abscheidung von 0,3 Monolagen Nb hin. Das strukturierte Nb-$(Bi_xSb_{1-x})_2Te_3$, welches mit einer schützenden Se-Schicht versehen ist, wird für STM optimiert. Die supraleitende Energielücke im Leitfähigkeits-Spektrum auf Nb verschwindet an der Grenzfläche zu $(Bi_xSb_{1-x})_2Te_3$, wobei gelegentlich eine Spitze bei Nullspannung auftritt. Eine in das Nb eingedrückte Wolframspitze erzeugt eine supraleitende Mikrospitze, die zu einem Josephson-Übergang führt, was durch einen Suprastrom-Spitze bei Nullspannung und charakteristischen Spitzen durch Andreev-Reflektionen bestätigt wird. Aussagekräftige STM-Ergebnisse stehen noch aus, da der Herstellungsprozess nicht vollständig optimiert ist. Die weitere Optimierung der Proben erfordert einen kontinuierlichen Abgleich mit STM-Charakterisierungen sowie die Erforschung von Alternativen, wie z.B. verschiedenen Schutzmaterialien.

Abstract

The engineering of the lateral interface between a three-dimensional topological insulator and a superconductor for studying proximity effects is approached in two ways.

Firstly, the fabrication of patterned samples using an ultrahigh-vacuum mask aligner is demonstrated. The piezomotor-driven mask aligner employs a silicon nitride shadow mask with capacitive sensors to read out the mask-sample distance. The fabrication process of such masks for the mask aligner is established. Consecutive evaporations can be made through this mask, with a horizontal sample position offset between each evaporation. This produces a superconducting layer with predefined holes on top of a topological insulator and provides access to the lateral interface via scanning tunneling microscopy (STM). Proof of principle for shadow mask evaporation using the mask aligner with evaporation of Au on Si(111) and Pb on Si(111) show sharp edges with penumbra less than 100 nm and partly down to 10 nm at safe mask-sample distances below 1 μm without contact between them.

Secondly, the influence of Nb on $(Bi_xSb_{1-x})_2Te_3$ is probed via angle-resolved photoemission spectroscopy (ARPES) and STM. Preliminary ARPES measurements indicate a shift in $(Bi_xSb_{1-x})_2Te_3$ bandstructure of 50 meV – 200 meV toward lower energies after the deposition of 0.3 monolayers of Nb. Patterned Nb-$(Bi_xSb_{1-x})_2Te_3$ covered with a protective Se-capping was optimized for STM. A superconducting gap in the tunneling spectrum on the Nb disappears at the interface to the $(Bi_xSb_{1-x})_2Te_3$, occasionally exhibiting a zero-bias peak. The tungsten tip indented into the Nb creates a superconducting microtip, resulting in a Josephson junction as confirmed by a supercurrent peak at zero bias and signature peaks of Andreev reflections. Conclusive STM results are impending since the fabrication process is not optimized as yet. Further pursuits for sample optimization require continuous feedback with STM characterization and exploring alternatives such as different capping materials.

Contents

List of abbreviations

CF	conflat
AFM	atomic force microscopy
ARPES	angle resolved photoemission spectroscopy
BdG	Bogoliubov de-Gennes
BCS	Bardeen Cooper Schrieffer
CdG	Caroli de Genne
CF	conflat
DI	deionized
DOS	density of states
EBL	electron beam lithography
EDX	energy-dispersive X-ray spectroscopy
FWHM	full-width half maximum
GHS	gas handling system
ICP	inductively coupled plasma
JT	Joule-Thomson
LDOS	local density of states
LHe	liquid Helium
LN_2	liquid Nitrogen
LPCVD	low pressure chemical vapor deposition
MBE	molecular beam epitaxy
MFP	mean free path
ML	monolayer
PECVD	plasma-enhanced chemical vapor deposition
PL	photolithography
QHI	quantum Hall insulator
QL	quintuple layer
QSHI	quantum spin Hall insulator
RIE	reactive ion etching
RF	radio frequency
PMS	root mean square
SEM	scanning electron microscope (micropscopy)
SIS	superconductor-insulator-superconductor
SOC	spin-orbit coupling
STM	scanning tunneling microscope (microscopy)
STS	scanning tunneling spectroscopy
TI	topological insulator
TI-SC	topological insulator-superconductor
TKNN	Thouless, Kohmoto, Nightingale and den Nijs
TRIM	time reversal invariant momentum
TRS	time reversal symmetry
TSC	topological superconductivity
UHV	ultrahigh vacuum

1 Introduction

Topological superconductivity has been at the forefront of fundamental studies for the development of topological quantum computation. The basic recipe for systems that can markedly host the elusive Majorana modes, warrants topological superconductivity together with low density of states at the Fermi level. The search for such systems, with experimentally realizable materials, has been long ongoing. From a materials perspective, it can be widely categorized into single material systems with an inherent topological superconductivity and heterostructures of materials where topological superconductivity is realized by means of proximity effects. While intrinsic topological superconductors like $Cu_xBi_2Se_3$ [1, 2], $Sn_{1-x}In_xTe$ [3] and FeTeSe [4] have gained interest, the realization of topological superconductivity by interfacing of topological insulators with conventional s-wave superconductors [5, 6] has piqued the interest of experimentalists in the past decade due to its probably larger versatility. The present state of experimental research has been successful towards selecting promising materials that should provide a high spin-orbit coupling such that bands have a strong and unique spin-momentum locking. These bands should be prone to a large topological superconducting gap induced via a low Schottky barrier and good epitaxial contact to a superconductor. Finally, low defect densities are required [7]. Thin film heterostructures of s-wave superconductors and topological insulators have shown indications of topological superconductivity [8, 9] but lack a detailed characterization of topography and potential fluctuations at the interface, making it ambiguous to attribute any zero bias signal to a Majorana mode.

A scanning tunneling microscope (STM) provides the required ability to laterally resolve atomic scale features, including magnetic disorder and to probe electrostatic disorder with nm resolution [10, 11], making it an adequate tool for addressing these ambiguities. This also opens the possibility for in-situ ultrahigh vacuum (UHV) fabrication combined with STM to avoid contamination of the interface. In addition to atomic details STM provides insight into the lateral evolution of proximity effects [12]. The addition of a magnetic field opens up the possibility for induced vortices, which

together with topological superconductivity may reveal a zero bias peak associated with Majorana modes. The STM can also provide confirmation of analytical descriptions of the lateral and energetic distribution of such a Majorana mode's local potential fluctuations from, e.g. disorder and band bending at the interface. Knowing the lateral distribution of the proximity gap provides information on the lateral distribution of the Majorana-induced zero-bias peaks [13]. STM and STS detection of proximitized superconductivity has been explored in various systems including Bi_2Se_3 on top of $NbSe_2$ [14, 15]. Proximitized superconductivity has also been reported by transport measurements in e.g., Bi_2Se_3 interfaced to Pb [16] and Sn [17] and Bi_2Te_3 with Pb [18].

In order to obtain a system of a topological insulator and a superconductor with a high prospect of Majorana zero mode detection and, a thorough interface characterization, the following aspects should be considered.

Firstly, since the detection of a Majorana zero mode requires an inherently low LDOS at the Fermi level, the first requirement is to have a topological insulator (TI) with Fermi level residing within the bulk bandgap, ideally at the Dirac point, which also lies within the bandgap. Ternary TIs like $(Bi_{1-x}Sb_x)_2Te_3$ (generally referred to as BST) make a good candidate via the tunability of the Fermi level by changing x. While the Fermi level in Bi_2Te_3 lies in the bulk conducting band and in the bulk valence band in Sb_2Te_3, Bi-Sb-Te can be tuned to bring the Fermi level into the bulk band gap. In addition to Fermi level tuning, the Dirac point itself also shifts with respect to the bulk valence band with Sb doping, and can be tuned to be within the bulk bandgap. This allows a tuning of the Dirac point (E_D) with respect to the Fermi level (E_F), of around 300 meV [19], with E_D crossing the Fermi level around $x = 0.94$ [20]. Quarternary TIs such as $Bi_{2-x}Sb_xTeSe_2$ offer similar tunability where replacement of Bi with Sb shifts the Fermi level with respect to the Dirac points [21, 22] with E_D crossing the Fermi level around $x = 1$ [21].

Secondly, the band bending at the interface by proximitization of the TI with a superconductor should be negligible. To a first approximation, it befits to select superconducting materials with the least workfunction mismatch with the TI. Superconductors with T_c above 1 K and work functions between 4-5 eV like Al and Nb [23] are good candidates for ternary TIs with work functions around 4.5 eV. It is necessary to tune the Fermi level at the interface to the Dirac point, since this distance determines the energetic distance of the Majorana mode at zero bias to the excited states within a vortex core. This scales inversely with $E_D - E_F$ [13, 24, 25]. To resolve the Majorana

mode from excited states requires $E_F - E_D$ of about 10 meV for Nb (T_c=9.2 K) using $\Delta_{TSC} = 1.7\, k_B T$ and assuming 300 mK operation with energy resolution of 0.1 meV. For other superconductors, like Tl, $E_F - E_D$ must be as small as 5 meV. Although this number can be more forgiving when potential fluctuation might lead to accidental $E_F \approx E_D$ areas, this emphasizes the importance of experimental verification of band bending via detailed photoemission spectroscopy, followed by fine-tuning of the Fermi level and Dirac point by further stoichiometry optimization.

Thirdly, the presence of a superconductor on top of the TI is a challenge, since its vortex contains dense Caroli-de Gennes-Matricon (CdGM) states. These states, placed energetically close to the Majorana-induced zero-bias peak, couple to the Majorana mode at higher temperatures rendering it undetectable [26–28]. The best approach is to remove the superconductor on top of the TI by means of pierced holes with diameter on the scale of the coherence length [13]. This still permits vortices, albeit pinned. The detection of Majorana modes as a zero-bias peak is then limited by the energy distance to the nearest peak stemming from the excited states in the vortex at $\Delta E = \frac{0.83\Delta_{TSC}}{\sqrt{\Delta^2+(E_F-E_D)^2}}$, for hole sizes comparable to the coherence length [13, 25]. Sufficient energy resolution for its detection is realistically achievable in the 300–600 mK range. One can also determine the spatial dependence of the zero-bias peak, its robustness, and its oscillating appearance and disappearance with multiple flux quanta within the vortex. With the creation of an array of varying inter-vortex distances, one can also quantify the hybridization of neighbouring Majorana modes.

Finally, the realization of such a pierced heterostructure with a diameter up to 100 nm, using appropriate TI and superconductor, must be practical through pristine fabrication methods. One method is the removal of the superconductor, e.g. by ion bombardment [29]. However, the effect of this on the electronic properties of the underlying TI is questionable. It is indeed better to evaporate the superconductor priorly patterned, e.g. via shadow mask evaporation [30], or deposition of nanospheres that are removed after deposition of the superconductor [31].

This project describes the preparation and characterization of the interfaces of topological insulators and superconductors cogitating these four aspects, to host Majorana zero modes. While the realization of highly stable Majorana modes remains a long-term goal, this work describes the required revising of material selection, sample design, development of fabrication techniques and other challenges that come with such an ambitious

experimental goal.

After laying out the theoretical groundwork in **Chapter 2**, this thesis continues in **Chapter 3** by describing the experimental setups. Notably, the low-temperature STM has been characterized after the implementation of the gas handling system for He-3 operation.

Next, the design of a UHV mask aligner is presented which enables the close approximation of a dedicated mask towards a sample surface in ultrahigh vacuum conditions. **Chapter 4** addresses the UHV fabrication of a holey "antidot-like" superconductor on TI thin film heterostructures using the mask aligner. It lays the pathway to create an immaculate surface by an in-situ fabrication technique, in principle, as a tool for a clean interface between any evaporable materials. By providing a UHV fabrication technique such as the mask aligner, one can fabricate patterned heterostructure samples with a sharpness of $\sim 10\,\mathrm{nm}$ at the mesa edge of the evaporated material. Silicon nitride masks can be used to fabricate an array of holes to explore the aforementioned Majorana mode hybridization.

Chapter 5 contends with the selection of materials via photoemission spectroscopy of Nb on the ternary TI BST. Subsequent STM characterizations were made on patterned superconductor Nb on BST, fabricated by selective area growth via a mask-on-sample system, an alternate fabrication technique to the UHV mask aligner. These preliminary characterizations show potential for Nb as a candidate due to sharp mesa edges created on BST. Further discussions are made to provide insight into future redesign and fabrication of Nb-BST samples.

2 Theoretical background

The campaign to understand why electricity flows through some materials and not others is over 200 years old. We have made many strides from Benjamin Franklin's classification of insulating and conducting materials to their response to lightning discharges. Much of the credit for discoveries of exotic states of matter in recent decades, go to the developments of new tools in the 20th century that could probe electronic properties by means of quantum effects. In the following sections, a brief summary is made of the concept behind two types of materials from both ends of history: the more novel material topological insulator and the more known superconductor. Three-dimensional strong topological insulators are a class of bulk insulating materials that form unique surface states, with linear energy-momentum dispersion and spin-momentum locking, comprising a two-dimensional system of massless electrons. While these surface states alone have spurred great interest, their interaction with superconductors in close proximity has exposed opportunities to engineer topological superconductivity using topological insulator-superconductor heterostructures. The combination of these two materials opens up a myriad of physics, some of which are described to motivate the experimental work around these materials.

2.1 Topological insulators

The class of quantum materials called topological insulators can be reductively described as a material that insulates in bulk and conducts on the surfaces. The surface states are robust against backscattering. They form a helical metal wherein the 2D massless Dirac electrons have linear energy-momentum dispersion and spin momentum locking. In order to understand the physics of these materials, we follow the historic evolution of materials physics that led up to their discovery. Starting from the quantum Hall effect in terms of transport physics, and correlating it to the concept of topology through a topological invariant, the idea behind bulk-boundary correspondence is introduced.

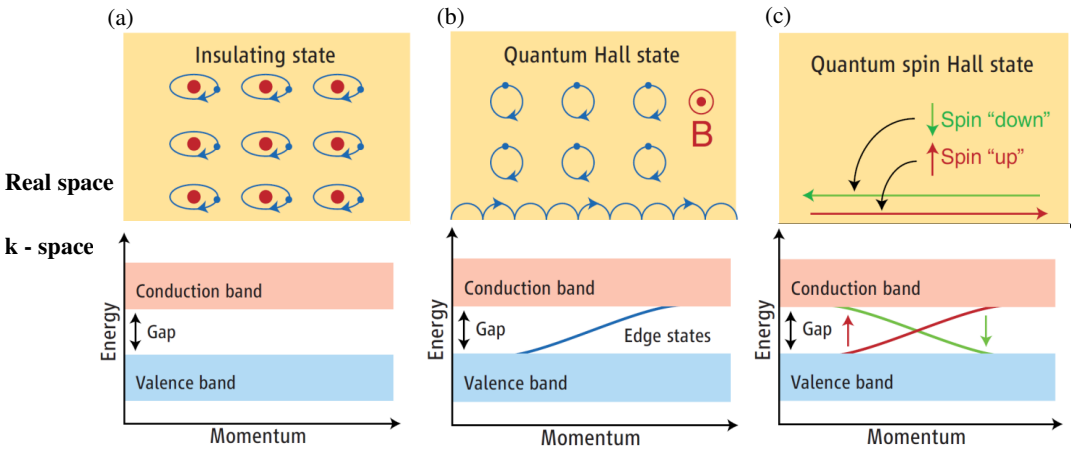

Figure 2.1: **Two-dimensional insulator phases in real space and k-space (a)** Trivial insulating state. Red points are atoms surrounded by electrons (blue arrows). The band gap separates the conduction and valence bands. **(b)** Quantum Hall insulating state, with magnetic field forcing electrons into orbits. 1D edge state transports charge along the sample boundary. **(c)** Quantum spin Hall state at a zero magnetic field with spin-polarized edge states at the boundary. Figure adapted from [32].

Band inversion is described in Quantum spin Hall insulators, followed by the extension of topological invariant to include these materials. Finally, the concept of 3D topological insulators is described.

2.1.1 Insulating states

Figure 2.1 shows the concept of topological insulators in comparison with trivial insulators and quantum Hall insulators. The accurate description of topological insulators demanded an extension of classical band theory to include topology in the form of a topological invariant $n \in \mathbb{Z}$. This allowed for the differentiation between topologically trivial and non-trivial materials [33]. A classical band insulator, characterized by a substantial band gap separating valence and conduction bands, would classify as a topologically trivial material as in figure 2.1 (a).

Quantum Hall insulating state

In 1980, Klaus von Klitzing demonstrated the quantum Hall effect, occurring at low temperatures when electrons confined to two dimensions are subject to a strong magnetic field perpendicular to the plane of electron movement. The quantized conductance in

fundamental units is described as

$$\sigma_{xy} = \nu \left(\frac{e^2}{h} \right) \quad , \tag{2.1}$$

where ν is an integer known as the filling factor [34]. The description of this effect led to the first introduction of topological indices into solid-state physics, i.e. ν is a topological index, also called Chern number. A visualization of this index separates the bulk and boundary of the sample, where the boundary carries the current. As depicted in figure 2.1 (b), electrons in a magnetic field B, move in circles at the cyclotron frequency $\omega_c = {}^{eB}/_{m}$, where m is the mass of the electron. Quantum mechanically this motion exhibits discrete kinetic energies $E_n = (n + {}^1/_2)\hbar\omega_c$. Placing the Fermi level between such so-called Landau levels would make the bulk insulating. However, at the edge, there are still states at the Fermi level for each occupied Landau level in the bulk. This state originates from the bulk due to the electrostatic potential confining the electron in the lateral direction. For hard wall potential, the electrons would be reflected during their circular motion leading to the semi-circular orbits in figure 2.1 (b) that move the electron along the edge in one direction. This edge state carries a Hall conductor of ${}^{e^2}/_{h}$ (if not exhibiting any degeneracy such as spin or valley degeneracy). Hence the number of edge states is identical to the topological Chern number.

Topology of the quantum Hall state

The quantum Hall insulator (QHI), thus distinguishes itself from a topologically trivial insulator, by highly conductive states at the boundaries. The trivial and non-trivial insulator phases follow clear rules for transformation, namely the topological invariant is only changed if the band order is changed. In 1982, Thouless, Kohmoto, Nightingale and den Nijs (TKNN) described the topological [35] origin of the quantized Hall effect and identified this as markedly different from the topology of a classical band insulator. They introduced a topological invariant n being an integer known as the TKNN invariant and demonstrated the Hall conductivity is proportional to this invariant. This shows that one can assign the Quantum Hall state to a topologically non-trivial state, ensuring that the boundary channels are robust so long as the topology is not altered [36].

This topological invariant, later recognized to be equivalent to the Chern number was deduced from occupied wave functions within the insulating bulk, independent of the

specifics of the edge state [37, 38].

An intuitive understanding of the Chern number comes in terms of the geometric Berry phase that is accumulated in a quantum mechanical system when a parameter completes a closed path, like that accumulated by a Bloch wavefunction $u_m(\mathbf{k})$ when $\mathbf{k}$ propagates around a closed loop. Then a Chern number C is described as the sum of Berry phases over all occupied bands divided by 2π as

$$C = \sum_m C_m = \sum_m \frac{1}{2\pi} \cdot \underbrace{\oint d\mathbf{k} \overbrace{(\nabla_k \times \mathbf{A}_m(\mathbf{k}))}^{\text{Berry curvature}}}_{\text{Berry phase}} \tag{2.2}$$

where $A_m(k) = i \langle u_m(k) | \nabla | u_m(k) \rangle$ is the Berry vector potential. The closed loops are selected in a way that they surround areas in the BZ that are continuous. In a trivial insulator, the closed loops can be around the BZ boundary such that they do not accumulate any phase, $C = 0$. In a QHI state, some loops are not resulting in $C_m = 0$, such that $C \neq 0$. One can show that each C_m is an integer, such that σ_{xy} gets an integer multiple of $^{e^2}/_h$.

Bulk-boundary correspondence

Let us construct a simplified scenario where a trivial insulator ($n = 0$) is interfaced with a non-trivial quantum Hall insulator ($n = 1$). Here, we assume for the sake of simplicity that the energy gap of a solid is a local property and that bands can only change smoothly as a function of parameters. Then, the interface experiences at some point a vanishing energy gap in order to allow the Chern number to change. In particular, at the interface between a QHI and a trivial insulator, the insulating gap closes giving rise to a gapless surface state (edge state in 2D) [39]. More stringently, Laughlin argued that for a charge to be transferred from a first boundary to the second one of a non-trivial Chern insulator across the insulating bulk mandates the existence of edge states at each boundary at the Fermi energy, that are ready to receive or donate electrons without energy penalty. This bulk-boundary correspondence relates the topological invariant C to the number of boundary states at the Fermi level. We will later see that the odd/even parity in the number of states determines the topological triviality of the material.

Quantum Spin Hall Insulating State

Motivated by the quest for a class of materials with robust edge states without the need for an external magnetic field, in 2005, Kane and Mele surmised the possibility of a quantum spin Hall effect by considering the incorporation of spin-orbit coupling in graphene [40]. In contrast to the magnetic field-driven Lorentz force acting on both spins identically, the time-reversal symmetry is preserved by spin-orbit coupling, which depends on spin and direction of motion, both of which reverse sign upon time reversal. Consequently, edge states can propagate in both chiral directions. The edge channels are not spin degenerate like in some QHI but rather spin-polarized for each direction of motion as depicted in figure 2.1 (c). This creates an archetype for a system where electron spin is locked to a certain propagation direction of the edge state. This spin-momentum locking is the origin of the spin Hall conductance, with the exact direction determined by the spin-orbit interaction in the system. Time reversal symmetry requires that the Hall conductance for one spin channel $\sigma_{xy,\uparrow} = e^2/h$ compensates the other spin channel $\sigma_{xy,\downarrow} = -e^2/h$ such that the net Hall conductance is zero, albeit, with a non-zero quantized spin Hall conductance $\sigma_{xy,\uparrow} - \sigma_{xy,\downarrow}$.

The characteristic of a topologically non-trivial insulator to experience a change of band order at the interface to a trivial insulator refers to the term band inversion. The physical reason for such an inversion can be spin-orbit coupling (SOC). Typical topological insulators have p-orbitals contributing to their valence band and conduction band. The spin-orbit coupling has the effect of energy level splitting in p-type and d-type orbitals, while not in s-type orbitals because of vanishing orbital moment. When the bulk band gap without SOC is smaller than the strong SOC, the relatively shifted valence band can cross the conduction band at certain locations in the k-space [42]. If a band gap opens at these crossing points by such interaction, a band inversion is realized. Figure 2.2 (a) shows a schematic representation visualizing band inversion due to SOC resulting in a band gap opening.

2.1.2 Topological insulator: 2D and 3D description

The above considerations form the basis for the prototype of a topological insulator, proposed first by Bernevig, Hughes and Zhang [43] and experimentally realized by Koenig et al [44]. Such a quantum spin Hall insulator (QSHI) is also referred to as a 2D topological insulator. A second characteristic is the conductance of these edge states,

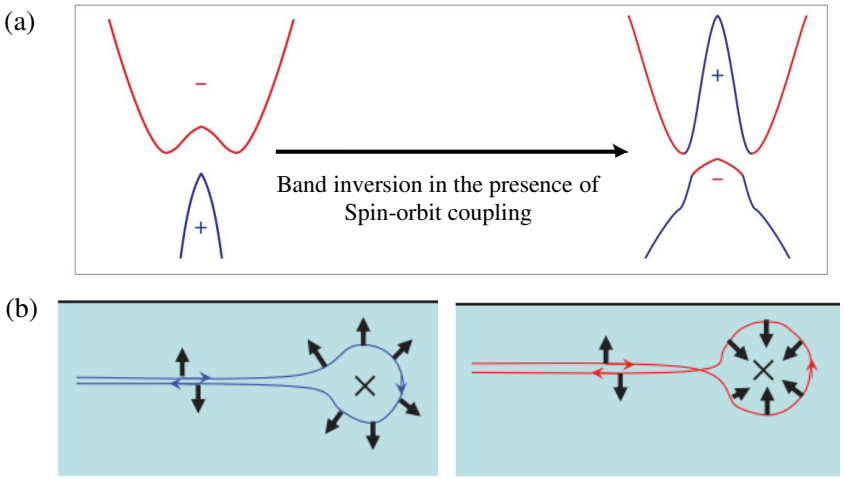

Figure 2.2: **Band inversion and robust states in QSHI. (a)** Schematic representation of QSHI to visualize the effect of SOC on the band structure. The "+" type valence band is pushed above the "-" type conduction band, resulting in an inversion of band order in the central part. A band gap develops at the crossing points due to the hybridization of the orbitals. The different parities are indicated in red/blue. **(b)** Two possible paths taken by an electron on a QSH edge when scattered backwards. The electron spin rotates by π clockwise (blue curve) or counterclockwise (red curve). The geometrical phase factor associated with the rotation of the spin leads to destructive interference between the two paths. Figure adapted from [41].

in that they are robust to backscattering. Qi and Zhang [41] provided a semiclassical argument for the absence of backscattering owing to the time-reversal symmetry in these edge states. Figure 2.2 (b) visualizes that a forward-moving spin-up state, upon encountering an impurity site, can either make a clockwise or anticlockwise flip of its spin. Because the electron propagating in the backward direction can only have a spin-down state, electron spin must adiabatically flip. This changes the phase either by $\pi/2$ or $-\pi/2$. Adding up these two paths with the same probability, the wavefunction picks up a phase π, leading to destructive interference for backscattering. Therefore, the breaking of time-reversal symmetry can cause backscattering. The spin-polarized edge states in a QSHI are thus protected from backscattering by time-reversal symmetry.

The topological $\mathbb{Z}_2$ invariant

In a QSHI, despite non-zero Hall conductivity, the TKNN invariant is $n = 0$, due to the net zero Hall conductivity. To distinguish this from the trivial insulting state, requires

another topological invariant. Kane and Mele introduced the invariant ν_0 as a $\mathbb{Z}_2$ index[1]. The parity $\nu_0 = 0$ or $\nu_0 = 1$ is used to distinguish a trivial insulator and a QSH phase. While a 3D TI is fully described by four $\mathbb{Z}_2$ invariants ν_0, ν_1, ν_2 and ν_3, here we only discuss ν_0, the so called strong topological invariant [45–47].

In order to describe the $\mathbb{Z}_2$ invariant, one first examines the role of time-reversal symmetry (TRS). For a spin 1/2 particle, the TRS operator can be described by the anti unitary operator as $\Theta = \exp\left(\frac{i\pi}{\hbar} S_y\right) K$, where S_y is the spin operator, K the complex conjugate and the TRS operator satisfies $\Theta^2 = -1$. A system with Hamiltonian H follows TRS if it satisfies

$$\Theta H(\mathbf{k}, \uparrow)\Theta^{-1} = H(-\mathbf{k}, \downarrow). \tag{2.3}$$

Hence, for every Bloch wave which is an energy eigenstate $|u(\mathbf{k}, \uparrow)\rangle$, the time-reversed state with the opposite wave vector and spin is also an eigenstate at the same energy. They are called Kramers' partners. The presence of SOC lifts spin degeneracy on most parts within the BZ, except at certain points called *time reversal invariant momentum* (TRIM) points. At these particular momentum points one has $\mathbf{k} = \mathbf{-k}$, and consequently $E(\mathbf{k}, \uparrow) = E(\mathbf{-k}, \downarrow)$. Due to its spin degeneracy, these points are also referred to as Kramers points [33, 37]. Topological edge states around these points can be described by the massless Dirac Hamiltonian

$$H = \hbar v_{\mathrm{F}} \sigma_x k_y \tag{2.4}$$

where v_{F} is the Fermi velocity and σ_x is the Pauli operator of the spins. The Eigenenergies given by $E = \pm\hbar v_{\mathrm{F}} k_y$ shape a Dirac cone crossing. Knowledge of a material's bulk band structure around the TRIM points allows for the calculation of its $\mathbb{Z}_2$ invariant. When the material has additional e.g. inversion symmetry, it is simplified (for four bulk TRIMS) by

$$(-1)^{\nu_0} = \prod_{i=1}^{4} \delta(\Gamma_i) = \prod_{i=1}^{4} \prod_{m=1}^{N} \xi_m(\Gamma_i) \tag{2.5}$$

where the parity invariant $\delta(\Gamma_i) = \prod_{m=1}^{N} \xi_m(\Gamma_i)$ is defined with $\xi_m(\Gamma_i) = \pm 1$ as parity

[1] $\mathbb{Z}_2$ is the subset of all integers $\mathbb{Z}$, that separates odd and even numbers. The $\mathbb{Z}_2$ index can take value 0 or 1.

eigenvalue of the state at the bulk TRIM points Γ_i. The parity of all N occupied bulk bands at all bulk TRIM points Γ_i must be multiplied to get ν_0. The parity can be deduced, e.g., from band structure calculations.

3D topological insulator

A 3D topological insulator can be envisioned as an extension of 2D where an insulating 3D bulk is surrounded by 2D surfaces that interface the bulk with the vacuum. At low energies, the planar extension of the linear dispersion behaviour from 2.4 reads:

$$H = \hbar v_{\mathrm{F}}(\sigma_x k_y - \sigma_y k_x) \tag{2.6}$$

giving eigenenergies and eigenvectors

$$E = \pm\hbar v_{\mathrm{F}}\left|\vec{k}\right| \tag{2.7}$$

$$|\psi_k\rangle = \frac{1}{\sqrt{2}}(\pm ie^{-i\theta}\,|\uparrow\rangle + |\downarrow\rangle)e^{i\mathbf{kx}} \tag{2.8}$$

where the momentum vector is $\left|\vec{k}\right| = \sqrt{k_x^2 + k_y^2}$ and $|\uparrow\rangle$ and $|\downarrow\rangle$ the spin up and spin down states, respectively. The phase $ie^{i\theta}$ describes the direction of the spinor, which is pointing in the x-y plane at $\pi/2$ with respect to the momentum $\vec{k}$.

Equation 2.5 is replaced in 3D by the sum over all eight TRIM points, corresponding to the corners of the basic unit of 3D BZ as

$$(-1)^{\nu_0} = \prod_{i=1}^{8} \delta(\Gamma_i). \tag{2.9}$$

The characteristic spin-momentum locking in topological surface states is distinct from the more complex spin-momentum relationship in normal metals and fixed spin independent from momentum in ferromagnets. Topological insulators are the base of interesting physics including proximity effects leading to topological superconductivity [48] and Majorana zero modes [5, 39, 41, 49].

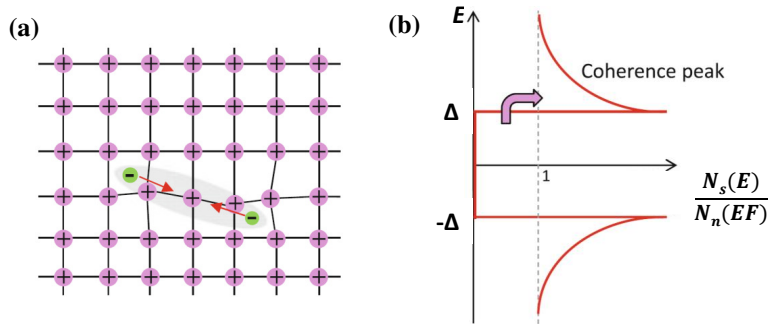

Figure 2.3: **Concept of Cooper pair formation. (a)** Lattice distortion due to one electron provides an attractive potential for a second electron passing later. **(b)** The energy distribution of density of states of single particle excitations in the superconducting state. States are moved from within the gap and are stacked at the coherence peaks, while Cooper pairs are formed. Figures adapted from [51].

2.2 Superconductivity

Since its discovery in 1911 by Heike Onnes [50], the field of superconductivity has evolved abundantly. Starting with the simplistic definition of "perfect conduction" in mercury below 4.2 K to the many-body theory attempts in explaining the microscopic origins of high T_c superconductivity, often more questions arise with an answer. The most remarkable result in the course of understanding is the Bardeen-Cooper-Scrieffer (BCS) theory, which describes superconductivity as a macroscopic effect due to the formation of Cooper pairs which are created by electron-phonon interactions, condensing into a coherent bosonic state.

Qualitatively, the BCS ground state is made out of pairs of electrons called Cooper pairs. Below a certain temperature $T_{\mathrm{BCS}} \propto n^{\frac{2}{3}}$, they condense into a Bose-Einstein condensate where all the Cooper pairs coherently occupy the lowest energy state. Overall, this is possible only if the cost of creating a Bosonic Cooper pair is less than the energy of the constituting pair of single Fermionic electrons. There are two aspects to consider for this to be realized.

Firstly, the electron-electron Coulomb repulsion must be overcome. To overcome this electron-electron repulsion and form a Cooper pair, the effective interaction needs to be attractive. A simplistic picture of phonons playing this role is shown in figure 2.3 (a). An electron moving through a lattice with negligible mobility, causes the lattice to "squeeze" in a way that an electron passing through later, will experience an attractive potential. This way a link is created between the first electron, the local lattice per-

turbation (or phonon), and the second electron. This picture is feasible in all metals at all temperatures. But at higher temperatures, thermal fluctuations disassociate a Cooper pair. The interplay between Coulomb repulsion, thermal fluctuations, the resulting strength of the weakly-bound electrons, and statistical requirements will decide if a metal is superconducting at a finite temperature.

A second-order perturbation process facilitates the electron-electron attraction without the need for phonon energy. The Cooper pairs can be created by an attractive interaction between electrons that is caused by a virtual exchange of phonons [52]. This interaction is attractive when the energy difference between the two participating electron states is less than the phonon energy. Moreover, the attractive phonon interaction must dominate the inherently repellent Coulomb interaction between the electrons [53].

Thereafter, the energy gain from Cooper pair formation must be maximized.

One can describe the BCS Hamiltonian in terms of a two-body electron system with a certain attractive electron-phonon-electron interaction $V_{k,k'}$ as:

$$H = \underbrace{\sum_{k\sigma}(\epsilon_k - \mu)c^\dagger_{k\sigma}c_{k\sigma}}_{\text{single electron Bloch states}} + \underbrace{\sum_{kk'} V_{k,k'}c^\dagger_{k\uparrow}c_{-k\downarrow}\dagger c_{-k'\uparrow}c_{k'\downarrow}}_{\text{phonon-corelated electron pairs}} \tag{2.10}$$

where $c^\dagger_{k\sigma}(c_{k\sigma})$ is the electron creation (annihilation) operator, $\epsilon_k - \mu$ is the single electron energy, $V_{k,k'}$ is the electron-phonon-electron (attractive) interaction potential.

Following henceforth the Bogoliubov-de Gennes (BdG) transformation to introduce operators on quasiparticle excitations of holes and electrons, allows us to diagonalize the Hamiltonian. It also provides a physical interpretation that allows us to visualize electron-like and hole-like quasiparticle excitations of the superconductor. The resulting BdG Hamiltonian

$$H_{BdG} = \begin{pmatrix} \epsilon_k - \mu & -\Delta_k i\sigma_y \\ \Delta^\dagger_k i\sigma_y & \mu - \epsilon_k \end{pmatrix} \tag{2.11}$$

in the basis of

$$\psi = (u_{k\uparrow}, u_{k\downarrow}, v_{k\uparrow}, v_{k\downarrow})^T \tag{2.12}$$

where $u(v)$ represents quasiparticle (quasihole) wavefunctions, with each electron cre-

ation/annihilation operator ($c/c^\dagger$) being a superposition of quasiparticle creation and annihilation operators. The gap Δ_k depends on the pairing symmetry of the superconductor. In the realm of BCS theory discussed below, $\Delta_k = \Delta_0$ is constant and represents s-wave orbital pairing [54].

Cooper showed such a state [55] to occur with electrons of opposite momenta. Such Cooper pairs formed with net zero momentum are energetically most favoured. Pauli's exclusion principle is taken into account for s-wave pairing by the opposite spins of the electrons in each pair. They form an antisymmetric singlet spin state ($k\uparrow$, $-k\downarrow$). The Cooper pair wave function is

$$\Phi_{2e} = u_k \left|0_k\right\rangle + v_k \left|1_k\right\rangle \tag{2.13}$$

with u_k and v_k the probabilities of finding the electron pair unoccupied and occupied respectively. If the gain in energy is favourable, electron pairs condense into this state, forming a Fermi sea of Cooper pairs that can be described by

$$\prod_{\forall k} (u_k + v_k c^\dagger_{k\uparrow} c^\dagger_{-k\downarrow}) \left|0_k\right\rangle \tag{2.14}$$

where u_k and v_k obey $u_k^2 + v_k^2 = 1$. One can then describe the system in terms of the superconducting gap Δ by computation of the fraction of occupation as:

$$v_k^2(E) = \frac{1}{2}\left(1 - \frac{E}{\sqrt{E^2 + \Delta^2}}\right) \tag{2.15}$$

for the energy window $E_\mathrm{F} \pm \hbar\omega_D$. The corresponding density of states of single particle excitation reads

$$\rho(E) = \mathrm{Re}\left\{\frac{E - i\delta}{\sqrt{(E - i\delta)^2 + \Delta^2}}\right\} \tag{2.16}$$

where the relatively small imaginary δ [56] accounts for a finite lifetime of the quasiparticles. This is plotted in figure 2.3 (b). It provides an intuitive understanding of

the superconducting gap as the energy required to break the Cooper pairs and excite quasiparticles above or below the Fermi energy. The occupation $v_k^2(E)$ at $T = 0\,\mathrm{K}$ behaves like a Fermi-Dirac distribution for a hypothetical temperature $T_\mathrm{c} = \frac{\Delta}{1.76 k_\mathrm{B}}$. T_c is also called the critical temperature of the superconductor since at T_c the superconductor disappears and becomes a metal. The eigenvalues of the quasiparticles are described as

$$E_k = \pm\sqrt{(\epsilon_k - E_\mathrm{F})^2 + |\Delta|^2} \tag{2.17}$$

and shows a finite superconducting gap $2\Delta_0$ centered around the Fermi energy E_F. As such, the electron-phonon-electron scattering requires a change of the distribution function as an energy penalty in the area $\hbar\omega_D$ around the Fermi energy, the width of which is determined by Δ. This order parameter, Δ, also determines the strength of the energy gain per Cooper pair contributing within this broadened area as $\Delta/2$. The density of states at the Fermi level sets the statistical requirement which determines whether the system is in the superconducting phase in terms of energy gain.

2.3 Andreev reflections

2.3.1 Second and third order Andreev reflections

Andreev reflection can occur when an electron traverses a normal metal to its interface with a superconductor. A hole is retroreflected back into the metal, and a Cooper pair is injected into the superconductor [52, 57]. This doubles the conductivity.

When two superconductors are coupled across a normal conductor or vacuum ($R_\mathrm{tunnel} \lesssim 1\,\mathrm{M\Omega}$), these retroreflections can also appear and manifest as subgap features in the $I(V)$ curve [57–59]. The process of retroreflection, described in Fig. 2.4 (a), considers two superconductors with gap Δ_1 and Δ_2.

In the most obvious case, an electron incident from an occupied quasiparticle state in superconductor 1 can travel to an unoccupied quasiparticle state in superconductor 2 at $V \geq \Delta_1 + \Delta_2$. However, if no state is available for this process at $V \leq \Delta_1 + \Delta_2$, the incident electron $\psi_i(k, \uparrow)$ with energy E_i is "reflected" back to superconductor 1 as a hole $\psi_r(-k, \downarrow)$ with energy $E_r = -E_i$ with respect to E_F2. This description uses electron-hole symmetry and is valid in both directions of propagation.

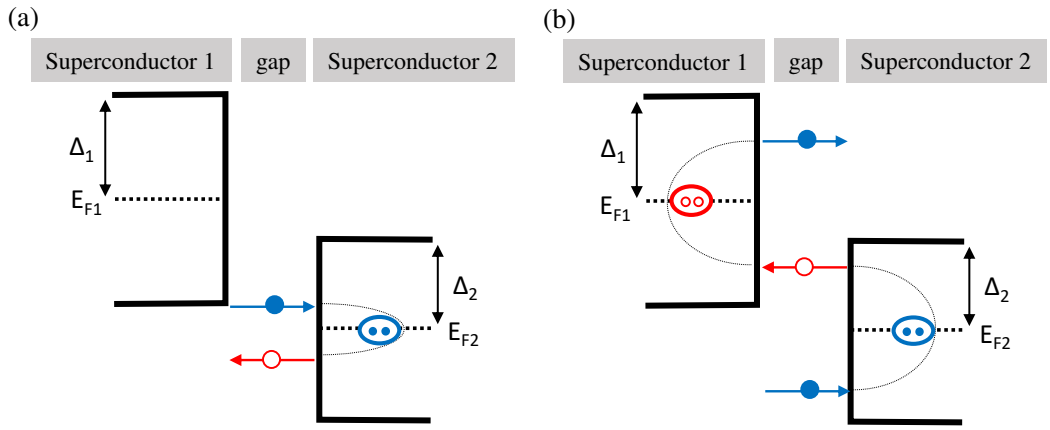

Figure 2.4: **Andreev reflection between two superconductors.** Sketches of the quasiparticle excitation spectrum to describe the Andreev reflection process at the interface between two superconductors as a **(a)** second-order process and **(b)** third-order process. Blue and red refer to electron and hole states.

Solving for boundary conditions gives us a probability a for the occurrence of such an Andreev reflection in case of a perfect interface that does not lead to normal electron reflections as

$$\begin{cases} |a|^2 = 1, & |E| < \Delta \\ |a|^2 = \frac{|E|-\sqrt{E^2-\Delta^2}}{|E|+\sqrt{E^2-\Delta^2}}, & |E| \geq \Delta \end{cases} \tag{2.18}$$

The Andreev reflection coefficient $|a|^2$ diminishes significantly for quasiparticles with energies $|E| \geq \Delta$ whereas all electrons with subgap energies $|E| < \Delta$ are completely reflected as holes. Whilst this process describes the second-order Andreev reflection, involving the participation of two quasiparticles, it is possible to extend the notion to higher order reflections. For example, a third-order Andreev reflection involves three quasiparticles as shown in figure 2.4 (b), where two electrons and one hole are induced. In general, in case of $\Delta_1 = \Delta_2 = \Delta$, for n quasiparticles transferred over the junction, described as the n-th order Andreev reflection process, $n-1$ Andreev reflections take place at voltage

$$eV_n \geq \frac{2\Delta}{n} \tag{2.19}$$

where Δ is the gap of the superconductor into which the Cooper pair is transported.

While conventional Andreev reflection is currently well understood, atomic-scale tun-

neling techniques exploiting this phenomena remain relatively unexplored. Understanding Andreev measurements in nanoscales and atomic scales like that provided by STM probe atomistic superconductivity properties. This prospects the deciphering of disorder [60], competing order parameters [61], interfaces [62], topological defects [63, 64] and supplementing local density of states measurements from scanning tunneling spectroscopy [65, 66]. However, this comes with the challenge that junction by STM remains uncontrolled [67]. This stipulates the extension of theoretical models to account for micro tip geometries and asymmetry in such junctions [68].

Measurements of superconductors with STM tips open a route to the creation of superconductor-insulator-superconductor (SIS) type Josephson junctions. This can occur either by using superconducting tips or metallic tips coated by superconductors [65, 69–74]. The superconducting tip and sample thereby form a weakly coupled pair of electrodes through which a Josephson current may flow. Using STM, it then is possible to map out local variations in the Josephson current in the vicinity of defects. This demands low spectroscopic energy resolution (μeV) and low voltage noise (μV), even when probing superconductors with a relatively high T_c like Nb ($T_c = 9.25\,K$, $\Delta = 1.4\,\text{meV}$).

Chapter 5 shows the experimental observation of Andreev of reflections in asymmetric junctions created between the tip and sample.

2.3.2 Josephson junction and Andreev bound states

The Josephson effect is described as the Cooper pair tunneling across a junction between weakly coupled superconductors (Δ_1 and Δ_2), leading to a supercurrent that can also flow in unbiased junctions. The phase difference $\Delta\phi$ between wave functions of the Cooper pair condensates on either side of the junction drives this supercurrent. This phase difference couples the superconductors to macroscopic electric quantities as

$$I = I_0 \sin \Delta\phi \tag{2.20}$$

$$V = \phi_0 \frac{d\Delta\phi}{dt} \tag{2.21}$$

where V and I are voltage and current in the junction, I_0 the critical current and flux quantum $\phi_0 = \hbar/2e$. Equation 2.20 describes the dc-Josephson effect where current flows

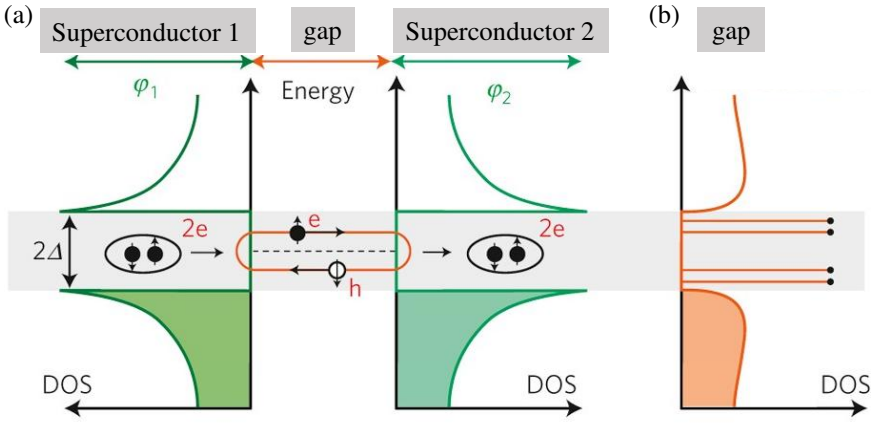

Figure 2.5: **Andreev bound states. (a)** Schematic representation of Andreev bound states between two superconducting leads, each gapped by Δ with respecting superconducting phases $\phi_{1,2}$. The grey band indicates energies within the gap. Andreev reflections lead to the formation of discrete resonant states of e-h pairs confined between the superconductors. **(b)** The local density of states of excitations in the gap exhibits peaks at the energies of resonance. Figure adapted from [78].

between the superconductors without any voltage drop. This cooper pair *supercurrent* depends on the phase difference and on the gaps through the critical current as

$$I_0 = \begin{cases} \frac{\pi\Delta}{2R_T}\tanh\frac{\Delta}{k_BT} & \text{if } \Delta_1 = \Delta_2 \\ \frac{1}{R_T}\Delta_2(T)K\left(\sqrt{1-\frac{\Delta_2(T)^2}{\Delta_1(T)^2}}\right)\tanh\frac{\Delta_2}{k_BT} & \text{if } \Delta_1 \neq \Delta_2 \end{cases} \tag{2.22}$$

where R_T is the junction resistance in the normal state, temperature T, and $K(x)$ is the Jacobi's complete elliptic integral of the first kind. These Josephson relations describe the zero-voltage supercurrent [75], also measured by STM [76, 77]. In Chapter 5, such a supercurrent in a Josephson junction created by a superconducting tip and superconducting sample is presented.

Equation 2.21 describes the ac-Josephson effect where a small voltage across the junction causes an alternating supercurrent due to time variation in phase difference $\Delta\phi$ with the frequency of this ac supercurrent being $f = \frac{V}{2\pi\phi_0}$. By exciting the junction with a high-frequency electromagnetic wave, one can enhance the tunneling probability across the junction, resulting in sharp steps in the I-V curve when the voltage crosses multiples of $2\pi\phi_0 f$, called the Shapiro steps. This discretization can be understood in terms of Andreev bound states.

When Andreev reflection occurs and the quasiparticles that are reflected from the

first interface have a sufficient coherence length to reach the other interface and get (Andreev) reflected again, bound states are formed. These bound states, called Andreev bound states are formed due to the continuous transfer of Cooper pairs between the superconductors, as depicted in Figure 2.5 (a). However, while Andreev reflection can occur at any energy, Andreev bound states can only form at discrete levels of energy E_n as in figure 2.5 (b), which ensures that after a full loop across the junction, the phase develops as $\oint d\phi = 2\pi n$ where n is an integer. The discrete energy modes, which varies as a function of the phase difference between the superconductors ϕ is given by [79, 80]

$$E_n(\phi) = \pm\Delta\sqrt{1 - \tau_n \sin^2 \frac{\phi}{2}} \tag{2.23}$$

where $\tau_n = \frac{h}{2e^2 R_T} \approx \frac{13\,k\Omega}{R_T}$ is the transmission probability for the individual mode E_n at the interface between gap and superconductors for a symmetric junction (equal superconductors). The current-phase relation, which can be obtained by summing up the derivatives of all the energetic contributions from the energy-phase dispersion, is a 2π periodic via the $\sin^2(\phi/2)$ term.

2.4 Proximity effect and Majorana zero modes

2.4.1 Proximity induced superconductvity

While intrinsic superconductors were discussed in section 2.2, materials that do not have an intrinsic pairing mechanism can display superconductivity when brought in proximity to a superconductor. This can be physically understood in terms of Cooper pairs diffusing into the non-superconductor before decaying into quasiparticles over a certain length scale as depicted in figure 2.6.

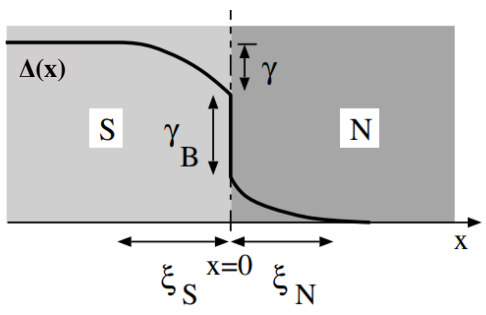

Figure 2.6: **Proximity effect inducing superconductivity in a normal metal (N) placed in proximity to a superconductor (S).** The energy-space diagram shows the superconducting pair potential $\Delta(x)$ evolving as the cooper pairs diffuse into the normal metal upto a coherence length ξ_N. In general, there is a discontinuity at the interface. Figure adapted from [81].

The reduction in the pairing potential within the superconductor, as a result of the Cooper pair diffusion into the normal metal, is described by the so-called pair-breaking parameter given by

$$\gamma = \frac{\xi_S \cdot \rho_S}{\xi_N \cdot \rho_N} \tag{2.24}$$

where ρ_S and ρ_N are the specific normal state resistance of the superconductor and metal. Within the normal metal, far from the interface ($k_N x \gg 1$)

$$\Delta_N(x) = \exp\{-k_N x\} \tag{2.25}$$

takes an exponential form, where k_N represents the inverse of the penetration depth of the pairs into the normal metal [82]. However, close to the interface, this is not so due to the fact that the assumptions of equation 2.25 do not apply. This emphasizes the importance of experiments where one can measure the proximity effect in particular close to the interface. When such a normal metal is thinner than ξ_N, the entire layer turns superconducting and the lowest value $\Delta(x = \text{thickness of N})$ is denoted as the induced gap Δ_{ind}.

This concept also transfers to a topological insulator in the place of a normal metal. Here, the superconductor in proximity with a 3D topological insulator induces a pairing potential in the topological surface state and the 2D Dirac states open up an induced gap Δ_{TSC}.

2.4.2 Majorana zero modes in 3D TI-superconductor systems

The study of topological insulators and superconductors in heterostructures in the pursuit of topological superconductivity is heavily motivated as a host for Majorana zero modes. As opposed to the spin-singlet superconductivity discussed in section 2.2, Majorana zero modes are expected to arise in spin-triplet superconductors e.g. p-wave superconductors. Applying the corresponding pairing symmetry in 2.11 as $\Delta_k = \Delta_0(k_x + ik_y)(\sigma_x + i\sigma_y)$, and diagonalizing the Hamiltonian gives eigenvalues

$$E_k = \pm\sqrt{(\epsilon_k - \mu)^2 + (\Delta_0|k|)^2}. \tag{2.26}$$

This differs from the s-wave eigenenergies in equation 2.17 in that the gap term is now k-dependent. For large energies, the change in spectrum is negligible. However, Read and Green [83] describe a significant difference for small energies $(\epsilon_k - \mu) \to -\mu$, when the spectrum evolves similarly to that of relativistic Dirac fermions. In such a system, when one introduces a domain wall between a trivial superconducting state and a non-trivial topological superconducting state, it creates a spectrum with linear Majorana modes residing at the center of the domain wall. Experimentally, for example, in a p-wave superconductor, this can be created by a vortex with a magnetic field, where Majorana modes may be hosted at the core of the vortex, where Δ disappears.

Fu and Kane described a p-type superconductor to be artificially created when a topological insulator is brought in close proximity to a conventional s-wave superconductor [47]. Such a system, in the presence of a domain wall between superconducting order parameters, may also host Majorana modes. They described this with a BdG Hamiltonian, with pairing term consistent on both the TI and the superconducting sides, providing a spectrum as given by:

$$E = \sqrt{|\Delta|^2 + (v_{\mathrm{F}}|k| \pm \mu)^2} \tag{2.27}$$

which is analogous to the p-wave superconductor in equation 2.26, and behaves with similar dispersion in the regime $\mu \to 0$ with a mass term Δ. This mass term (which can be tuned to close the gap in the spectrum), if allowed to spatially flip sign, creates a Majorana mode localized where $\Delta(x) = 0$. It has a linear dispersion as the p-wave superconductor edge state. This description of topological superconductivity motivates the creation of systems such as that investigated in this thesis. These systems show potential for engineering proximity effects as the induced gap on the topological insulator in the immediate vicinity of the superconductor. The lateral mesa edge makes this accessible for probing (akin to figure 2.7 described later).

While the measurements of Majorana modes are beyond the scope of this thesis, the picture below is provided to understand the design of the samples and the choice of materials. We begin by constructing the ingredients for the Majorana modes in a 3D TI – s-wave superconductor system. Then, we proceed to pinpoint the experimental challenges in probing these modes, that factor into the sample design. We know that the edge modes of the quantum spin-Hall insulator are protected from backscattering by time-reversal symmetry. To gap them out, we need to break time-reversal symmetry,

which can be done by a magnetic field. The magnet and the superconductor both introduce a gap in the helical edge, through different physical mechanisms. We can capture this behaviour with the following Bogoliubov-de Gennes Hamiltonian for the surface state

$$H_{\mathrm{TSC}} = \underbrace{(-iv\sigma_x\frac{\delta}{\delta x} + \sigma_y k_y - \mu)\tau_z}_{\mathrm{QSHI}} + \underbrace{m(x)\sigma_z}_{\text{Zeeman effect}} + \underbrace{\Delta(x)\tau_x}_{\text{Superconducting pairing}} \tag{2.28}$$

where σ are Pauli spin matrices and τ the Pauli isospin matrices acting on the electron-hole space [5]. The first term is the surface Hamiltonian of the quantum spin-Hall insulator, describing opposite spins moving in opposite directions, at a chemical potential μ. The second term, the Zeeman term introduced with an external magnetic field, breaks the time-reversal symmetry. The third term describes the superconducting pairing. The formation of a vortex in the superconductor, by magnetic field or defect, means that the Δ is suppressed at the core, going to 0 at the center, and the superconducting phase winds by 2π around a closed path surrounding it. The strength of the Zeeman field $m(x)$ and the pairing $\Delta(x)$ both depend on position. At a domain wall where the mass term $\Delta(x)$ changes sign, the Hamiltonian yields a Majorana mode. If one introduces a vortex, this can be regarded as being surrounded by a domain wall. An unpaired Majorana mode must come with a second mode somewhere in the system. There are two such locations in the system where the superconducting gap closes, the boundary of the system and at the core of a vortex. The experimental challenge in identifying this zero-energy mode lies

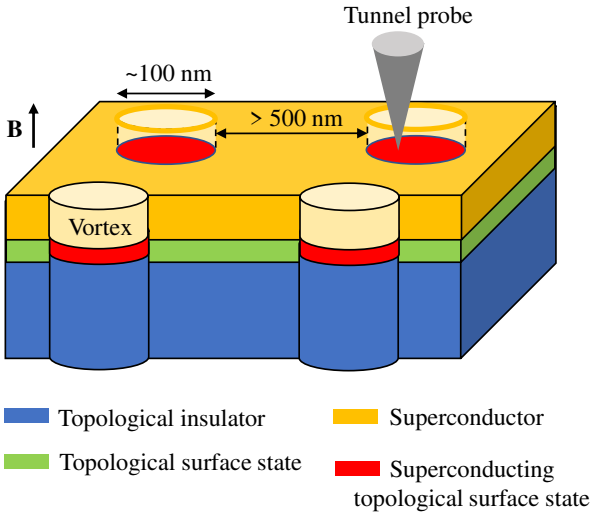

Figure 2.7: **Engineering topological superconducitvity** Pierced superconductor on the topological insulator creates proximity-induced superconductivity in the topological surface state inside the hole (radius∼coherence length). The lateral mesa edge between the superconductor and topological insulator is accessible with a tunnel probe. Figure based on [13, 84]

in its energetic resolution from other sub-gap states that can also exist in vortices, that can lie close in energy and are called Caroli de Genne states (CdG states) [24]. These are low-energy excitations at discrete energy $E_{\mathrm{CdG}} = \pm n\Delta^2/E_{\mathrm{F}}$ ($n = 1/2, 3/2, 5/2...$). While the typically small Δ/E_{F} makes it challenging to experimentally resolve them, they have been observed in higher T_c superconductors like FeTeSe [4]. For typical s-wave superconductors like Nb, the CdG states overlap with the Majorana states [28]. Thus, many experimental works of topological insulator-superconductor systems that show zero-bias peaks remain ambiguous due to their indistinguishability from CdG states. Apart from pushing the boundaries of experimental capabilities, one approach to solving this problem was proposed by Rakhmanov[13]: remove the superconductor, without compromising the ingredients for the Majorana. This would translate to a scenario like figure 2.7, where holes are pierced in the superconducting film with a relevant size $R \simeq \xi$ comparable to the coherence length of the superconductor ($\sim 100\,\mathrm{nm}$). Such a proposed device consists of an array of holes spaced by a relevant distance, where vortices may be pinned in the presence of a magnetic field, and probed by an STM. This allows for lateral mapping of the proximity superconducting gap, Majorana modes and the possibility to tune the flux in each vortex. This can provide a rather strong fingerprint for the Majorana, in that, odd/even flux quanta through the holes make for an oscillating appearance and disappearing of the Majorana mode at zero bias.

The piercing of the superconductor with holes comparable in size to the coherence length relaxes the energy resolution demands. The next nearest subgap state is given by [13, 25]

$$E_1 - E_{\mathrm{F}} \approx \frac{0.83\Delta^2}{\sqrt{\Delta^2 + (E_{\mathrm{D}} - E_{\mathrm{F}})^2}} \tag{2.29}$$

where Δ is the induced gap in the TI and E_{D} the energy of the Dirac cone crossing, called the Dirac point. This brings us to the next sample design factor, the choice of materials, which is limited by the extent of mismatch in the Dirac point with respect to the Fermi level. This must also take into consideration the influence of the superconductor on the Dirac point itself, due to e.g. doping effects at the interface.

3 Experimental methods

The framework of this thesis comprises primarily of two surface science probing techniques, namely, angle-resolved photoemission spectroscopy (ARPES) and scanning tunneling microscopy (STM). While they both detail atomic and electronic structures of materials, they work on different length scales. ARPES probes a material on a length scale of 1 μm to 1 mm, depending on the dimension of the focussed incident beam, and maps the electronic bandstructure of materials in the k-space. STM is capable of imaging atomic arrangements on a conductive surface and probing electronic properties in a sub-nm length scale in the form of the local density of states in real space. In the following sections, the principles of both methods are briefly summarized.

3.1 Angle-resolved photoemission spectroscopy

ARPES is a means to probe the electronic structure of solid material surfaces. It is possible to obtain the electronic band structure E(k) in momentum space by momentum-based acquisition of the surface electrons that are emitted upon incidence of a photon of energy $h\nu$. Einstein's interpretation [85] of the photoelectric effect in terms of absorption of quantized light particles causing excitation of electrons from a material can be summarized in the following relationship, visualized in figure 3.1 (b)

$$E_{\text{kin}} = h\nu - \Phi - E_{\text{B}} \tag{3.1}$$

where $h\nu$ is the energy of the incident photon, E_{kin} is the kinetic energy of electron emitted from the surface of the solid in a vacuum, E_{B} is the binding energy of the electron with respect to the Fermi level E_{F} and Φ is the work function of the material, which is the barrier the electron needs to overcome in order to escape (typically 4-5 eV for metals). In ARPES, the kinetic energies of the photoelectrons are resolved based on the escape angles, which is a function of the surface k-vector. The incident photon is

supplied by a beam of monochromatic radiation of a certain energy $h\nu$ either by a gas-discharge lamp, LASER, or synchrotron beamline. The emitted electrons are typically collected by a hemispherical electron energy analyzer[1] through a slit aperture. It detects electrons of specific kinetic energy $E_{\text{kin}}^{\text{out}}$ and emission direction described by azimuthal and polar angles Θ and ϕ [87] (figure 3.1 (a)). The momentum vector components are then described by:

$$k_x = \frac{1}{\hbar}\sqrt{2mE_{\text{kin}}^{\text{out}}}\sin\Theta\cos\phi \tag{3.2}$$

$$k_y = \frac{1}{\hbar}\sqrt{2mE_{\text{kin}}^{\text{out}}}\sin\Theta\sin\phi \tag{3.3}$$

$$k_z = \frac{1}{\hbar}\sqrt{2mE_{\text{kin}}^{\text{out}}}\cos\Theta \tag{3.4}$$

and consequentially the magnitudes of the momentum vector parallel and perpendicular to the surface of the solid are respectively given by:

$$k^{\text{out}} = \frac{1}{\hbar}\sqrt{2mE_{\text{kin}}^{\text{out}}} \tag{3.5}$$

$$k_{\parallel}^{\text{out}} = \sqrt{k_x^2 + k_y^2} \tag{3.6}$$

$$k_{\perp}^{\text{out}} = k_z \tag{3.7}$$

Usually, the count of photoelectrons as a function of their kinetic energy and angle is displayed as a 2D spectrum $I(E_{\text{kin}}^{\text{out}}, k_{\parallel}^{\text{out}})$ [88]. While equation 3.1 can relate the binding energy to the kinetic energy of the exiting electron, correlating the initial and final momentum vectors is more complicated. A primary assumption is that the photoelectrons exit the system faster than the system relaxes [89]. This is called the sudden approximation. It neglects the interaction between the photoelectron and the relaxation mechanisms, thereby treating it as an independent single-particle picture. This assumption will not hold for slower photoelectrons (lower k) whose escape time will be closer to the system's relaxation time [87].

One approach was made by Berglund and Spicer in [91] to reduce the photoemission event into three independent steps, using the three-step model described in figure 3.1 (c). First, photo-excitation results in a transition of bulk states from occupied bands

[1] In more recent developments, the energy resolution is also accomplished by a time-of-flight-based analyzer [86]

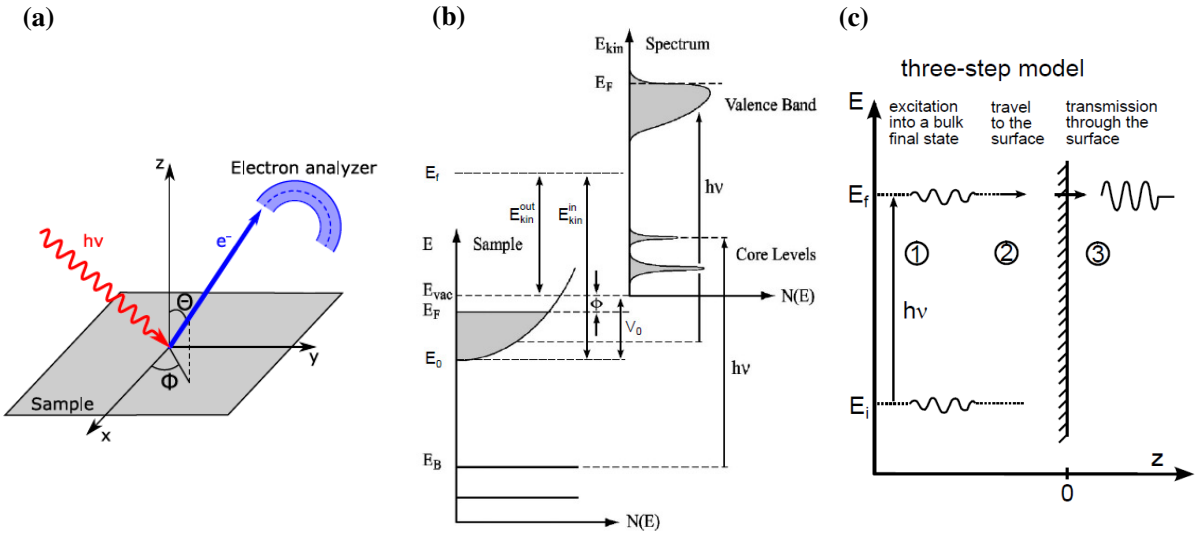

Figure 3.1: **Overview of the photoemission process in ARPES. (a)** Sketch of typical geometry in ARPES: A photon source incident on a crystalline sample surface leads to the emission of electrons at emission angles Θ and ϕ with a certain kinetic energy E_{kin}. The electron distribution in intensity $I(E_{\text{kin}}, \Theta, \phi)$ can be measured by a hemispherical analyzer. Figure adapted from [87]. **(b)** Photoemission process: On the left is the energy distribution of the crystal in binding energy E_{B}. The grey region marks the density of states in the valence band with all states occupied up to the Fermi level $E_{\text{B}} = 0 \equiv E_{\text{F}}$. The work function of the crystal and vacuum energy is depicted as Φ and E_{vac}. Upon incident photon excitation at $h\nu$, electrons at initial state E_i are converted to final state E_f whose spectrum is depicted on the right as a function of their kinetic energy $E_{\text{kin}}^{\text{out}}$. In order to be detected, the photoelectrons must be excited above the vacuum level $E_{\text{vac}} = E_{\text{F}} + \Phi$. **(c)** Three-step model of the photoemission: (1) Optical excitation of initial states E_i to final Bloch states E_f (2) travel of excited electrons to the surface (3) escape of these electrons through the surface barrier potential into the vacuum. Figures adapted from [90].

to unoccupied bands, corresponding to the photoenergy such that $E_f - E_i = h\nu$. Since the photon momentum is much smaller than electron momentum, the conversion can be applied in a reduced Brillouin zone in a way that $k_f = k_i$. In an extended zone, it is connected via a reciprocal lattice vector $\vec{G}$, $\vec{k}_f = \vec{k}_i + \vec{G}$, and transitions can happen between $\vec{k}$ points connected by the $\vec{G}$ vector.

Second, the excited bulk electron is transported to the surface. In the presence of inelastic scattering, there is a loss of kinetic energy. ARPES is, therefore, a surface-sensitive spectroscopic method, with a probing depth that is much smaller than the light penetration. The inelastic mean free path, is the average distance between two inelastic scattering processes between the photoelectrons and other electrons, phonons,

or defects. This length scale λ determines how the photoelectron intensity $I(d)$ develops as $I(d) = I_0 e^{-\frac{d}{\lambda}}$ where I_0 is the initial photoelectron intensity before any scattering and d the path length up the surface. The main contribution to the undisturbed photoelectron intensity therefore originates from a probing depth (typically $\sim 3\lambda$). Inelastically scattered electrons contribute to a broadened largely featureless background called inelastic or secondary background. Unscattered or elastically scattered electrons provide sharp features indicative of the spectrum. Typical inelastic mean free paths range from $5 - 100\,\text{Å}$, which makes the probing depth highly surface sensitive. Kinetic energies in the range of $40 - 100\,\text{eV}$ provide for the most surface-sensitive probe. On the other hand, Xenon excitation ($E_{\text{kin}} = 4 - 5\,\text{eV}$) gives a higher bulk-sensitivity spectrum than that obtained with Helium excitation ($E_{\text{kin}} = 4 - 21\,\text{eV}$).

Third, when the photoelectron that reaches the surface has a kinetic energy large enough to overcome the work function of the surface material, then it can escape from the bulk. At this point, the total moment is not conserved since the perpendicular component is reduced in overcoming the barrier. Also, the periodicity of the crystal does not extend into the vacuum. However, the parallel component of the moment remains conserved. Hence

$$k_{\parallel}^{\text{in}} = k_{\parallel}^{\text{out}} = \frac{1}{\hbar}\sqrt{2mE_{\text{kin}}^{\text{out}}}\sin\theta \tag{3.8}$$

A reasonable assumption for the non-conserved perpendicular component of the momentum comes from the near free-electron description of final states in the material as adopted from [87].

$$E_f(k) = \frac{\hbar^2 k^{\text{in}2}}{2m} - V_0 = \frac{\hbar^2(k_{\parallel}^{\text{in}2} + k_{\perp}^{\text{in}2})}{2m} - V_0 \tag{3.9}$$

where V_0 is the crystal potential. Thus, in reference to the vacuum $E_f(k) = E_{\text{kin}}^{\text{out}}(k)$. This gives us

$$k_{\perp}^{\text{in}} = \frac{1}{\hbar}\sqrt{2m(E_{\text{kin}}^{\text{out}}\cos^2\theta + V_0)} \tag{3.10}$$

Without knowing the crystal potential, often estimated by theoretical calculations or deduced from measurements in different BZs, the perpendicular component is uncertain. However, in the case of 2-dimensional states, like low-dimensional systems or surface

states, the electronic structure is dominated by the parallel component of $\vec{k}$. ARPES can then provide a complete set of information based on exit angle and kinetic energy from equations 3.1 and 3.8. Further details on ARPES can be obtained from [36, 87, 90, 92–94].

3.1.1 Experimental details: ARPES instrument in PGI-6

The ARPES experiments were conducted in PGI-6, Forschungszentrum Jülich (Group L. Plucinski). The chamber with the most significant components depicted in figure 3.2, is built out of a μ-metal alloy with very high magnetic permeability, shielding the insides of the chamber from stray fields such as a geomagnetic field ($25 - 40\,\mu T$) and ensuring no Lorentz force deflection of the electrons reaching the detector.

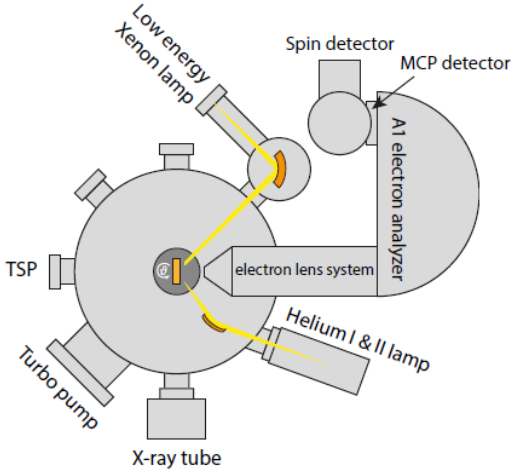

Figure 3.2: **Simplified scheme of the PGI-6 ARPES chamber**. Figure adapted from [81]

This setup uses a hemispherical electron energy *A1* type analyzer comprising electrostatic lens systems and two hemispherical plate capacitors that act as an energy filter. Photoelectrons emitted by the sample are focussed by the electrostatic lens system onto a slit at the entrance of the capacitor plates. The electrons that pass the slit enter between the concentric capacitor plates. These plates are held at a potential difference, V, between the inner and outer hemispheres, and set the incoming electrons in a circular trajectory whose radius is determined by the applied $V + E_{\text{kin}}$. Due to this energy-dependent deflection, the electrons are filtered according to their kinetic energy. The transmitted electrons arrive at a multichannel plate that detects, multiplies and visualizes them as a two-dimensional image of kinetic energy vs. emission angle (polar angle). In order to change the azimuthal angle, the sample must be rotated. The system

is equipped with a universal manipulator that can move in all three spatial directions and rotate around the azimuthal angle θ. The manipulator hosts a liquid helium flow cryostat, allowing to cool down of the sample to 15 K as determined by analysis of the metallic Fermi-Dirac distribution. Thermal contact between the sample and the manipulator is determined mechanically by two screws that press the sample holder onto the manipulator, tightened by a custom-made vacuum screwdriver. Further details on the setup can be found in [95].

3.2 Scanning tunneling microscopy and spectroscopy

3.2.1 Principles of scanning tunneling microscopy

The surface of a conducting or semi-conducting material can be studied in atomic detail using the strong distance dependence of quantum tunneling of electrons using STM. By applying a bias across a tip-sample junction a tunneling current is created, which is then maintained using a feedback system. As the tip is scanned over the sample, the variation of the tip as the feedback tries to maintain the tunneling current translates to the topography map of the sample. In its most elementary model, we consider the tunneling to occur through a one-dimensional potential barrier of height U created by vacuum with tip and sample on either side. In the classically forbidden region of $E < U$, the solution is the tunneling wave function $\psi(z) = \psi(0)e^{-\chi z}$ where $\chi = \frac{\sqrt{2m(|U|-E)}}{\hbar}$ is the decay constant that describes electron tunneling into the barrier towards +z. The work function Φ of a material is defined by the minimum energy required to move an electron from the bulk to the vacuum level. Therefore, if the electrons involved in tunneling are lying close to the Fermi energy on both electrodes, we can replace $|U| - E$ by Φ. In the vacuum tunneling regime, a change in tip-sample distance of 1 Å translates to an order of magnitude in tunneling current $I(z) = I_0 e^{-2\chi z}$ given by the decay constant $\chi = \frac{\sqrt{2m\Phi}}{\hbar}$ for a typical work function of $\Phi \approx 5$ eV. Table 3.1 shows typical work functions and corresponding decay constants of common STM tip materials [96]. I_0 is the tunneling current defined at point contact.

The sensitivity is governed by decay constants smaller than typical atomic distances.

Binnig and Rohrer argued that the ability of STM to achieve drastic lateral resolutions (2 Å) arises due to vacuum tunneling allowing resolutions much smaller than the tip radius R if the tip-sample distance z is much smaller than tip radius [97].

Then, the tunneling current $I(z) \propto e^{-2\chi z}$ follows an exponential decay with a typical decay constant of $\chi \sim 1\,\text{Å}^{-1}$ and the current drops by an order of magnitude per Å tip-sample distance.

This one-dimensional model has been extended by Bardeen [98], and Tersoff and Hamann [99, 100] for 3D elastic tunneling assuming s-type tunneling or s-orbitals of the tip. Considering that commonly used tips like W and PtIr have tunneling p or d orbitals, Chen [101–103] extended the description to include such tip states by deriving a general sum rule. The sharper p_x and d_z orbitals, which typically dominate the tunneling current, provide a better lateral resolution enabling atomic resolution in STM measurements. An overview of these models is recounted below in the view of the access to the local density of states via STM experiments.

3.2.2 Scanning Tunneling Spectroscopy

STM provides a probe into the electronic structure of the sample via scanning tunneling spectroscopy (STS). By applying a bias voltage across the tip and sample, the Fermi level of the electrodes shifts with respect to each other. As the system seeks to achieve equilibrium, electrons will tunnel from the negative to the positive electrode. In the constant current mode of operation, the feedback strives to keep the tunneling current constant, by varying tip-sample distance. The tip-sample tunneling current can be described by a perturbation theory. The tunneling current flowing from the negative to positive potential, that is from the occupied states of the negative potential to the unoccupied states of the positive potential is given by:

$$I_{\text{np}}(\epsilon) = -2e\frac{2\pi}{\hbar} \mid M \mid^2 (\rho_{\text{n}}(\epsilon).f(\epsilon))\,(\rho_{\text{p}}(\epsilon + eV)\,.\,[1 - f(\epsilon + eV)]) \tag{3.11}$$

given the density of states of negative electrode $\rho_{\text{n}}(\epsilon)$ and positive electrode $\rho_{\text{p}}(\epsilon)$, Fermi distribution $f(\epsilon) = \left(1 + e^{\frac{\epsilon}{k_{\text{B}}T}}\right)^{-1}$ and transmission $\mid M \mid^2$.

The minority flow in the opposite direction that is flowing from the occupied states of

Element	Al	Au	Cu	Ir	Ni	Pt	Si	W
$\Phi(eV)$	4.1	5.4	4.6	5.6	5.2	5.7	4.8	4.8
$\chi(\text{Å}^{-1})$	1.03	1.19	1.09	1.21	1.16	1.22	1.12	1.12

Table 3.1: Work function and decay constants of selected materials

the positive potential to the unoccupied states of the negative potential can be described as:

$$I_{\mathrm{pn}}(\epsilon) = -2e\frac{2\pi}{\hbar} \mid M \mid^2 (\rho_{\mathrm{p}}(\epsilon + eV).f(\epsilon + eV)) (\rho_{\mathrm{n}}(\epsilon) . [1 - f(\epsilon)]) \tag{3.12}$$

Thereby, the net tunneling current that flows from the negative to positive potential is given by the sum of the two above integrated over a full energy range.

$$I(eV) = -\frac{4\pi e}{\hbar} \int_{-\infty}^{+\infty} \mid M \mid^2 \rho_{\mathrm{n}}(\epsilon)\rho_{\mathrm{p}}(\epsilon + eV) \{f(\epsilon) - f(\epsilon + eV)\} d\epsilon \tag{3.13}$$

The integral is simplified with the following assumptions. By lowering the operating temperature of an STM, the Fermi energies of the tip and sample are sharpened. At room temperature, the Fermi function cutoff is at $k_{\mathrm{B}}T = 25\,\mathrm{meV}$ and $k_{\mathrm{B}}T = 51.7\,\mu\mathrm{eV}$ at 600 mK. At the typical low-temperature operation of STM in this thesis (600 mK - 4.2 K), the energy scale ($51.7\,\mu\mathrm{eV} - 0.34\,\mathrm{meV}$) is much smaller than typical bias voltages of 100 meV, which makes it reasonable to assume a sharp Fermi level for the tip and sample, which means tunneling primarily occurs between these two Fermi levels. This simplifies Equation 3.13 to

$$I(eV)_{k_{\mathrm{B}}T \ll V} \approx -\frac{4\pi e}{\hbar} \int_{-eV}^{0} |M|^2 \rho_{\mathrm{n}}(\epsilon)\rho_{\mathrm{p}}(\epsilon + eV) d\epsilon \tag{3.14}$$

STS always provides a convolution between the tip and sample density of states. To eliminate the complexity of the problem, the tip is usually chosen to be a material of well-known flat (within a reasonable $\pm 100\,\mathrm{meV}$ of Fermi energy) density of states such as W, Pt, Cr or Au. Thus, in a system where the sample is biased negatively with respect to the flat density of states tip we have:

$$I(eV) \approx -\frac{4\pi e}{\hbar}\rho_{\mathrm{tip}}(0) \int_{-eV}^{0} |M|^2 \rho_{\mathrm{sample}}(\epsilon) d\epsilon \tag{3.15}$$

The $I(V)$ in equation 3.15 reflects features of the sample bandstructure enabling access to information like the bandgap. However, the conductance dI/dV as a function of bias sweep provides a more detailed picture. Spectroscopy is typically acquired by turning off

the feedback intermittently in order to maintain a tip-sample distance while obtaining the tunnel current response while sweeping bias. Bardeen's approach [98] assumed that under typical circumstances, the matrix element is independent of the energy. This allows for the matrix element to be taken out of the integral

$$I(eV) \approx -\frac{4\pi e}{\hbar}|M|^2 \rho_{\text{tip}}(0) \int_{-eV}^{0} \rho_{\text{sample}}(\epsilon) d\epsilon \tag{3.16}$$

Specifically, this is a reasonable assumption when the tip and sample have independent DOS, i.e. the states decay into the vacuum without significant overlap. The tunneling matrix is then largely determined by the tunneling barrier. When the applied voltage is much smaller than the work functions of tip and sample, one can assume a square tunneling barrier in between tip and sample. Additionally, the tip-sample distance is assumed to be large (> 5 Å) so that the tunneling can be treated as a small perturbation.

The *a priori* assumption that the tunneling matrix element M is constant in energy is correct if the energy scale is few eV. The variation of $|M|$ in energy must then be considered. It depends on the dominant wave function of the tip atom and the wave function being probed on the sample.

Shortly thereafter, J. Tersoff and D. R. Hamann [99, 100] provided an analytical solution for the matrix element, based on Bardeen's model of a simplified tunneling system with an atomically sharp tip. This helped to interpret the STS with regard to the sample states. In their solution, they considered the tunneling contribution from the last atom of the tip, described by an s-like orbital wavefunction. The density of states of the tip over the energy range of interest is considered constant. Chen expanded the Tersoff-Hamann model by generalizing the wave functions for the tip, which allowed for tunnel matrix elements for different tip orbital. For the widely used expression for tunneling current in STM, we assume a spherical tip model with the last atom of the tip probing electronic states on the sample with an s-orbital. In this case, the dI/dV probes the LDOS of sample at the center position of the s-orbital. Considering only elastic tunneling, i.e., the energy is conserved during tunneling, and assuming low voltage ($eV \ll \Phi$), the tunneling current is

$$I(eV) = \frac{16\pi^3 C^2 \hbar^3 e}{\chi^2 m^2} \rho_{\text{tip}} \int_{-eV}^{0} \rho_{\text{sample}}(\epsilon) d\epsilon \tag{3.17}$$

where C is a constant.

In the typical case for spectroscopy, the barrier height is largely constant and the tip-sample distance is constant as the feedback is turned off, allowing us to sweep the bias voltage and record the corresponding tunneling current, which provides the integral of the local density of states (LDOS) in the energy range. For a constant LDOS of tip and low temperatures (such that the Fermi-Dirac distribution becomes a delta function),

$$\frac{\partial I_T}{\partial V}\Big|_{V_T} = \rho_{\text{tip}}\, \rho_{\text{sample}}(eV_T) \tag{3.18}$$

Experimental measurement of LDOS and limitations to energy resolution

The tip is positioned at a distance z above the sample determined by the chosen V_T and I_T. If V_T is ramped with the feedback off, and the current recorded at this fixed z, the resulting $I_T(V)$ allows for a numerical calculation of the LDOS. However, the typically noisy tunneling current impairs this process.

The more common experimental approach as also used in this thesis employs a lock-in method. One adds a small modulation to the bias voltage with an amplitude V_{mod} at frequency f_{mod}. The resulting tunneling current is multiplied with a reference signal also at f_{mod} and integrated over a time interval $t > 3\tau_{\text{lock-in}}$. The output amplitude read out by a Lock-in amplifier is proportional to the first derivative of the $I(V_T)$ curve at V_T. For the measurement of a $^{dI}/_{dV}(x, y)$ at a selected V_T, the dI/dV signal is recorded in parallel with the standard constant-current image. In contrast, the tip-sample distance for $^{dI}/_{dV}(V)$, is determined by the stabilization parameters V_{stab} and I_{stab} prior to scanning V.

The energy resolution [104] is limited by thermal broadening and V_{mod} as

$$\Delta E \approx \sqrt{(3k_{\text{B}}T)^2 + (2.5eV_{\text{mod}})^2} \tag{3.19}$$

To achieve a high energy resolution, spectroscopy must be taken at low temperatures with small modulation amplitudes. To this end, the working temperature for the STM

used in this thesis was reduced from 1.2 K [105] to 640 mK by the implementation of He-3 operation through a Joule-Thompson stage as described in the following section. However, it is worth noting here that the experimentally relevant temperature is not necessarily the measured temperature, by a sensor spatially separated from the tunneling event. In addition, at low temperatures, the temperature T_{el} of the electron system may differ from the lattice temperature T.

The reduction of modulation voltage demands high mechanical stability and calls for the minimization of electronic noise in the tunnel current and bias voltage lines, as well as modulation voltage itself by careful design of the instrument. Any potential fluctuation at f_{mod} between tip and sample can lead to a reduction of the energy resolution and smearing of features and an apparent enhancement in electron temperature. The influence of finite temperature and the corresponding thermal energy should ultimately be the limiting factor for approaching the best resolution. The performance indicator for the setup is therefore the characteristic electron temperature, which is presented for the STM setup in chapter 5.

3.3 Operation and characterization at 640 mK

3.3.1 Operation of the STM with He-3

The STM and cryostat (designed by Cryovac GmbH and Co.) are described in detail in the dissertation of Dr. Florian Muckel [105]. The cryostat consists of radiation shields, surrounding a 20 l LN_2 tank and 10 l LHe tank, that screens the sample from external thermal radiation. This enables a temperature reduction at the sample down to ≈ 4 K. Further cooling down is possible via the Joule-Thomson (JT) stage. He-3 gas is brought into a capillary at room temperature at pressure $p \simeq 1.7$ bar using a **Gas handling system** (GHS). The GHS, consists of a 15 l reservoir with 180 mbar of He-3, from which the gas can be inserted into a low-pressure line in pulses (see Appendix 7.1). This allows for the gradual introduction of the He-3 into the GHS so as to not develop a drastic pressure difference across the scroll pump (operating between $\approx 8 \times 10^{-3}$ mbar to 800 mbar). A 1 μm metal filter thereafter ensures the filtering of particles expunged from the rotating tip seal in the scroll pump. The He-3 is then compressed into a high-pressure line by means of a compressor (operation up to 3 bar overpressure). The He-3 gas in the high-pressure line is thereafter filtered through a LN_2 cold trap, consisting of

an active sintered material dipped in a LN_2 dewar, before entering the cryostat with a maximal pressure of 1.7 bar. This marks the onset of the operation of the GHS, when the He-3 begins to flow through the JT-stage.

The He-3 gas that enters the cryostat is precooled at counterflow heat exchangers, filtered, and cooled to $T = 4.2\,\mathrm{K}$ at a pipe that is thermally anchored to the LHe_4 tank [105]. This is followed by a second counterflow heat exchanger, which uses the backflow of the cold He-3 gas that ends at the expansion state, using a small diameter capillary. The precooled He-3 gas effectively undergoes the JT effect, thus cooling down the STM, and subsequently reaches its liquefication temperature at 3.3 K. Typical time span to reach thermal equilibrium at $T_{\mathrm{He-3}} \approx 640\,\mathrm{mK}$ is about 4.5 hours. The normal operating pressure (measured in the high-pressure line) of the He-3 gas in thermal equilibrium is 800 mbar. More details can be found on the operation and automation of the GHS in [106].

3.3.2 Characterization of the STM at 640 mK

Stability of image

The STM was characterized on a Au(111) single crystal with a W-tip. The Au(111) crystal was prepared with repeated cycles of Ar-ion sputtering with partial pressure $p_{\mathrm{Ar}} = 1 \times 10^{-5}\,\mathrm{mbar}$ and sample current during sputtering was $I_e = 3\,\mu\mathrm{A}$ for 15 minutes leading to an estimated etch rate $\approx$ 2 ML/minute, followed by annealing at T =530 °C for 20 mins between each cycle. Figure 3.3 (a) shows a constant current image of the surface showing flat terraces with the herringbone reconstruction [107–110] formed by stress-induced surface contraction along the $[\bar{1}10]$ direction which is perpendicular to the zigzag ridges. The ridges are formed by surface atoms occupying the bridge sites between fcc (25 Å wide) and hcp (38 Å wide) region [111], creating a periodicity (23 atoms with 2.83 Å) of 63 Å as indicated in figure 3.3 (c). Figure 3.3 (b) shows part of the herringbone reconstruction at atomic resolution, measured at $V = 50\,\mathrm{mV}$ and $I = 8\,\mathrm{nA}$.

For the scanning on Nb, such as presented in chapter 5, the tip was prepared on such Au(111) surfaces priorly. The tip was coated with Au by dipping it 1-2 nm into the crystal. A spectroscopic measurement as that presented in figure 3.3 (d), is achieved after stabilizing the tip height at $V_{\mathrm{stab}} = 1\,\mathrm{V}$ and $I_{\mathrm{stab}} = 1\,\mathrm{nA}$ followed by ramping the bias from 1 V to -1 V, while maintaining the tip stationary with the feedback off. A clear

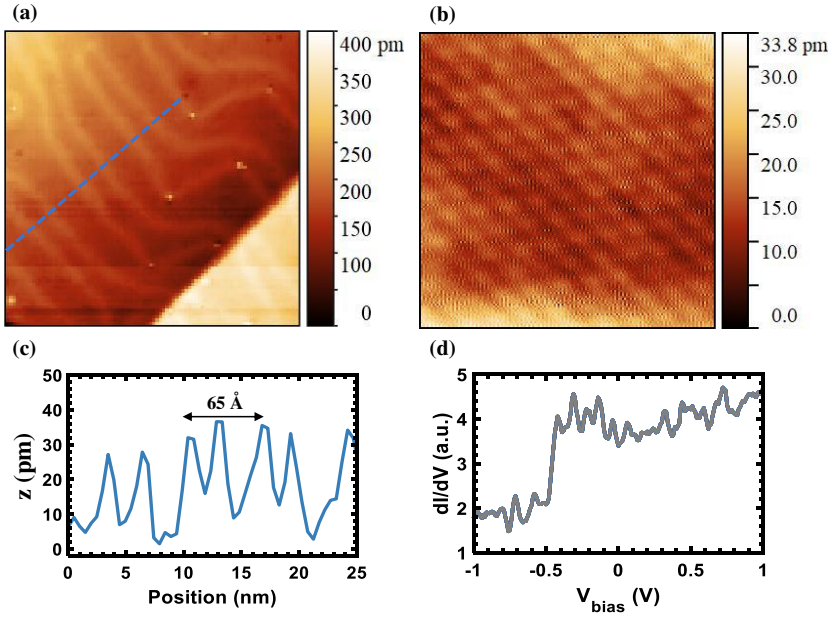

Figure 3.3: **Measurements on Au(111) demonstrating stable imaging ability (a)** Constant current image on Au(111) scan area $30 \times 30\,\mathrm{nm}^2$ with monoatomic steps (height 2.4 Å) separating flat terraces where the herringbone reconstructions can be observed ($V = 50\,\mathrm{mV}$, $I = 2\,\mathrm{nA}$). **(b)** Atomic resolution image on $3 \times 3\,\mathrm{nm}^2$ area with bright and dark regions depicting part of the herringbone pattern as bright and dark regions ($V = 50\,\mathrm{mV}$, $I = 8\,\mathrm{nA}$). **(c)** Height profile along the blue line in (a) traces 3 periodic herringbone patterns. **(d)** dI/dV spectrum taken on a single point ($V_{\mathrm{stab}} = 1\,V$, $I_{\mathrm{stab}} = 1\,\mathrm{nA}$)

suppression in the density of states is observed as the bias voltage passes the surface state band edge at $V \approx -0.5\,V$ [112].

The stability of the STM with respect to vibrations was measured on a different sample, W(110) single crystal with 0.5 ML of Pb evaporated on top, in configurations with mechanical pumps running and switched off. These mechanical pumps are typically operated during load lock operation when new samples/tips are introduced or sample preparation with process gases. The turbomolecular pump which is directly mounted onto the aluminium frame of the system and an additional scroll pump is positioned on the floor inside the lab, are both operating for figure 3.4 (a)–(c) and are switched off for figure 3.4 (d)–(f). The W(110) crystal was prepared for Pb evaporation first with flashing cycles at 2500 °C, creating migrating carbon contamination forming R(15 × 3) surface reconstructions [113]. Subsequent annealing is done in an oxygen partial pressure to remove these C-sites. Thereafter, 0.5 ML of Pb was evaporated from a W-crucible at a flux of 25 nA for 10 minutes forming Pb clusters, likely nucleating at C-sites not

completely eliminated from the oxygen-annealing.

The vibration movement of the tip with respect to the sample was characterized by switching off the feedback while recording the tunnel current for 1 second. A part of this time trace $I(t)$ is shown in figure 3.4 (a) with an inset showing the $I(z)$-curve used to connect the $I(t)$ data to $z(t)$ data. The resulting $z(t)$-noise is presented as a histogram in figure 3.4 (b). A Gaussian fit of this histogram (red curve) yields a σ-width of $G = 3.2\,\mathrm{pm}$. For standard tip preparation and sample characterizations, the pump operation is hence not detrimental. This stability also suffices for resolving superstructures (e.g. herringbone pattern on Au(111)), atomic steps and stable scanning on Nb. In figure 3.4 (c), the frequency dependence of the noise is plotted over the bandwidth of the current preamplifier (1 kHz). It shows a small distinct contribution from the operating frequency of the turbomolecular pump at 1 kHz.

The stability measurements were repeated without mechanical pumps running. The stability measurements are shown in figure 3.4 (d)–(f). It shows a tip-sample displacement of $G = 2.7\,\mathrm{pm}$, marginally improved from (b). Peak around 650 Hz might relate to the operation of the JT-stage as indicated by the lack of prominence at 4 K [105].

The noise level without pumps remains less than $1\,\mathrm{pm}/\sqrt{\mathrm{Hz}}$ below 200 Hz and less than $100\,\mathrm{fm}/\sqrt{\mathrm{Hz}}$ above 200 Hz, with an average of about $10\,\mathrm{fm}/\sqrt{\mathrm{Hz}}$. In both cases presented above, the passive damping was in operation and the Cernox temperature sensors were turned off.

The achieved noise level is larger than in similar STMs ($G \approx 1\,\mathrm{pm}$) probably due to the direct mounting of the STM to the JT-stage.

Sample drift

The sample drift at $T \approx 640\,\mathrm{mK}$ is evaluated on W(110) with 0.5 ML Pb clusters. A series of 13 images were recorded over a span of 8.7 hours. Figure 3.5 (a) is a $15 \times 15\,\mathrm{nm}^2$ image exhibiting multiple Pb clusters. The Pb clusters maintain their distinct shapes and do not noticeably alter during scanning over these 8.7 hours. Prior to these images, the same region was scanned for 12 hours with the same parameters to exclude creep effects from the piezotube as a source for lateral displacement. An automated Matlab script is applied to enhance features in the topography image with a global plane fit, and a band-pass filter corresponding to 2–4 pixels, creating the images shown in figure 3.5 (b).

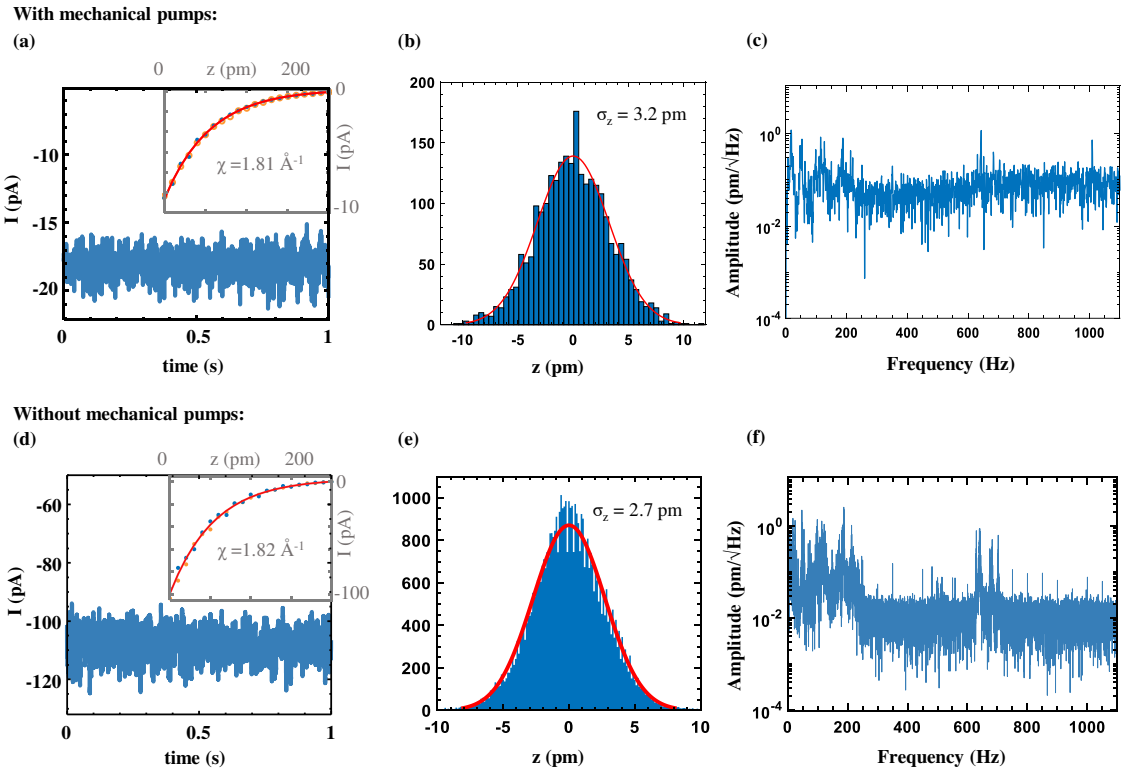

Figure 3.4: **Vibratoinal noise measured at 640 mK in tunnel current**. Measurements **(a)**–**(c)** made **with mechanical pumps** running (a) Tunneling current measured without feedback on W(110) at $I_{\text{tunnel}} = -10\,\text{pA}$, $V_{\text{bias}} = -400\,\text{mV}$. Inset: $I(z)$ curve at the same position, with exponential fit providing decay constant $\kappa = 1.81/\text{Å}$ and $I_{\text{max}} = -11\,\text{pA}$. **(b)** Histogram of the z-noise (blue bars) fit with a Gaussian (red curve) yields $\sigma_z = 3.2\,\text{pm}$. **(c)** Frequency spectrum of the z-noise. **(d)**–**(f)** Similar measurements **without mechanical pumps** running.

The drift is then detected by finding the minimal deviation in the interpolated minima and maxima between two consecutive images. Figure 3.5 (c) shows the absolute value of the deviation vectors between the first image and subsequent images, the linear fit providing the long-term lateral drift as $v_{d_{xy}} = 13\,\text{pm/h}$. Figure 3.5 (d) shows the displacement component in the slow scan direction d_y.

Figure 3.5 (e) shows the vertical displacement of the scanner, i.e. drift in the direction perpendicular to the sample surface (z-drift). It is calculated as the deviation in the average scanner z-value of each image with respect to the initial image. The average scanner z-value is computed over all image pixels after the lateral drift is compensated. The resulting z-drift is $v_z = 0.6\,\text{pm/h}$. Figure 3.5 (c) also shows the STM temperature as recorded during the measurement interval. The marginal temperature change of 1 mK

and linearity in d_{xy} are suggestive of remaining creep effects, which would require a longer waiting period to eliminate. However, the achieved stability will be sufficient for measurements on the single-atom level.

Over the course of 100 hours (period of filling of nitrogen tank), the temperature changes in the operating STM can range from $12 - 45\,\mathrm{mK}$ with higher changes observed with the use of the coarse motion stage. In general, drift and creep depend on factors such as the filling level of nitrogen, helium and other heating sources, and scanning histories such as speed of scanning, scanning position and area of scan.

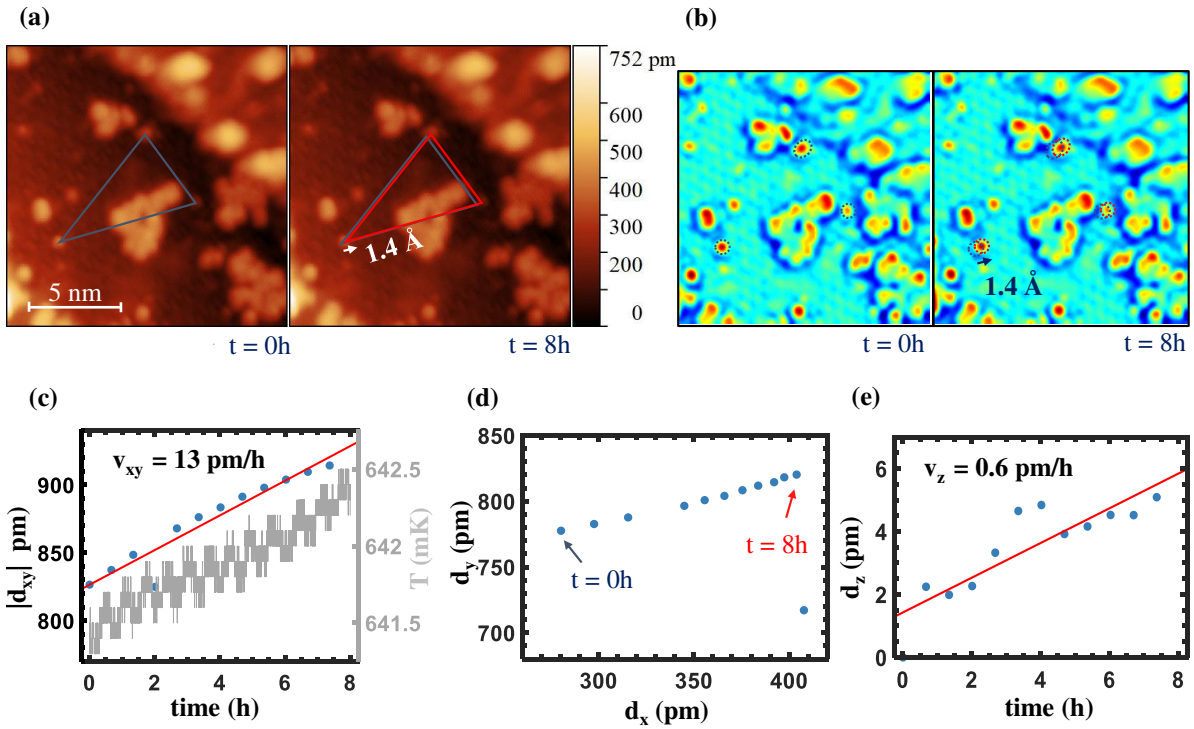

Figure 3.5: **Drift during STM operation at 640 mK. (a)** Constant current STM image of Pb clusters evaporated on W(110) crystal with R(15×3) carbon reconstructions. $15 \times 15\,\mathrm{nm}^2$, $I = 300\,\mathrm{pA}$, $V = 20\,\mathrm{mV}$, $v_{\mathrm{scan}} = 2.5\,\mathrm{nm/s}$ Blue and red triangles indicate displacement of individual features in the left image after a time interval of 8 hours on the right image. **(b)** Filtered images corresponding to (a) at time t = 0 and 8 hours. **(c)** Lateral displacement d_{xy} in time, with linear fit line (red) plotted along with temperature measured during the acquisition of all images. **(d)** Vector components of d_{xy} in (c), showing lateral displacement in fast (x) and slow (y) axis of subsequent images recorded at interval $\Delta t = 0.67\,\mathrm{h}$ per image. **(e)** Vertical displacement of the piezo-scanner during sequential scanning with feedback. A linear fit is shown in red.

4 Ultrahigh vacuum mask aligner

The study of lateral proximity effects at topological insulator/superconductor interfaces is experimentally challenged by the creation of lateral nanostructures with pristine interfaces. Lateral nanostructuring is the foundation for various fields of experimental research, such as mesoscopic physics, solid-state-based quantum computing, nanoelectromechanical systems (NEMS), and photonics. The most common fabrication processes involve electron beam or optical lithography, in which the use of solvent-based resists inevitably leaves residues that compromise the surface quality, especially for probing methods like ARPES and STM.

Fabrication of surface-sensitive samples has been an enduring challenge in condensed matter physics. It becomes ideal to fabricate samples in UHV and measure in situ, avoiding any exposure to ambient conditions. Attempts both in bottom-up as well as top-down fabrication approaches are discussed below. It is worth noting that each method comes with drawbacks that limit compatibility with UHV-suitable fabrication methods in surface science.

An example of a non-UHV compatible method is local anodic oxidation [114], which is a single-step nanolithography with sub-10 nm resolution [115]. It has been applied to fabricate mesoscopic structures in GaAs [116] or graphene [117, 118]. The choice of material is inevitably limited due to the essential step of oxidation.
There are UHV-based methods for nanostructuring that are focused on a particular material, such as defect charging of boron nitride below graphene [119]. This method enabled the fabrication of ultraclean graphene quantum dots of mesoscopic size to be probed by STM [120].

A notable bottom-up fabrication approach involves assembling individual atoms using scanning probe techniques [121–124]. An advantage is its capability to be automated [125, 126], which allows for the technique to be combined with standard mesoscopic device technology [127, 128]. However, the timescale of fabrication is at best a few weeks. The benefit of high precision at the atomic level [129–131] outweighs the tediousness of

more complex mesoscopic structures.

When exploring the possibilities for a more generalized application, the most conventional and widely implemented technique uses stencil mask lithography. The basic idea of shadow mask evaporation is to evaporate a material through a stencil onto the sample. The difference in the various methods lies then in (a) the type of mask used and (b) the method to align the mask with the sample. Both (a) and (b) will determine the limitations of its UHV compatibility and surface contamination.

The development of conventional complementary metal-oxide semiconductor (CMOS) compatible methods like electron-beam lithography [132] and focused ion-beam lithography [133] have enabled the fabrication of shadow masks with feature size less than 10 nm [134]. Larger throughput of such masks is possible by employing ultraviolet optical lithography [135]. The bigger challenge, therefore, is an appropriate method of sample-mask alignment, to bring the sample and mask close enough in order to minimize the penumbra during evaporation. The direct solution is rigidly placing the mask onto the sample [136–138]. This comes with a drawback of additional contamination of the sample [139] and difficulties to remove the mask inside UHV in order to subsequently measure with STM. One may circumvent this by creating rigid pillars to prevent direct contact between the mask and the sample. However, here the mask-sample distance is typically limited to tens of μm [140] and comes with additional limitations on creating patterned structures.

A more novel development incorporates the fabrication into scanning probe methods. In particular, a scanning force microscope (SFM) cantilever has been utilized, to conventionally sense the surface while carrying the mask on top [141, 142]. This can produce evaporated structures with edge sharpness as small as 10 nm [142], but comes with the instrumental overhead of a fully operational SFM. A faster alternative, which avoids chemical resists, is the direct imprinting of structures by an atomic force microscope [143]. However, the corresponding lithography is restricted to selected materials and typically requires an environment that is not compatible with UHV.

Single crystal membranes with pattern line widths of 10 nm have been used with pick and place methods to fabricate various forms of patterns including arrays of dots and stripes, and narrow lines. The versatility of hard masks as applied to substrates of fragile nature and irregular shapes has been demonstrated by pattern transfer onto an optical fiber facet [144]. The compatibility of silicon nitride with high-temperature processing, robustness against ion milling, and flexibility in shape and size of patterns make hard

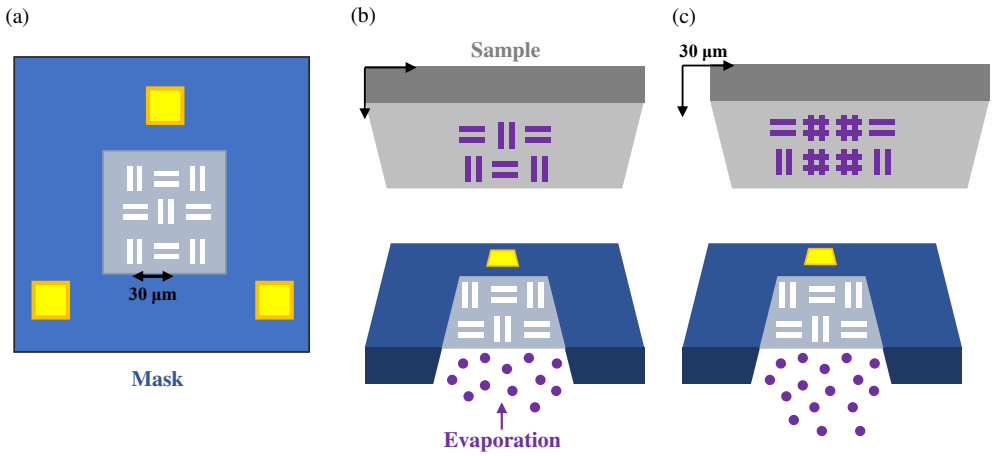

Figure 4.1: **Creating a superconductor layer with holes using a shadow mask (a)** The mask with alternating horizontal and vertical stripes. **(b)** First evaporation creates stripes of the evaporated material on the sample. **(c)** Second evaporation performed after a horizontal offset creates an anti-dot like structure of evaporated material on the sample.

masks a contender for the fabrication of arrays of a sub-micron ferroelectric cell for mass-storage applications. Arrays of ferroelectric nanodots with lateral sizes of 120 nm and interdot distances of 200 nm were patterned on STO (001) substrate to demonstrate the capabilities of a hard mask [145].

Finally, piezomotors have been utilized to move either the sample [146] or the mask [147] in all three dimensions However, so far, the distance calibration in the small distance range required an initial touching of the mask to the substrate, before the distance can be monitored, e.g., by a field emission current [148]. Again, an edge sharpness in the 10 nm range has been achieved, where diffusion of the deposited material is likely the limiting factor [139, 149].

The following sections describe an ultrahigh vacuum compatible mask aligner based on piezo motors [150], in order to align and approach a Si-SiN based mask to a conducting sample. As previously described in section 2.4, in order to eliminate the CdG states, an anti-dot-like structure is required. Such a structure can be created by means of this UHV mask aligner and a shadow mask. Figure 4.1 (a) shows a schematic representation of the mask with alternating stripes in different directions. A material, such as a superconductor, evaporated through the mask creates a pattern on the sample surface as shown in figure 4.1 (b). A second evaporation through the mask with a horizontal offset develops the sample into an antidot-like structure as in figure 4.1 (c). The pattern of evaporated superconductor must have a sharp mesa-edge, comparable to the coher-

ence length of the superconductor. Therefore, a shadow mask evaporation must create a pattern with sub-100 nm penumbra along the mesa-edge. The solution presented in this thesis has been partly published as [151].

4.1 Fabrication of mask for mask aligner

Commercially produced masks from *Norcada* Inc. are a $3 \times 3\,\mathrm{mm}^2$ large highly doped ($\rho \approx 3{-}30\,\Omega\mathrm{cm}$) Si-chip of 250 μm thickness, that consists of four trenches in the Si which expose a suspended SiO_2 (thickness 100 nm) and Si_3N_4 (thickness 1 μm) membrane, as shown in figure 4.2 (a) and 4.2 (b). The three outside trenches, $50 \times 50\,\mu\mathrm{m}^2$ in size, each serve the purpose of a parallel plate capacitor that is used for mask-sample alignment and distance control. The central trench, $100 \times 100\,\mu\mathrm{m}^2$ in size, serves as the shadow mask. The shadow mask is patterned into an array of holes (inset of (b)), through which material may be evaporated onto the sample.

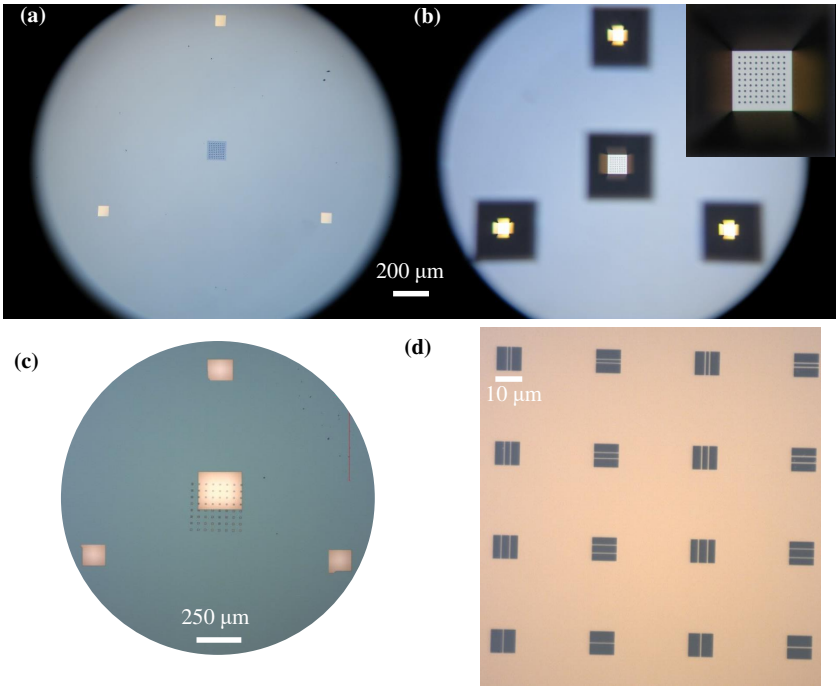

Figure 4.2: **Optical images of masks (a)** The front side and **(b)** back side of *Norcada* mask. Inset shows 10×10 array of circles 3 μm in diameter. **(c)** The front side of the *home-fabricated* mask. The pattern (black) is larger than the central membrane (yellow) to accommodate misalignment. **(d)** A portion of the patterned membrane with horizontal and vertical slits and bridges separated by 3 μm.

Masks commissioned from *Norcada* were constrained to feature sizes $\geq 1\,\mu$m with pre-selected geometries of the pattern. In addition, the contact pad on the capacitor trenches was placed entirely within the trench, eliminating the possibility to use bonding tools for contacting (detailed later). Given these limitations in *Norcada* masks, a fabrication process was developed in collaboration with Group Grützmacher, PGI-9 at the HNF cleanroom in Forschungzentrum Jülich.

These *home-fabricated* Si-based masks also measure $3 \times 3\,\text{mm}^2$ and consist of four trenches similar to the *Norcada* masks. The central patterned structure is larger at $250 \times 250\,\mu\text{m}^2$ as shown in figure 4.2 (c). The pattern in this mask comprises of alternating horizontal and vertical bridges (light) and slits (dark), as shown in 4.2 (d). The width of the bridge is increasing from 250 nm to $5\,\mu$m along the row, and the width of the slit is increasing from 250 nm to $5\,\mu$m along the column.

Two subsequent evaporations through such a patterned mask, with a horizontal offset of $30\,\mu$m in between the evaporations, will create a holey pattern of evaporated material as portrayed in figure 4.1.

4.1.1 Cleanroom fabrication process of SiN-mask

The process flow described here is executed on $1 \times 1\,\text{cm}^2$ chips that can be diced post-fabrication into four masks each measuring $3 \times 3\,\text{mm}^2$. The primary constraint on the $1 \times 1\,\text{cm}^2$ dimensions is the compatibility with fabrication chucks, particularly for KOH etching and metallization processes (described later in the section).

The Si(100) wafer is purchased from *AMO GmbH Aachen* (specifications as in table 7.1 in appendix). On both sides of this wafer, 100 nm of Si_3N_4 is grown via Low-Pressure Chemical Vapor Deposition (LPCVD) at *AMO GmbH*. The resulting wafer forms the basis substrate for the mask fabrication.

Prior to the mask fabrication described in the process flow, the substrate needs the following pre-fabrication preparations:

Wafer processing for dicing: The 4-inch wafer substrate is spin-coated with a protective resist AZ5214E for 30 s at 4000 rpm ramped at 4000 rpm/s. It is then baked at 90 °C for 5 mins. Dicing of the wafer into $1 \times 1\,\text{cm}^2$ chips is done with a diamond saw of $20\,\mu$m width at HNF dicing facility.

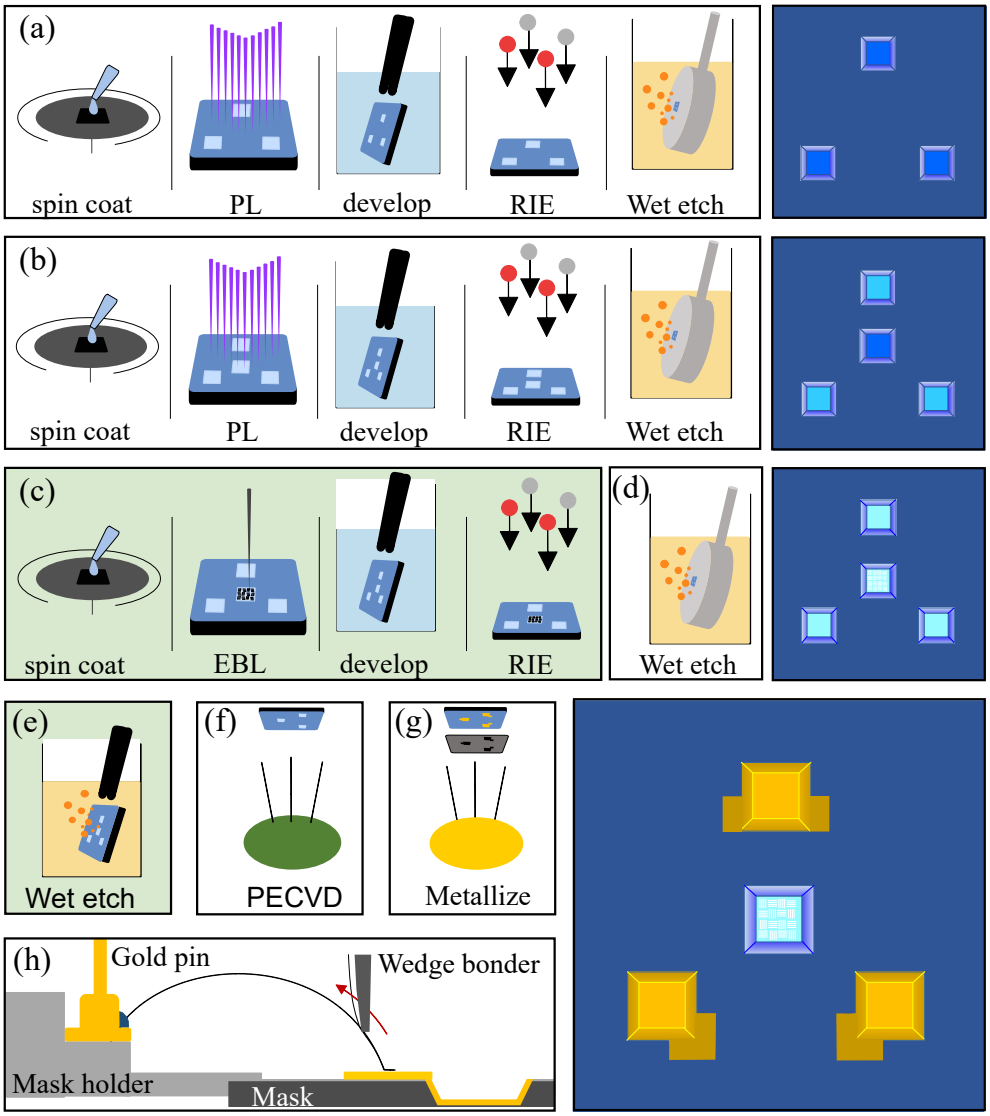

Figure 4.3: **Schematic representation of the mask fabrication process.** White and green backgrounds indicate processes at the back and front sides respectively. **(a)** A partial definition of trenches excluding the mask trench. Right: backside of the mask at the end of (a). **(b)** A partial definition of trenches including the mask trench. Right: backside of the mask at the end of (b). **(c)** Definition of the mask pattern. **(d)** Wet etching of all trenches. Right: backside of the mask at the end of (d). **(e)** Controlled wet etching of all trenches **(f)** PECVD of 100 nm thick SiO_2. **(g)** Shadow mask evaporation of Cr/Au bond pads **(h)** Bonding process for electrical connection of sensors to gold pins on the mask holder. Right: backside of the final mask.

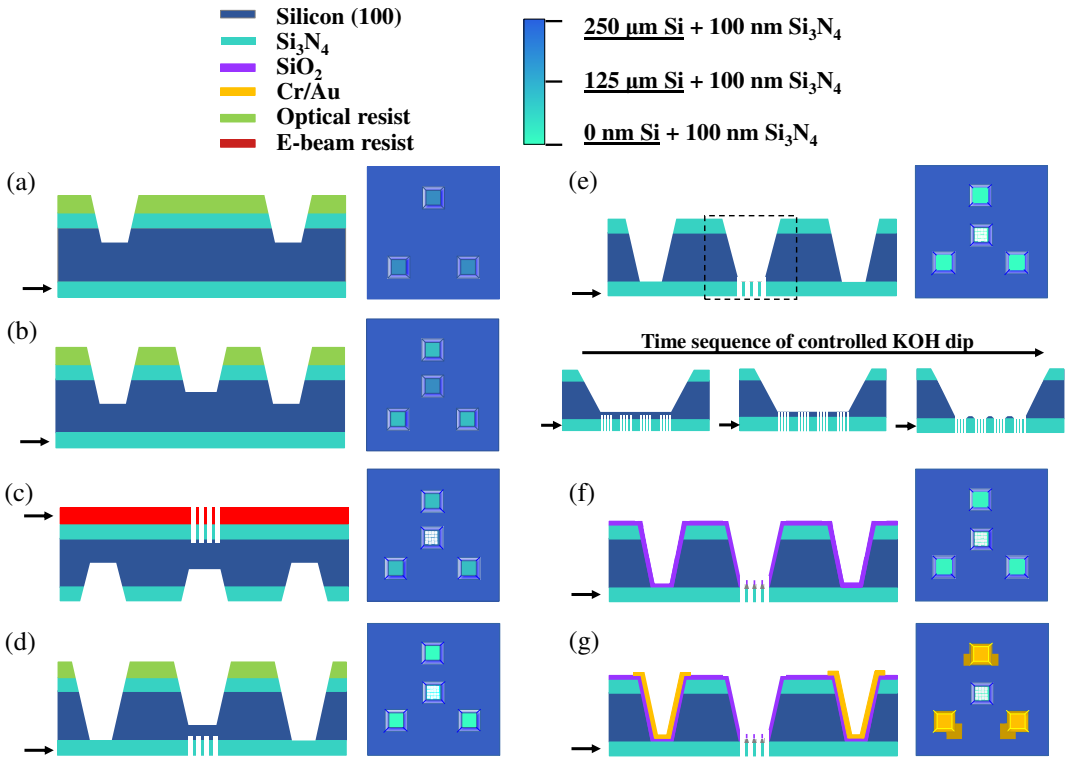

Figure 4.4: **Schematic representation to show the progress of mask fabrication in cross-sectional view.** The black arrow marks the front side of the mask. The corresponding top view of the backside of the mask is on the right side where the color bar of Si is defined in thickness gradient as indicated in the scale bar on top. **(a)** A partial definition of trenches excluding the mask trench. **(b)** A partial definition of trenches including the mask trench. **(c)** Definition of the mask pattern. **(d)** Wet etching of all trenches from the backside. **(e)** Controlled wet etching of all trenches from both sides. Bottom: Time sequence showing the pattern etching in the dashed box region. **(f)** PECVD 100 nm thick SiO_2. **(g)** Shadow mask evaporation of Cr(10 nm)/Au(100 nm).

Wet cleaning of chip: Typically, two chips of $1 \times 1\,\mathrm{cm}^2$ may be fabricated simultaneously. The limiting factor is the number of chucks available for KOH etching in HNF acid wet bench. The chip is first cleaned in acetone, isopropyl alcohol, and de-ionized water, each for 5 mins. Given the fragility of masks after etching, any further ultrasonication must be done at this stage to remove Si-particles from dicing or other impurities that are not removed by wet cleaning. The last ultrasonication may be performed before the trenches are fully etched and the suspended membranes have been exposed (Step (d) in figure 4.3).

Following this, the fabrication process flow begins as described in figure 4.3. The cor-

responding cross-sectional view of the mask in figure 4.4 aids in visualizing the etching processes that create the trenches and mask pattern.

(a) Back-side: Partial definition of trenches excluding mask trench

(i) Spin coating of photoresist
The backside of the chip is spin-coated with AZ5214E for 30 s at 4000 rpm ramped at 4000 rpm/s and baked at 90 °C for 5 min.

(ii) Photolithography of sensor trenches
This optical lithography step defines the sensor (capacitor) trenches and excludes the central mask trench. The exposure is done with an Hg lamp with 365 nm light at 7 mW power for 4 s.

(iii) Development
The chip is then developed in AZ MIF 326 developer solution for 40 s, followed by thorough rinsing in DI water.

(iv) Dry etching of sensor trenches
Reactive ion etching (RIE) accomplishes the removal of nitride in the photo-exposed capacitive trenches and reveals the Si underneath. RIE is performed with active gases CHF_3 at 55 sccm and O_2 at 5 sccm flowrates, at Inductively Coupled Plasma (ICP) power of 100 W and accelerating RF power of 25 W for 4 min 20 s at 20 °C. The sample is then rinsed for 5 mins each in acetone and isopropyl alcohol to strip any remaining resist.

(v) Partial wet etching of sensor trenches
The nitride that is not removed by RIE, acts as a self-stopper for KOH wet etching due to its inherently lower etch rate compared to the Si that is exposed under the RIE etched nitride in the previous step. Therefore, before dipping the chip in KOH solution, one then needs to protect the side walls of the chip where no nitride is grown. The sample is placed in a chuck that is KOH-safe and seals the Si chip from the sides, allowing the etchant to access the exposed capacitors. A partial etching of the Si bulk is performed for a duration of 30-40 min with 44 % KOH mixed 1:1 with de-ionized water, heated at 86 °C. The etch rate is about 1.2 μm per minute.

(b) Back-side: Partial definition of trenches including mask trench

(i) Spin coating of photoresist

The backside of the chip is spin-coated with AZ5214E for 30 s at 4000 rpm ramped at 4000 rpm/s and baked at 90 °C for 5 mins.

(ii) Photolithography of sensor trenches

This optical lithography step exposes the sensor trenches as well as the central mask trench. The photomask is aligned manually to the partially etched sensor trenches to position the mask trench in the center.The exposure is done with an Hg lamp with 365 nm light at 7 mW power for 4 s.

(iii) Development

The chip is then developed in AZ MIF 326 developer solution for 40 s, followed by thorough rinsing in DI water.

(iv) Dry etching of sensor trenches

Since the nitride at the sensor trenches is already removed and the etch rate of Si in the parameters used, is negligible, the sensors remain mostly unaffected by this step. The nitride etching by RIE is limited to the mask trench. RIE is performed with active gases CHF_3 at 55 sccm and O_2 at 5 sccm flowrates, at ICP of 100 W and acelerating RF power of 25 W, for 4 min 20 s at 20 °C. The sample is then rinsed in acetone for 5 mins each and isopropyl alcohol to strip any remaining resist.

(v) Partial wet etching of sensor trenches

A partial etching of Si is performed for 30-40 min with 44 % KOH mixed 1:1 with DI water, heated at 86 °C (etch rate about 1.2 μm per minute).

(c) Front-side: Definition of mask pattern

(i) Front Spin coating of e-beam resist

The front side of the chip is spin-coated with CSAR 62 for 30 s at 4000 rpm ramped at 4000 rpm/s and baked out at 150 °C for 1 min.

(ii) Electron beam lithography

The central mask trench is patterned via e-beam lithography at 50 kV electron acceleration voltage, 2 nA beam current and 250 $\mu C/cm^2$ dose.

(iii) Cold development

The chip is then cold-developed at 0 °C in AR 600 546 developer solution for 1 min.

(iv) Dry etching of mask pattern

The exposed regions of the mask pattern are removed by RIE, defining the regions without material in the final mask, that is, slits in the pattern. RIE is performed with active gases CHF_3 at 55 sccm and O_2 at 5 sccm flowrates, at a forward power of 25 W, and ICP of 100 W for 4 min 20 s at 20 °C.

(d) Back-side: Wet etching of all trenches

Etching the residual Si in the trenches results in suspended nitride membranes at the sensors and a suspended patterned membrane at the mask. In order to reduce the risk of suspended patterned membrane breakage, a two-step process was optimized. The first step is the wet etching of the backside in the KOH chuck for 3 h. After 3 h, the etching is interrupted every 5 min for optical inspection of the capacitive trenches. Since the capacitors have had a lead on the etching, the suspended nitride is exposed at the sensors ahead of the mask trench. This has been visualized in figure 4.4 (d). The etching can be concluded as soon as the capacitor trenches are fully etched. The residual Si thickness in the mask trench at this point is typically 10 μm–25 μm and can be verified with a profilometer.

(e) Front and back sides: Controlled wet etching

The next wet etching step is performed without the chuck. The chip is held dipped in the KOH solution for 30 s, allowing for the etching to take place from both the front and the back sides of the patterned mask region. The chip is transferred into DI water after 30 s to cease etching.

Etching from both sides creates a Si frame that remains in the regions where the bridges are wider, e.g. in the gap between arrays of patterns, as shown in the time sequence in figure 4.4 (e). This Si frame, a few micrometers thick, provides mechanical sturdiness to the patterned bridges. It is therefore important to not over-etch in this step, to the extent that the Si frame is lost. Regular control is realized via an optical microscope, by comparing the transparency of the central trench to that of the fully etched capacitor trenches. After drying the DI water from the sample, one can verify the creation of holes in the pattern by observing if a droplet of DI water that is placed inside the mask trench, seeps through to the front. If it does not,

then KOH etching can be repeated for 30 seconds (about 600 nm Si). Such a controlled wet etching is iteratively performed until the patterns are fully etched. A final confirmation of the complete incision of the pattern can be made via SEM. In the case that SEM indicates remaining nitride, the etching can be repeated as above.

(f) Back-side: SiO_2 deposition

A thin film of SiO_2 is deposited on the backside of the mask to decouple the capacitors, which otherwise will be connected electrically through the Si bulk between the capacitive trenches in the following step (g). SiO_2 of 100 nm thickness is deposited with Sentech Plasma-Enhanced Chemical Vapor Deposition (PECVD) at 100 °C on the backside of the mask.

(g) Back-side: Metallization of capacitors

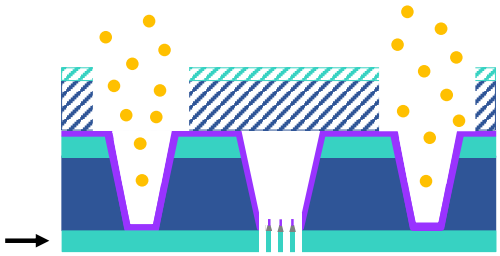

Figure 4.5: **Metallization of capacitor bond pads** Schematic profile view of the *mask aligner* SiN-mask (solid) and the *metallization* Si-mask (striped) attached together for the evaporation of Au bond pads on the backside of the *mask aligner* SiN-mask.

The Au bond pads for the capacitors are created using a Si-based shadow mask. This Si-mask has structures larger than the capacitors such that bond pads are extended outside the trench. The nitride membrane in this exposed region is completely removed and Si below it is etched through, such that a bulk-Si mask is created in the shape of the capacitor trench and bond pads. This Si-mask (also $1 \times 1\,cm^2$) is placed in contact with the SiN-mask and attached together to the metallization chuck of the gold evaporator (Figure 4.5). Evaporation of 10 nm Cr sticking layer and 100 nm Au is done through the Si-mask onto the backside of the SiN mask creating Au bond pads that protrude out of the trenches, where bonding can be done using a wedge bonder.

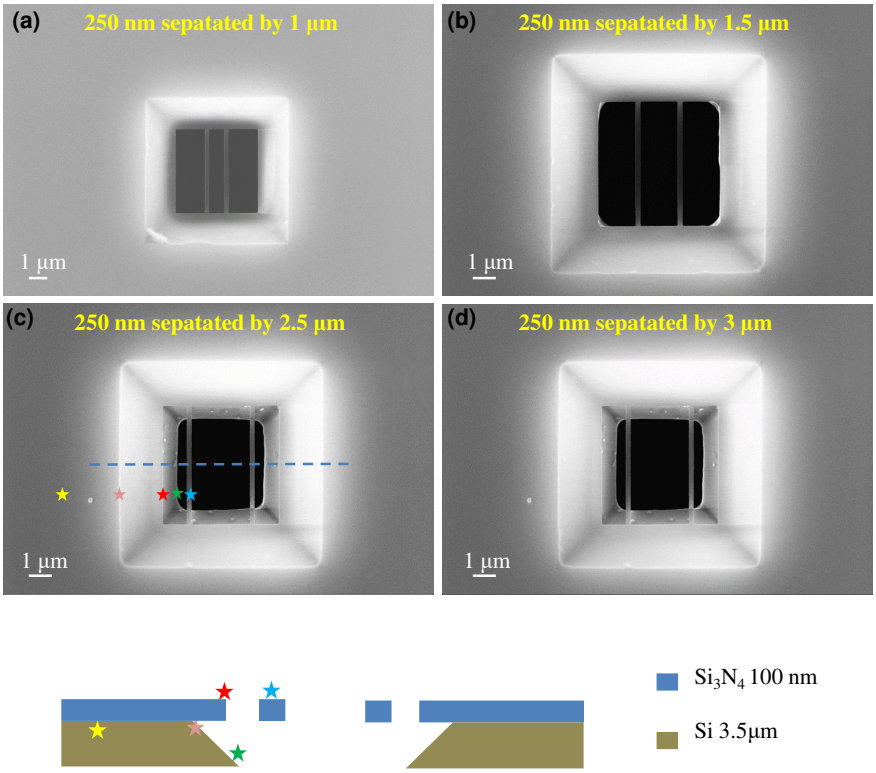

Figure 4.6: **Scanning electron microscope images of the mask** Patterns in a 10×10 array of alternating vertical and horizontal stripes described in figure 4.2. **(a)–(d)** have been imaged along the same column, with constant bridge width and increasing slit width. Schematic (bottom) displays material stacking in the cross-section along the dashed blue line in (c).

Dicing into four masks of $3 \times 3\,\mathrm{mm}^2$: The $1 \times 1\,\mathrm{cm}^2$ chip is diced into four parts of $3 \times 3\,\mathrm{mm}^2$ using a diamond dicing saw. For the sake of protection during dicing, the chip is spin-coated with AZ5214E for 30 s at 4000 rpm with 4000 acceleration and baked at 90 °C for 5 min.

Post fabrication cleaning: To remove the resist, the diced masks must be gently rinsed in warm acetone at 40 °C and isopropyl alcohol each for a few minutes in a final wet cleaning step. Although not necessarily done inside the cleanroom, it is extremely important to ensure that this step is done in a low-dust environment with fresh beakers and cleanroom quality solutions in hermetically sealed bottles. The fabrication process is described in detail as a process flowchart in figure 7.2. The final outcome is imaged with scanning electron microscopy as in figure 4.6. This $3 \times 3\,\mathrm{mm}^2$ can now be attached to a mask holder and mask shuttle to create a mask-on-shuttle assembly that is compatible with the mask aligner.

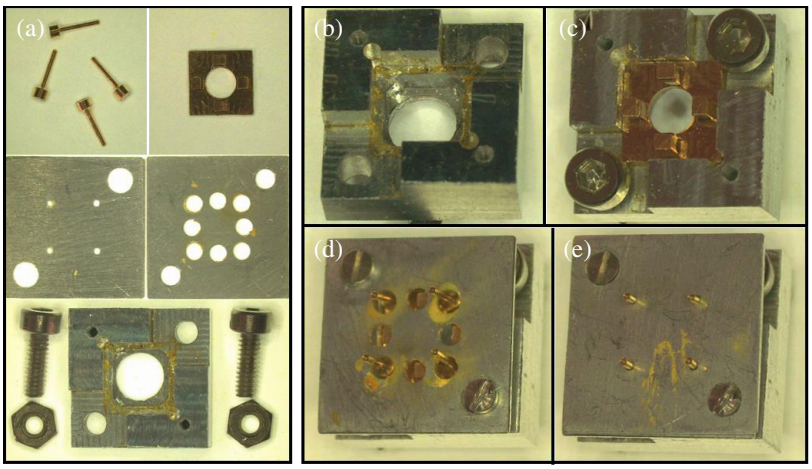

Figure 4.7: **Photographs instructing the contacting of mask holder with contact pins.** Top frame: **(a)** All required parts including male gold pins, mask holder, two alignment Al plates and an assisting chuck with screws. **(b)** Assisting chuck. **(c)** Mask holder placed in assisting chuck. **(d)** Al plate with larger holes inserted and gold pins attached through the Al plate. **(e)** Al plate with smaller holes inserted to align the gold pins.

4.1.2 Mask-on-shuttle assembly

The mask-on-shuttle assembly comes in three parts: (1) Contacting the mask holder with male gold pins, (2) Bonding the mask to the male pins on the mask holder, and (3) Contacting the mask shuttle with female gold pins. Followed by this, the bonded mask-mask holder and mask shuttle may be assembled together.

Preparation of mask holder

The $6 \times 6\,\mathrm{mm}^2$ molybdenum mask holder is 0.4 mm thick and has a 2.8 mm hole in the centre that allows evaporated material to reach the backside of the mask. A 150 μm deep trench allows for the 275 μm thick mask to be placed into it. The parts of the mask holder to be assembled are shown in figure 4.7 (a) (top), and the parts required for assisting in the assembly are shown in figure 4.7 (a) (center and bottom). The assisting parts ensure that the gold pins can be attached to the molybdenum plate without bending and placed with a precision of 100 μm.

As instructed in figure 4.7 (b–d), the mask holder is placed into the assisting chuck with the mask-side facing down. The first aluminium plate is attached to the chuck with screws. The holes in the plate are large enough to insert the gold pins through

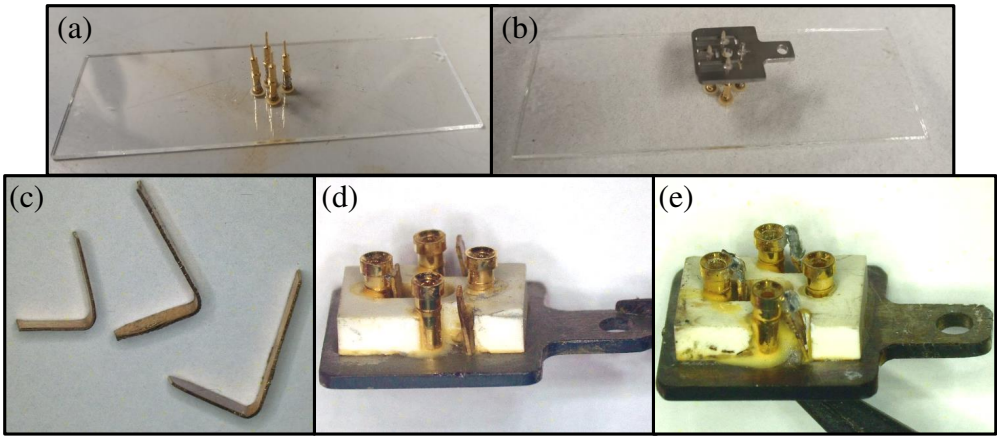

Figure 4.8: **Photographs instructing the assembly of mask shuttle with contact pins** **(a)** Preparation of pin assist on a glass slide. **(b)** Placement of ceramic spacer and shuttle onto pins. **(c)** CuBe plates for contacting gold pins, **(d)** Placement of CuBe plates through shuttle with insulating epoxy. **(e)** Contacting of CuBe plates to gold pins.

them. The capacitor contacts pins are glued with electrically insulating epoxy[1] and the grounding contact with electrically conducting epoxy[2], as shown in figure 4.7 (d). Finally, before curing the epoxy, the second aluminium plate is inserted through the gold pins, thus aligning their position as shown in figure 4.7 (e). This assembly is then cured at 150 °C for 1 hour.

Preparation of mask shuttle

The $12 \times 12 \times 1\,\mathrm{mm}^3$ molybdenum mask shuttle has a flag compatible with existing transfer mechanisms in UHV via a wobble stick. It has a 2.8 mm hole in the center corresponding to the mask holder for the evaporated material. On the bottom (non-mask side), it consists of three 300 μm deep trenches for capacitor contact plates. A slide with a male pin assists such as in figure 4.8 (a) may be used to stack a set of female pins. The capacitor contact pins are coated with electrically insulating epoxy and the ground pin is with electrically conducting epoxy. A shapal ceramic spacer[3] (white component seen in figure 4.8 (d) and (e)) is inserted through the pins before inserting the shuttle (trench-side facing up) as in figure 4.8 (b). The ceramic prolongs the re-usability of the mask shuttle. The epoxies are cured at 150 °C for 1 hour. The

[1] EPO-TEK H77, EPOXY Technology, INC.
[2] EPO-TEK E2101, EPOXY Technology, INC.
[3] http://www.tokuyama.co.jp/eng/products/specialty/shapal/hi_msoft.html

gold pins can then be filed down to the plane of the trenches in the molybdenum shuttle. The CuBe contact plates as shown in figure 4.8 (c) are prepared to fit the three trenches and each bent at a 90° angle. They can be inserted through the shuttle as shown in figure 4.8 (d), and secured with insulating epoxy into the trench. Finally, the plate is soldered with a tin alloy filler to the female gold pin as shown in figure 4.8 (e).

Bonding the capacitor contacts

(a)

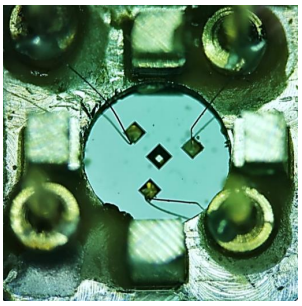

(b)

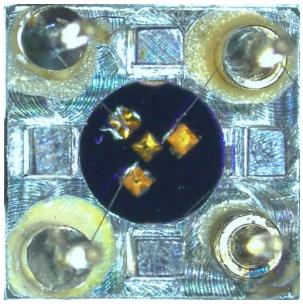

(c)

Norcada mask		Home-fabricated mask	
Bond 1 (sensor trench)	**Bond 2 (gold pin)**	**Bond 1 (senson bond pad)**	**Bond 2 (gold pin)**
Epoxy EPO-TEK E2101 EPOXY Technology, INC. **Curing** 150 ^{0}C for 1 hour	**Epoxy** EPO-TEK E2101 EPOXY Technology, INC. **Curing** 150 ^{0}C for 1 hour	**Wedge bonder**	**Epoxy** EPO-TEK E4110-LV EPOXY Technology, INC. **Curing** 23 ^{0}C for 3 days

Figure 4.9: **Bonding in *Norcada* and *home-fabricated* masks. (a)** Bonded *Norcada* mask. **(b)** Bonded *home-fabricated* mask. **(c)** Summary of bonding technique based on mask type.

Before assembling the mask holder into the shuttle, the mask is attached to the holder and the Au bond pads of the capacitive sensors are bonded to the respective gold pins on the mask holder. The bonding process is summarized in the table below for both *Norcada* and *home-fabricated* mask designs. The *Norcada* masks are bonded with 40 μm Al wire, using epoxy on both ends of the wire. The wire is dipped in epoxy to create a droplet and placed into the trench, ensuring the size of the epoxy droplet is no more than half the volume of the trench (see e.g. figure 4.9). The first bond is then cured to harden the epoxy. The second bond is created at the gold pin on the mask holder ensuring maximum distance between each bond and minimal length of wires in order

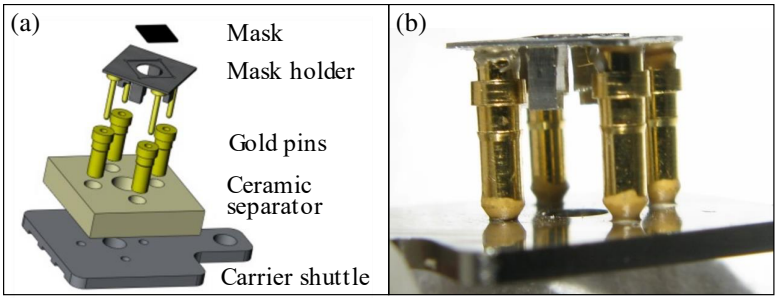

Figure 4.10: **The mask module. (a)** Explosive schematic showing the parts of the mask module assembly. **(b)** Side view of the mask holder inserted into the mask shuttle showing the mask at the highest protrusion.

to reduce cross capacitance. The cross capacitance between two capacitors can vary from 0.2 fF at 3 mm distance up to 2 fF at 0.5 mm distance between the contact wires. The *home-fabricated* masks are bonded with 40 μm Al wire using a wedge bonder at the mask and epoxy at the gold pin. The epoxy is cured at room temperature to increase the throughput of bonding by avoiding thermal expansion-related fracture of the nitride membranes.

Assembly of mask holder and shuttle

Finally, the mask holder containing the bonded mask, and the mask shuttle may be assembled together via the gold pins. Figure 4.10 (a) depicts how all the parts of the mask module come together and figure 4.10 (b) emphasizes that the mask is the highest point in the mask module, thus ensuring that the capacitive signal arises primarily from the mask, and eventual contact with the sample only occurs at the mask.

4.2 Instrumentation and performance of UHV mask aligner

4.2.1 Molecular beam evaporation chamber

A modular mask aligner compatible with ultra-high vacuum chambers was designed. In it, various evaporators can be combined to evaporate through the mask onto the sample without breaking the vacuum. The CF100-mounted mask aligner employs a Si-based mask to capacitively measure the distance from a conductive sample, as described in

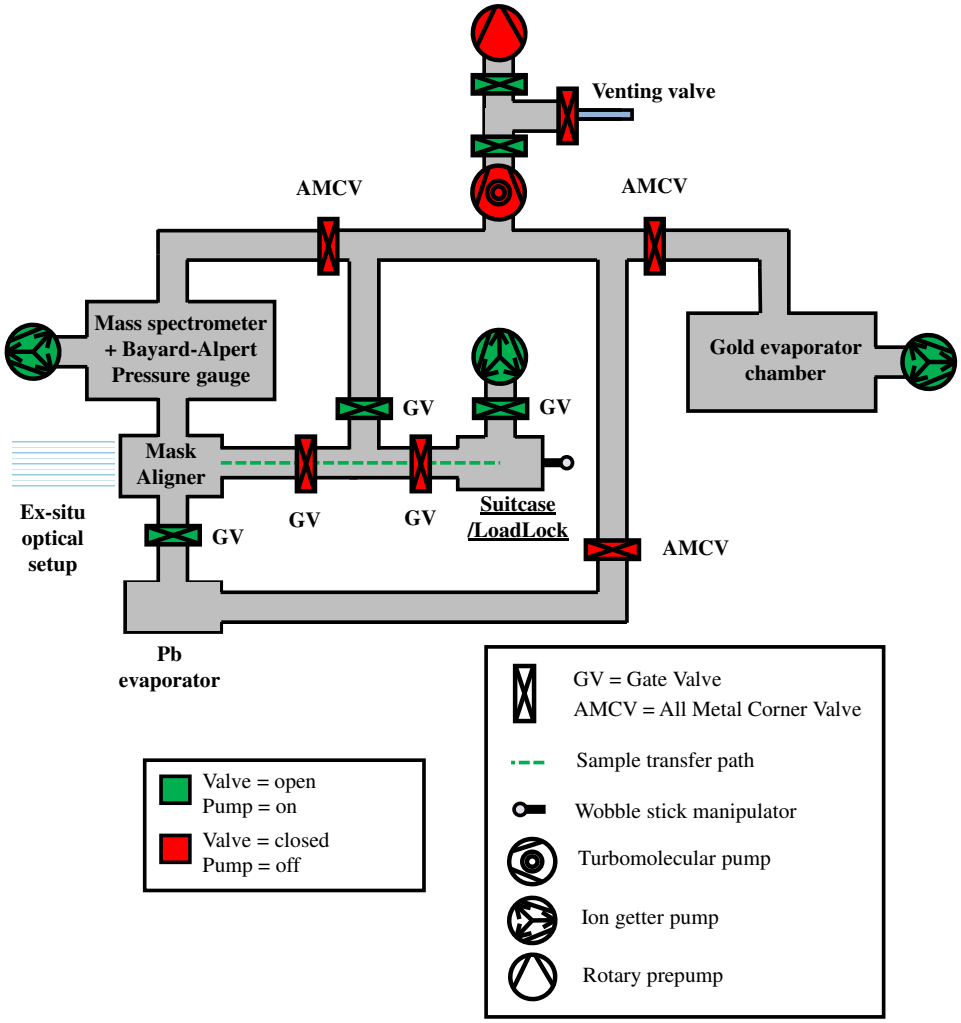

Figure 4.11: **Circuit description of the molecular beam evaporation chamber** consisting of mask aligner, Pb evaporator and Cr+Au evaporator. The status of the valves and pumps are indicated for the evaporation configuration.

section 4.1. The mask aligner is incorporated in a molecular beam evaporation chamber, placing an exchangeable Pb evaporator directly below it (see figure 4.11). Mask and sample transfers can be done in situ with the help of a vacuum suitcase that is attached via a gate valve to the load lock and contains a sample garage, getter pump, and wobble stick.

The use of screws at the CF100 flange allows for rotation of the mask aligner ex-situ such that it is either mountable from the top (180° to evaporation direction) or from the side (90° or 270° to evaporation direction) as shown in figure 7.3. Both configurations

provide optical access via a viewport on the back of the mask and sample (180° to the wobble stick).

4.2.2 Working principle of the mask aligner

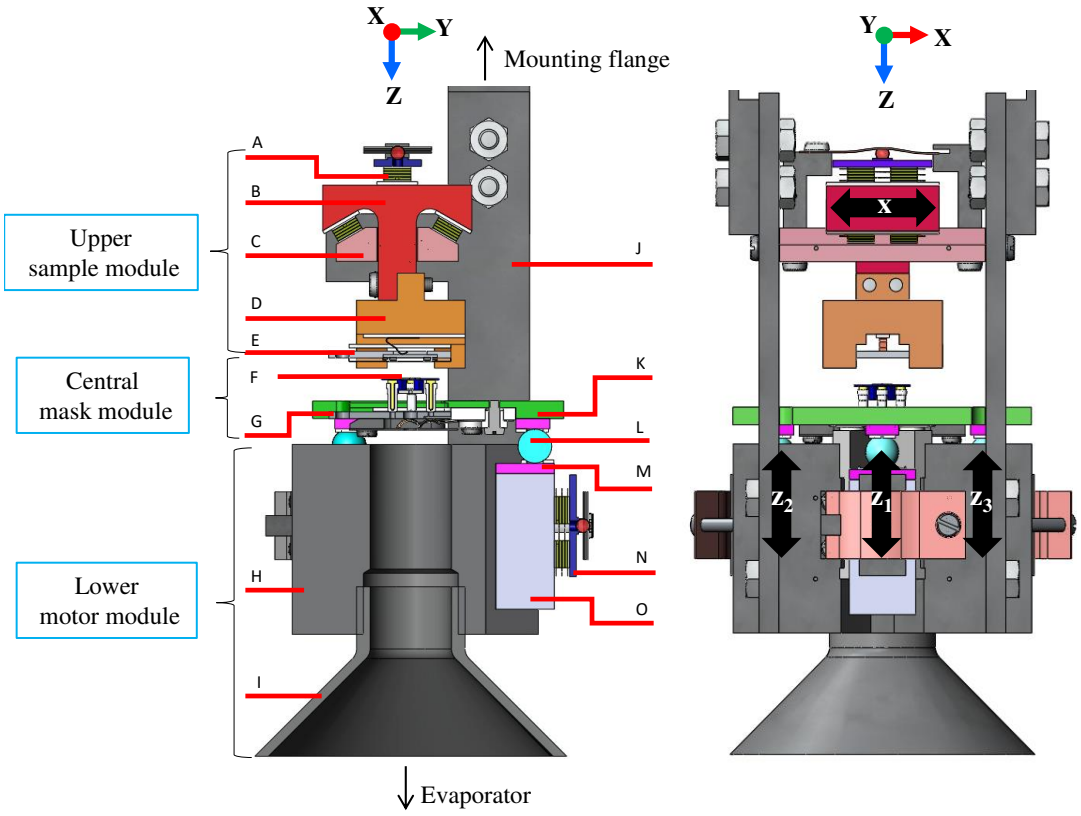

Figure 4.12: **Cross-sectional drawing of the mask aligner Left (side view):** (A) piezostack, (B) T-slider for horizontal sample movement, (C) sliding rail, (D) sample stage, (E) sample holder with the sample, (F) shadow mask, (G) mask shuttle carrying mask assembly, (H) steel frame for piezomotors, (I) metal cone protecting the piezostacks from the molecular beam, (J) steel frame carrying the sample stage, (K) frame carrying the mask shuttle, (L) magnetic sphere, (M) two plates glued on top of the sapphire prism (Al_2O_3, Ni), (N) pressure plate, (O) sapphire prism. Directions towards the evaporator and mounting flange are marked by arrows. **Right (view through viewport):** The black arrows indicate the direction of motion of the three Z-piezomotors for the vertical translation of the mask towards the sample and one X-piezomotor for the horizontal translation of the sample.

Figure 4.12 (left) describes the entire mask aligner which comprises three modules: a lower module for the coarse approach of the mask towards the sample, a central module which carries the mask, and an upper sample module for holding the sample and shifting

it laterally with respect to the mask.
The **lower motor module** (H, I, M, N, O) consists of three vertical piezoelectric motors (lower inset) and stainless steel mounting rods for attaching the mask aligner to a CF flange. The stainless steel body H is pierced by a hole with a diameter of 12 mm, enabling the molecular beam of evaporated material to hit the mask. A metal cone (I) prevents the evaporation of material on the piezostacks and prisms.

The capacitively controlled UHV mask aligner employs three piezomotors for motion and alignment of the mask towards the sample, and one piezomotor for the motion of the sample in the horizontal direction as can be seen in figure 4.12 (right).

The three piezomotors for the approach of the mask to the substrate [150, 152] are placed at a relative angle of 120° in the sample plane as shown in figure 4.13 (right). A cross-section of one such corresponding motor is shown in figure 4.13 (left). The piezomotor is assembled into a V-shaped recess in the steel frame (H). Each piezostack uses polished Al_2O_3 plates as gliding surfaces and consists of four layers of piezo material contacted by CuBe plate (*PI Ceramic* GmbH). There are four such piezostacks placed into the two facets of the V-shaped recess. A sapphire prism (O) with a triangular base of 10 mm edge length, and height of 20 mm is clamped into the recess on top of the four piezoelectric stacks. Additional two piezostacks are clamped to the front facet of the sapphire prism by use of a pressure plate (N). A screw can strain a 0.2 mm thick CuBe spring in contact with the pressure plate via a ruby ball (diameter 2 mm) [74], and serves as a tuning knob for the extent of pressure that is applied on the plate. This in turn decides the friction between the piezostacks and the sapphire prism, altering the step size of the piezomotor. Since each step is sub-100 nm, and the three capacitive sensors are placed directly on the backside of the 1 μm thick SiN mask, the mask can be aligned with sub-μm precision relative to the substrate on a lateral scale of millimeters.

The **central mask module** (F, G, K) enables propagating the slip-stick motion from the motors to the mask which lies on top of the three prisms via three magnetic Nd spheres (L). The sphere shape enables an inclination of the mask stage with respect to the individual piezomotors as required for the desired mask alignment. Each sphere is magnetically attached to the frame carrying the mask shuttle (K) and a prism (O) via Ni plates and ceramic plates (M) glued to the prism and frame. Small grooves in the Ni plates allow horizontal adjustment of the sphere. The frame (K) carries the mask shuttle which allows the exchange of the mask by means of a standard sample holder of size $12 \times 12\,\mathrm{mm}^2$. The frame (K) has a hole pierced with a diameter of 12 mm aligned

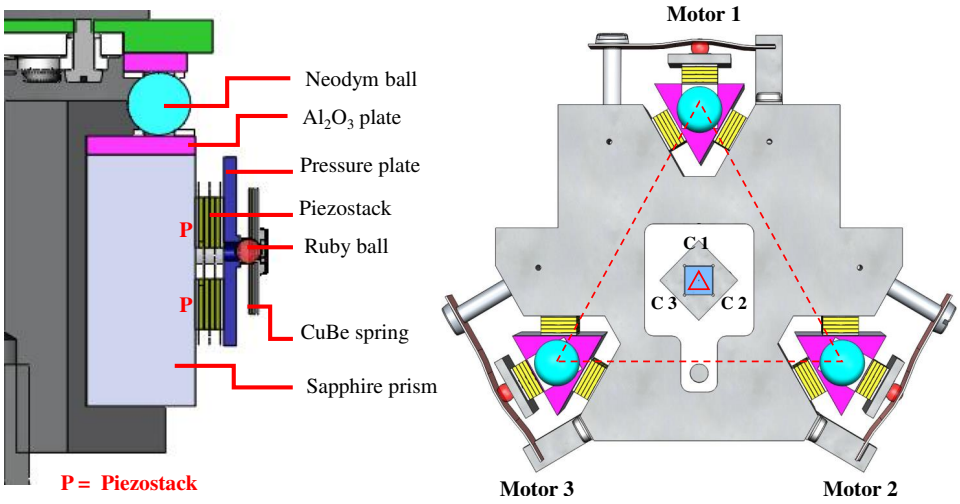

Figure 4.13: **The Z-piezomotors. Left:** One of three vertical translation motor (Z-piezo motor). **Right:** Top view of the relative placement of the three Z-piezomotors and the capacitive sensors on the mask C1, C2 and C3.

with the steel body (H) such that the evaporated material hits the backside of the mask. The front and back stoppers prevent the frame carrying the mask shuttle from rolling over the magnetic spheres when the mask shuttle is inserted or removed with a wobble stick. The stoppers are therefore aligned to the mask stage in its lowest Z-position when the wobble stick may be safely operated on the mask shuttle as shown in appendix figure 7.4.

The **upper sample module** (A−E, J, and upper inset) allows motion of the sample parallel to the mask (detailed figure in appendix figure 7.5). It consists of a T-shaped stainless steel slider (B) holding the sample stage (D). It can slide via a fourth horizontal piezomotor, in addition to the three vertical piezomotors, across a fixed sapphire rail (C). Sample holder (E) and sample stage (D) are electrically isolated in order to reduce stray capacitances, since the sample surface acts as the counter electrode for the capacitive sensors on the mask. The sample can be exchanged in situ with a wobble stick using a standard sample holder of size $12 \times 12\,\mathrm{mm}^2$. A horizontal motion range of 3.3 mm is possible in this construct. The horizontal piezomotor enables lateral movement of the substrate relative to the mask making it possible to achieve several subsequent stencil lithography steps [153].

When a saw-tooth voltage is applied to all six piezostacks of the slider simultaneously, a prism can be moved via a slip-stick motion. Slow voltage ramps during the stick phase

glide the prism along with the elongating piezostacks. The sudden voltage drop during the subsequent slip phase contracts the piezostacks faster than the prism reacts due to its mass inertia such that the force at the interface overcomes the static friction. Each of the four piezomotors can be moved independently. Step sizes during the movement depend both on the amplitude of the sawtooth voltage ($\sim$ 40 V-120 V) and the spring tension as tuned by the tightness of the screw on the pressure plate. Step size is typically in the range 50-200 nm (10% standard deviation) as measured by an optical telescope or Vernier scale after $\sim 10^5$ consecutive steps. For typical voltages around 60 V, the step size is sub-100 nm. The maximum vertical displacement of each vertical motor amounts to 9.5 mm. Step sizes in the retracting direction are slightly larger than the approaching direction due to gravity.

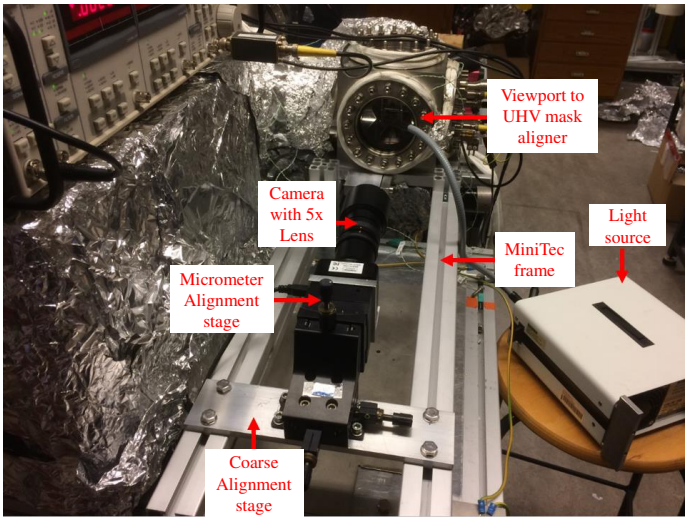

Figure 4.14: **Ex-situ optical setup.** A camera with 5× lens mounted on a translational and angular alignment stage with micrometer precision allows viewing the mask and sample through the viewport of the mask aligner. The setup is attached to a *MiniTec* frame via a coarse alignment stage with screws. The setup is used for positioning the mask and sample within the field-of-view of the camera.

4.2.3 Optical measurement of mask-sample distance

A CF100 viewport provides optical access to the mask and sample. The setup as shown in figure 4.14 employs a camera[4] with an optical lens system[5] that enables measurement

[4]Bresser Mikrocam II 20 MP
[5]EHD6X, 2/3" Makrozoom-Objektiv f=18–108mm

of the mask and sample positions with a pixel resolution of 6 μm. It is mounted on translation and angular alignment stages allowing control of the camera position with length precision $\pm 100\,\mu m$ and angle precision $\pm 1°$. In order to obtain the mask-sample distance optically, an oblique viewing angle such as in figure 4.16 (a) must be adjusted to a zero angle view of the sample and the mask as shown in figure 4.16 (b) in order to observe the direction of misalignment of mask and sample. For example, as in the case of figure 4.16 (b), the blue lines indicate that the mask is not parallel to the sample plane, and the mask is tilted backwards (the blue circle highlights the out-of-plane tilt). The mask can then be optically parallelized to the sample in an iterative manner as follows (definition of symbols as in figure 4.15):

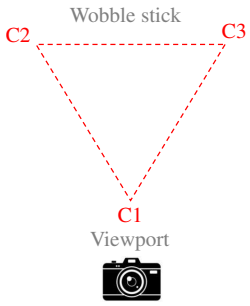

Figure 4.15: **Capacitor naming scheme.** The capacitors in relation to the piezomotors can be seen in figure 4.13 (right).

1. Move C1 down such that the corners of C2 and C3 on the mask, as well as the top plane of the mask, are all visible.
2. Paralellize the C2 - C3 edge of the mask to the sample.
3. Move C1 up.
4. Repeat steps (2) and (3) until the top plane of the mask is no longer visible, and the front and profile sides of the mask are along the same line.

Following these iterative steps, the mask can be aligned from a tilt such as in figure 4.16 (b), in which the mask is tilted backwards and the side and front edges are not aligned with the indicated blue line, to figure 4.16 (c) where the mask is parallel to sample at 125 μm. The mask is then advanced toward the sample in iterations of parallelization and approach. A typical approach to within 20 μm distance, starting at a distance of 125 μm is shown in figure 4.16 (d). The red arrows at kinks in the curve indicate where the approach was interrupted to correct mask tilting using the optical parallelization method. The preliminary distance d_p is related to the optically measured mask-sample distance. From here, the number of calibrated steps of the piezomotor [154] are used to determine d_p. A final optical parallelization is typically made at a distance of about 25 μm (i.e. 4 pixels of the optical camera). From now on, the d_p is related to this optical distance of 25 μm. At distances closer than this, the distance-dependent capacitances can be used for determining the mask-sample distance as discussed in the following subsection.

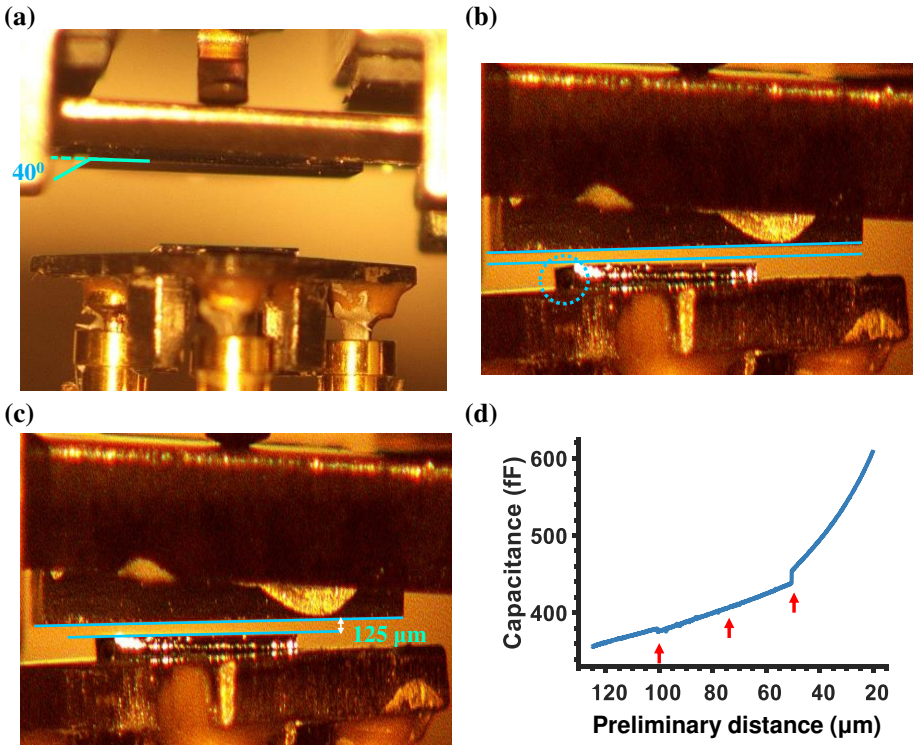

Figure 4.16: **Optical measurement of mask-sample distance.** Camera images of oblique side view of the sample at **(a)** 40° angle and **(b)** 0° angle. Blue lines are guides to the eye along the sample surface and a parallel line shifted downwards. The deviation of the mask surface from the bottom blue line indicates misalignment. **(c)** Mask parallelized to the sample at a distance of 125 μm. **(d)** Stitched approach curves from 125 μm to 20 μm. Red arrows indicate positions at which the mask was optically parallelized to the sample before the continuation of the approach.

4.2.4 Capacitive measurement of mask-sample distance

The capacitance signals are measured employing an ac voltage while reading out the current response via a lock-in amplifier, with a sensitivity of $\sim 0.03\,\mathrm{fF}$.

After optical parallelization, the approach from distances closer than 25 μm is conducted by evaluating the distance-dependent readout of the individual capacitances C1, C2, C3. To this end, a critical look at the performance of the capacitive sensors has to be taken.

The experimental measurements deviate from the trivially expected $C = \epsilon_0 \epsilon_r A/d_{\mathrm{vac}}$, with capacitor area A and dielectric constants of vacuum ϵ_0 and material ϵ_r. The $C(d)$ curves (such as figure 4.17 (a)) instead can be modelled by $C(d) = a + c/(b + d)$ with a, b, and c being fit parameters, and d the distance [154]. The deviations are related to

remaining stray capacitances which can also exhibit a d dependence. In order to minimize these stray capacitances, contacts to the capacitive plates are provided from the backside of the mask. Since the capacitive sensors are ending at the backside of the 1 μm (in *Norcada*) or 100 nm (*home-fabricated*) thick Si_3N_4 mask, there is an additional vertical offset $d_0 = 1\,\mu$m or $d_0 = 0.1\,\mu$m in $C(d)$, which contributes to b. In addition, cross-capacitances may also add an offset contributing to c [155]. While cross-capacitances can be minimized by efficient bonding as discussed in section 4.1.2, they cannot be completely eliminated. The absolute value of capacitance and shape of the capacitance-distance curves vary between different masks and different sensors on the same mask due to these factors. The influence of cross capacitances has to be investigated further to reduce it in future experiments. Prospects are using different wires, different bonding techniques, and different mask/shuttle designs.
The maximum capacitance $C(d = 0)$ is larger by a factor 50 than the theoretical value of 144 fF in *Norcada* masks (experimental range 150 fF–7 pF) and deviates within factor 3 of the theoretical value of 1.4 pF in *home-fabricated* masks (experimental range 700 fF – 3.2 pF). Therefore, bonding of capacitors by wedge bonding (as in *home-fabricated* masks) rather than epoxy (as in *Norcada* masks) at the mask is highly recommended to minimize the offset in a or c. A constant cross-capacitance between each sensor can account for up to a factor 3 increase in the capacitance and cannot fully explain offsets larger than this. Further investigation is required to understand the physical source of such distance-dependent stray capacitances.

When the cross-capacitance exceeds 40 fF for *Norcada* masks (400 fF for *home-fabricated* masks), full contact of all three capacitors to the sample, cannot be deduced unambiguously due to the fact that more than half of the capacitive signal arises from the cross-capacitance to the other sensors. Below 40 fF, the individuality of the distance-dependent curves is still sufficiently preserved (Figure 4.7 in [155]). Therefore, a set of selection criteria must be enforced for the masks that can be reliably used for the evaporation of patterns (4.2.4). For approaching the mask reliably, a zero-point must be established, where the mask-sample contact occurs. For an approach curve, the zero-point is defined as the first contact that occurs before a self-parallelization of the mask and sample occurs during the subsequent approach. For a retract curve, the zero-point is defined at parallel full contact of mask and sample where all three capacitors will leave the sample. This will be explained further in the following paragraph.

Reference measurement to establish the touching point of mask and sample (zero-point)

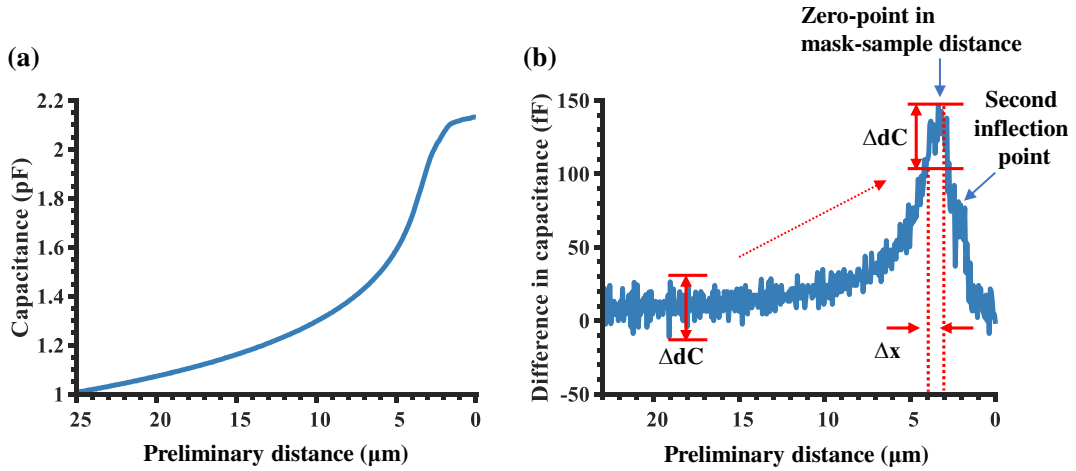

Figure 4.17: **Typical reference curve of a capacitive sensor (*home-fabricated* mask) (a)** Approach curve for a capacitive sensor plotted as a function of the preliminary distance which is related to the optically measured mask-sample distance at the onset of approach ($25\,\mu m$). **(b)** The difference in capacitance per step (67 nm) as a function of the preliminary mask-sample distance.

The approach-based *reference measurement* is made without interruptions to parallelize the mask and the sample until contact between them, as shown in figure 4.17 (a). The maximum preliminary distance is defined as measured optically at the start of the approach (typically around $25\,\mu$m as explained in section 4.2.3) and deduced from the calibration of step sizes. The first point of contact, i.e. zero-point for each individual capacitor, is defined as the piezomotor step where the maximum change in capacitance per step (see figure 4.17 (b)) occurs. Given the finite uncertainty in optical parallelization of $6\,\mu$m (i.e. 1 pixel), and the difference in stepsizes of individual motors of about 10 nm, each capacitor may come in contact at a different step, that is, each capacitor may have its own zero-point. The smallest distance to which the mask later may approach without touching the sample is limited by the noise ΔdC in the $dC(d)$ curve and depicted as distance uncertainty $\Delta x \approx 1\,\mu$m in figure 4.17 (b). Due to the uncertainties of stepsize and optical alignment, the first contact between the mask and the sample will either occur at one of the corners or one of the edges of the mask. The capacitors do not lie directly above the motors, but about 12.5 mm inwards, i.e., towards the center of the mask. The distance between the sensors is approximately 1 mm, and the distance

between the sapphire prisms is about 3 cm. Therefore, when motor 1 approaches by a step of 100 nm with respect to the other two motors, capacitive sensor 1 approaches by 52 nm, and capacitors 2 and 3 approach by 48 nm each. The first contact, referred to as a virtual point of contact, has been modelled for contact at an edge in [155], exhibiting the first inflection point in the capacitance-distance curves, referred to as the virtual peak in $dC(d)$. In the subsequent steps, the mask pivots around the virtual point of contact to self-parallelize towards full-contact with the sample. This implies reduced step-sizes of the motors henceforth until the full-contact, marked by a peak in $dC(d)$ referred to as the full-contact peak. The scenario of a virtual point of contact is described in appendix figure 7.7 and figure 7.8. The tilted distance (a physically more intuitive measure than the equivalent tilt angle of the mask), is the largest mask-sample distance at the first contact between the mask and the sample (d_{pixel} in figure 7.7). For a tilted distance $d_{\text{pixel}} < 1.5\,\mu$m, the virtual peak is at least as high as the subsequent full-contact peak. By correcting the mask tilt down to $d_{\text{pixel}} < 1.5\,\mu$m (appendix figure 7.6 for an experimental flowchart to achieve this), one can ensure that the maximum uncertainty on the zero-point distance arising during the mask approach is below this acceptable value. It places the patterned region of the mask at a distance $< 1\,\mu$m from the sample rendering a penumbra below 25 nm.

For example, in figure 4.17 (b), the first inflection point is a virtual point of contact ($\approx 3\,\mu$m), and the second inflection point ($\approx 2\,\mu$m) is achieved at full contact after 15 more steps (step size = 67 nm). This indicates a tilted distance of only $d_{\text{pixel}} = 180$ nm for a reduced step size of 12 nm. The zero-point in such a situation is safely defined at the maximum of the $dC(d)$ curve in figure 4.17 (b) with an error of only 180 nm. Therefore, the safe distance of approach is $\Delta x + 180\,\text{nm} \approx 1.18\,\mu$m limited by the noise of the $C(d)$ curve. It is worth noting that a retract-based reference curve can eliminate the error by the virtual point contact, if it is measured after the mask has made a full-contact thereby parallelizing itself to the sample assuming a hard mask that cannot bend due to adhesion forces. With a statistical, more quantitative study of the virtual peak, a full-contact may be completely avoided in the future. For *Norcada* masks, a safe mask-sample distance of $d_{\text{pixel}} < 1.5\,\mu$m (tilt $< 0.029°$) was achievable using approach-reference curves for a typical dC noise of 1.5 fF ($< 25\,\%$ of dC_{max}) [155].

If the mask is only optically parallelized to the sample, the 1-pixel error ($6\,\mu$m) in parallelization (0.115° tilt of the mask) to a virtual point of contact, where the capacitive sensors are between 1.6 μm and 3.7 μm from the sample. This transforms a 3 μm circle

at the centre of the mask into an ellipse of evaporated material on the surface with a penumbra of 50 nm – 100 nm. Therefore, even a mask with damaged capacitive sensor(s) may be used for evaporation, if optical parallelization is performed within an accuracy of 6 μm.

Mask selection criteria

The (distance-dependent) capacitance of each sensor can be used to judge the reliability of the sensor based on the following selection criteria.

The sensor may be included if:

- **Ex-situ measurement of cross-capacitance** Cross-capacitance must be below 40 fF for each pair of the three sensors.
- **Capacitance-distance relation:** $C(d)$ must behave as $a + b/(c + d)$ at optical distances $< 100\,\mu$m with visible change of $C(d)$ by d.
- **Signal to noise ratio:** The difference in capacitance at the inflection point must be $dC_{max} \geq 3 \times \Delta dC$, where ΔdC is the highest noise in dC observed below an optical distance of 25 μm.

A detailed description including other possible abnormal behaviours of capacitance curves and suggestions for experimental remedies can be found in Table 5.2 of [155].

Capacitive parallelization using reference measurement

The large variation in capacitive signal from the sensors implies that a universal method for capacitative parallelization cannot be achieved. It is, however, possible to capacitively parallelize the mask using the respective reference curve for each capacitor of the respective mask as obtained on a reference sample.

This allows one to parallelize the mask capacitively at distances smaller than optically accessible. Of course, this is limited by the extent of reproducibility of $C(d)$ of a certain capacitor at the same position as well as at different lateral positions on the sample. For a given mask and sample, consecutive capacitance curves are reproducible at the same position within an error in the mask-sample distance of only 250 nm as shown in figure 4.18 (a) and (b). The margin of 250 nm on each capacitive sensor allows capacitive parallelization with mask tilt $< 0.03°$. Figure 4.18 (d) shows that the curves deviate by

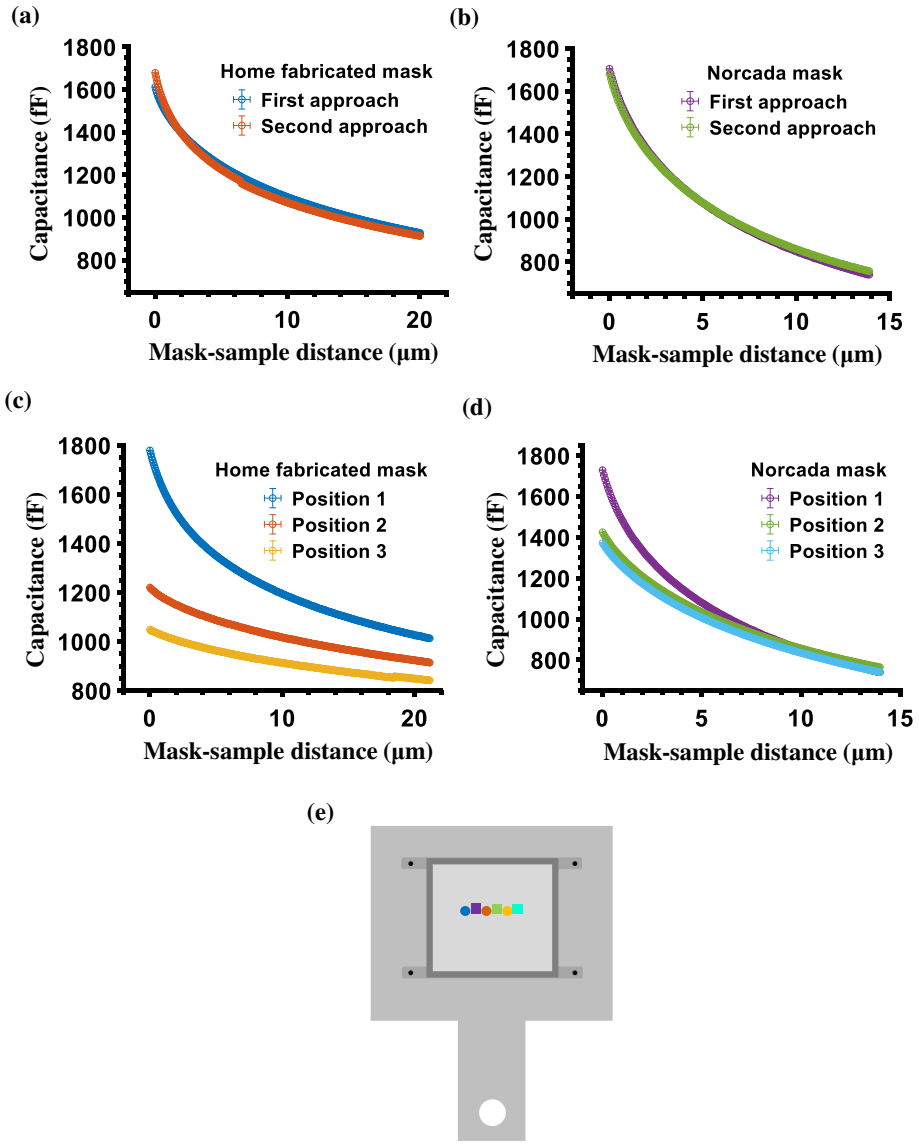

Figure 4.18: **Reproducibility of capacitance-distance curves.** Subsequent curves of a single capacitive sensor at the same position on Si sample **(a)** with *home-fabricated* mask, **(b)** with *Norcada* mask. Subsequent curves as numbered at different positions on Si sample. The positions are marked in **(e)** using same color as the curves with **(c)** *home-fabricated* mask (circles) and (d) *Norcada* mask (squares).

only 1.5 μm for the three lateral positions marked in figure 4.18 (e) allowing mask tilts $< 0.115°$ for three different positions. In figure 4.18 (c), however, it is observed that the maximum capacitance, i.e. the capacitance at zero-point is reduced after each contact with the sample. This might be explained by a nitride membrane that picks up particles from the sample each time, thereby creating an offset distance of the capacitor to the initial zero-point. This scenario is supported by the fact that prior to figure 4.18 (d), the mask had one contact with the sample only, while prior to figure 4.18 (c) the mask had four contacts with the sample, each at their respective position 1. The reduction in $C(d = 0)$ has also been observed in the same position after three or more contacts [155]. It is a plausible explanation that sub-micron particulates on the sample are transferred to the capacitive membrane and act like a pillar between mask and sample upon successive contact. Nevertheless, a single contact with the sample is sufficient for the purpose of calibration of mask-sample distance prior to evaporation through the mask at multiple locations on the sample without touching.

It would be worthwhile in the future to evaluate the first and second full-contact curves (akin to figures 4.18 (a) and (b)) at different positions directly and to use clean samples for the calibration measurements.

4.2.5 Evaporation using mask aligner

Evaporation of Au on Si(111)

As proof of principle, Au was evaporated on Si(111) without an initial touching of the mask to the sample. For a distance D between evaporation source and mask, distance d between mask and substrate, and lateral extension of evaporation source W, a penumbra width of the evaporated structure for a ballistic path of the evaporated atoms leads [139].

$$\Delta = \frac{d \cdot W}{D} \tag{4.1}$$

A conservative estimate for the mean free path of the atoms in the evaporated beam [156, 157] is given by the ideal gas equation:

$$\lambda_{\mathrm{MFP}} = \frac{\sqrt{k_B T m_{\mathrm{At}}}}{2\pi^{3/2} R \rho \sigma^2} \tag{4.2}$$

with temperature T, deposition rate R, atomic mass m_{At}, density of the deposited

material ρ, and atomic scattering diameter σ. A range of $\lambda_{\mathrm{MFP}} = 100\,\mathrm{m}$ for typical $R \approx 1\,\text{Å/s}$ and $D \approx 20\,cm$ confirms a ballistic regime. At typical $D = 0.2\,\mathrm{m}$ and $W = 5\,\mathrm{mm}$, a penumbra of $\Delta = 10\,\mathrm{nm}$ requires $d = 400\,\mathrm{nm}$.

The highly doped $0.1\,\Omega\mathrm{cm}$ Si(111) sample was pre-cleaned with acetone, isopropyl alcohol, and oxygen plasma etching at 40 W. The evaporation was performed at room temperature, pressure $p = 5 \cdot 10^{-8}\,\mathrm{mbar}$ and flux rate $R = 0.18\,\text{Å/s}$. The mask was approached optically to $25\,\mu\mathrm{m}$, and further approached by theoretical estimation based on the calibrated step size, to about $6\,\mu\mathrm{m}$. Consecutive fields were evaporated, with each field consisting of an array of 9×9 holes of diameter $3\,\mu\mathrm{m}$. Between each field, the mask was offset horizontally by $\sim 100\,\mu\mathrm{m}$ and moved closer to the sample. The final field was evaporated at full contact. Figure 4.19 (c) displays a scanning electron microscopy (SEM) image of two overlapping fields which have been used to crosscheck the steps of the horizontal piezo motor, revealing a discrepancy of only 4 % with respect to the calibration ($(73 \pm 2)\,\mathrm{nm}$ per step at amplitude 60 V).

Figure 4.19 (a) and (b) show subsequent characterization by atomic force microscopy (AFM) of fields evaporated at a distance of (a) 700 nm and (b) $4.5\,\mu\mathrm{m}$. The circle with 7 nm height consists of multiple clusters with diameters of 40 nm–100 nm. It exhibits sharp edges, and a flat, clean surrounding, which reveals a successful transfer of the holey mask structure to the sample. The edge sharpness basically determined by the cluster sizes reveals individual profile lines with a value as small as $\sim 10\,\mathrm{nm}$ (figure 4.19 (f)).

To quantify the edge sharpness, the profile lines from the center of the disk towards its rim are angular averaged [158] and fitted with an error function as shown in figures 4.19 (d) and (e). Figure 4.20 shows the 2σ widths of the fitted error functions as a function of mask-sample distance d, with the theoretical limit according to $\Delta = d \cdot W/D$ provided for comparison (blue line).

The offset of the data points with respect to the blue line is roughly the cluster size, implying that it is limited by diffusion. A diffusion-induced broadening of $\sim 100\,\mathrm{nm}$ has also been found for Au evaporation on Si(111) at room temperature, after pressing a shadow mask directly onto the sample [139].

It is crucial that during evaporation, the turbo pump mounted on the chamber is not in operation. The resulting vibration induces an elliptical distortion of the evaporated circles with peak-peak variations of diamter of about $1\,\mu\mathrm{m}$. In appendix figure 7.9, the effect of mechanical vibrations on evaporated patterns is shown by an SEM image.

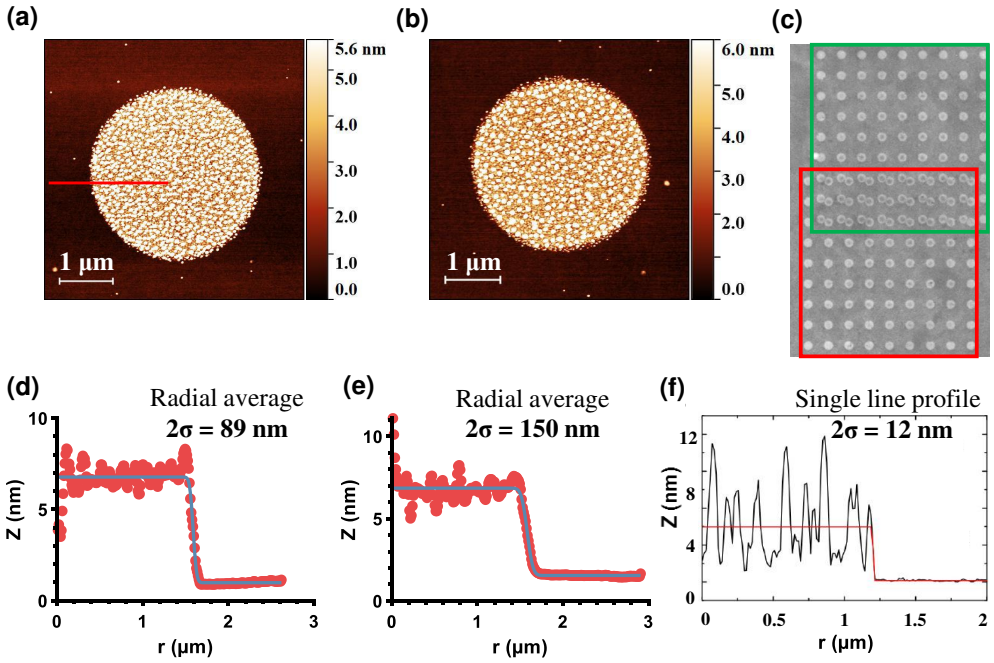

Figure 4.19: **Evaporation of Au on Si(111) using a *Norcada* mask.** AFM images of Au circle evaporated at **(a)** mask-sample distance of 700 nm and **(b)** mask-sample distance of 4.5 μm. **(c)** SEM image with consecutive evaporation fields marked by different colors rectangles with an offset in lateral position. **(d)** Radial average of the height profile in (a) with fitted error function (blue line) of indicated 2σ width. **(e)** Radial average of the height profile in (b) with fitted error function (blue line) of indicated 2σ width. **(f)** Individual line profile along the red line in (a) with fitted error function (red line) of indicated 2σ width.

Pb evaporation on Si(111)

Evaporation of Pb on Si(111) using a similar *Norcada* mask was performed [155] showing regions of penumbra of about 60 nm as shown in figure 4.21 (a). The angular average of the penumbra across a circle was typically less than 160 nm at a safe mask-sample distance of 1 μm. A limiting factor to the penumbra is the diffusion of lead on Si at 300 K [159], resulting in no clear mask-sample distance dependence in the penumbra up to a mask-sample distance of 4 μm. A clogging of Pb was observed on the sidewalls of the mask via SEM as shown in figure 4.21 (b). The mask radius clogged by about 195 nm after several evaporations adding to a corresponding thickness of 90 nm of Pb on the sample. *Home-fabricated* masks have a feature size of about 100 nm and require 2 consequent evaporations. Assuming a linear clogging rate, this limits the feature size of the mask to twice the material thickness to be evaporated.

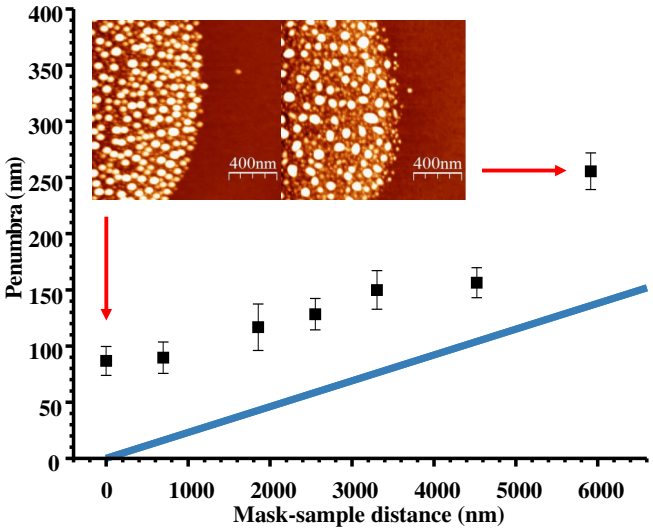

Figure 4.20: **Mask-sample distance dependence of the penumbra.** Plot of the penumbra 2σ from fits as in figures 4.19 (d) and (e) for several evaporation fields at different mask-sample distances. The blue line is the penumbra Δ as theoretically expected based on geometry (equation 4.1). The AFM images in the inset, correspond to the mask-sample distances indicated by the arrows and show part of an evaporated Au circle.

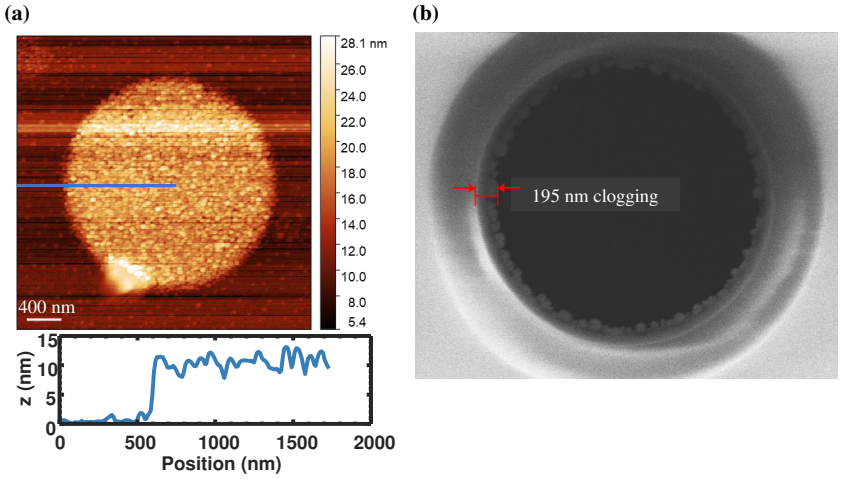

Figure 4.21: **Evaporation of Pb on Si(111) using a *Norcada* mask (a)** AFM image of a circle of Pb evaporated at a mask-sample distance of 500 nm. The line profile along the blue line is shown on the bottom with an edge sharpness of about 60 nm. **(b)** SEM image of the mask after 90 nm of Pb evaporations showing clogging on the sidewalls. Figures adapted from [155].

4.2.6 Summary and outlook

The ultrahigh-vacuum mask aligner has been established for the in-situ preparation of patterned samples with the use of Si-based shadow masks. Three independent piezomotors placed beneath the mask allow for control of the tilt and distance between the mask and the sample. The mask-sample distances are measured via three capacitive sensors placed on the backside of the mask. With the use of a reference measurement involving contact between the mask and sample, the mask can be approached to the sample within a distance $< 1.5\,\mu$m, eliminating the requirement for further contact in subsequent cycles of evaporation. The reproducibility of such distance-dependent capacitances enables capacitive parallelization and mask-sample distance control with a margin of 250 nm on the same position and $1\,\mu$m at different positions on the same sample, corresponding to mask tilts of $< 0.03°$ and $< 0.115°$, respectively.

The mask aligner has been established for successful evaporation of Au and Pb on Si(111), creating sharp edges with penumbra less than 100 nm at safe distances between the mask and sample of $1\,\mu$m. The exchangeable evaporator allows for the implementation of other materials, e.g. vanadium, in the future. For the fabrication of an ideal interface, it is beneficial to avoid any contact of the mask with the sample to be patterned. It is therefore advantageous to test the reproducibility of capacitances between different samples of the same material. This also requires a study of the influence of other experimental parameters such as the removal and insertion of the sample with the wobble stick. If the reference curve is pre-established, this later minimizes the time lapsed before a material may be evaporated onto a freshly prepared sample. This is particularly significant in the fabrication of a pristine patterned superconducting film on a topological insulator.

5 ARPES and STM measurements on patterned Nb-BST

Fu and Kane's proposal [5, 45] to use topological insulator–superconductor (TI-SC) heterostructures to host and manipulate Majorana fermions was immediately followed by proposals and experimental developments in semiconductor-superconductor heterostructures [25, 26, 160–162] that revived the interest in superconducting proximity effect using materials with spin-orbit coupling. These have also motivated more complex systems of TI-SC heterostructures, using ferromagnets [63, 163] and unconventional superconductors [49]. The immense theoretical interest has pushed experimentalists to catch up in realizing various TI-SC proximity structures [164, 165], in order to understand if the superconductivity of the Fu-Kane Hamiltonian can be realized in a solid and indeed results in an induced gap in the TI surface state. The situation can be discussed in the strong and weak coupling limit. In the strong coupling limit, the modification of superconductivity by the TI becomes significant, including suppression of the order parameter and formation of interface states within the bulk superconducting gap [166]. This is referred to as the inverse-proximity effect. The weak coupling limit will be of primary interest in the following discussions. Several studies have shown proximity-induced effects in heterostructures such as Bi_2Se_3-$NbSe_2$ [14, 167], Bi_2Se_3-Sn [17], and Bi_2Se_3-W [168]. A superconducting gap observed in these Bi_2Se_3 films, coexisting with topological surface states, potentially indicates topological superconductivity in the TI film. Bi_2Se_3-$Bi_2Ca_2Cu_2O_{8+\delta}$ heterostructures created by growing the Bi_2Se_3 on top of the d-wave superconductor have shown fully-gapped topological surface states detected by ARPES, whose isotropic gap structure differ from the bulk superconducting gap [169, 170]. Zero-bias peaks in vortex cores measured by STM in Bi_2Te_3-$NbSe_2$ heterostructure have shown promise for such heterostructures as a device platform for realizing Majorana modes [9, 171].

In most of the works mentioned, the binary TI Bi_2Se_3 was used. But despite its

relatively large bulk gap of 0.3 eV, it is doped by Se vacancy sites, such that the Fermi level is in the conduction band. The existence of topological surface states has been experimentally verified by ARPES [172–178], isolating the effects of the topological states from the bulk contribution to the total conductance remains challenging. This is similar to the binary compounds Bi_2Te_3 and Sb_2Te_3 [179, 180]. Telluride TIs are preferred over selenide TIs, due to the relatively lower vapor pressure of Te as compared to Se, which helps reduce vacancies that contribute bulk charge carriers. Therefore, one possible approach to reduce bulk carriers is to alloy the binary compounds, for example Bi_2Te_3 and Sb_2Te_3 [19, 181–184]. The rationale for this is that mixing Te vacancy rich n-type Bi_2Te_3 [179] with anti-site impurities rich p-type Sb_2Te_3 [179, 180] in appropriate ratios will result in a net zero bulk charge carrier density. This method has led to optimized Fermi-level tuning in MBE grown $(Bi_{1-x}Sb_x)_2Te_3$ [20], where fine-tuning of the ratio to $x = 0.94$ minimizes the bulk current. More detailed ARPES shows that the Fermi level shifts from above to below the Dirac point between $x = 0.94$ to $x = 0.96$ [19]. Fabrication differences can, however, level to uncontrolled disorder in the MBE grown samples such that the exact stoichiometry for a tuned Fermi level is not reproducible.

The typical MBE technique to epitaxially grow the topological insulator on top of the superconductor involves either a direct layer-by-layer growth [171] or a two-step growth, wherein a passivation layer is formed priorly [185]) to the epitaxial growth of the topological insulator. These techniques have shown steady success with TI and Nb-based superconductors such as in [171] and [9] where 5 QL of Bi_2Te_3 were grown on top of $NbSe_2$ and the Abrikosov vortices induced on the Bi_2Te_3 probed via STM. However, these works are afflicted by the high bulk carrier contribution in Bi_2Te_3 as well as the lack of studies on the length scale of the induced gap that would require samples of different thicknesses and the missing access to impurities at the interface. Moreover, for these samples with $\Delta \approx 1$ meV and $E_D - E_F \approx 100$ meV, the minigap to the Caroli-de-Gennes-Matricon states is ≈ 0.01 meV only, which is much smaller than the energy resolution of 0.1 meV using standard STS at 400 mK. On the other hand, creating a lateral interface such as in figure 2.7 is challenging due to the requirement of in-situ patterning. So far, this has been mostly been used for transport devices with conventional lithography [185]. The mask aligner fabrication process as described in the previous chapter is certainly a tool to aid in in-situ patterning. In the following section, an alternate fabrication process based on a "mask-on-sample" method is examined for STM applications.

5.1 Preparation of STM samples

Institute PGI-9 at Forschungszentrum Jülich has developed a fabrication process for selective molecular beam epitaxy (MBE) growth of topological insulator - superconductor patterned structures that has been successfully implemented for transport devices [186, 187]. The optimization of such samples for characterization by STM are explored in this thesis. Heterostructures of topological insulator BST (ranging from $Bi_{0.22}Sb_{1.78}Te_3$ to $Bi_{0.35}Sb_{1.65}Te_3$) and s-wave superconductor Nb were fabricated by Michael Schleenvoigt, Group Gruetzmacher, PGI-9, Forschungszentrum Juelich. The samples were fabricated in a UHV chamber (HNF Nanocluster) consisting of dedicated sections for the growth of topological insulators and Nb respectively, interconnected by a UHV transfer. This ensures that the heterostructure is fabricated without breaking the vacuum, resulting in a pristine interface. The sample is then capped with a protective Se layer for its ambient transport to the STM chamber at RWTH Aachen University.

The patterning of the Nb on BST is realized by a mask-on-sample process [187, 188] depicted in figure 5.1. The mask-on-sample chip is fabricated ex-situ within a cleanroom (HNF classes ISO 1-3). After the required surface passivation of Si, described below, it can be mounted on a standard omicron sample holder compatible with the MBE growth chambers.

The substrate wafer comprises a stacking of 100 nm Si_3N_4 above 300 nm SiO_2 deposited via low pressure chemical vapor deposition (LPCVD) onto a highly doped (5 mΩ cm) Si (111) 4-inch wafer. The wafer is diced into 7 mm $\times$ 7 mm chips, compatible with standard Omicron sample holders.

The chip is then spin-coated at 4000 rpm with the negative photolithography resist AZ 2020 (nLOF), mixed in a ratio of 1:1 with AZ EBR to render the resist sensitive to electron beam lithography. A pre-exposure bake is performed for 5 mins at 100 °C. The samples are subsequently exposed to e-beam lithography with a dose of 91 $\mu C/cm^2$ at an acceleration voltage of 100 kV. A post-exposure bake is done at 110 °C for 3 mins. The sample is developed in AZ MIF 326 for 25 s, succeeded by a rinse in distilled water. The result, depicted in figure 5.1 (b) shows the exposed pattern in black. Via RIE with a CHF_3/O_2 plasma, 55/5 sccm, 25 W radio frequency (RF), 100 W inductively coupled-plasma (ICP) at 20 °C for 185 s, the unexposed Si_3N_4 is removed. The exposed Si_3N_4 bridges remain intact with SiO_2 beneath them. The nitride etch is also performed on the backside of the substrate in order to ensure electric contact of the doped Si with the STM

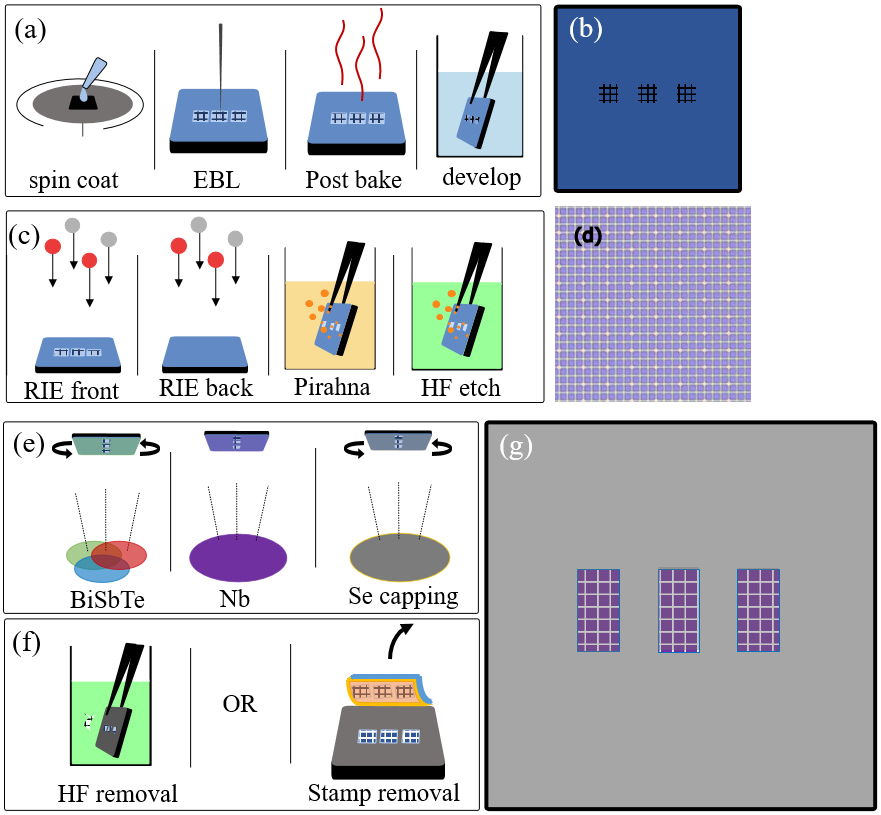

Figure 5.1: **Schematic representation of the mask-on-sample fabrication process.** **(a)** Lithographic definition of the pattern. **(b)** Schematic of the sample after the lithographic definition of the patterned fields. **(c)** Etching steps to create mask structure held by a SiO_2 pillar grid. **(d)** Optical micrograph of patterned mask-on-sample that is ready for growth. One of the three patterned regions measuring 0.5 mm × 0.5 mm each, has been imaged here. **(e)** Growth of BST onto the rotated sample, growth of Nb onto a stationary sample and protective capping of the sample by the growth of Se onto the rotated sample. **(f)** Grid removal by etching of SiO_2 pillar grid by hydrofluoric acid (HF) (left) or mechanical removal of SiO_2 pillar grid with a polymer stamp. **(g)** Schematic view of the final sample with three fields of the pattern.

sample holder. Before MBE growth, the samples are cleaned in a piranha solution (2:1 by volume of 96 % H_2SO_4 : 33 % H_2O_2) and hydrofluoric acid (1 % HF) for 10 mins and 16.5 mins respectively, with DI rinses for 10 mins after each step. The HF dip releases suspended nitride bridges by etching away the SiO_2 underneath. These nitride bridges will then be held only by pillars of SiO_2 at the ends of the bridges i.e. at the intersecting corner junctions between bridges. There, complete etching would require more time. Additionally, it passivates the exposed Si by H as required for subsequent MBE growth of BST. The result, imaged in figure 5.1 (d) shows exposed Si (purple) everywhere except of the nitride bridges that appear white.

This fabricated mask-on sample chip is mounted on the Omicron holders and inserted into the MBE chamber. A pre-growth annealing is done at 700 °C for 10 mins removing the H and cooled to 305 °C over 25 mins. During the cooldown, the source material cells are heated to their growth temperatures of 465 °C for Bi, 475 °C for Sb and 325 °C for Te. Growth of BST is performed on a rotating sample chuck (figure 5.1 (e) left). The sample is rotated at 10 rpm when the main shutter is opened. The sample is initially exposed for 30 s to Te only, then for 30 s to Te and Bi and finally to Sb as well for a growth period of 45 mins.

Thereafter, the rotation of the chuck is ceased and Nb is grown with the molecular beam having a direction parallel to one of the sample edges. The Nb is evaporated at a rate of 2 Å/s from a 8 cm^3 FABMATE®crucible via electron beam effusion with 10 kV for the electron acceleration voltage. The substrate temperature during the growth is held at 50 °C while the evaporator chamber is cooled with liquid nitrogen to ensure clean deposition of the Nb. Finally, the sample is capped with a 20 nm thick amorphous layer of Se (crucible temperature 300 °C) grown at a substrate temperature of 10 °C for 180 mins. The Se capping is performed with a rotating chuck again, ensuring that it is covering the entire sample surface.

The sample can then be removed from the UHV chamber. The Se capping protects the underlying heterostructure from contamination during exposure to ambient and from the HF or polymer stam used to remove the nitride grid. The detachment of the nitride bridges from the supporting SiO_2 pillars is a necessary requirement for STM such that the tip can access the Nb-BST interface. Removal of the grid of bridges in-situ is in principle possible, e.g. using a focused ion beam combined with a nanomanipulator for holding the grid. However, the design of a compatible holder and the subsequent growth optimization is a large effort that has not been pursued. Alternatively, the removal of pillars via

RIE which might require an additional e-beam lithography step to make holes directly above the pillars which might damage the near vicinity of the underlying sample. The used ex-situ removal of the grid makes the protective capping layer necessary. Ambient exposure of TIs is known to oxidize the surface, in particular when Sb is present [189], leading to SbO_x and TeO_x. This manifests as a bristle surface that may not be visible in SEM where the typical penetration depth is too large ($\sim 100\,\text{nm}$). Control via surface probing methods like AFM and STM is necessary to optimize the effective thickness of the capping layer as discussed in section 5.1.2.

There are two viable methods for the ex-situ removal of the grid (figure 5.1 (f)). The first method is the chemical etching in an HF solution removing the silicon pillars, hence, releasing the grid from the sample. The second is the exfoliation of the grid by a polymer stamp. These methods and their advantages and disadvantages will be discussed later in section 5.1.2. For the STM measurements in the following chapters, the chemical etching method was used.

The sample after grid removal is controlled by SEM to ensure that no physical damage has been caused to the Nb and BST. The sample is then transported from FZJ to RWTH Aachen in a nitrogen-filled box and inserted into the load lock of the STM chamber within two hours. A storage of the sample in ambient for much longer periods than this results in adsorbates on the Se capping that do not get removed by decapping. Therefore, it is important to minimize the time between the removal of the sample from the Se growth chamber and the insertion into the load lock of the STM chamber. As presented in the SEM image in figure 5.2 (a), the sample consists of multiple fields of grid patterns, each $800\,\mu\text{m} \times 1600\,\mu\text{m}$. This makes it feasible to locate the field optically and approach the tip onto the patterned field (See figure 7.10 in appendix).

Each of the patterned fields consists of squares $3\,\mu\text{m} \times 3\,\mu\text{m}$ separated by 250 nm strips. Figure 5.2 (b) shows a tilted top view SEM image with a larger BST square underneath a smaller Nb square. The penetration depth in SEM, which is proportional to the incident electron energy and inversely proportional to the density of the specimen (500 nm to $1.25\,\mu\text{m}$ for typical voltage ranges of 5 keV to 20 keV for the density of Si $= 2.33\,\text{g/cm}^3$), is much larger than the thickness of the grown films. The shown SEM image at 5 kV thus allows imaging of the Nb and BST. Figure 5.2 (c) shows the top view SEM image with cross section sketches along corresponding dashed lines on the right and bottom. Typically, about 200 nm width of exposed BST appears adjacent to the Nb. This width can vary by up to 100 nm due to fabrication differences in the width of

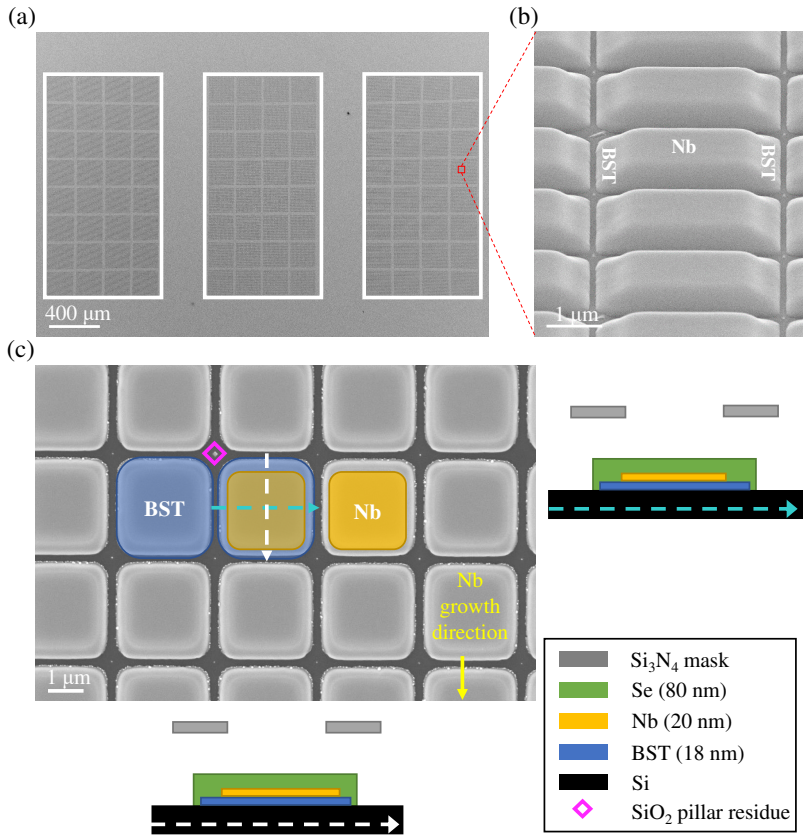

Figure 5.2: **Scanning electron micrographs and schematic of the patterned Nb-BST structure. (a)** Scanning electron micrograph with 3 fields of patterns marked by white boxes. **(b)** SEM (tilted top view) of patterns within a field with marked areas of Nb and exposed BST. **(c)** SEM (top view) of patterns within a field. Profile along the blue dashed line is on right. Profile along the white dashed line is on the bottom.

the nitride bridges.

Despite promising transport measurements [186, 187] on samples fabricated by this method, their efficacy for surface-sensitive methods needs to be investigated. A particular distinction is that the transport samples use a 5 nm Al_2O_3 capping layer that is not easy to remove for STM. The optimization of removable Se-capped STM samples, via the mask-on-sample fabrication process, is accordingly twofold:

1. The ability to decap Se without impairing the BST.
2. The efficacy of Se capping to protect the underlying Nb and BST from
   a) HF that is used for grid removal,
   b) ambient contamination (including oxidation).

5.1.1 Decapping the Se layer in UHV

The preparation chamber in which the sample is decapped is connected via UHV valves to the STM. This ensures quick and pressure-efficient transfer of the decapped sample into the 640 mK cryostat, for minimal surface contamination. This is critical due to the strong gettering property of gases by Niobium. The preparation chamber shown in figure 5.3 (a) consists of a resistive heater at the center of the chamber where the sample is placed for decapping via heating. A mass spectrometer is placed a few centimeters above, thus providing a direct line of sight during decapping. The pressure in the chamber is monitored via the Bayard-Alpert gauge located below the heater. The heater is cleaned by degassing at about 550 °C ($P_{\text{filament}} = 29\,\text{W}$) for 12 hours. Immediately before the decapping, it is degassed again at about 350 °C for 15 mins.

At the onset of decapping, the preparation chamber has a typical base pressure of $p_{\text{base}} = 1 \times 10^{-10}$ mbar with a liquid nitrogen cryogenic pump implemented in the main chamber that captures molecules that are released during decapping or sample transfer. The decapping is performed at 260 °C ($P_{\text{filament}} = 7.7\,\text{W}$) for 5.5 mins. The sample can be transferred into the STM within 5 mins. Typical pressures during the decapping process are between $p = 1 \times 10^{-7}$ mbar to $p = 6 \times 10^{-7}$ mbar. The mass spectrometer signal for Se and the pressure during the decapping process are shown in figure 5.3 (d). While the mass spectrometer identifies Se desorbed from the sample, there is no immediate pressure rise during the rise in the mass spectrometer signal. This suggests that despite the rather direct line of sight of the Bayard-Alpert gauge, there is no pressure signature of the Se. An optical contrast change on the sample, however, indicates the decapping as can be seen in figures 5.3 (b)–(c). Ex-situ characterization of decapped samples by TEM is shown in figure 5.4. The diffusion of Nb extends about 5 nm into the BST as evidenced by the different contrast of this later. Tis diffusion length is much smaller than for commonly used superconductors like Al [186]. The Nb growth on BST is polycrystalline.

Desorption of amorphous Se from Bi_2Se_3 and Bi_2Te_3 has been shown to start at 150 °C after initially coalescing into micron-sized islands [190]. Prior Ar milling to remove contaminants before decapping at 210 °C can result in STM-compatible surfaces [191]. However, this milling step demands precise optimization to not influence the underlying BST. In addition, thermal annealing after decapping is often required to optimize the sample surface [192–194].

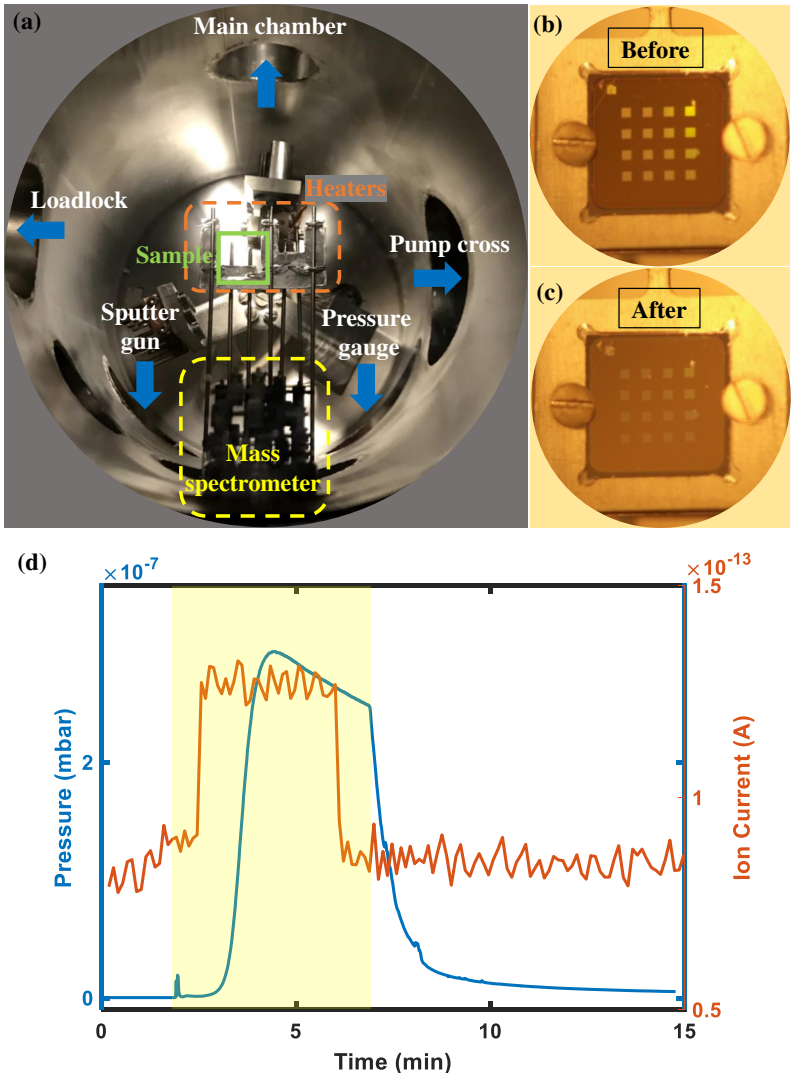

Figure 5.3: **Optimization of the decapping of Se via annealing (a)** Photograph of preparation chamber including mass spectrometer and heater. The resistive heater (orange) is located in the center of the chamber where the sample (green) is heated for decapping of Se. The mass spectrometer (yellow) is located about 10 cm above the heater. **(b)** Optical image of sample before and **(c)** immediately after decapping. **(d)** Pressure and mass spectrometer ion current for Se measured in time. The highlighted section marks the time period of sample heating to 260 °C.

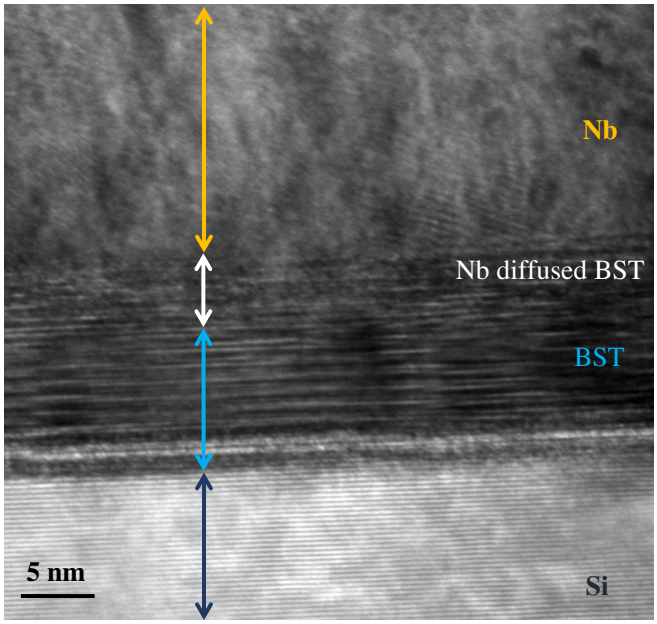

Figure 5.4: **Diffusion of Nb into BST.** Transmission electron micrograph of a sample with 20 nm Nb and 15 nm BST grown on Si. Each material layer is marked with arrows as indicated by the corresponding colour.

Another effect that has to be taken into account is the possible incorporation of Se into the Nb and the BST during decapping. Thermal desorption of Se is known to change the surface stoichiometry in Te-based TIs. Se incorporates into the top 3 nm of Bi_2Te_2Se by substituting Te when decapping at 160 °C [195], and up to 7 nm in Bi_2Te_3 when decapped at 150 °C [190]. In figure 5.5 (a), the chemical composition in nominally grown $Bi_{0.35}Sb_{1.65}Te_3$ is characterized with Energy-dispersive X-ray spectroscopy (EDX) on different locations as indicated on the SEM image of figure 5.5 (b). Both, Nb and the topological insulator show a higher intensity of Se than of Bi. The sample for these measurements was decapped with a resistive heater at 200 °C for 10 mins in the MBE growth chamber and then removed to ambient for the SEM/EDX characterization. Figures 5.5 (c)–(f) are the scanning transmission electron microscopy (STEM) analysis of a cross-section lamella created by a focussed-ion beam with a protecting Pt-based glue layer on top (STEM measured by Jin Hee Bae of PGI-9 in the TEM instruments of the *Ernst Ruska-Centrum für Mikroskopie und Spektroskopie mit Elektronen*). Figure 5.5 (c) shows the high-angle annular dark-field image (HAADF) of the cross-section marking the regions of the glue, Nb and BST. In HAADF, elements with a higher atomic number Z scatter more electrons due to larger electrostatic interactions between the nucleus

and the electron beam. This results in a brighter appearance of atoms with a higher Z [196]. An oxide layer is visible at the interface between the Nb-BST structure and the Pt-glue as a grey area. Figures 5.5 (d)–(j) show the intensities of the corresponding elements as determined by EDX is indicated on the top left. Figure 5.5 (j) shows no Se after decapping by DC-heating at 300 °C for 6 hours. This is akin to the Te-decapping process that is successfully performed in the same chamber at Universität Köln by Jens Brede. The extent of Se incorporation, therefore, appears to depend on the decapping procedure with higher temperatures being favorable. Anti-site defects of Bi/Sb in the Te lattice are common in BST [179]. Se is smaller and higher electronegative than Bi/Sb. This makes it an energetically favourable replacement for these defects. In addition, Se can be incorporated as interstitial or within van der Waal gaps. The decapping temperature of 300 °C is close to the typical growth temperature of 330 °C. Te-vacancies may be created, making it easier for the Se atoms to move to the surface for desorption. Overall, Se incorporation must be characterized for individual decapping procedures. Unfortunately, it remains unknown for the decapping process performed here. However, Se incorporation into the TI, combined with the re-evaporation of incorporated Se after decapping, is a possible explanation for the observation of regions of rough surfaces of BST, especially in Nb-BST samples. But this cause could not be isolated from the fabrication-induced damage that will be discussed in section 5.1.2. While it is plausible that $NbSe_x$ forms as a consequence of Se annealing under Nb rich conditions [197], it is known that the most stable compound $NbSe_2$ is superconducting as well [198].

5.1.2 Optimization of patterned samples for STM

Unfortunately, a reliable method for the removal of the stencil mask and subsequent preparation of the sample for STM measurements could not be established. Some of the trials are described in the following.

The main problem was that the Se did not protect the BST during the mask removal process. Using a Se to cap the sample, the BST was removed during the HF dip. Figure 5.6 shows SEM and TEM images on such samples after decapping and some STM measurements. In figure 5.6 (b), there is no BST adjacent on the side of Nb and in figure 5.6 (c), it appears that the Nb is even undercut. The reason is that the HF attacks the BST sideways, where the Se might not be thick enough to avoid contact between BST and HF.

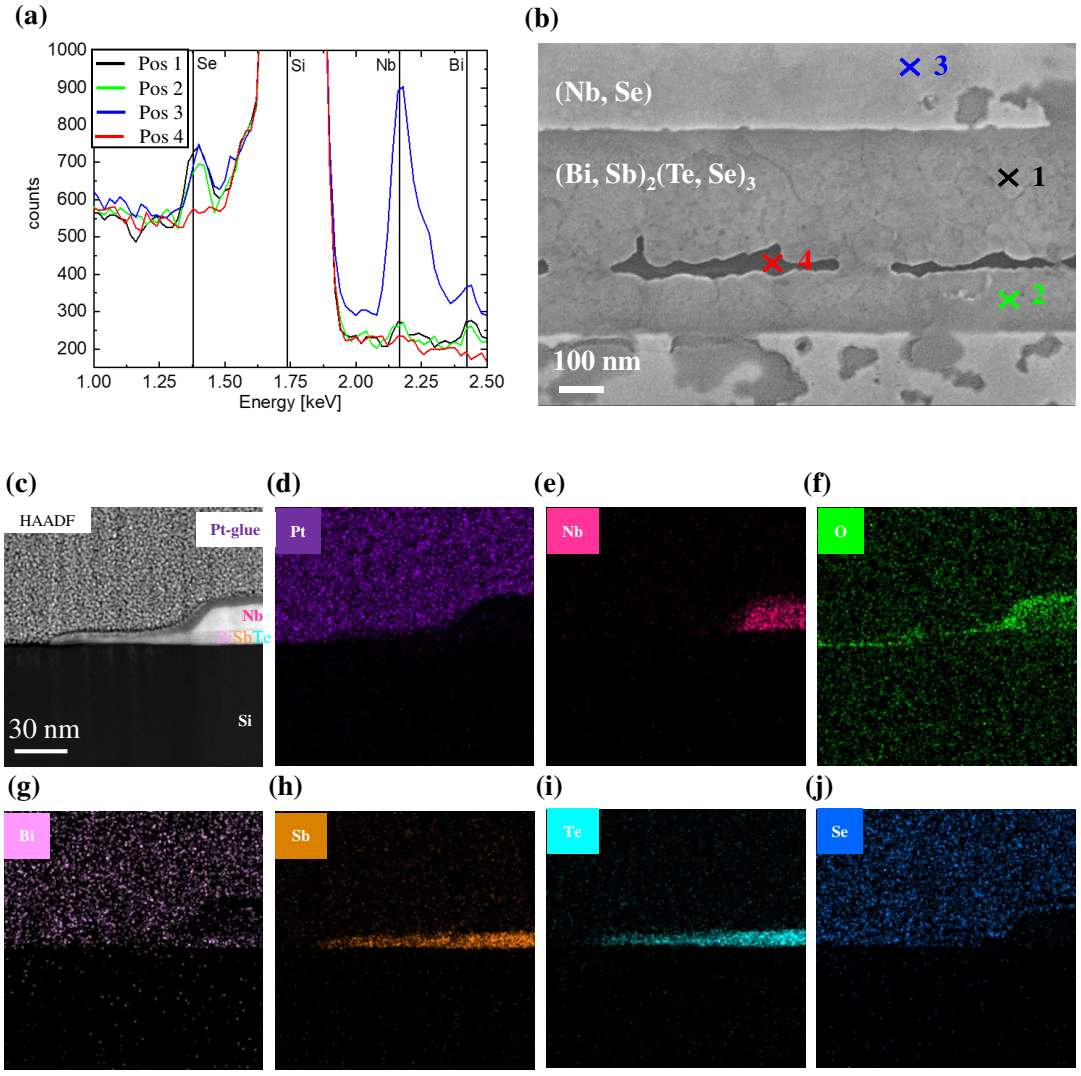

Figure 5.5: **Characterization of Se incorporation into Nb and $(Bi,Sb)_2Te_3$.** **(a)** EDX spectra at different positions. **(b)** SEM image of the patterned Nb-BST sample imaged from the top. The markers indicate the positions where the EDX spectra were acquired. **(c)** High-angle annular dark-field (HAADF) image of a Nb-BST/Si lamella in cross-section. **(d)–(j)** STEM-EDX maps of respective elements as indicated on the top left.

A possible remedy would be to minimize the etching time. Therefore, the pre-growth etching of the mask (figure 4.3 (c)) is increased, reducing the diameter of the SiO_2 pillars without making them unstable. The pre-growth etching time was increased from 15 mins to 17.5 mins such that the post-growth etching time was only 3 mins – 5 mins (reduced from 10 mins –12 mins).

The second optimization parameter to avoid etching of BST is the thickness of the Se. While thicker Se provides better protection, it might prohibit the detachment of the mask during the HF dip. It was found that 70 nm of Se thickness is the maximum enabling removal of the mask by HF dip (In general, the total thickness of BST/Nb/Se stack must not exceed a third of the height of SiO_2 pillars).

Removal of the mask by exfoliation (figure 4.3 (f)) could even enable a maximum Se thickness of 120 nm. Here, a First Contact polymer[1] is placed on the sample, dried for 30 mins, contacted by a sticky tape and then removed. Figure 5.7 shows the result. Figure 5.7 (a) shows that this removes the mask, but also partly the Se capping. Indeed exposing such a sample to an HF dip removes large parts of the BST. Moreover, these did not show a superconducting gap in STM on the Nb parts after Se decapping probably due to surface oxidation.

Finally, alternative capping materials were explored such as Te capping and a combination of Te and Se cappings. The Te capping and decapping already enabled ARPES mapping of BST films [199], but was not resistant to the HF dip. It is also known that Te capping and decapping changes the stoichiometry of BST [190, 195]. Te capping followed by Se capping was HF resistant and showed no damage indicated by SEM. However, these samples did not show any superconducting gap via STS yet.

Further work to find appropriate solutions for capping is required. One possibility is to use exfoliation for both the removal of the mask and the in-situ removal of Te [192]. This avoids both the HF dip removal of the Te and the stoichiometry change. The Te decapping by exfoliation works even for $MnBi_2Te_4$ that revealed good ARPES data afterwards [200]. The adhesive tape-based technique is commonly used in UHV to cleave bulk crystals. A Se cap on top might be added if an HF dip cannot be avoided. Despite incomplete preparation of the samples, some STM and STS data are presented in the sections 5.3 and 5.4.

[1] http://www.photoniccleaning.com/default.asp

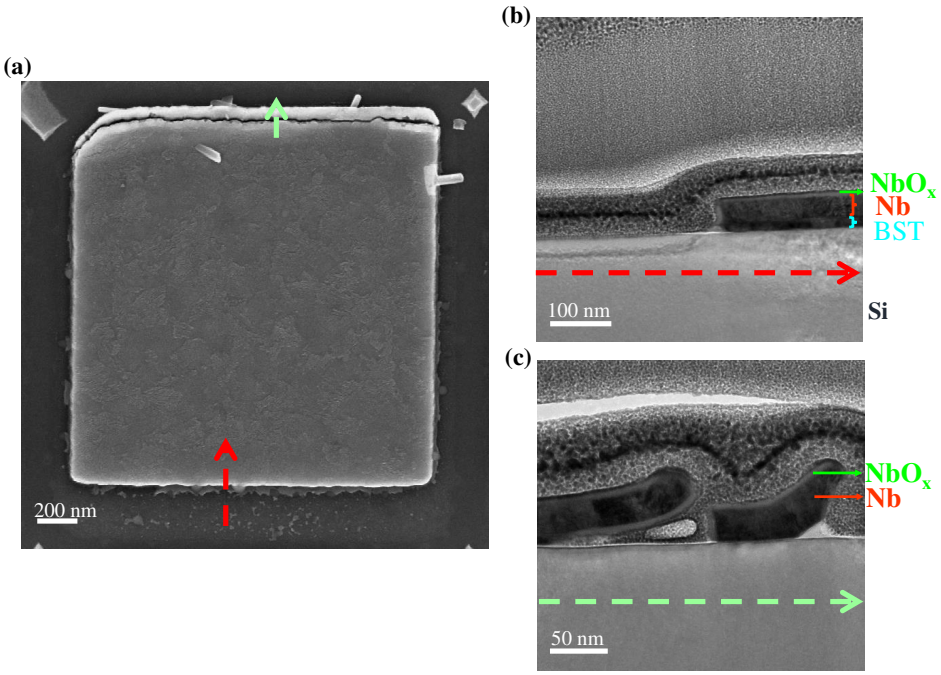

Figure 5.6: **Post-STM characterization of sample (a)** SEM image of one of the patterned Nb square on BST. **(b)** TEM across the cross-section indicated by red arrow in (a). **(c)** TEM across the cross-section indicated by green arrow in (a).

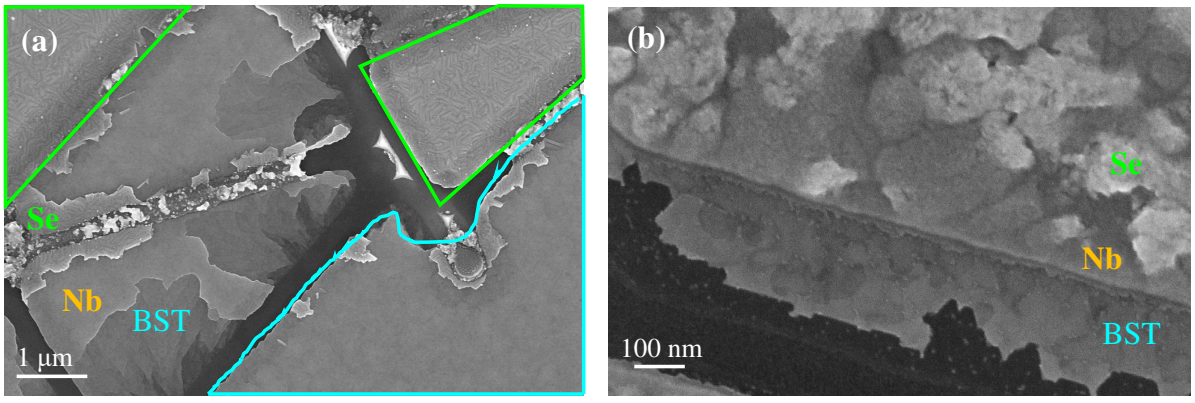

Figure 5.7: **Failure of exfoliation method for removal of grid. (a)** SEM image after exfoliation of grids without HF dip. The green regions show remaining Se capping. The blue region shows exposed BST. The remaining parts are prone to uncontrolled exfoliation, where different regions are exposed as marked. **(b)** SEM image after exfoliation, followed by a dip in HF. Remaining Se appears on the Nb and regions of BST are completely removed.

5.2 ARPES measurements of Nb-BST

While TEM (figure 5.4) probes the diffusion of Nb into BST and vice versa, the resulting band-bending is characterized by ARPES. The BST is measured first without the Nb, to establish a clean surface with a sharp Dirac cone.

A 20 nm thick film of $(Bi,Sb)_2Te_3$ is grown via MBE on surface passivated Si(111) and subsequently transferred to the ARPES chamber via a vacuum shuttle (pressure $p_{\text{shuttle}} < 3\times10^{-10}$ mbar). During a typical transfer, the maximum pressure is $p_{\text{max}} \approx 1\times10^{-9}$ mbar for <1 min. The ARPES experiments were conducted in PGI-6, Forschungszentrum Jülich with the help of T. Heider and L. Plucinski.

Figure 5.8 shows ARPES characterization using He and Xe sources on $Bi_{0.3}Sb_{1.7}Te_3$. Figure 5.8 (a) is the constant energy cut at the Fermi level (binding energy $E_B = 0$ meV) showing the bulk states indicative by the star-shaped appearance of the upper bulk valence bands. The directions k_x and k_y are the $\Gamma-M$ and $\Gamma-K$ directions, respectively. Figures 5.8 (b)–(d) display the cuts taken at k_y as marked in (a) measured with the He source at $h\nu = 21.2$ eV. Figures 5.8 (e)–(g) shows the same with the Xe source at $h\nu = 8.44$ eV. *Cut 1* traces also through the surface states, while *Cut 2* and *Cut 3* trace through the bulk valence bands only for different k_z, depending on the photon energy.

For both photon energies, the Dirac point appears around 70 meV above the Fermi energy. Slight discrepancies to previous data of Dirac points [201] might be attributed to a different disorder, i.e. a different bulk doping. However, the Fermi level can be tuned by stoichiometry change as evidenced in figure 5.9. The increased Sb content is accompanied by about 100 meV upward shift of the bulk valence band with respect to the Fermi level in a p-type manner as found previously [19].

Temperature dependence of Dirac point

Since STM measurements are performed at lower temperatures, it is beneficial to investigate temperature-induced effects on the band structure. To this end, the Dirac point position of $Bi_{0.3}Sb_{1.7}Te_3$ was measured at various temperatures.

At 300 K, the ARPES band structure in figure 5.10 (a) features a Dirac cone with Dirac point at about 50 meV above E_F. The photoemission intensity has been divided by the Fermi-Dirac function to compensate for the reduced state occupation around E_F still providing relatively sharp bands. This method is known to show a reasonable dispersion up to $5k_BT$ above the Fermi level [202]. The procedure is sensitive to the

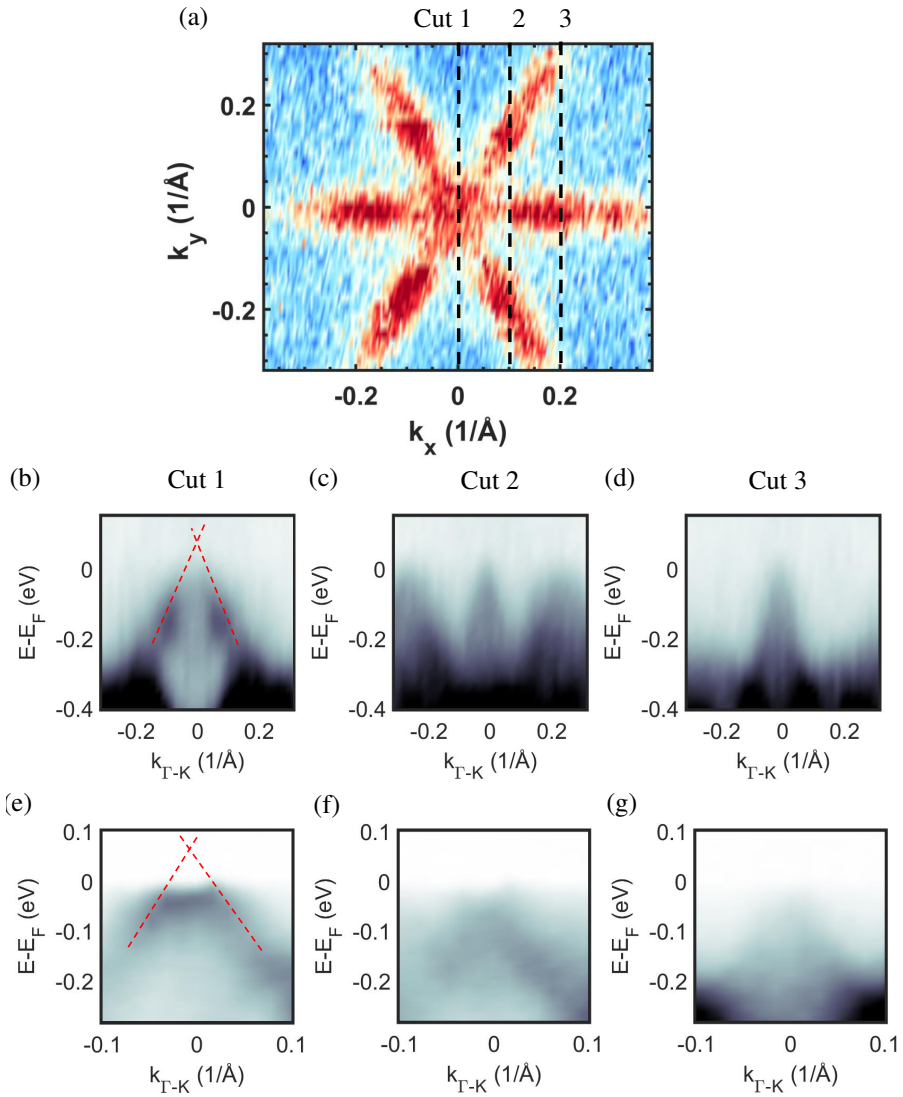

Figure 5.8: **Photoemission spectroscopy of $Bi_{0.3}Sb_{1.7}Te_3$ with He and Xe sources both measured at 55 K. (a)** Constant energy cut at Fermi level recorded $h\nu = 21.2\,\mathrm{eV}$. **(b)–(d)** Cuts taken at k_x corresponding to *Cuts 1–3* and measured with He source ($h\nu = 21.2\,\mathrm{eV}$). **(e)–(g)** measured with Xe source ($h\nu = 8.44\,\mathrm{eV}$). Red dashed lines in *Cut 1* extrapolate the Dirac cone to the Dirac point.

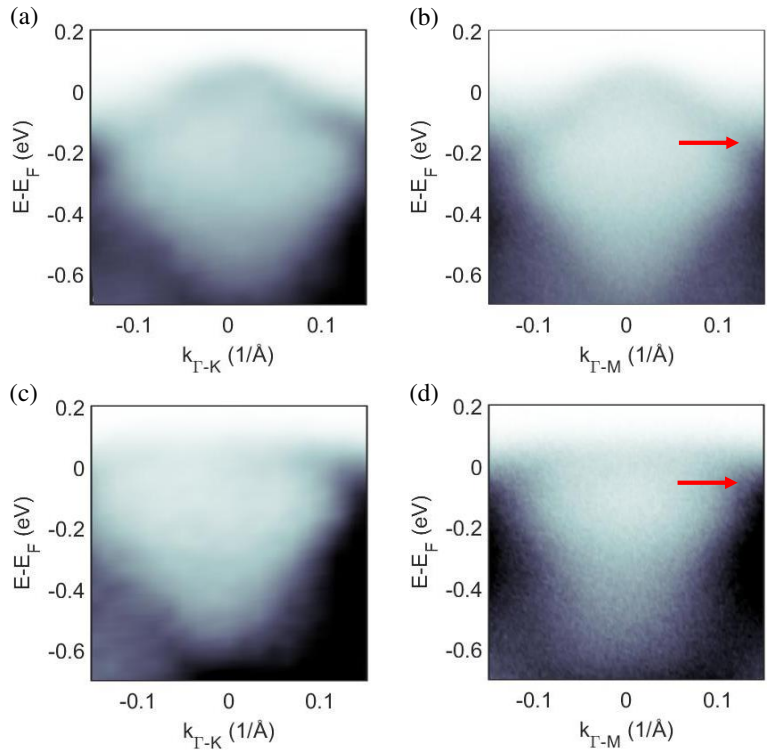

Figure 5.9: **Change in bandstructure with Bi:Sb composition (Xe source $h\nu$ = 8.44 eV, 300 K).** ARPES data of $Bi_{0.3}Sb_{1.7}Te_3$ along **(a)** Γ-K and **(b)** Γ-M. ARPES data of $Bi_{0.22}Sb_{1.78}Te_3$ along **(c)** Γ-K and **(d)** Γ-M. The red arrows point to the bulk valence bands.

correct choice of E_F, which was measured for each temperature on a polycrystalline Cu sample with an uncertainty of 6 meV.

The sharpness of the ARPES signal is limited by instrumental restrictions and by phonon-induced perturbations. The sharpness of the observed Dirac cone indicates high-quality surface states. Such sharp topological surface states above the Fermi level are, at least, unusual [203].

The temperature dependence of the Dirac point was obtained as the sample was warmed up from 25 K to room temperature. Typically, the thermal expansion of the lattice constant, results in a shift of the binding energy. A shift in DP of 40 meV has been previously observed in Bi_2Se_3 [203]. However in figure 5.10 (c) no clear trend in temperature can be established. Ruling out spurious effects from the adsorption or desorption of residual gases would require a cyclic temperature measurement would be required.

The Dirac points presented in figure 5.10 (c) were obtained from extrapolation of

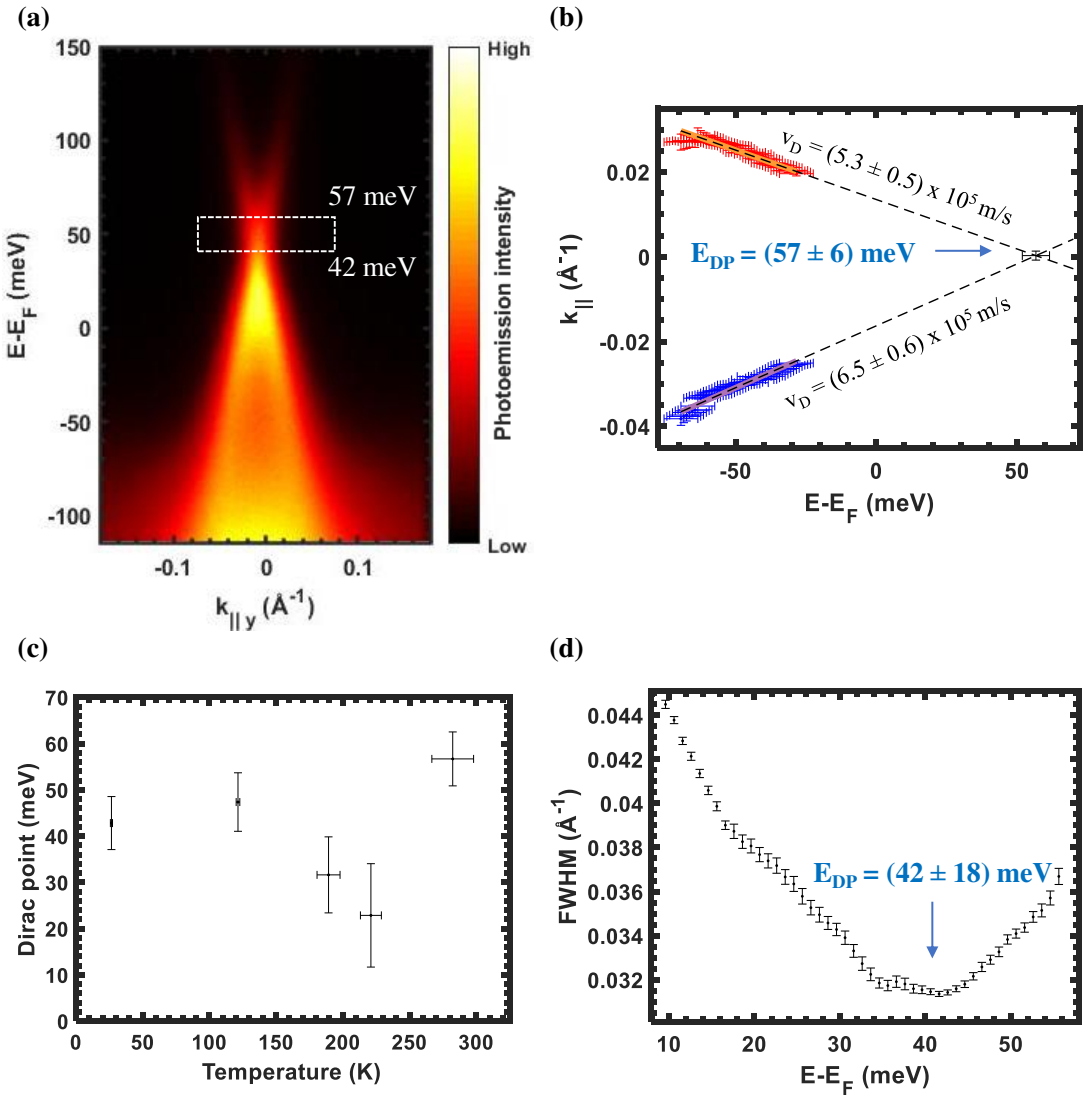

Figure 5.10: **Influence of temperature on the Dirac point (a)** Photoemission spectroscopy of $Bi_{0.3}Sb_{1.7}Te_3$ at $h\nu = 6\,\mathrm{eV}$, divided by the Fermi-Dirac function, as measured at 300 K. **(b)** Peak positions obtained by fitting double Voigt functions on the momentum distribution curves at 300 K. The Dirac point is determined by the extrapolated point of intersection of the lines. **(c)** Dirac point obtained from (b) for different temperatures. **(d)** FWHM of the Voigt function fit in the momentum distribution curve in the energetic vicinity of the Dirac point for 300 K.

the TSS peaks as shown in figure 5.10 (b) for 300 K [20]. The peaks were deduced from fitting momentum distribution curves at various binding energies with Voigt curves, with error bars obtained from the fitting procedure. Black dashed lines are linear regressions with intersection at $E_{\mathrm{DP}} = (57 \pm 6)$ meV and the corresponding Dirac velocities for $+k_{\parallel}$ and $-k_{\parallel}$ as $v_{\mathrm{D}} = (5.3 \pm 0.5) \times 10^5$ m/s and $v_{\mathrm{D}} = (6.5 \pm 0.6) \times 10^5$ m/s, respectively. In figure 5.10 (d), the position of the Dirac point was verified using a second method [20]. The full-width at half maximum (FWHM) of a single Voigt fit is displayed for the MDC peaks close to the Dirac point, where the two TSS are not resolved. The minimum is obtained at $E_{\mathrm{DP}} = (42 \pm 18)$ meV. These two methods reasonably place the Dirac point in the region depicted by the white box in figure 5.10 (a).

Influence of Nb on the bandstructure of BST

In order to characterize the influence of Nb on the band structure of BST, concurrent ARPES characterizations at room temperature are made on 20 nm BST and with 0.3 ML Nb grown on top. Cooling is avoided to prevent the adsorption of contaminants on the surface of the Nb or BST. The photoemission spectroscopy of the BST obtained at room temperature is shown in figure 5.11 (a) and its curvature plot is shown in 5.12 (a).

The sample is thereafter transferred to HNF Nanocluster for evaporation of 0.3 ML Nb. The niobium is evaporated using an e-beam evaporator with incorporated liquid nitrogen cooling of chamber walls, which ensures the cleanliness of evaporated layers on the sample held at room temperature. The sample is then transferred back to ARPES for characterizing changes in the band structure. Figure 5.11 (b) and figure 5.12 (b) show the band structure and curvature of 0.3 ML Nb on BST, respectively. Energy distribution curves of both bandstructures at indicated momenta are compared in figure 5.11 (c)–(f). The bands marked by numbered boxes in figure 5.11 (a) feature peaks in the corresponding black boxes of (c)–(f). These indicate upto 200 meV shift of different bands towards lower energies (black arrows). A similar shift has been observed by ARPES of Nb grown on $Bi_{1.5}Sb_{0.5}Te_{1.7}Se_{1.3}$ where coverage dependent studies are done at various temperatures [204]. For 300 K at 0.3 ML the shift is about 200 meV in accordance with my estimates, while the Dirac point shifts further down by additional 50 meV upto a coverage of 0.6 ML, before moving up again. At 38 K, these authors observe a Dirac point about 150 meV below the Dirac point at room temperature without Nb on top, but a very different coverage dependence.

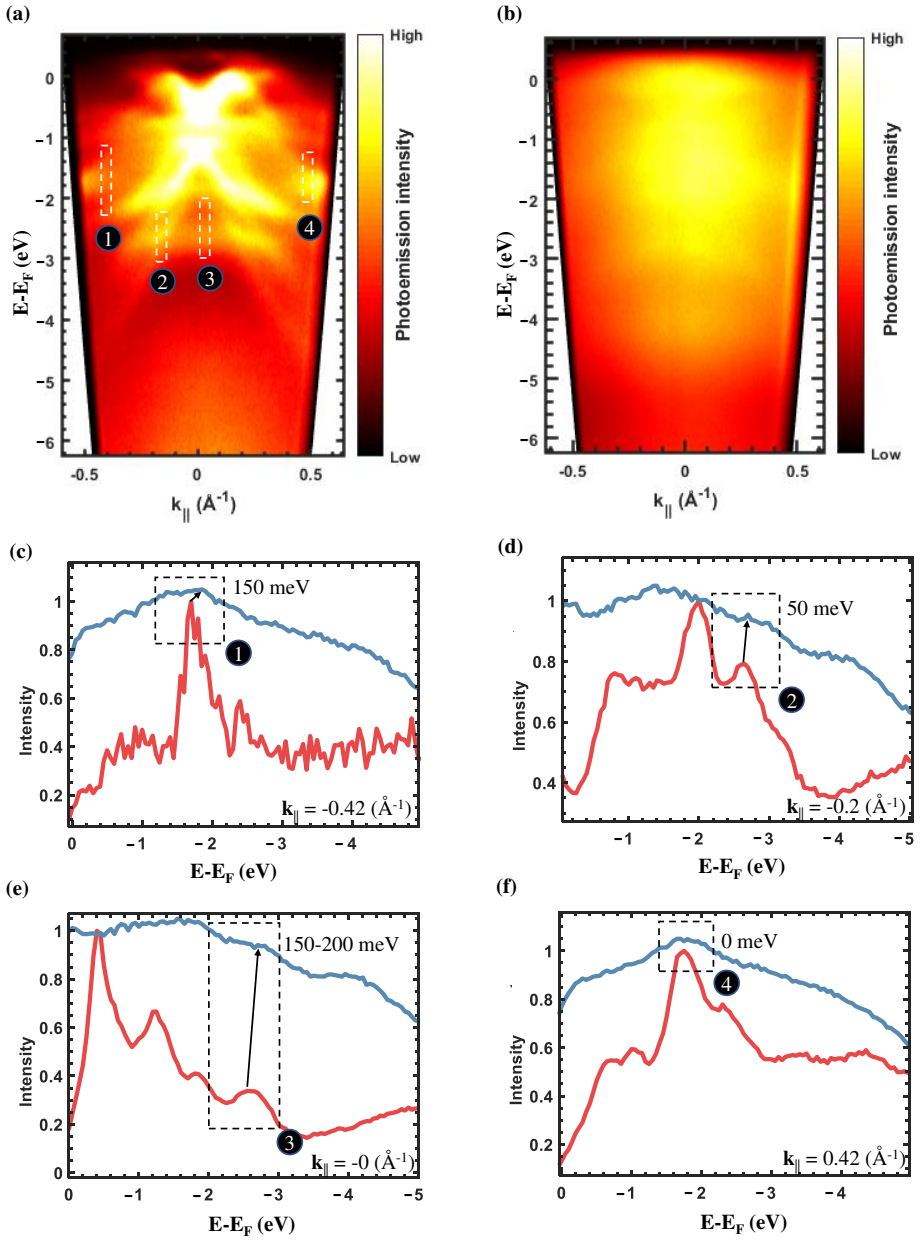

Figure 5.11: **ARPES on BST and Nb-BST measured with He source at $h\nu = 21.2\,eV$ and 300 K. (a)** Photoemission spectroscopy for 20 nm thick $Bi_{0.3}Sb_{1.7}Te_3$. **(b)** Photoemission spectroscopy for 0.3 ML Nb grown on the same sample. **(c)–(f)** Energy distribution curves at the $k_{||}$ indicated in (a). The black dashed boxes correspond to the features highlighted in the white dashed boxes in (a). The possible shift of the blue curves (Nb-BST) with respect to the red curves (BST) is indicated for each.

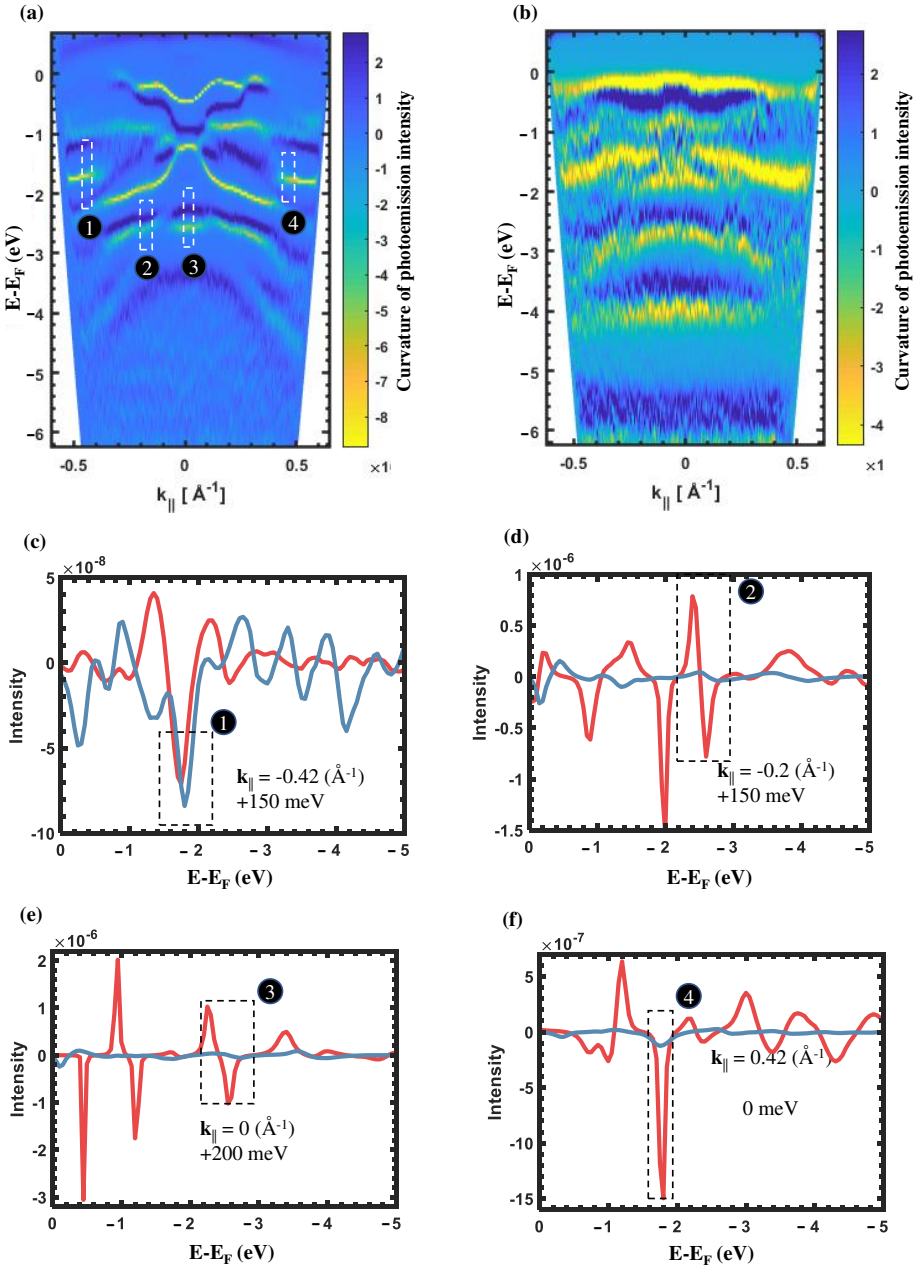

Figure 5.12: **Curvature of the data on BST and Nb-BST in figure 5.11.** (a) on 20 nm thick $Bi_{0.3}Sb_{1.7}Te_3$, (b) on 0.3 ML Nb grown on same sample, (c)-(f) energy distribution curves at the $k_{||}$ indicated. The black dashed boxes correspond to the features highlighted in the white dashed boxes in (a). The shift of the blue curves (Nb-BST) with respect to the red curves (BST) is indicated for each. Note: The curvature is calculated as $\frac{d''f(x)}{c+d'f(x)}$ where $c = 0.003$ and $f(x) = I(E)$ is taken from the raw ARPES image in figure 5.11. A gaussian weighted smoothening of this curvature, with a width of 19 pixels results in the curvature data presented in (a) and (b).

The curvature plots in figure 5.12 (a) and (b) show that the bands themselves have been strongly changed by the Nb deposition, making the determination of the band bending ambiguous. One has also to consider that the addition of any adatoms can create band bending strong enough to create confined conduction and valence band states, as has been observed for Bi_2Se_3 [205, 206]. This includes a time-dependent shift of the surface bands as observed in BSTS [207]. Given that the deposition of Nb was performed about 12 hours after the measurements on pure BST, the residual gases might have contributed to the measured changes in the ARPES data, in particular to the strong blurring.

Consequently, a more clean coverage-dependent study of the Dirac point shift would be beneficial. Ideally, it would take place within the same chamber as the growth of Nb.

5.3 STM measurements of Se-capped Nb-BST at room temperature

Samples for room temperature STM measurements were fabricated on doped 50 mΩcm Si(111) substrates. Considering that the heater design deviates from the previously described preparation chamber (section 5.1), the process of decapping differed. Due to heavier objects in direct connection to the heater, the thermocouple placed in proximity to the sample holder needs longer to equilibriate in temperature. The decapping was done between 140 °C and 180 °C for 1 hour with a total of 3 hours above 80 °C, i.e. after the first optical changes of contrast occured (see appendix figure 7.10 (a)–(c)). The pressure during the decapping remained below $p_{\max} = 1.4 \times 10^{-9}$ mbar.

STM measurements were performed at $p_{\mathrm{STM}} = 2.6 \times 10^{-10}$ mbar using a W tip coated with Au by means of indentations into an Au(111) crystal. The tip was approached to the sample with the guide of optical contrast of the patterned regions on Si (see Figure 7.10 (d) in appendix). Figure 5.13 (a) shows a $1\,\mu\mathrm{m} \times 3\,\mu\mathrm{m}$ area at the junction of four square patterns as in the red dotted box of the schematic in figure 5.13 (b). The height profile along the white line in figure 5.13 (a) is shown in figure 5.13 (c), with the different material regions of the pattern marked where BST is exposed and covered by Nb, respectively. The metallic Nb was found to be a good platform for tip preparation, using gentle pulses of up to 3 V for the longevity of the gold coating. The Nb on the

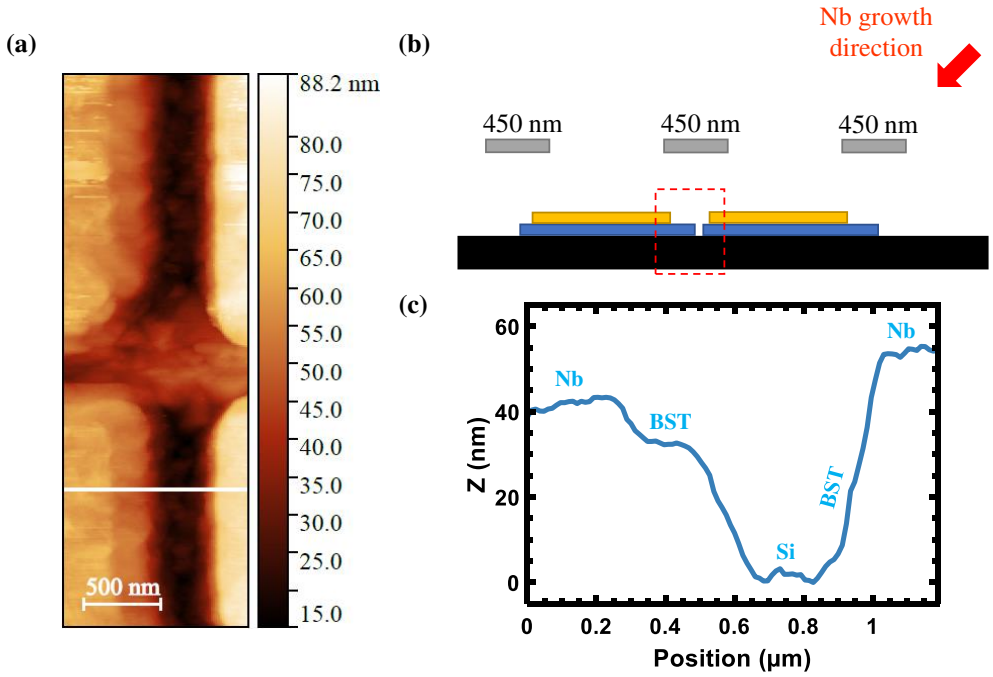

Figure 5.13: **STM measurements at room temperature (a)** STM image of the mesa edge of Nb-BST measured with $I_{\text{tunnel}} = 300\,\text{pA}$ and $V_{\text{bias}} = 1\,\text{V}$. The location on the sample is a region akin to the red dashed box shown in the schematic of **(b)**. **(c)** Height profile along the white line is displayed in (a) with marked regions.

sample typically attracts atoms from the tip and therefore contaminates the region where pulsed. On the other hand, pulsing on BST was avoided due to flakes of BST attaching to the tip and resulting in multi-tip effects. While measuring on the BST close to the mesa-edge, one can pulse the tip on the Nb close-by, with the tip relatively far from the sample ($V_{\text{stab}} = 300\,\text{mV}$ to $500\,\text{mV}$, $I_{\text{stab}} = 50\,\text{pA}$ to $100\,\text{pA}$).

BST grows in 1 nm thick quintuple layers consisting of alternating lattice layers of randomly distributed Bi/Sb and Te as depicted in figure 5.14 (d). Figure 5.14 (a) shows the topography measured on a $30\,\text{nm} \times 30\,\text{nm}$ area of BST. It shows terraces 10 nm to 30 nm in size. The atomic resolution is shown in figure 5.14 (c) evidencing that the top Te layer at the BST is intact.

Following the proof of principle in the room-temperature STM, including decapping and mesa edge locating, the process was tailored for characterization in the 640 mK STM.

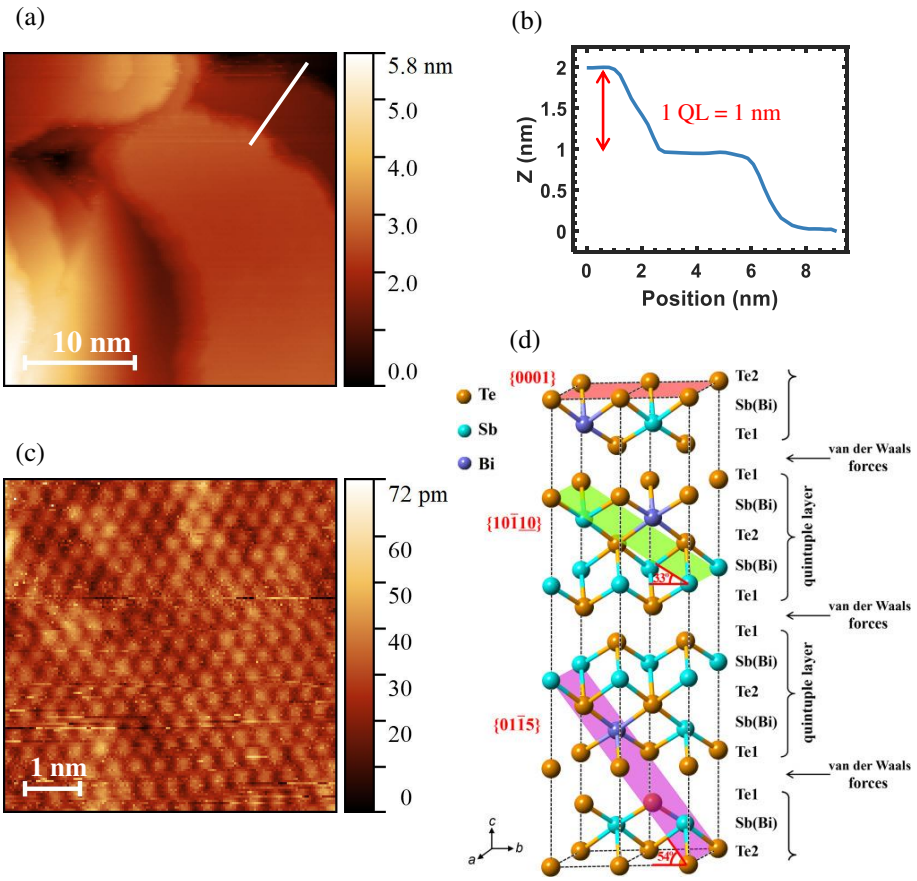

Figure 5.14: **STM measurements on BST at room temperature (a)** STM image measured on BST showing terraces 10 nm to 30 nm in size ($I_{\text{tunnel}} = 600\,\text{pA}$, $V_{\text{bias}} = 400\,\text{mV}$). **(b)** Height profile along the white line given in (a) with 1 nm steps of single quintuple layers. **(c)** Atomic resolution STM image ($I_{\text{tunnel}} = 600\,\text{pA}$, $V_{\text{bias}} = 400\,\text{mV}$). **(d)** Schematic representation of quintuple layers of BST crystal adapted from [208].

5.4 STM measurements of Se-capped Nb-BST at 640 mK

The highly doped Si substrates ($\rho = 50\,\text{m}\Omega\text{cm}$) proved to be insufficiently conducting at 4 K (see figure 7.13 in appendix). Therefore, growth re-optimization was required for the very highly doped Si $\rho = 5\,\text{m}\Omega\text{cm}$. The decapping recipe was thereafter optimized in the preparation chamber as discussed in section 5.1.1.

5.4.1 Characterization of BST and impact of annealing

A $Bi_{0.35}Sb_{1.65}Te_3$ thin film of 20 nm thickness with a 20 nm Se capping was decapped in the preparation chamber at 260 °C ($P_{\text{filament}} = 7.7\,\text{W}$) for 5:30 mins. During the decapping, a cryogenic pump was implemented in the main chamber that halved the base pressure in the preparation chamber to $p_{\text{base}} = 2.1 \times 10^{-10}$ mbar. The maximum pressure during decapping was $p_{\text{max}} = 5.9 \times 10^{-7}$ mbar, and the sample was transferred within 3 minutes into the cryostat to minimize any contamination of the decapped sample. During the transfer, the sample experiences a typical pressure $\simeq 10^{-9}$ mbar.

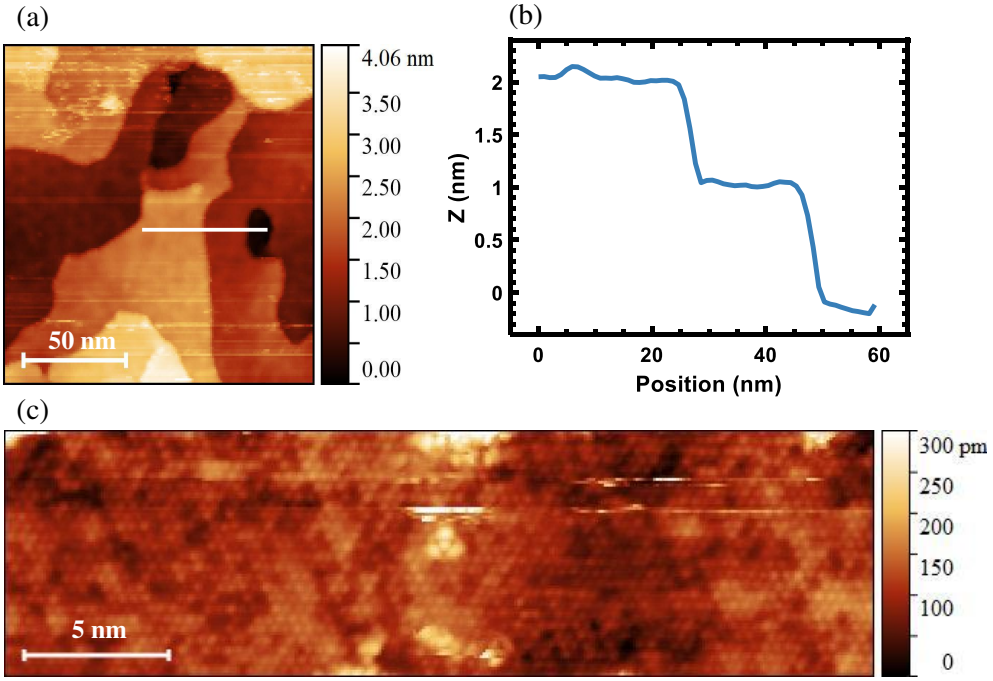

Figure 5.15: **STM characterization of BST at 640 mK. (a)** STM image measured on BST showing terraces up to 100 nm in size ($I_{\text{tunnel}} = 500\,\text{pA}$, $V_{\text{bias}} = 500\,\text{mV}$). **(b)** Height profile along the white line is plotted in (a). **(c)** Topography zoom on to a BST terrace mostly showing the hexagonal Te lattice ($I_{\text{tunnel}} = 70\,\text{pA}$, $V_{\text{bias}} = 300\,\text{mV}$).

Figure 5.15 corroborates the optimized decapping showing clean terraces in figure 5.15 (a) with 1 nm quintuple layers (figure 5.15 (b)). Atomic resolution of the Te top layer on a 10 nm × 30 nm area is shown in figure 5.15 (c). The RMS roughness is 50 pm – 200 pm. The lattice constant of $4.2\,\text{Å} \pm 0.1\,\text{Å}$ reasonably corroborates the Te lattice constant in $Bi_{0.45}Sb_{1.55}Te_3$ of 4.1 Å in [209] and is within the typical lattice variations within Bi:Sb compositions [210, 211]. The light and dark regions are indicative of the random

distribution of Bi and Sb in the subsurface layer [182]. This is similar to observations made on the surfaces of $Bi_{1-x}Sb_x$ alloy [177], $Bi_{2+x}Te_xSe$ [212] and $Bi_{1.5}Sb_{0.5}Te_{1.7}Se_{1.3}$ [213].

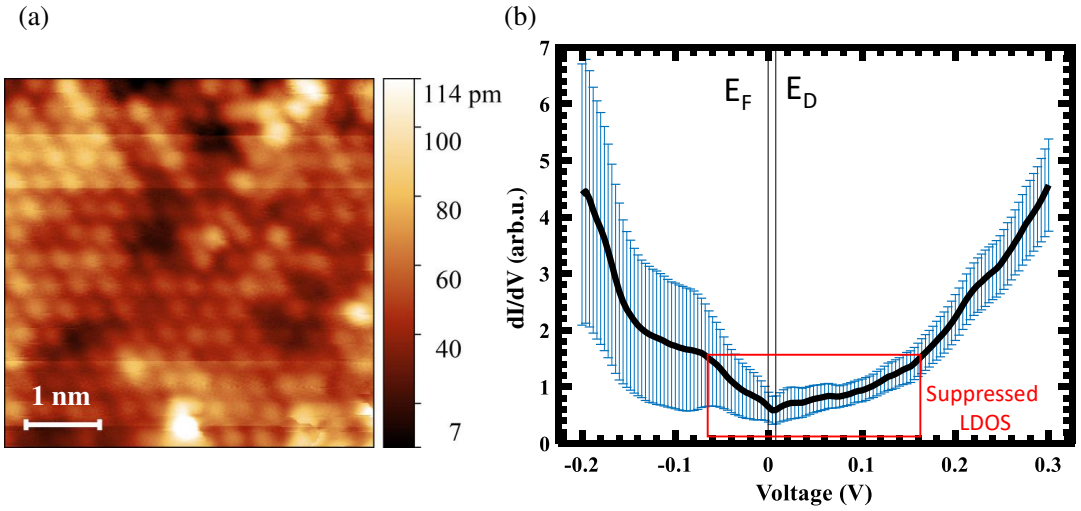

Figure 5.16: **dI/dV map on BST**. **(a)** STM topography image obtained during $^{dI}/_{dV}(V)$ mapping. **(b)** Averaged $^{dI}/_{dV}(V)$ spectroscopy over the area of (a) (black) with width of fluctuations (blue) ($I_{\text{tunnel}} = 70\,\text{pA}$, $V_{\text{stab}} = 300\,\text{mV}$, $V_{\text{mod}} = 40\,\mu\text{V}$).

A spectroscopy field has been acquired on a $5\,\text{nm} \times 5\,\text{nm}$ area on the BST shown in 5.16 (a). In figure 5.16 (b) the $^{dI}/_{dV}(V)$ curve averaged across the area is shown as the black solid curve with the corresponding deviations from the mean dI/dV signal in blue. STS on $(Bi_{1-x}Sb_x)_2Te_3$ has interpretted a similarly suppressed DOS in a range of 200 meV to 300 meV (280 meV in $Bi_{0.58}Sb_{1.42}Te_3$) as bulk bad gap with the minimum in dI/dV as Dirac point corroborated by Landau level spectroscopy [214].

Figure 5.17 makes an attempt at a qualitative correlation between the tunnelling spectra on Se-decapped $Bi_{0.35}Sb_{1.65}Te_3$ in figure 5.17 (a) and ARPES on vacuum transferred $Bi_{0.3}Sb_{1.7}Te_3$ in figures 5.17 (b)–(e)).

The ARPES data show a well-developed Dirac cone above E_F as a ring in the (k_x, k_y) plane (Figure 5.17 (e)). This develops towards a circle at lower energy indicating the overlap of a bulk band with the Dirac cone as found previously for similar stoichiometry [184]. The smallest circle appears around 40 meV above E_F, likely evidencing the Dirac point. Figure 7.11 in the appendix shows constant energy cuts at closer energy intervals. Below, the circle gets more and more hexagonal and eventually develops star like rays from the corners of the hexagon below −70 meV. These rays can be identified as bulk

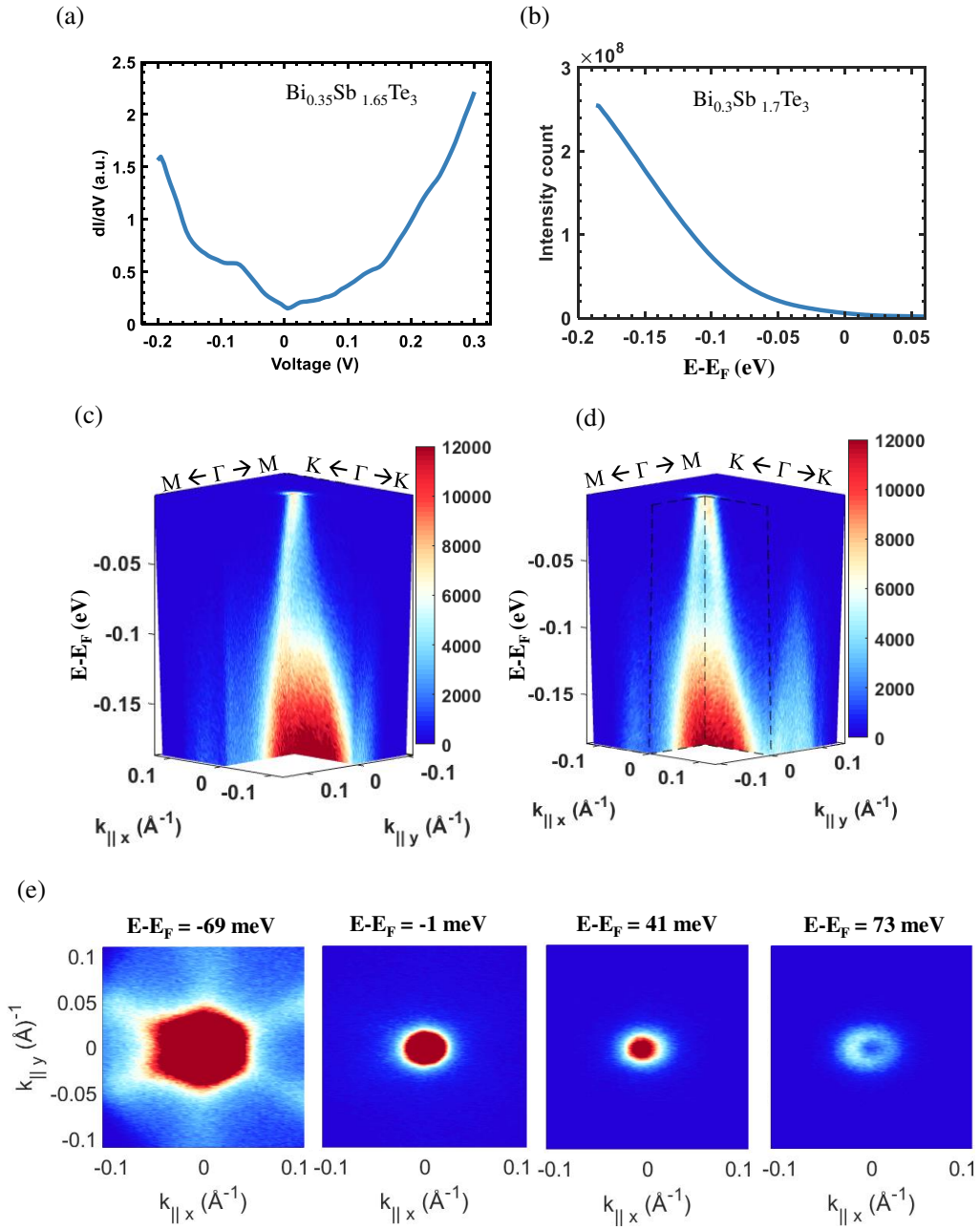

Figure 5.17: **Comparison of STS and ARPES (a)** Spatially averaged dI/dV spectrum made on $Bi_{0.35}Sb_{1.65}Te_3$ after Se decapping in UHV. The spectra is averaged across $5 \times 5\,\mathrm{nm}^2$ area ($I_{\mathrm{stab}} = 70\,\mathrm{pA}$, $V_{\mathrm{stab}} = 300\,\mathrm{mV}$). STS measurements made at $T = 640\,\mathrm{mK}$, is the same as figure 5.16 (b). **(b)** ARPES intensity integrated across the (k_x, k_y) plane at each energy, representing the occupied density of states, as a function of binding energy. **(c)** Photoemission intensity in both $k_{\|x}$ $(\Gamma - K)$ and $k_{\|y}$ $(\Gamma - M)$ directions. The 3-D data are cut along the centre rendering the Dirac cone visible. **(d)** Same as (c) cut along the opposite k-directions. **(e)** Constant energy cuts at indicated energies. The ARPES data for (b)–(e) was acquired at $h\nu = 6\,eV$ and 300 K on $Bi_{0.3}Sb_{1.7}Te_3$.

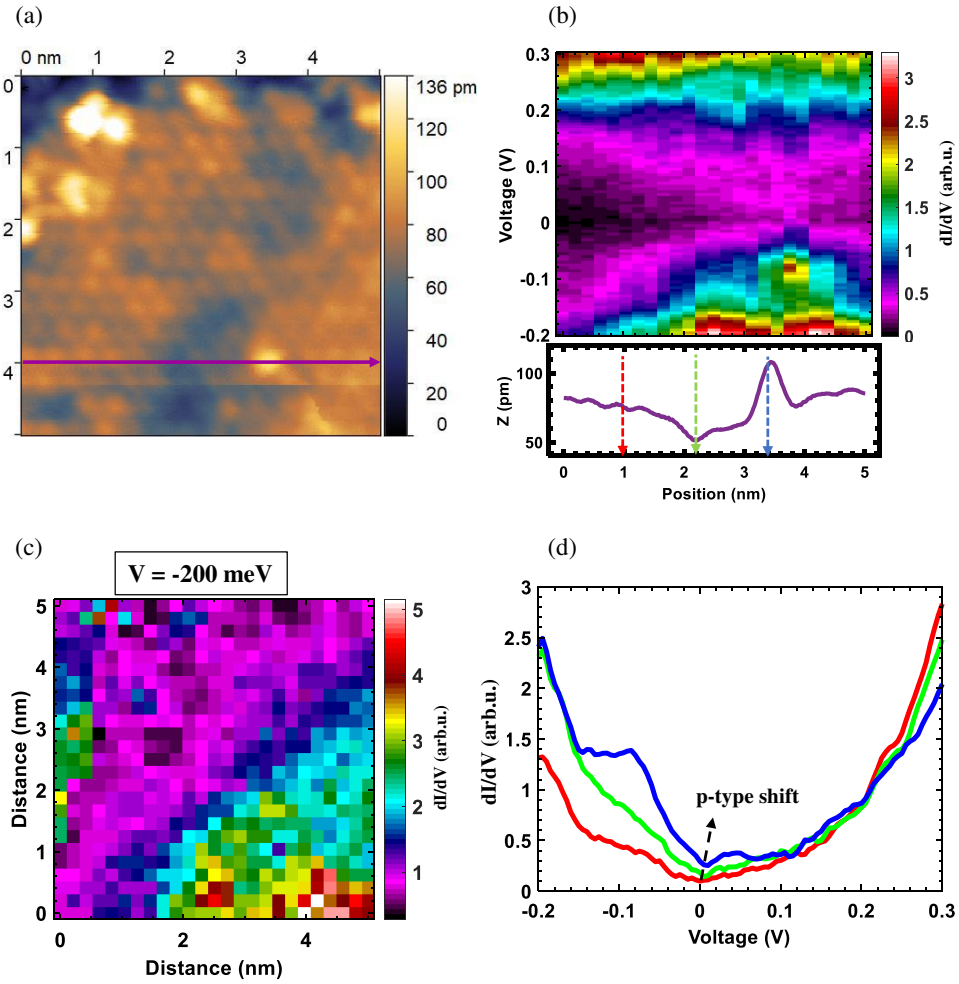

Figure 5.18: **Variation in dI/dV spectra on BST for a 5 nm length scale** ($I_{\text{tunnel}} = 70\,\mathbf{pA}$, $V_{\text{stab}} = 300\,\mathbf{mV}$) **(a)** STM image on 5 nm×5 nm showing Te atoms. **(b)** $^{dI}/_{dV}(V)$ color map along the purple line in (a), with the corresponding height profile on the bottom. **(c)** dI/dV intensity at $V = -200$ mV on the 5 nm×5 nm area in (a). **(d)** dI/dV spectra at the positions marked with red, green and blue arrows in (b).

bands that have their maxima towards the Γ-M direction (Figure 5.17 (c)–(d)). The appearance of these bulk states is also visible in the (k_x, k_y)-integrated ARPES intensity (Figure 5.17 (b)). it shows a change of slope exactly at this energy. In the STS data a plateau develops at this energy towards lower energy. The intensity raises only at −150 meV again. Interestingly, the ARPES show the onset of a strong feature at Γ at similar energy, which might be responsible for the rise of STS intensity.

Figure 5.18 shows the spatial changes of the $^{dI}/_{dV}(V)$ curves. It appears that changes at the valence band edge are much more dramatic than at the conduction band edge, in particular, concerning the plateau feature described above, i.e. strong changes in the valence band can be seen in particular around −100 meV. Figure 5.18 (c) shows the variation of $^{dI}/_{dV}(V)$ intensity at −200 meV for stabilization at $V_{\text{stab}} = 300$ meV. The variations are up to a factor of 4. I ruled out that this is due to creep or thermal drift, since forward and backward $^{dI}/_{dV}(V)$ curves are overlapping. There is also no clear correlation to the topography in figure 5.18 (a), albeit larger intensity is partly correlated to a decreased tip height with respect to the sample. So, the subsurface distribution of Sb and Bi are most likely responsible for a change of the valence band LDOS, where Sb(Bi) leads to local p-(n-) doping, but also can change the bandstructure directly.

Indeed, ab initio band structure calculations and ARPES show that Sb has a strong influence on the valence band instruction, but much less on the conduction band [184] and that upper and lower Dirac cone in Sb_2Te_3 originate from different layers with the upper cone mostly located at the top Te layer [215].

Finally, it looks like that the minimum identified as Dirac point shifts, but a more detailed analysis shows that this is inconclusive and below 10 meV (appendix figure 7.15).

Effect of annealing on BST

As discussed previously, the stoichiometric adjustments in BST have generally been established as a tuning knob for the bulk carrier density. However, the fine-tuning of chemical potential remains challenging [20, 182, 216]. This is in part due to doping inhomogeneities and local variations in chemical potential [217]. It is also conceivable that post-growth annealing may change the chemical potential by reordering of the atoms. Since annealing is beneficial for Nb, by desorbing gettered adsorbates, it is essential to establish any effect this may have on the BST (see appendix figure 7.14 for cleaning effect of annealing on Nb).

Figure 5.19 shows the averaged dI/dV spectra before and after annealing at 170 °C for 5 mins. A minimal effect is a change of the position of the Dirac point downwards by $\sim 5 - -10$ meV crossing E_F.

Post-growth annealing at high temperatures has been shown to provide increased Te vacancy density that add n-type carriers as well as better crystallinity and surface roughness [214].

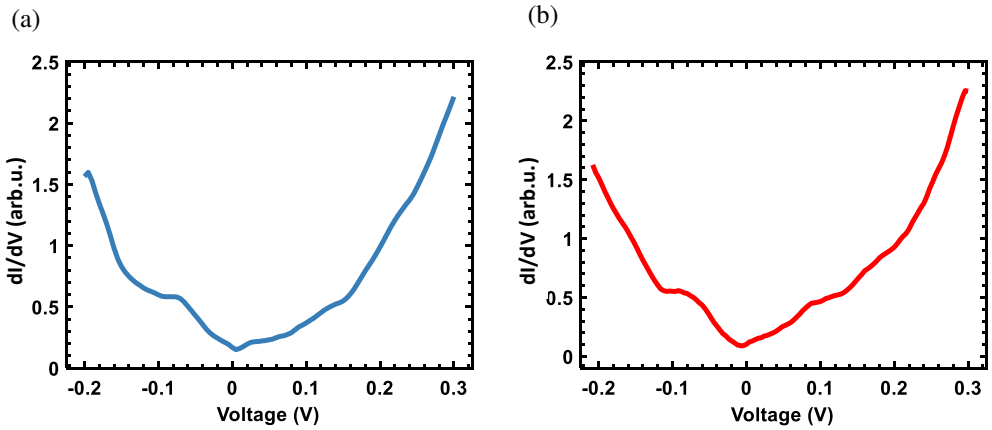

Figure 5.19: **Influence of annealing on $Bi_{0.35}Sb_{1.65}Te_3$ (a)** dI/dV spectrum averaged on $5 \times 5\,nm^2$ area before annealing ($I_{stab} = 70\,pA$, $V_{stab} = 300\,mV$) and **(b)** after annealing at 170 °C for 5 min ($I_{stab} = 70\,pA$, $V_{stab} = 300\,mV$).

5.4.2 STS on Nb

Typical topography and spectroscopy on Nb is shown in figure 5.20. The fit[2] in red in figure 5.20 (b) of the BCS superconducting gap convoluted by the finite-temperature broadening effect, gives an electronic temperature of $T_{el} = 670\,mK$ and $2\Delta = 1.81\,meV$. While this is smaller than the expected $2\Delta_{Nb-bulk} = 2.32\,meV$ [219], it is possible that at 15 nm nominal thickness (with a typical 5 nm roughness), finite size effects may suppress the superconducting gap locally [220, 221]. The fit result reveals an energy resolution of $3.4k_BT_{fit} \approx 0.2$ meV.

Figure 5.21 shows little variation of the gap size on a scale of 5 nm. In contrast, on the 100 nm scale, variations can be observed in the gap size. size For example, the peak-peak average distance of the coherence peaks is 3.3 meV ± 1.7 meV in figure 5.21 (a),

[2]The fit formalism applies a convolution of the Maki equation with the Fermi function derivative as given in [218] (equations A1-A3) with broadening by temperature and induced by the modulation voltage as fit parameters.

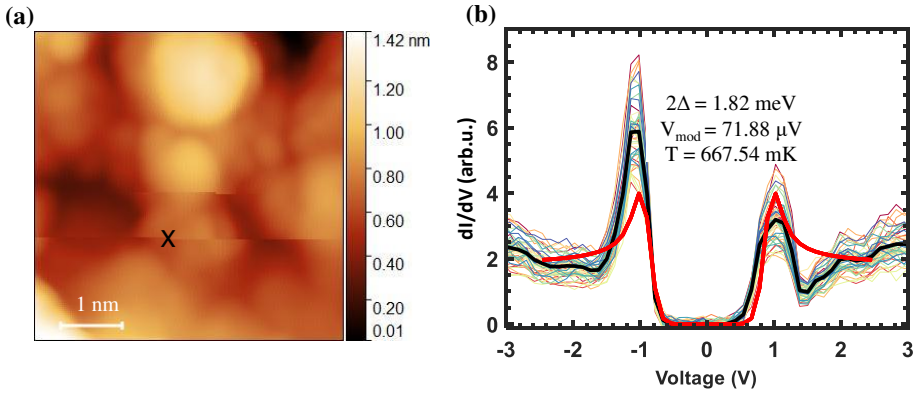

Figure 5.20: **STS on Nb (a)** STM image of $5\,\mathrm{nm} \times 5\,\mathrm{nm}$ area on Nb ($I_{\mathrm{tunnel}} = 150\,\mathrm{pA}$, $V_{\mathrm{bias}} = 20\,\mathrm{mV}$). **(b)** dI/dV spectrum on the location marked by X in (a), with the average spectra (**black**) and a BCS gap fit (**red**) ($I_{\mathrm{stab}} = 150\,\mathrm{pA}$, $V_{\mathrm{stab}} = 6\,\mathrm{mV}$, $V_{\mathrm{mod}} = 120\,\mu\mathrm{V}$).

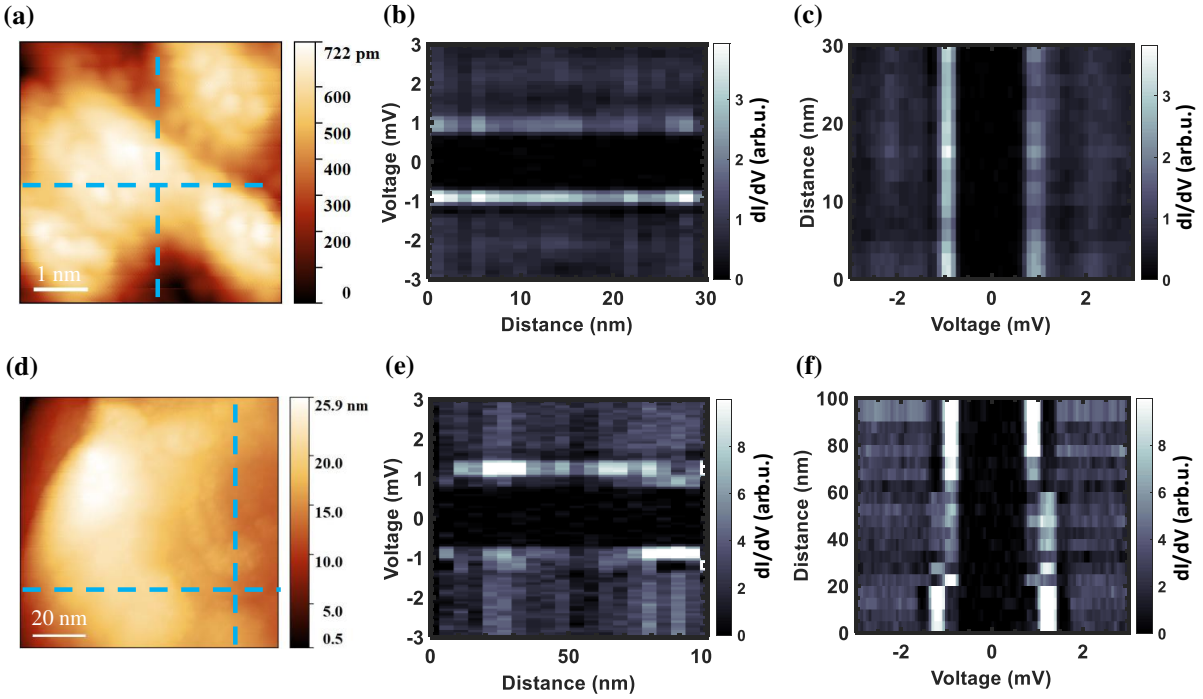

Figure 5.21: **Variation of gap on Nb (a)** STM image of $100\,\mathrm{nm} \times 100\,\mathrm{nm}$ area on Nb (distance from interface about 350 nm) ($I_{\mathrm{tunnel}} = 500\,\mathrm{pA}$, $V_{\mathrm{bias}} = 6\,mV$). **(b)** Greyscale map of $^{dI}/_{dV}(V, x)$ along the horizontal dashed line in (a). **(c)** The same as (a) along the vertical dashed line in (a). **(d)** STM image of $5\,\mathrm{nm} \times 5\,\mathrm{nm}$ area of Nb (distance from interface about 350 nm) ($I_{\mathrm{tunnel}} = 70\,\mathrm{pA}$, $V_{\mathrm{bias}} = 6\,mV$). **(e)** Greyscale map of $^{dI}/_{dV}(V, x)$ along the horizontal dashed line in (d). **(f)** Same as (e) along the vertical dashed line in (d).

and up to 3.7 meV ± 1.9 meV in figure 5.21 (d). Often, while measuring across larger areas, shoulders appear beyond the coherence peaks, suggesting Nb is picked up by the tip. Such tips were in general more stable than tungsten tips. Its spectroscopic results are discussed in the following subsections.

STS on Nb with Nb microtip

The tungsten tip was also coated intentionally with Nb by indenting the tip into the full thickness of the Nb film (15 nm to 25 nm). The Nb tip is uncontrolled, since it lacks the ability to control the size of the microcrystal attached to the tip apex. However, finite size effects reduce the energy gap of the microcrystal compared to the bulk Nb sample [222, 223]. This resulted in different micro-tips with gaps $\Delta_{\mathrm{tip}} = 0.3\Delta_{\mathrm{sample}}$ to $\Delta_{\mathrm{tip}} = 0.55\Delta_{\mathrm{sample}}$ in this thesis, where $\Delta_{\mathrm{sample}} = \Delta_{\mathrm{Nb-bulk}} \approx 1.2\,\mathrm{meV}$. The Nb tips were stable up to $I_{\mathrm{tunnel}} = 20\,\mathrm{nA}$ at $V_{\mathrm{bias}} \approx 10\,\mathrm{mV}$.

Andreev reflections between tip and sample

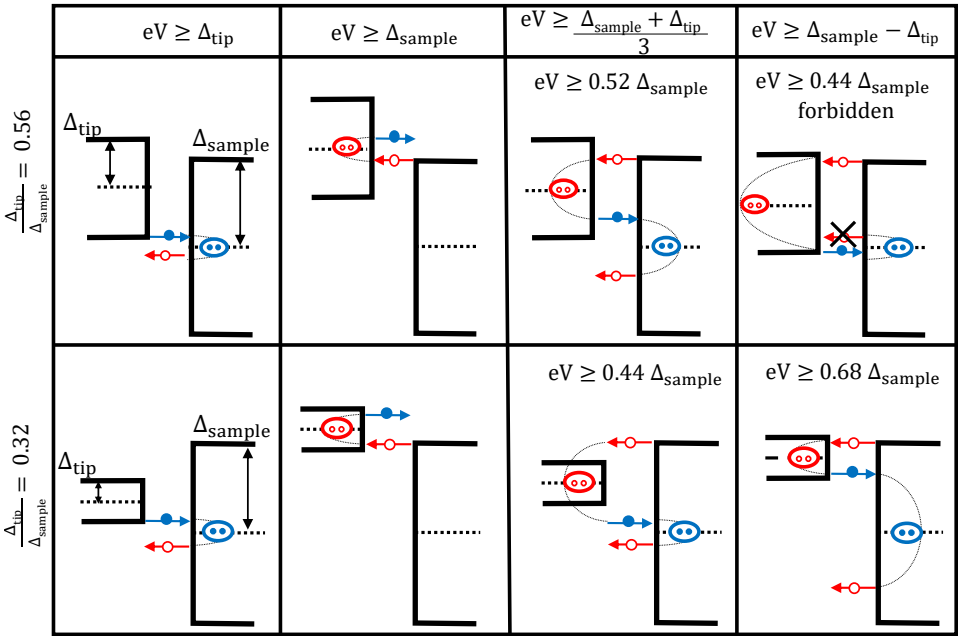

Figure 5.22: **Schematic description of Andreev reflections in an asymmetric tunnel junction.** The top and bottom rows are two separate experimentally observed scenarios for $\Delta_{\mathrm{tip}}/\Delta_{\mathrm{sample}} = 0.56$ and $\Delta_{\mathrm{tip}}/\Delta_{\mathrm{sample}} = 0.32$, respectively. The schematic is based on [224] where the $\Delta_{\mathrm{sample}} - \Delta_{\mathrm{tip}}$ peak was first attributed to a junction asymmetry.

A superconducting tip in a tunnel contact ($R_{\text{tunnel}} \gtrsim 1\,\text{M}\Omega$) with a superconducting sample can be described as an SIS-type junction that is weakly coupled. It may be asymmetric since the gaps on either side may differ. The corresponding $^{dI}/_{dV}(V)$ curve can be understood by convoluting the LDOS of the two superconducting materials. Using a tip and a sample, both described by their superconducting DOS (eq. 2.16), one obtains a $^{dI}/_{dV}(V)$ spectrum with a gap of $\pm(\Delta_{\text{tip}} + \Delta_{\text{sample}})$ around the Fermi energy.

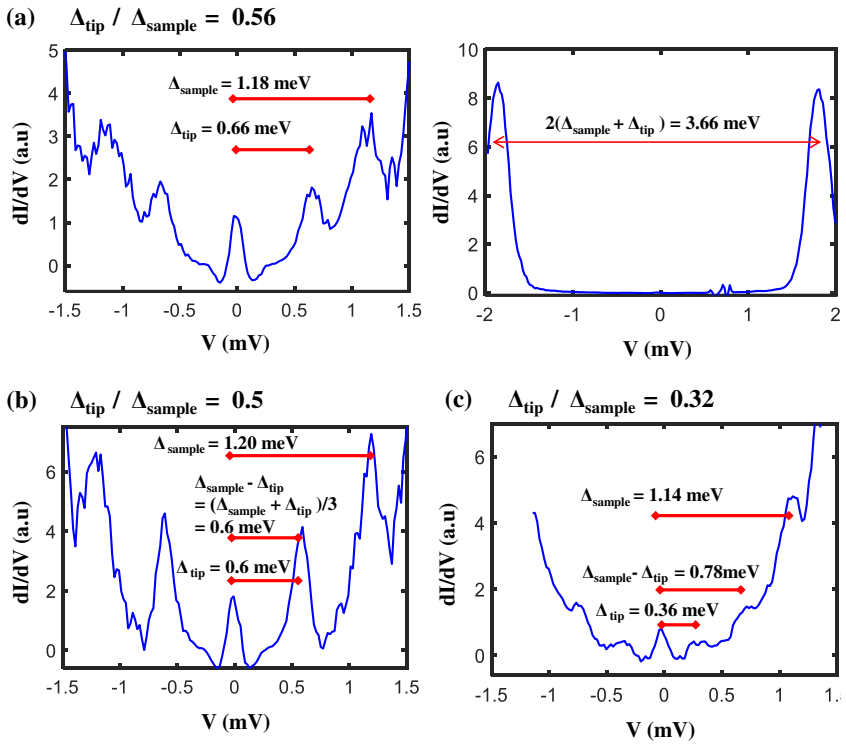

Figure 5.23: **Andreev reflection between tip and sample with different microtips ($I_{\text{stab}} = 20\,\text{nA}$, $V_{\text{stab}} = 2\,\text{mV}$, $V_{\text{mod}} = 20\,\mu\text{V}$). (a)** $^{\Delta_{\text{tip}}}/_{\Delta_{\text{sample}}} = 0.56$. **Left**: $^{dI}/_{dV}(V)$ spectrum on Nb with a Nb tip showing Andreev reflection peaks at the respective tip and sample gap energies. A Josephson peak of Cooper-pair tunneling is appearing at 0 mV. **Right**: Normal tunneling process involving the transfer of electrons at $\Delta_{\text{tip}} + \Delta_{\text{sample}}$. *Right* was measured with a lower lock-in sensitivity from *left*. **(b)** The same as (a) for $^{\Delta_{\text{tip}}}/_{\Delta_{\text{sample}}} = 0.5$. **(c)** The same as (a) for $^{\Delta_{\text{tip}}}/_{\Delta_{\text{sample}}} = 0.32$.

In addition, as described in section 2.3, features may arise within the gap due to (multiple) Andreev reflection(s). Particularly, asymmetric junctions can host unique spectroscopic features due to the various Andreev reflection processes [224–226]. The STM measurements with asymmetric tunnel junctions provide the ability to tune the coupling between the junctions by tip-sample distance [73, 76].

In figure 5.23 (a), a pair of coherence peaks appear at the sum of the tip and sample gaps $\pm(\Delta_{\mathrm{tip}}+\Delta_{\mathrm{sample}})$ on the right, and correspondingly much smaller Andreev reflection peaks at $\pm\Delta_{\mathrm{tip}}$ and $\pm\Delta_{\mathrm{sample}}$ on the left. The Andreev reflection processes for the corresponding tip-sample asymmetry are schematically represented in figure 5.22 (top row). Peaks in $^{dI}/_{dV}(V)$ are predicted to occur at $\pm\Delta_{\mathrm{tip}}/m$, $\pm\Delta_{\mathrm{sample}}/m$ and $\pm(\Delta_{\mathrm{tip}}+\Delta_{\mathrm{sample}})/(2m+1)$, where m is an integer [225, 226] for nearly symmetric junctions as here. However, the close proximity of the $^{\Delta_{\mathrm{tip}}+\Delta_{\mathrm{sample}}}/_3 = 0.61\,\mathrm{meV}$ peak and the $\Delta_{\mathrm{tip}} = 0.66\,\mathrm{meV}$ peak renders these two peaks unresolved within the noise. Consistently, the $\Delta_{\mathrm{sample}} - \Delta_{\mathrm{tip}}$ peak is not present since it vanishes for $^{\Delta_{\mathrm{tip}}}/_{\Delta_{\mathrm{sample}}} \geq 0.5$ [224].

An asymmetric junction with $^{\Delta_{\mathrm{tip}}}/_{\Delta_{\mathrm{sample}}} = 0.32$ is presented in figure 5.23 (c), where the peak at $\Delta_{\mathrm{sample}}-\Delta_{\mathrm{tip}} = 0.78\,\mathrm{meV}$ indeed manifests. However, although [224] expects still a peak at $^{(\Delta_{\mathrm{tip}}+\Delta_{\mathrm{sample}})}/_3$ for $^{\Delta_{\mathrm{tip}}}/_{\Delta_{\mathrm{sample}}} > 0.3$, we do not observe any discernible peak here.

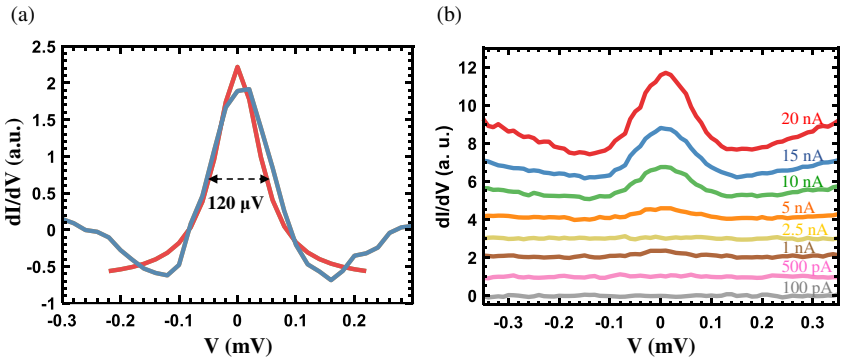

Figure 5.24: **Josephson supercurrent (a)** Josephson peak measured for $I_{\mathrm{stab}} = 20\,\mathrm{nA}$ and $V_{\mathrm{stab}} = 20\,\mathrm{mV}$ with a $V_{\mathrm{mod}} = 20\,\mu\mathrm{V}$ at $f_{\mathrm{mod}} = 1.213\,\mathrm{kHz}$. The red line is a Lorentzian fit of the peak. **(b)** Current dependence of the Josephson peak for $V_{\mathrm{stab}} = 20\,\mathrm{mV}$ measured with $V_{\mathrm{mod}} = 10\,\mu\mathrm{V}$ and $f_{\mathrm{mod}} = 1.213\,\mathrm{kHz}$.

Such as in [224], where the experimental data confirm the full counting statistics calculations, I also find, e.g. the peak at $\Delta_{\mathrm{sample}} - \Delta_{\mathrm{tip}}$ only for $^{\Delta_{\mathrm{tip}}}/_{\Delta_{\mathrm{sample}}} \leq 0.5$. At lower tunnel resistance, a peak in dI/dV arising from the tunnelling supercurrent appears at the Fermi energy. The formation of such a Josephson junction with zero-bias peak in $^{dI}/_{dV}(V)$ is depicted in figure 5.24. A Lorentian fit gives a full-width at half maximum of $120\,\mu\mathrm{V}$, which is narrower than the thermal broadening of $3k_{\mathrm{B}}T_{640\,\mathrm{mK}} = 160\,\mu\mathrm{V}$. This gives us an upper limit for the voltage noise as $\Delta V_{\mathrm{bias}} = 60\,\mu\mathrm{V}$ [227]. In figure 5.24 (b) is a set of STS curves for different stabilization currents. At 20 mV, a Josephson peak

appears at currents above 1 nA.

5.4.3 Preliminary measurements across the mesa edge

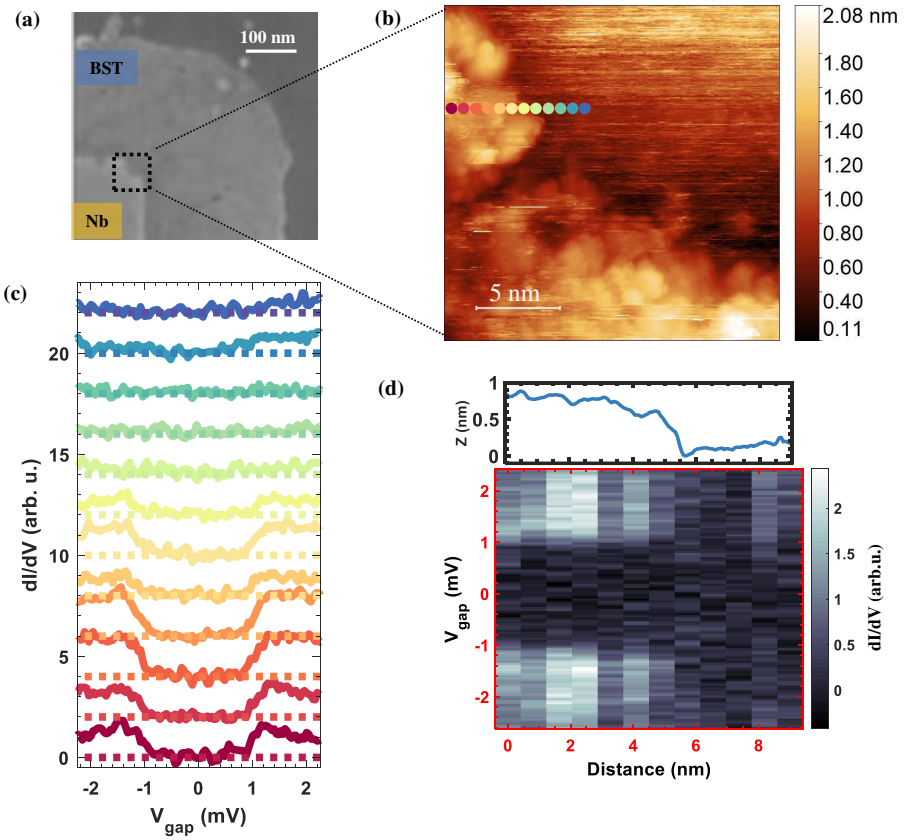

Figure 5.25: **Measurements across mesa edge (a)** SEM image of a patterned sample as guide for the relative location of tip. **(b)** STM image of the mesa-edge at the corner of Nb-BST ($I_{\text{tunnel}} = 50\,\text{pA}$, $V_{\text{bias}} = 20\,\text{mV}$). **(c)** dI/dV spectra at points marked in (b). **(d)** dI/dV spectra depicted as a color map with corresponding height profile on top ($I_{\text{stab}} = 50\,\text{pA}$, $V_{\text{stab}} = 2.4\,\text{mV}$, $V_{\text{mod}} = 40\,\mu\text{V}$).

The ultimate goal of accessing the mesa-edge has remained challenging due to the damage/removal of BST as explained in section 5.1.2. Figure 5.25 (b) shows the STM topography image measured across the mesa edge. The relative location of the mesa-edge on the pattern can be found using the SEM image in figure 5.25 (a). STS spectra across the junction depicted in figure 5.25 (c) show a distinct change between gapped and gapless curves. In figure 5.25 (d) a correlation is made between the $^{dI}/_{dV}(V)$ curves and a height profile. One can use the spectroscopic marker to distinguish Nb from the

adjacent BST. Figure 5.26 shows similar measurements across a different mesa edge. While some subgap features are seen, the noisy spectra and lack of atomic resolution on the BST make it inconclusive. As previously reported, the post-STM analysis via SEM (figure 5.6) revealed removed BST by the HF dip, explaining the challenge of finding a mesa edge with atomic resolution on the BST side. Another typical challenge was the observation of multi-tip effects rendering "ghost images" of Nb on the BST (Appendix figure 7.17). It would be beneficial to have a thinner Nb film (5 nm–10 nm) in future samples to avoid this.

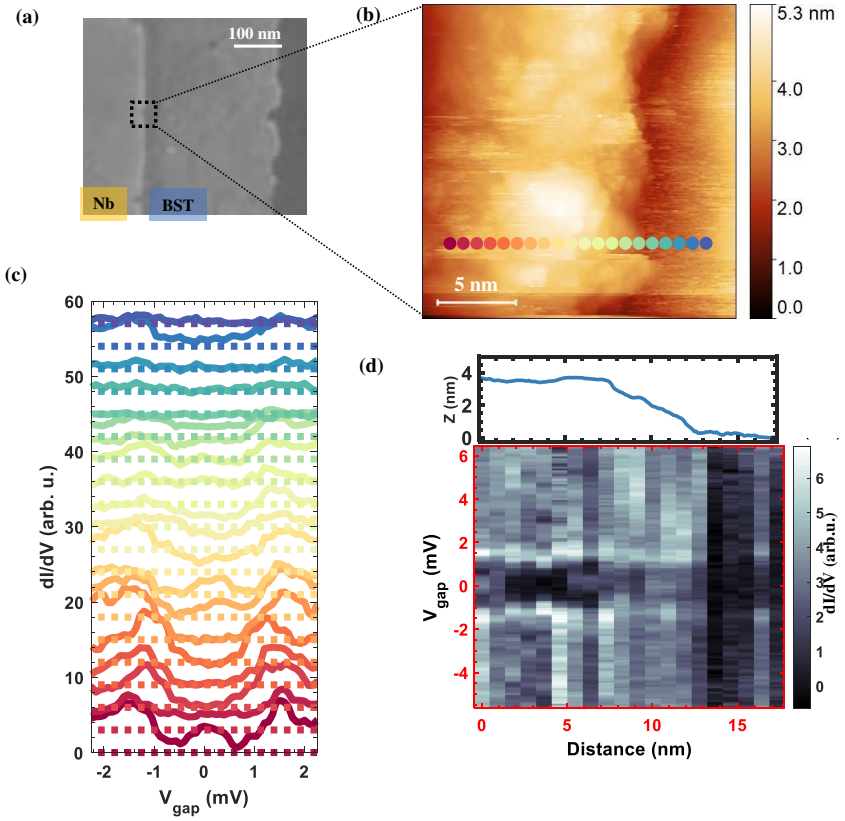

Figure 5.26: **Measurements across mesa edge (a)** SEM image of a patterned sample as guide for the relative location of tip. **(b)** STM image of the mesa-edge at the edge of Nb-BST ($I_{\text{tunnel}} = 50\,\text{pA}$, $V_{\text{bias}} = 10\,\text{mV}$). **(c)** dI/dV spectra at points marked in (b). **(d)** dI/dV spectra depicted as a color map with corresponding height profile on top ($I_{\text{stab}} = 50\,\text{pA}$, $V_{\text{stab}} = 6\,\text{mV}$, $V_{\text{mod}} = 80\,\mu\text{V}$).

5.4.4 Summary and outlook

This chapter investigated samples prepared in-situ with Nb-BST interfaces studying proximity-induced effects. Preliminary ARPES characterizations were performed to probe the influence of Nb on the BST. The temperature dependence on the Dirac point energy was shown to be below 50 mV, while an influence of adsorbates could not be excluded. Deposition of 0.3 ML of Nb shows minimal shifts of 50 meV–200 meV towards for the BST bands. However, the bandstructure changed rather completely, maybe due to additional contamination.

The sample-on-mask fabrication process to create a patterned structure of Nb on BST with a protective Se capping was developed. SEM and AFM characterizations provided feedback on the surface degradation of the sample due to fabrication processes, and STM characterization provided feedback for the optimization of the protective Se-capping growth. This optimization has not been finalized.

STM characterization of BST showed that flat terraces in the 10 nm range with 1 nm steps and Te terminating layer prevailed in the thermal decapping of the protective Se. The effect of annealing on the dI/dV spectra was below 10 meV. The subsurface stoichiometry affects the dI/dV spectra on a scale of 2 nm with a higher variation of the valence band features as compared to the conduction band. STM characterization of the patterned Nb-BST was only possible in a limited frame of sample optimization. Superconducting gaps are observed on the Nb disappearing at the interface to the BST. An inconclusive zero-bias feature was once observed at the interface. The tungsten tip indented into the Nb sample created an SIS-type junction as confirmed by a Josephson supercurrent peak at zero-bias. Asymmetric junctions were created via different microtips, displaying Andreev reflection peaks between the tip and the sample. The simultaneous availability of pristine Nb and BST near the mesa-edge was demanding due to fabrication issues that affected at least one material. The access to the mesa-edge was restricted due to multi-tip effects. Future evolution of the sample fabrication process warrants continuous optimization with feedback from STM characterization and SEM images.

6 Conclusion

This thesis addressed the engineering of the 3D topological insulator-superconductor lateral interface for studying proximity effects. The experimental challenges of such a system are approached in two ways.

The first part of the thesis describes the fabrication of patterned samples using an ultrahigh vacuum mask aligner. Three independent piezomotors operate to align the mask parallel to the sample and control the mask-sample distance. This piezomotor-based mask aligner employs silicon nitride shadow masks with capacitive sensors to read out the mask-sample distance. The sample can be additionally moved laterally with respect to the mask. The reproducibility of the distance-dependent capacitances allows for capacitive parallelization between the mask and sample and placement at a desired mask-sample distance within $\pm 250\,\mathrm{nm}$ on the same lateral position of the sample and $\pm 1\,\mu\mathrm{m}$ at a different position on the sample. With the use of a reference measurement, involving a full-contact between the mask and sample, the mask can be placed parallel to the sample at a distance of about $1.5\,\mu\mathrm{m}$ without further contact. Proof of principle for shadow mask evaporation using the mask aligner has been established with the evaporations of Au and Pb on Si(111), creating sharp edges with penumbra less than 100 nm and partly down to 10 nm at safe mask-sample distances below $1\,\mu\mathrm{m}$.

The second part examines the influence of Nb on BST via ARPES and STM. Preliminary ARPES measurements indicate a shift in BST bandstructure of 50 meV – 200 meV toward lower energies after deposition of 0.3 ML of Nb. STM characterization was made on patterned structures of Nb squares on top of BST covered with a protective Se-capping. Thermal decapping of the Se was optimized and the sample structure is retained as indicated by flat BST terraces with atomic resolution. The dI/dV spectra vary on a length scale of 5 nm, with the valence band being more sensitive to the subsurface stoichiometry arising from the random distribution of Bi/Sb, as compared to the conduction band. A superconducting gap appeared on the Nb that disappeared at the interface to the BST, once exhibiting a zero bias peak at the interface. The W tip

indented into the Nb created an SIS-type junction exhibiting a Josephson supercurrent at zero bias and signatures of Andreev reflection peaks. Crucially, since the fabrication process is not optimized yet, conclusive STM results are missing. Further pursuits for sample optimization demand continuous feedback with STM characterization and exploring of alternatives such as different capping materials.

7 Appendix

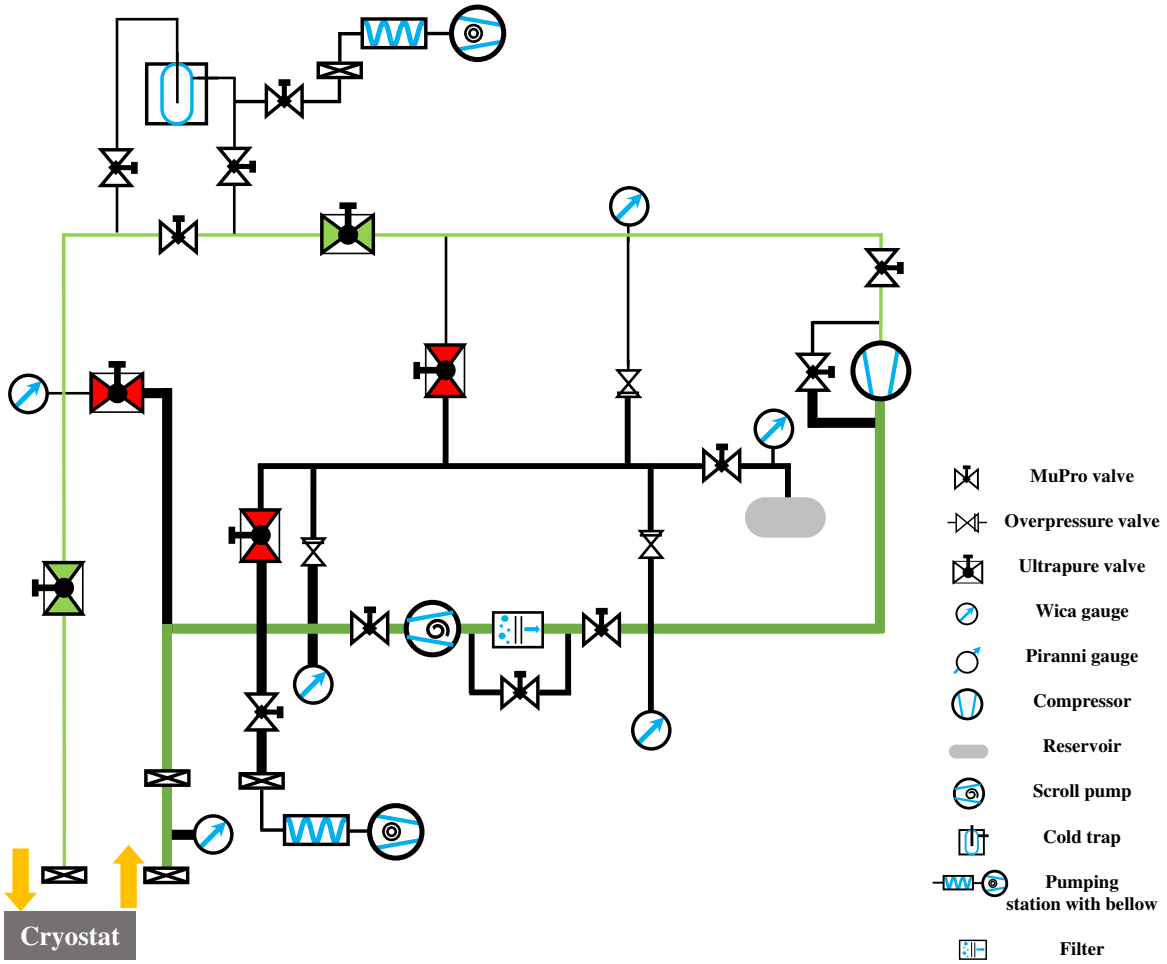

Figure 7.1: **Gas handling system.** Circuit diagram of the gas handling system for He-3 operation through the Joule-Thompson stage

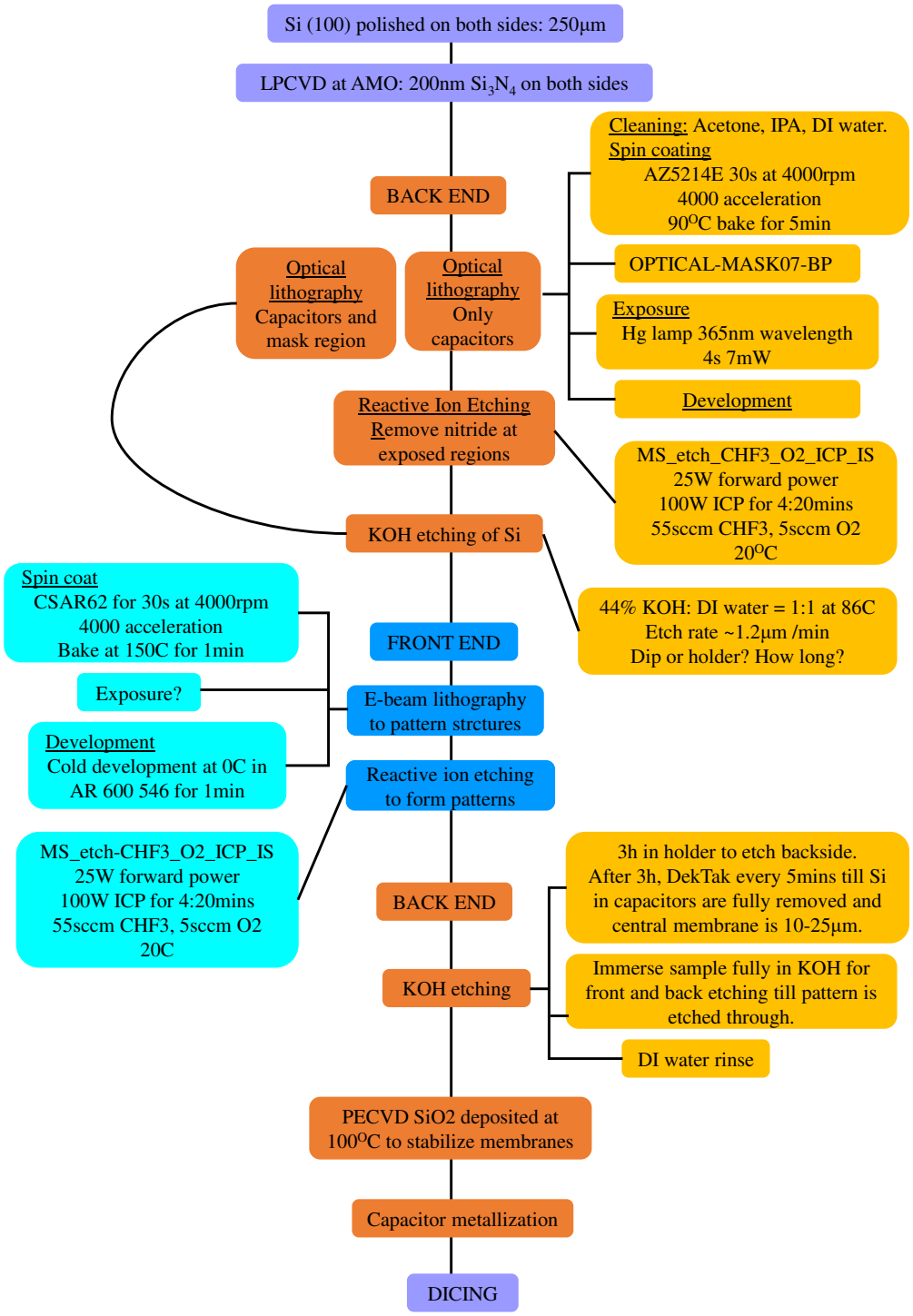

Figure 7.2: **Fabrication process flowchart for mask aligner shadow masks.** Flowchart of the process flow on $1 \times 1\,\mathrm{cm}^2$ substrates for simultaneous fabrication of four masks of $3 \times 3\,\mathrm{mm}^2$.

Property	Value
Diameter:	100 ± 0.3 mm
Material:	Silicon
Growth:	CZ
Grade:	Prime
Type/Dopant:	P/B
Orientation:	<100>
Resistivity:	1-10 Ohm-cm
Thickness:	275 ± 20 μm (measured: 287 - 292 μm)
Surface finish:	Double side polished
Flats:	2, SEMI-Std.
TTV:	<5 μm
Bow:	<30 μm
Warp:	<30 μm
Particles $\geq$ 0.3 μm:	<10

Table 7.1: **AMO Si wafer.** Parameters of the AMO Si wafer that forms the substrate for mask fabrication process

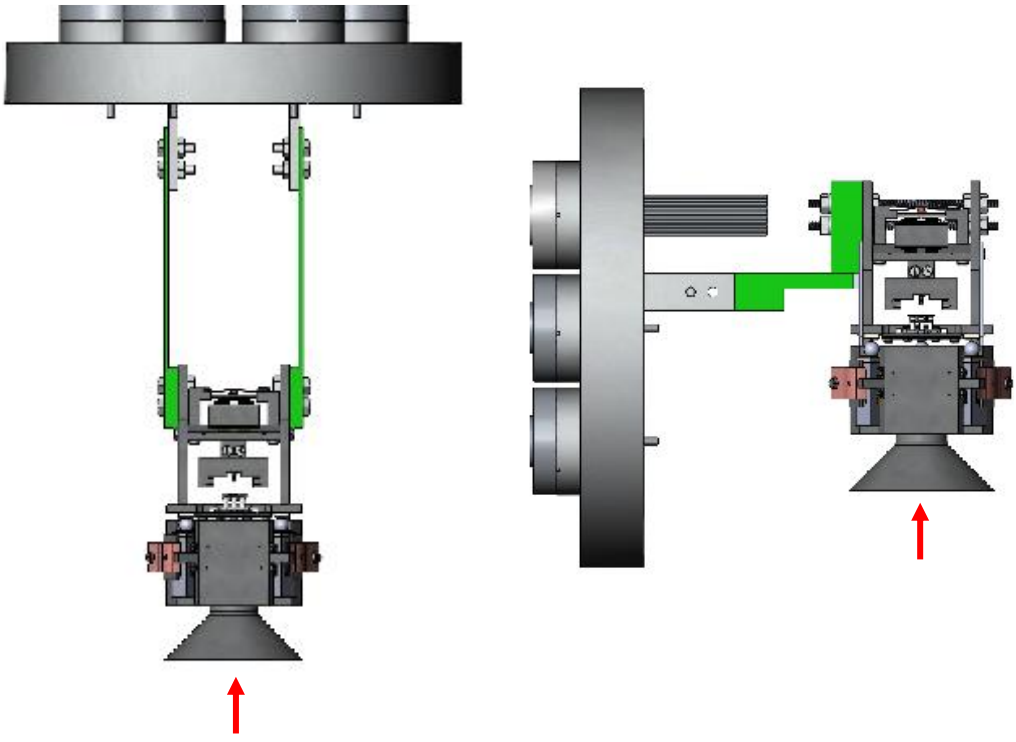

Figure 7.3: **Mounting of mask aligner. (a)** Solidworks drawing of the modular mask aligner attached to CF100 flange in top mount configuration. **(b)** Side mount configuration. The arrow indicates the direction of evaporation

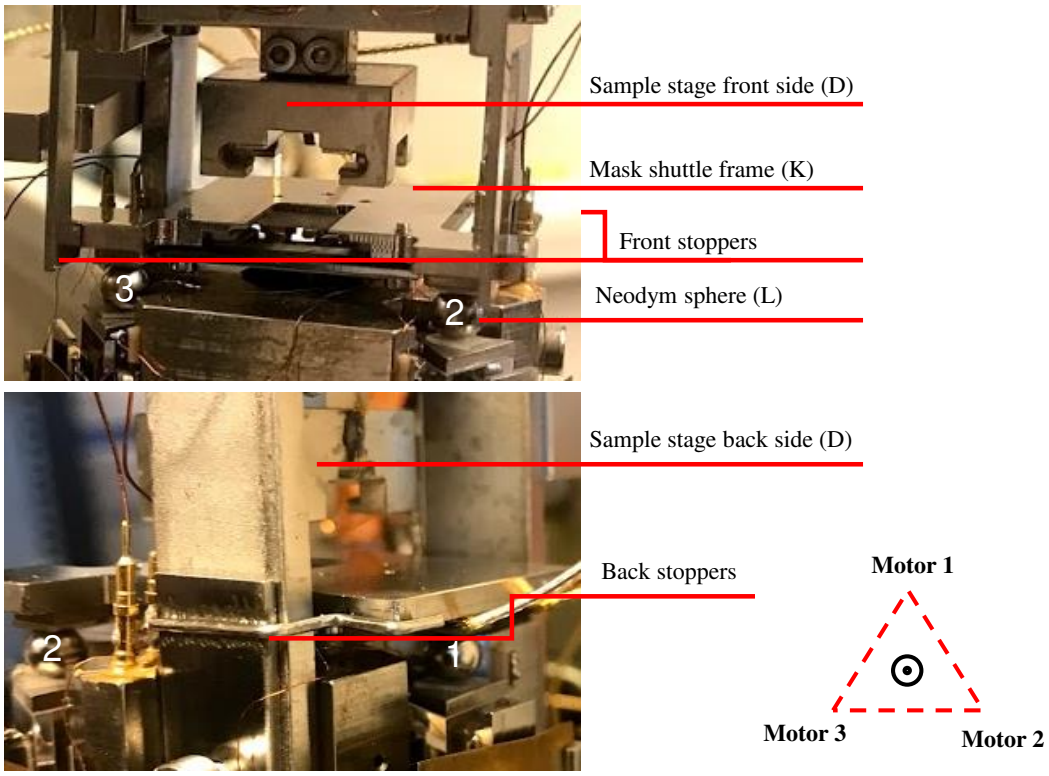

Figure 7.4: **Optical images of the central mask module** (top) tilted front view and (bottom) tilted back view (same labels as in figure 4.12). The mask stage is positioned between the front stoppers and back stoppers for safe operation of the wobble stick. The schematic on the right represents the nomenclature for the motors as seen from the top.

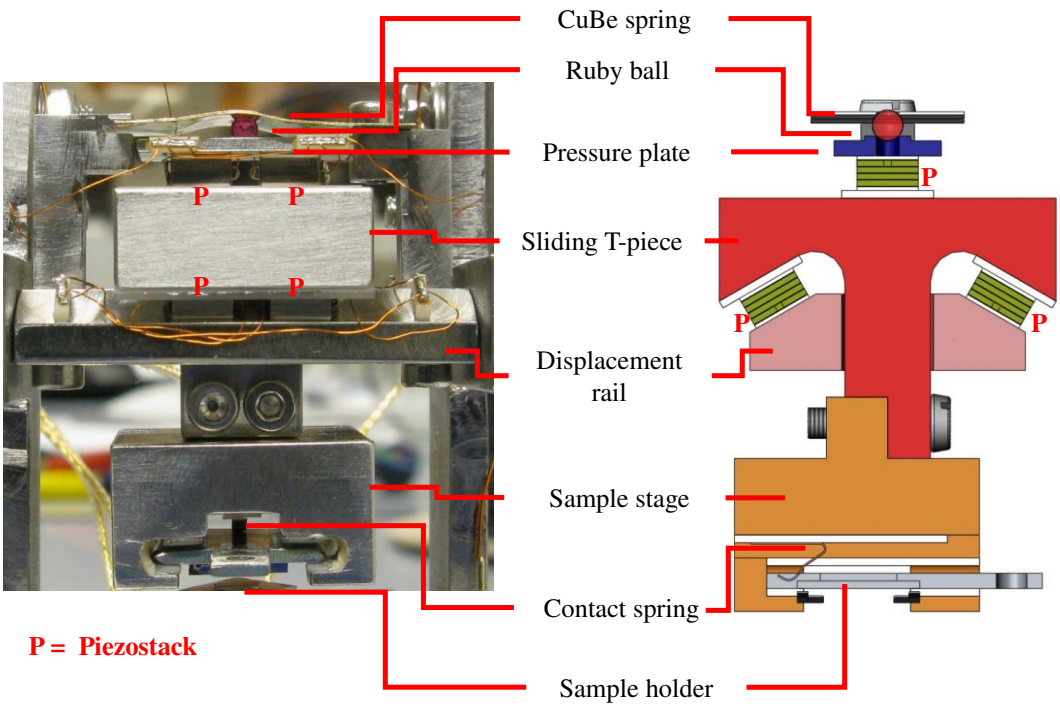

Figure 7.5: **Horizontal translation piezomotor.** Optical image (left) of the front view and cross-sectional drawing (right) of a profile view of the upper translation stage.

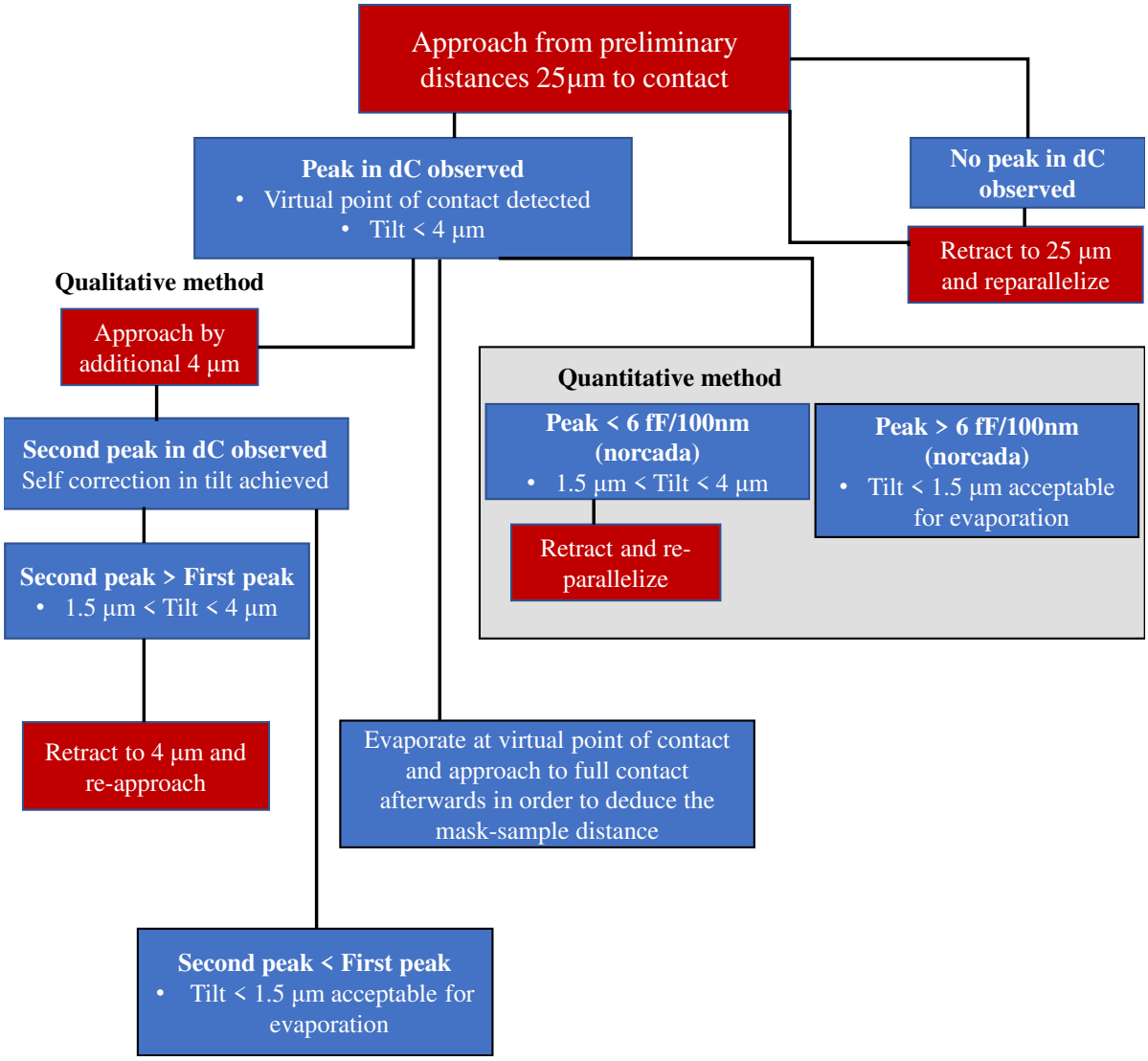

Figure 7.6: **Experimental flowchart to minimize mask tilt.** Flowchart describing the experimental strategy to reduce the mask tilt below 1.5 μm to ensure an acceptable influence of tilt on the shadow mask evaporation that must exhibit a penumbra below 100 nm. Blue boxes depict observations and orange boxes indicate actions. A quantitative method is proposed based on modeling results in section 5.2.1 of [155]

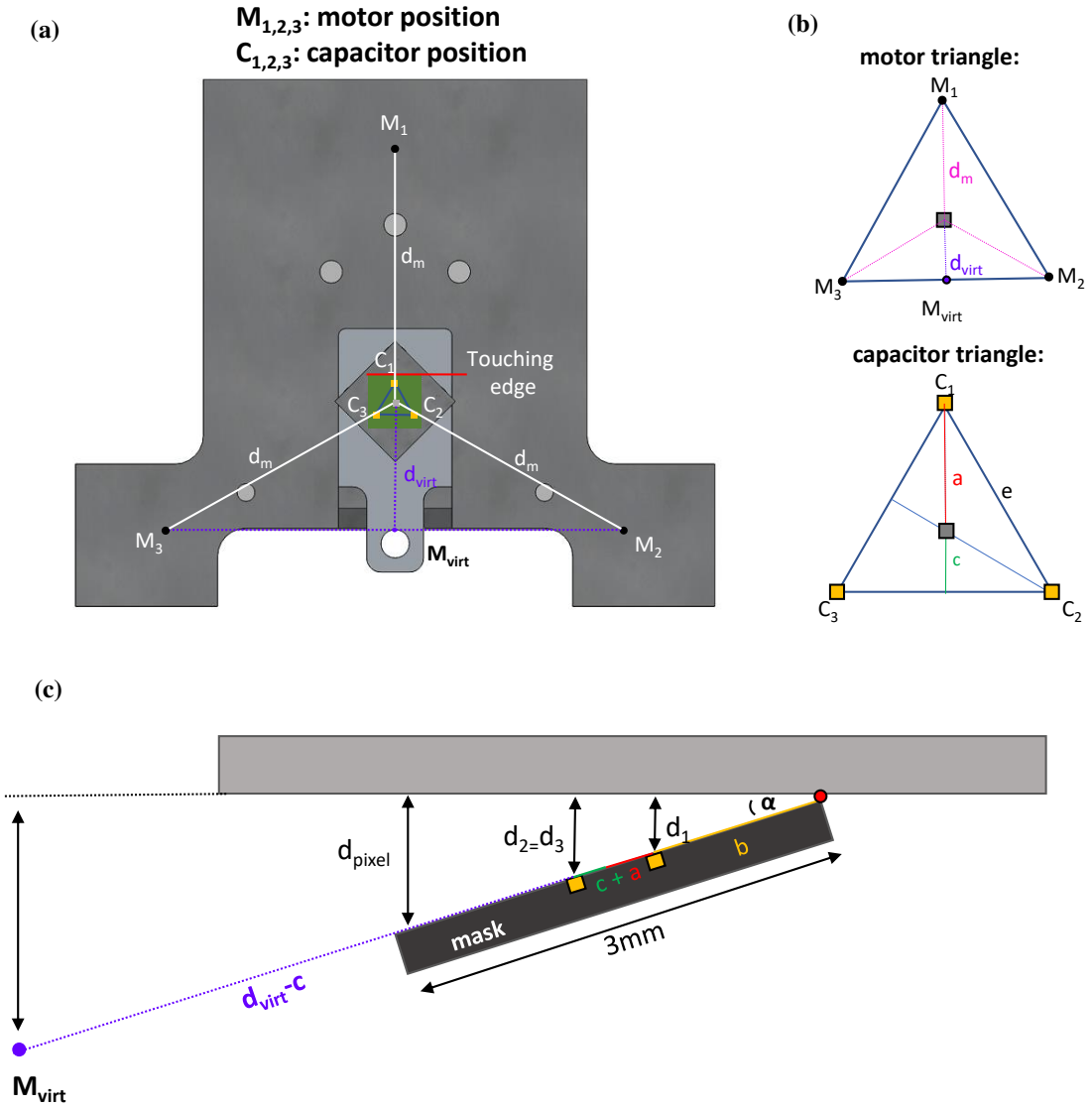

Figure 7.7: **Virtual point of contact. (a)** Layout of the motor positions M_1, M_2, M_3 and the virtual motor position of the combination of M_1 and M_2 being M_{virt}) as well as the capacitive sensor positions C_1, C_2 and C_3 with $d_m = 13\,mm$ the distance from the sample center to each motor and d_{virt} the distance of the front motor plane to the mask center. Since the motorsM_2 and M_3 move in unison when the C_1 edge of the mask touches the sample (red line in (a), a virtual motor M_{virt} is introduced to simplify the movement. **(b)** Sketches of the mask stage with motor positions and capacitor positions. **(c)** Tilted mask touches the sample at the C_1 edge and d_{pixel} designates the maximum distance between the mask and sample. This distance determines the distance of the capacitive sensors $d_{1,2,3}$ to the sample, at the virtual point of contact. After this touching point scenario, the mask pivots around the touching point by the virtual motor upon further approach. Further details in [155] section 5.1

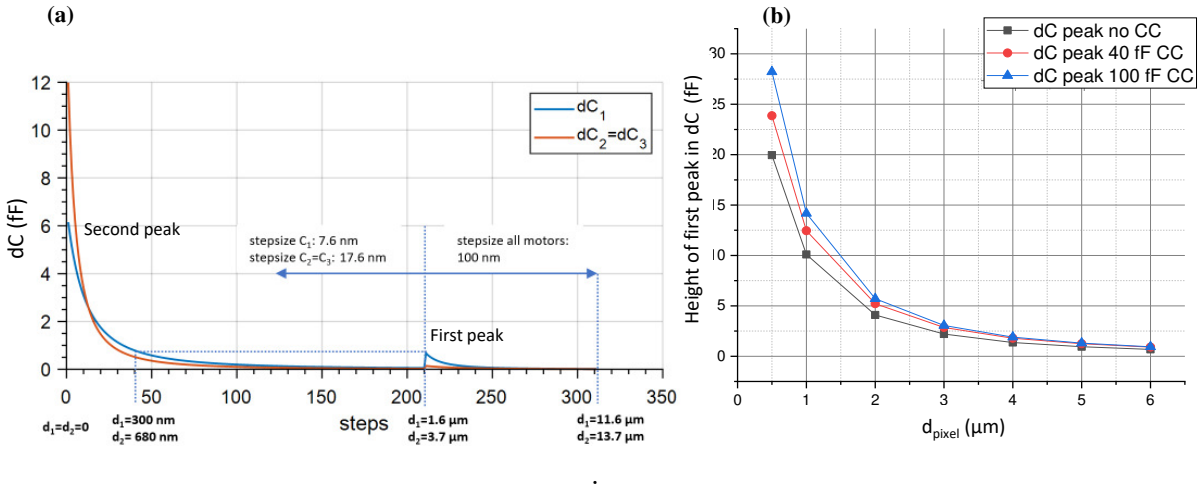

Figure 7.8: **Modelling the capacitance curves after the virtual point of contact.** Variables are as defined in figure 7.7. **(a)** Modelled approach curve dC per step with the back edge (C1) of the mask making a tilted contact to the sample at step 212 with an angle $\alpha = 0.115\,^\circ$ corresponding to a tilted distance $d_{\text{pixel}} = 6\,\mu$m. The cross capacitances between the channels are neglected and a stepsize of 100 nm is assumed. The stepsize after the virtual point of contact reduces to 7.6 nm at the sensor position of C1 and to 17.6 nm at the sensor positions of C2 and C3. **(b)** Magnitude of the first peak (virtual point of contact) in dC for different tilted mask-sample distances d_{pixel}. Various cross capacitances (CC) between the capacitors are assumed. Further details in [155] section 5.1

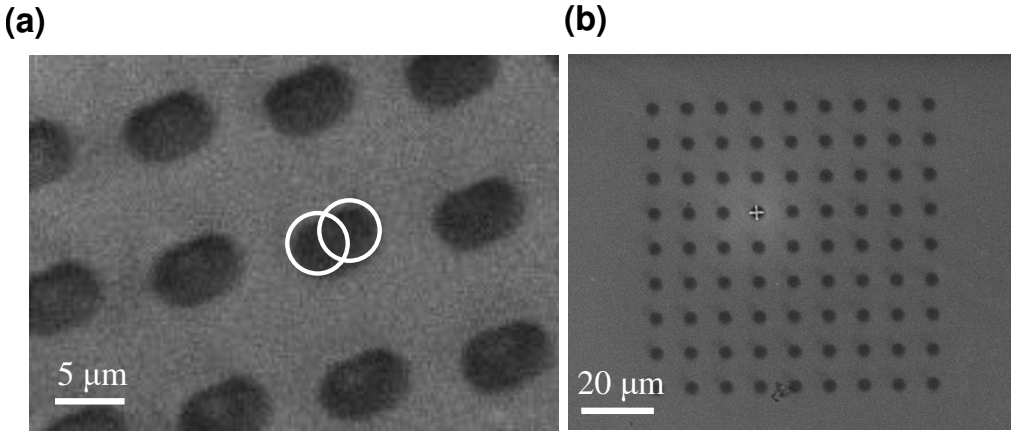

Figure 7.9: **Effect of mechanical vibrations during evaporating using the mask aligner.** Scanning electron micrograph indicating the effect of mechanical vibrations on the sharpness of evaporated structure **(a)** with turbo pump on **(b)** with turbo pump off. Both images show Au patterns on Si(111) using *Norcada* masks.

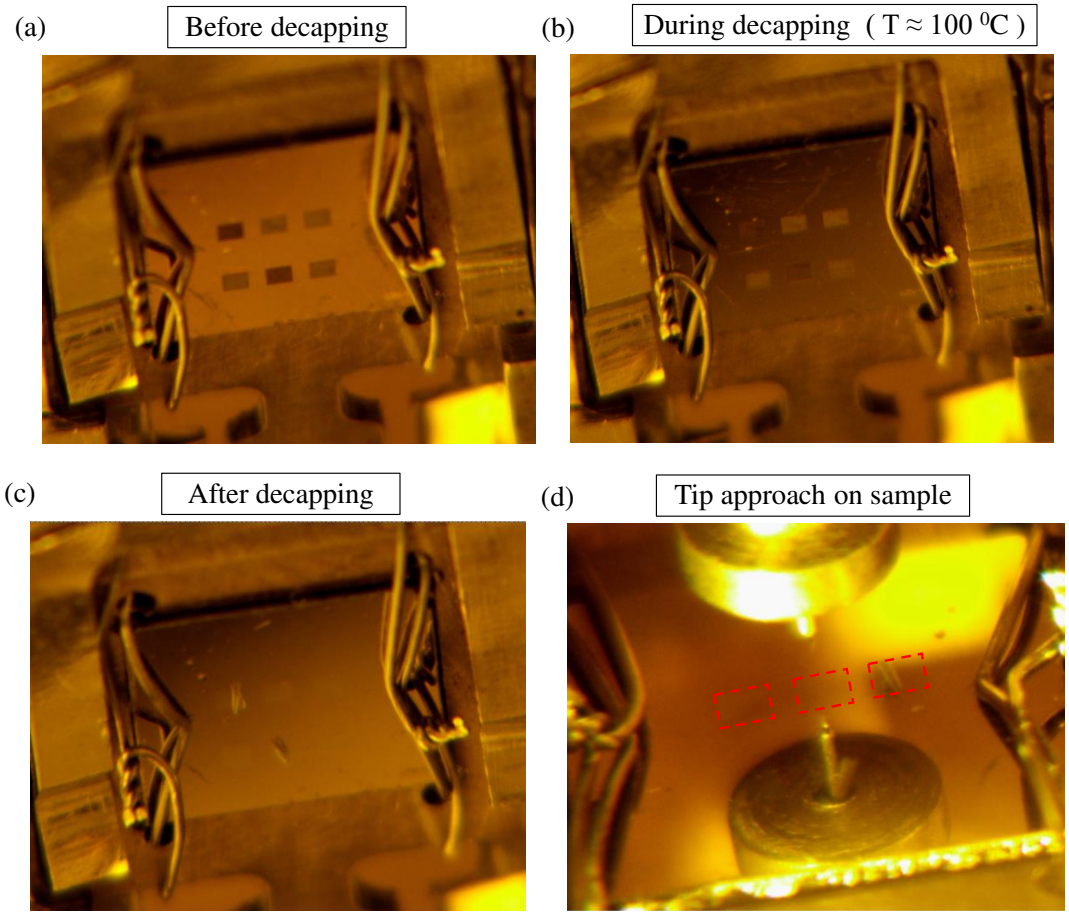

Figure 7.10: **In-situ preparation of patterned Nb-BST sample for STM measurements. (a)** Optical image of the sample before decapping with high contrast between patterned and unpatterned regions **(b)** Optical image of the sample around 100 °C when noticeable changes begin to appear in the contrast. **(c)** Optical image of the sample after the decapping. **(d)** Approaching the tip onto the patterned regions. The red rectangles mark three of the patterned fields deduced by optical overlap with (a).

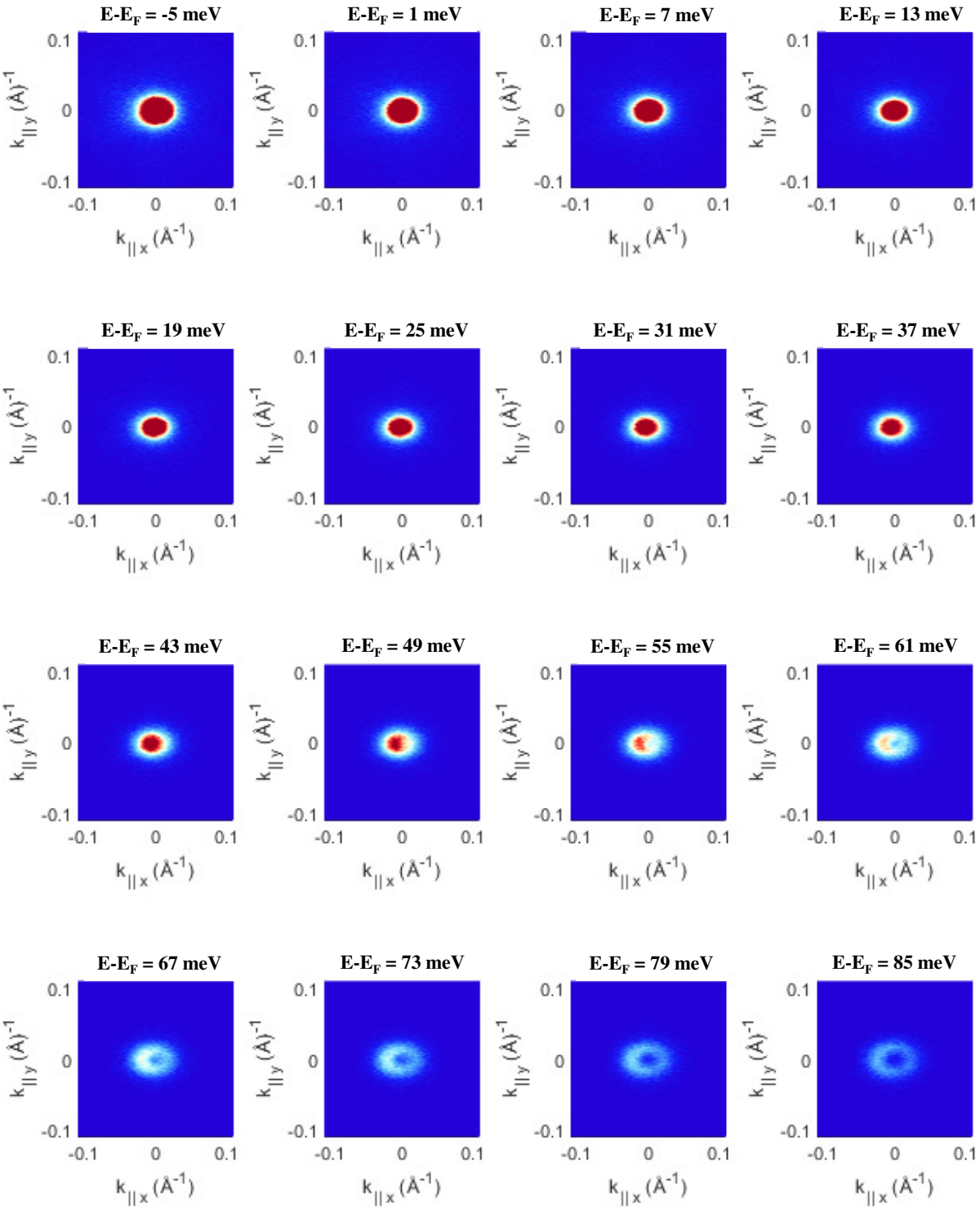

Figure 7.11: **Locating the smallest section of the Dirac cone.** ARPES constant energy cuts at different binding energies as indicated respectively. The smallest section of the Dirac cone is around $E - E_F = 43\,\text{meV}$, with the free-standing cone clearly visible above 60 meV. ($h\nu = 6\,eV$ at 300 K on $Bi_{0.3}Sb_{1.7}Te_3$)

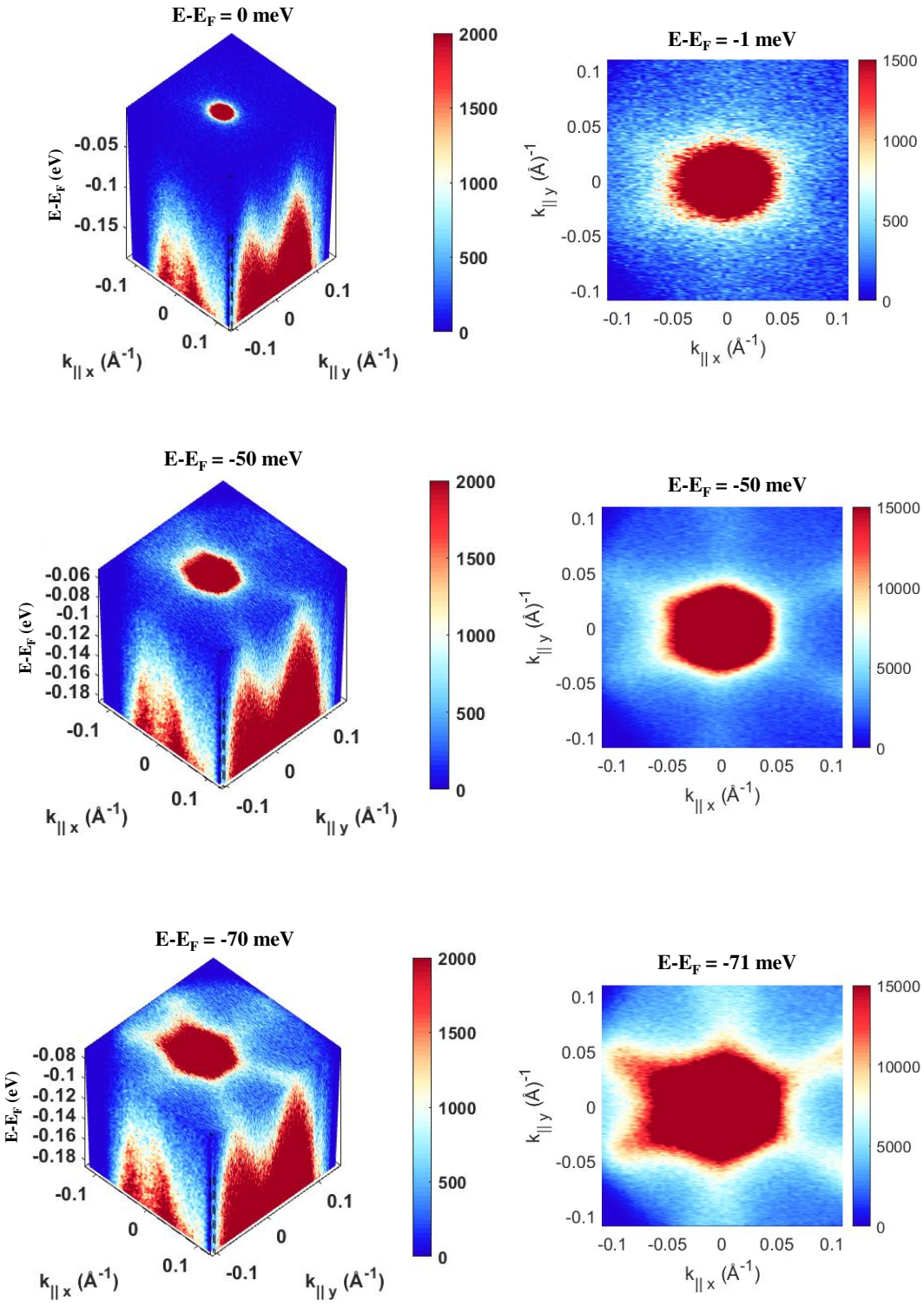

Figure 7.12: **3D ARPES images showing bulk bands ($h\nu = 6\,eV$ and 300 K on $Bi_{0.3}Sb_{1.7}Te_3$).** 3D maps sliced at binding energies as indicated on the left column, with the corresponding constant energy cut shown on the right

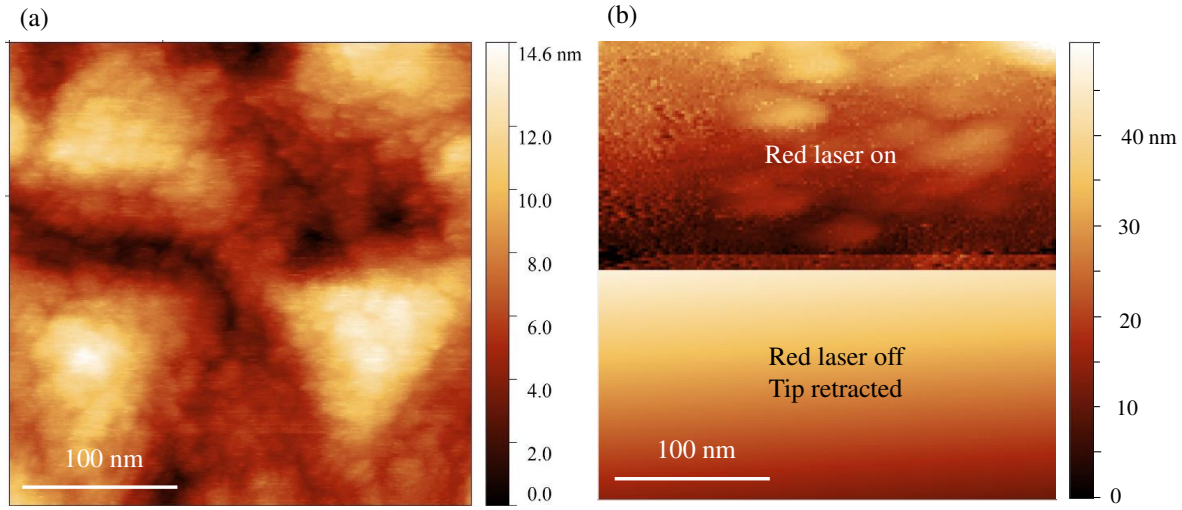

Figure 7.13: **Electronic freezeout in Si ($\rho = 50\,\mathrm{m\Omega cm}$). (a)** STM topography image measured on Nb region of the pattern with the cryo shield open and sample exposed to white light ($T = 10\,\mathrm{K}$, $V = 0.3\,\mathrm{V}$ and $I = 500\,\mathrm{pA}$). **(b)** STM topography image demonstrating the tip approach when a red laser is shined on the sample. Although at $\rho = 50\,\mathrm{m\Omega cm}$, Si is theoretically degenerate at low temperatures, it was found to be experimentally inconsistent between different wafers. Si with a higher doping ($\rho = 5\,\mathrm{m\Omega cm}$) was found to be reliably conducting at low temperatures and therefore used as substrate for low temperature measurements.

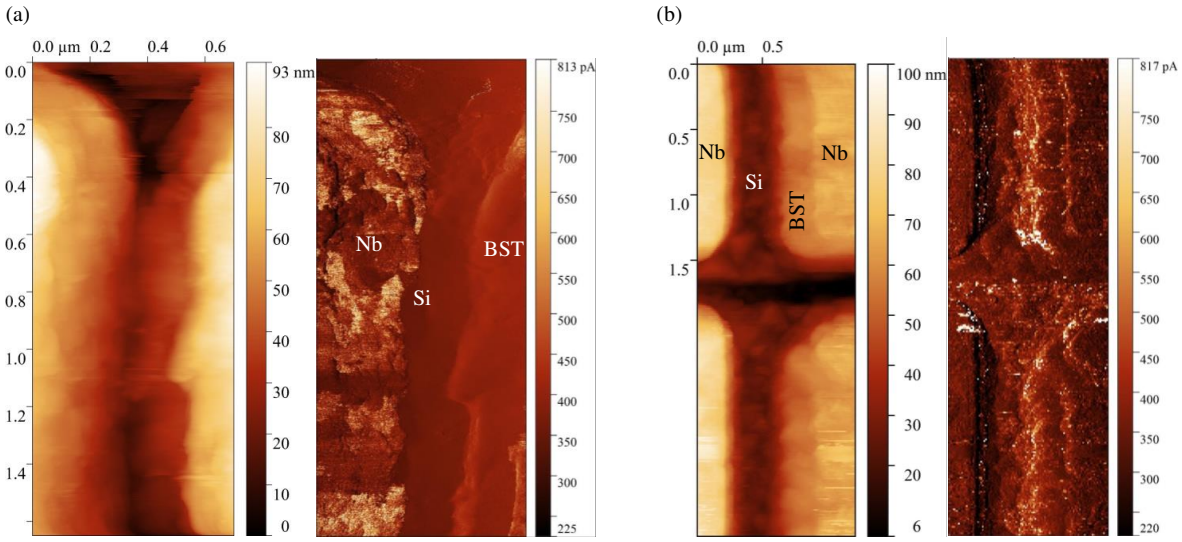

Figure 7.14: **Cleaning effect of annealing on Nb. (a)** Topography and current images ($V = 0.3\,\mathrm{V}$ and $I = 500\,\mathrm{pA}$) prior to annealing. The tip worsens continuously as the Nb grabs adsorbates over time **(b)** Topography and current images ($V = 0.3\,\mathrm{V}$ and $I = 500\,\mathrm{pA}$) after annealing at 200 °C for 5 mins ($p \leq 4 \times 10^{-9}\,\mathrm{mbar}$).

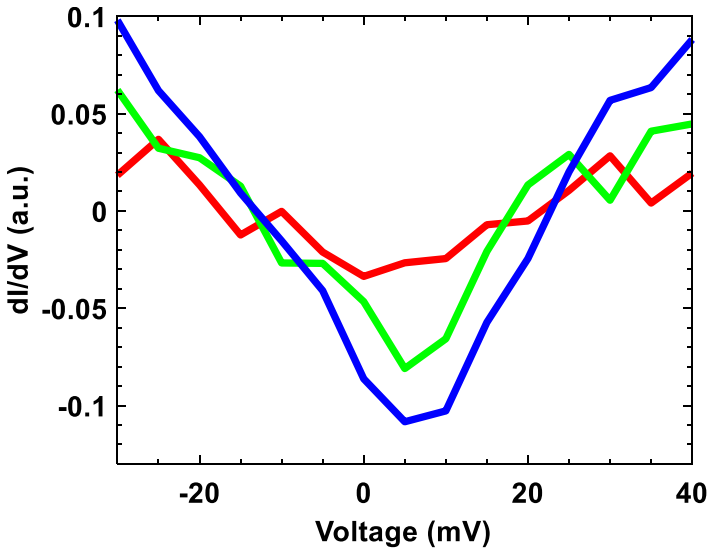

Figure 7.15: The dI/dV curves in figure 5.18 (d) after subtraction of a line that has been deducted from the slope between -20 meV and -30 meV.

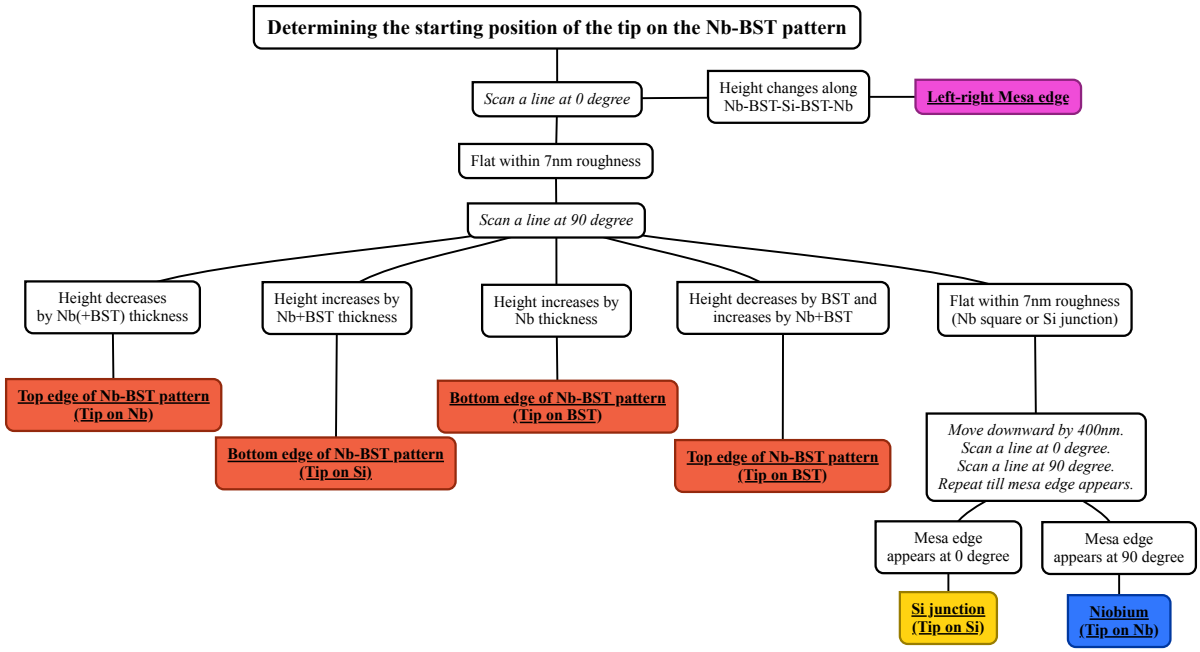

Figure 7.16: Flow chart to determine the relative position of the tip on the patterned sample, with utmost 10 line scans.

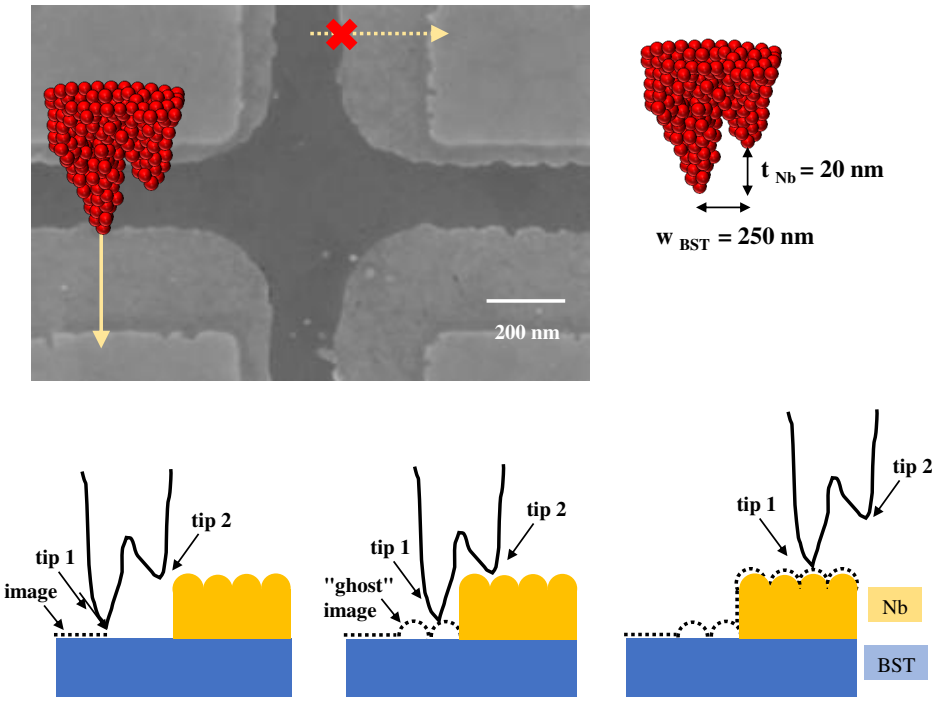

Figure 7.17: **Double tip effect. (a)** SEM image with arrows across the left-right mesa edge and top-bottom mesa edge. **(b)** With the tip shape depicted in (a), a ghost image of the Nb appears on the BST due to a double-tip effect, when the tip is scanned along the left-right mesa edge. While scanning the tip across the top-bottom interface is not leading to ghost images. Similarly, scanning on any of the rounded corners of the squares may also avoid the double-tip effect.

Bibliography

(1) Sasaki, S.; Kriener, M.; Segawa, K.; Yada, K.; Tanaka, Y.; Sato, M.; Ando, Y. "Topological Superconductivity in $Cu_xBi_2Se_3$". *Phys. Rev. Lett.* **2011**, *107*, 217001 (cit. on p. 9).

(2) Kirzhner, T.; Lahoud, E.; Chaska, K. B.; Salman, Z.; Kanigel, A. "Point-contact spectroscopy of $Cu_{0.2}Bi_2Se_3$ single crystals". *Phys. Rev. B* **2012**, *86*, 064517 (cit. on p. 9).

(3) Sasaki, S.; Ren, Z.; Taskin, A. A.; Segawa, K.; Fu, L.; Ando, Y. "Odd-Parity Pairing and Topological Superconductivity in a Strongly Spin-Orbit Coupled Semiconductor". *Physical Review Letters* **2012**, *109*, DOI: 10.1103/physrevlett.109.217004 (cit. on p. 9).

(4) Chen, M.; Chen, X.; Yang, H.; Du, Z.; Zhu, X.; Wang, E.; Wen, H.-H. "Discrete energy levels of Caroli-de Gennes-Matricon states in quantum limit in FeTe0.55Se0.45". *Nature Communications* **2018**, *9* (cit. on pp. 9, 32).

(5) Fu, L.; Kane, C. L. "Superconducting Proximity Effect and Majorana Fermions at the Surface of a Topological Insulator". *Physical Review Letters* **2008**, *100* (cit. on pp. 9, 20, 31, 83).

(6) Schnyder, A. P.; Ryu, S.; Furusaki, A.; Ludwig, A. W. W. "Classification of topological insulators and superconductors in three spatial dimensions". *Physical Review B* **2008**, *78*, DOI: 10.1103/physrevb.78.195125 (cit. on p. 9).

(7) Sarma, S. D.; Freedman, M.; Nayak, C. "Majorana zero modes and topological quantum computation". *npj Quantum Information* **2015**, *1* (cit. on p. 9).

(8) Xu, J.-P.; Liu, C.; Wang, M.-X.; Ge, J.; Liu, Z.-L.; Yang, X.; Chen, Y.; Liu, Y.; Xu, Z.-A.; Gao, C.-L.; Qian, D.; Zhang, F.-C.; Jia, J.-F. "Artificial Topological Superconductor by the Proximity Effect". *Phys. Rev. Lett.* **2014**, *112*, 217001 (cit. on p. 9).

(9) Sun, H.-H. et al. "Majorana Zero Mode Detected with Spin Selective Andreev Reflection in the Vortex of a Topological Superconductor". *Phys. Rev. Lett.* **2016**, *116*, 257003 (cit. on pp. 9, 83, 84).

(10) Morgenstern, M.; Klijn, J.; Meyer, C.; Getzlaff, M.; Adelung, R.; Römer, R. A.; Rossnagel, K.; Kipp, L.; Skibowski, M.; Wiesendanger, R. "Direct Comparison between Potential Landscape and Local Density of States in a Disordered Two-Dimensional Electron System". *Phys. Rev. Lett.* **2002**, *89*, 136806 (cit. on p. 9).

(11) Xue, J.; Sanchez-Yamagishi, J.; Bulmash, D.; Jacquod, P.; Deshpande, A.; Watanabe, K.; Taniguchi, T.; Jarillo-Herrero, P.; LeRoy, B. J. "Scanning tunnelling microscopy and spectroscopy of ultra-flat graphene on hexagonal boron nitride". *Nature Materials* **2011**, *10*, 282–285 (cit. on p. 9).

(12) Dubois, C.; Santi, G.; Cuttat, I.; Berthod, C.; Jenkins, N.; Petrović, A. P.; Manuel, A. A.; Fischer, Ø.; Kazakov, S. M.; Bukowski, Z.; Karpinski, J. "Scanning Tunneling Spectroscopy in the Superconducting State and Vortex Cores of the β-Pyrochlore KOs_2O_6". *Phys. Rev. Lett.* **2008**, *101*, 057004 (cit. on p. 9).

(13) Rakhmanov, A. L.; Rozhkov, A. V.; Nori, F. "Majorana fermions in pinned vortices". *Phys. Rev. B* **2011**, *84*, 075141 (cit. on pp. 10, 11, 31, 32).

(14) Wang, M.-X. et al. "The Coexistence of Superconductivity and Topological Order in the Bi_2Se_3 Thin Films". *Science* **2012**, *336*, 52–55 (cit. on pp. 10, 83).

(15) Dai, W.; Richardella, A.; Du, R.; Zhao, W.; Liu, X.; Liu, C. X.; Huang, S.-H.; Sankar, R.; Chou, F.; Samarth, N.; Li, Q. "Proximity-effect-induced Superconducting Gap in Topological Surface States – A Point Contact Spectroscopy Study of NbSe2/Bi2Se3 Superconductor-Topological Insulator Heterostructures". *Scientific Reports* **2017**, *7* (cit. on p. 10).

(16) Yang, F.; Qu, F.; Shen, J.; Ding, Y.; Chen, J.; Ji, Z.; Liu, G.; Fan, J.; Yang, C.; Fu, L.; Lu, L. "Proximity-effect-induced superconducting phase in the topological insulator Bi_2Se_3". *Physical Review B* **2012**, *86* (cit. on p. 10).

(17) Yang, F.; Ding, Y.; Qu, F.; Shen, J.; Chen, J.; Wei, Z.; Ji, Z.; Liu, G.; Fan, J.; Yang, C.; Xiang, T.; Lu, L. "Proximity effect at superconducting Sn-Bi_2Se_3 interface". *Phys. Rev. B* **2012**, *85*, 104508 (cit. on pp. 10, 83).

(18) Qu, F.; Yang, F.; Shen, J.; Ding, Y.; Chen, J.; Ji, Z.; Liu, G.; Fan, J.; Jing, X.; Yang, C.; Lu, L. "Strong Superconducting Proximity Effect in Pb-Bi_2Te_3 Hybrid Structures". *Scientific Reports* **2012**, *2* (cit. on p. 10).

(19) Zhang, J.; Chang, C.-Z.; Zhang, Z.; Wen, J.; Feng, X.; Li, K.; Liu, M.; He, K.; Wang, L.; Chen, X.; Xue, Q.-K.; Ma, X.; Wang, Y. "Band structure engineering in $(Bi_{1-x}Sb_x)_2Te_3$ ternary topological insulators". *Nature Communications* **2011**, *2*, DOI: 10.1038/ncomms1588 (cit. on pp. 10, 84, 97).

(20) Kellner, J.; Eschbach, M.; Kampmeier, J.; Lanius, M.; Młyńczak, E.; Mussler, G.; Holländer, B.; Plucinski, L.; Liebmann, M.; Grützmacher, D.; Schneider, C. M.; Morgenstern, M. "Tuning the Dirac point to the Fermi level in the ternary topological insulator $(Bi_{1-x}Sb_x)_2Te_3$". *Applied Physics Letters* **2015**, *107*, 251603 (cit. on pp. 10, 84, 101, 111).

(21) Neupane, M. et al. "Topological surface states and Dirac point tuning in ternary topological insulators". *Physical Review B* **2012**, *85* (cit. on p. 10).

(22) Jiang, R.; Wang, L.-L.; Huang, M.; Dhaka, R. S.; Johnson, D. D.; Lograsso, T. A.; Kaminski, A. "Reversible tuning of the surface state in a pseudobinary $Bi_2(Te\text{-}Se)_3$ topological insulator". *Phys. Rev. B* **2012**, *86*, 085112 (cit. on p. 10).

(23) Michaelson, H. B. "The work function of the elements and its periodicity". *Journal of Applied Physics* **1977**, *48*, 4729–4733 (cit. on p. 10).

(24) Caroli, C.; De Gennes, P.; Matricon, J. "Bound Fermion states on a vortex line in a type II superconductor". *Physics Letters* **1964**, *9*, 307–309 (cit. on pp. 10, 32).

(25) Sau, J. D.; Lutchyn, R. M.; Tewari, S.; Das Sarma, S. "Robustness of Majorana fermions in proximity-induced superconductors". *Phys. Rev. B* **2010**, *82*, 094522 (cit. on pp. 10, 11, 32, 83).

(26) Lutchyn, R. M.; Sau, J. D.; Das Sarma, S. "Majorana Fermions and a Topological Phase Transition in Semiconductor-Superconductor Heterostructures". *Phys. Rev. Lett.* **2010**, *105*, 077001 (cit. on pp. 11, 83).

(27) Oreg, Y.; Refael, G.; von Oppen, F. "Helical Liquids and Majorana Bound States in Quantum Wires". *Phys. Rev. Lett.* **2010**, *105*, 177002 (cit. on p. 11).

(28) Alicea, J. "New directions in the pursuit of Majorana fermions in solid state systems". *Reports on Progress in Physics* **2012**, *75*, 076501 (cit. on pp. 11, 32).

(29) Kellogg, G. "Field ion microscope studies of single-atom surface diffusion and cluster nucleation on metal surfaces". *Surface Science Reports* **1994**, *21*, 1–88 (cit. on p. 11).

(30) Zhang, Y.; Brar, V. W.; Wang, F.; Girit, C.; Yayon, Y.; Panlasigui, M.; Zettl, A.; Crommie, M. F. "Giant phonon-induced conductance in scanning tunnelling spectroscopy of gate-tunable graphene". *Nature Physics* **2008**, *4*, 627–630 (cit. on p. 11).

(31) Burmeister, F.; Schäfle, C.; Matthes, T.; Böhmisch, M.; Boneberg, J.; Leiderer, P. "Colloid Monolayers as Versatile Lithographic Masks". *Langmuir* **1997**, *13*, 2983–2987 (cit. on p. 11).

(32) Kane, C. L.; Mele, E. J. "A New Spin on the Insulating State". *Science* **2006**, *314*, 1692–1693 (cit. on p. 14).

(33) Shen, S.-Q., *Topological Insulators*; Springer-Verlag Berlin Heidelberg: 2012 (cit. on pp. 14, 19).

(34) Klitzing, K. v.; Dorda, G.; Pepper, M. "New Method for High-Accuracy Determination of the Fine-Structure Constant Based on Quantized Hall Resistance". *Phys. Rev. Lett.* **1980**, *45*, 494–497 (cit. on p. 15).

(35) Thouless, D. J.; Kohmoto, M.; Nightingale, M. P.; den Nijs, M. "Quantized Hall Conductance in a Two-Dimensional Periodic Potential". *Phys. Rev. Lett.* **1982**, *49*, 405–408 (cit. on p. 15).

(36) Xia, Y. *Photoemission studies of a new topological insulator class: experimental discovery of the Bi_2X_3 topological insulator class*, Ph.D. Thesis, Princeton University, 2010 (cit. on pp. 15, 37).

(37) Ando, Y. "Topological Insulator Materials". *Journal of the Physical Society of Japan* **2013**, *82*, 102001 (cit. on pp. 16, 19).

(38) Avron, J. E.; Osadchy, D.; Seiler, R. "A Topological Look at the Quantum Hall Effect". *Physics Today* **2003**, *56*, 38–42 (cit. on p. 16).

(39) Hasan, M. Z.; Kane, C. L. "Colloquium: Topological insulators". *Rev. Mod. Phys.* **2010**, *82*, 3045–3067 (cit. on pp. 16, 20).

(40) Kane, C. L.; Mele, E. J. "Quantum Spin Hall Effect in Graphene". *Phys. Rev. Lett.* **2005**, *95*, 226801 (cit. on p. 17).

(41) Qi, X.-L.; Zhang, S.-C. "Topological insulators and superconductors". *Rev. Mod. Phys.* **2011**, *83*, 1057–1110 (cit. on pp. 18, 20).

(42) Zhang, H.; Liu, C.-X.; Qi, X.-L.; Dai, X.; Fang, Z.; Zhang, S.-C. "Topological insulators in Bi2Se3, Bi2Te3 and Sb2Te3 with a single Dirac cone on the surface". *Nature Physics* **2009**, *5*, 438–442 (cit. on p. 17).

(43) Bernevig, B. A.; Hughes, T. L.; Zhang, S.-C. "Quantum Spin Hall Effect and Topological Phase Transition in HgTe Quantum Wells". *Science* **2006**, *314*, 1757–1761 (cit. on p. 17).

(44) König, M.; Wiedmann, S.; Brüne, C.; Roth, A.; Buhmann, H.; Molenkamp, L. W.; Qi, X.-L.; Zhang, S.-C. "Quantum Spin Hall Insulator State in HgTe Quantum Wells". *Science* **2007**, *318*, 766–770 (cit. on p. 17).

(45) Fu, L.; Kane, C. L.; Mele, E. J. "Topological Insulators in Three Dimensions". *Physical Review Letters* **2007**, *98* (cit. on pp. 19, 83).

(46) Moore, J. E.; Balents, L. "Topological invariants of time-reversal-invariant band structures". *Physical Review B* **2007**, *75* (cit. on p. 19).

(47) Fu, L.; Kane, C. L. "Topological insulators with inversion symmetry". *Physical Review B* **2007**, *76* (cit. on pp. 19, 30).

(48) Bernevig, B. A.; Hughes, T. L., *Topological insulators and topological superconductors*; Princeton University Press: 2013 (cit. on p. 20).

(49) Linder, J.; Tanaka, Y.; Yokoyama, T.; Sudbø, A.; Nagaosa, N. "Unconventional Superconductivity on a Topological Insulator". *Phys. Rev. Lett.* **2010**, *104*, 067001 (cit. on pp. 20, 83).

(50) H., K. O. "The superconductivity of mercury". *Comm. Phys. Lab. Univ. Leiden* **1911**, *122*, 122–124 (cit. on p. 21).

(51) Ichinokura, S., *Observation of Superconductivity in Epitaxially Grown Atomic Layers*; Springer Singapore: 2018 (cit. on p. 21).

(52) Tinkham, M., *Introduction to Superconductivity: Second Edition*, 2nd ed.; Dover Publications: 2004 (cit. on pp. 22, 24).

(53) Bardeen, J.; Cooper, L. N.; Schrieffer, J. R. "Theory of Superconductivity". *Phys. Rev.* **1957**, *108*, 1175–1204 (cit. on p. 22).

(54) Mineev, V. P.; Samochin, K. V., *Introduction to unconventional superconductivity*; Taylor & Francis Ltd: 1999 (cit. on p. 23).

(55) Cooper, L. N. "Bound Electron Pairs in a Degenerate Fermi Gas". *Phys. Rev.* **1956**, *104*, 1189–1190 (cit. on p. 23).

(56) Dynes, R. C.; Narayanamurti, V.; Garno, J. P. "Direct Measurement of Quasiparticle-Lifetime Broadening in a Strong-Coupled Superconductor". *Physical Review Letters* **1978**, *41*, 1509–1512 (cit. on p. 23).

(57) Andreev, A. F. "Thermal conductivity of the intermediate state of superconductors". *Zh. Eksperim. i Teor. Fiz.* **1964**, *46* (cit. on p. 24).

(58) Blonder, G. E.; Tinkham, M.; Klapwijk, T. M. "Transition from metallic to tunnelling regimes in superconducting microconstrictions: Excess current, charge imbalance, and supercurrent conversion". *Phys. Rev. B* **1982**, *25*, 4515–4532 (cit. on p. 24).

(59) Klapwijk, T. M.; Blonder, G. E.; Tinkham, M. "Explanation of subharmonic energy gap structure in superconducting contacts". *Physica B+C* **1982**, *109-110*, 1657–1664 (cit. on p. 24).

(60) Dubouchet, T.; Sacépé, B.; Seidemann, J.; Shahar, D.; Sanquer, M.; Chapelier, C. "Collective energy gap of preformed Cooper pairs in disordered superconductors". *Nature Physics* **2018**, *15*, 233–236 (cit. on p. 26).

(61) Park, W. K.; Sarrao, J. L.; Thompson, J. D.; Greene, L. H. "Andreev Reflection in Heavy-Fermion Superconductors and Order Parameter Symmetry in $CeCoIn_5$". *Phys. Rev. Lett.* **2008**, *100*, 177001 (cit. on p. 26).

(62) Oh, M.; Nuckolls, K. P.; Wong, D.; Lee, R. L.; Liu, X.; Watanabe, K.; Taniguchi, T.; Yazdani, A. "Evidence for unconventional superconductivity in twisted bilayer graphene". *Nature* **2021**, *600*, 240–245 (cit. on p. 26).

(63) Tanaka, Y.; Yokoyama, T.; Nagaosa, N. "Manipulation of the Majorana Fermion, Andreev Reflection, and Josephson Current on Topological Insulators". *Phys. Rev. Lett.* **2009**, *103*, 107002 (cit. on pp. 26, 83).

(64) Zhu, S. et al. "Nearly quantized conductance plateau of vortex zero mode in an iron-based superconductor". *Science* **2020**, *367*, 189–192 (cit. on p. 26).

(65) Pan, S. H.; Hudson, E. W.; Davis, J. C. "Vacuum tunneling of superconducting quasiparticles from atomically sharp scanning tunneling microscope tips". *Applied Physics Letters* **1998**, *73*, 2992–2994 (cit. on p. 26).

(66) Hoffman, J. E.; McElroy, K.; Lee, D.-H.; Lang, K. M.; Eisaki, H.; Uchida, S.; Davis, J. C. "Imaging Quasiparticle Interference in $Bi_2Sr_2CaCu_2O_{8+\delta}$". *Science* **2002**, *297*, 1148–1151 (cit. on p. 26).

(67) Tartaglini, E.; Verhagen, T. G. A.; Galli, F.; Trouwborst, M. L.; Müller, R.; Shiota, T.; Aarts, J.; van Ruitenbeek, J. M. "New directions in point-contact spectroscopy based on scanning tunneling microscopy techniques (Review Article)". *Low Temperature Physics* **2013**, *39*, 189–198 (cit. on p. 26).

(68) Bednorz, J. G.; Müller, K. A. "Possible highT c superconductivity in the Ba?La?Cu?O system". *Zeitschrift für Physik B Condensed Matter* **1986**, *64*, 189–193 (cit. on p. 26).

(69) Senkpiel, J.; Dambach, S.; Etzkorn, M.; Drost, R.; Padurariu, C.; Kubala, B.; Belzig, W.; Yeyati, A. L.; Cuevas, J. C.; Ankerhold, J.; Ast, C. R.; Kern, K. "Single channel Josephson effect in a high transmission atomic contact". *Communications Physics* **2020**, *3* (cit. on p. 26).

(70) Agraït, N.; Rodrigo, J. G.; Vieira, S. "Transition from the tunneling regime to point contact and proximity-induced Josephson effect in lead–normal-metal nanojunctions". *Physical Review B* **1992**, *46*, 5814–5817 (cit. on p. 26).

(71) Yazdani, A.; Jones, B. A.; Lutz, C. P.; Crommie, M. F.; Eigler, D. M. "Probing the Local Effects of Magnetic Impurities on Superconductivity". *Science* **1997**, *275*, 1767–1770 (cit. on p. 26).

(72) Bürgi, Lukas *Scanning tunneling microscopy as local probe of electron density, dynamics, and transport at metal surfaces*, en, Ph.D. Thesis, Lausanne, EPFL, 2005 (cit. on p. 26).

(73) Rodrigo, J. G.; Suderow, H.; Vieira, S. "On the use of STM superconducting tips at very low temperatures". *The European Physical Journal B* **2004**, *40*, 483–488 (cit. on pp. 26, 115).

(74) Wiebe, J.; Wachowiak, A.; Meier, F.; Haude, D.; Foster, T.; Morgenstern, M.; Wiesendanger, R. "A 300 mK ultra-high vacuum scanning tunneling microscope for spin-resolved spectroscopy at high energy resolution". *Rev. Sci. Instr.* **2004**, *75*, 4871–4879 (cit. on pp. 26, 67).

(75) Anderson, P. W.; Rowell, J. M. "Probable Observation of the Josephson Superconducting Tunneling Effect". *Phys. Rev. Lett.* **1963**, *10*, 230–232 (cit. on p. 27).

(76) Naaman, O.; Teizer, W.; Dynes, R. C. "Fluctuation Dominated Josephson Tunneling with a Scanning Tunneling Microscope". *Phys. Rev. Lett.* **2001**, *87*, 097004 (cit. on pp. 27, 115).

(77) Naaman, O.; Dynes, R. "Subharmonic gap structure in superconducting scanning tunneling microscope junctions". *Solid State Communications* **2004**, *129*, 299–303 (cit. on p. 27).

(78) Pillet, J.-D.; Quay, C. H. L.; Morfin, P.; Bena, C.; Yeyati, A. L.; Joyez, P. "Andreev bound states in supercurrent-carrying carbon nanotubes revealed". *Nature Physics* **2010**, *6*, 965–969 (cit. on p. 27).

(79) Furusaki, A.; Tsukada, M. "Dc Josephson effect and Andreev reflection". *Solid State Communications* **1991**, *78*, 299–302 (cit. on p. 28).

(80) Beenakker, C. W. J.; van Houten, H. "Josephson current through a superconducting quantum point contact shorter than the coherence length". *Phys. Rev. Lett.* **1991**, *66*, 3056–3059 (cit. on p. 28).

(81) Schäpers, T., *Superconductor/Semiconductor Junctions*; Springer Berlin Heidelberg: 2001 (cit. on pp. 28, 37).

(82) Clarke, J. "The Proximity Effect Between Superconducting and Normal Thin Films in Zero Field". *Le Journal de Physique Colloques* **1968**, *29*, C2–3–C2–16 (cit. on p. 29).

(83) Read, N.; Green, D. "Paired states of fermions in two dimensions with breaking of parity and time-reversal symmetries and the fractional quantum Hall effect". *Phys. Rev. B* **2000**, *61*, 10267–10297 (cit. on p. 30).

(84) Akzyanov, R. S.; Rozhkov, A. V.; Rakhmanov, A. L.; Nori, F. "Tunneling spectrum of a pinned vortex with a robust Majorana state". *Phys. Rev. B* **2014**, *89*, 085409 (cit. on p. 31).

(85) Einstein, A. "Über einen die Erzeugung und Verwandlung des Lichtes betreffenden heuristischen Gesichtspunkt". *Annalen der Physik* **1905**, *322*, 132–148 (cit. on p. 33).

(86) Schönhense, G.; Elmers, H.-J. "Spin- and time-resolved photoelectron spectroscopy and diffraction studies using time-of-flight momentum microscopes". *Journal of Vacuum Science & Technology A* **2022**, *40*, 020802 (cit. on p. 34).

(87) Damascelli, A. "Probing the Electronic Structure of Complex Systems by ARPES". *Physica Scripta* **2004**, *61* (cit. on pp. 34–37).

(88) Hsieh, D.; Qian, D.; Wray, L.; Xia, Y.; Hor, Y. S.; Cava, R. J.; Hasan, M. Z. "A topological Dirac insulator in a quantum spin Hall phase". *Nature* **2008**, *452*, 970–974 (cit. on p. 34).

(89) Wang, L.-L.; Huang, M.; Thimmaiah, S.; Alam, A.; Bud'ko, S. L.; Kaminski, A.; Lograsso, T. A.; Canfield, P.; Johnson, D. D. "Native defects in tetradymite $Bi_2(Te_xSe_{3-x})$ topological insulators". *Phys. Rev. B* **2013**, *87*, 125303 (cit. on p. 34).

(90) Hüfner, S., *Photoelectron Spectroscopy*; Springer Berlin Heidelberg: 1995 (cit. on pp. 35, 37).

(91) Berglund, C. N.; Spicer, W. E. "Photoemission Studies of Copper and Silver: Theory". *Physical Review* **1964**, *136*, A1030–A1044 (cit. on p. 34).

(92) Koralek, J. D.; Douglas, J. F.; Plumb, N. C.; Sun, Z.; Fedorov, A. V.; Murnane, M. M.; Kapteyn, H. C.; Cundiff, S. T.; Aiura, Y.; Oka, K.; Eisaki, H.; Dessau, D. S. "Laser Based Angle-Resolved Photoemission, the Sudden Approximation, and Quasiparticle-Like Spectral Peaks in $BiSr_2CaCu_2O_8$". *Physical Review Letters* **2006**, *96* (cit. on p. 37).

(93) *Very High Resolution Photoelectron Spectroscopy*; Hüfner, S., Ed.; Springer Berlin Heidelberg: 2007 (cit. on p. 37).

(94) Schönhense, G.; Medjanik, K.; Elmers, H.-J. "Space-, time- and spin-resolved photoemission". *Journal of Electron Spectroscopy and Related Phenomena* **2015**, *200*, 94–118 (cit. on p. 37).

(95) Eschbach, M. *Band Structure Engineering in 3D Topological Insulators Investigated by Angle-Resolved Photoemission Spectroscopy*, en, Ph.D. Thesis, Forschungszentrum Jülich GmbH, Peter Grünberg Institute (PGI), Electronic Properties (PGI-6), 2016 (cit. on p. 38).

(96) Chen, C. J., *Introduction to Scanning Tunneling Microscopy*; Oxford University Press, Pxford: 1993 (cit. on p. 38).

(97) Quate, C. F. "Vacuum Tunneling: A New Technique for Microscopy". *Physics Today* **1986**, *39*, 26 (cit. on p. 38).

(98) Bardeen, J. "Tunnelling from a Many-Particle Point of View". *Phys. Rev. Lett.* **1961**, *6*, 57–59 (cit. on pp. 39, 41).

(99) Tersoff, J.; Hamann, D. R. "Theory and Application for the Scanning Tunneling Microscope". *Phys. Rev. Lett.* **1983**, *50*, 1998–2001 (cit. on pp. 39, 41).

(100) Tersoff, J.; Hamann, D. R. "Theory of the scanning tunneling microscope". *Phys. Rev. B* **1985**, *31*, 805–813 (cit. on pp. 39, 41).

(101) Chen, C. J. "Theory of scanning tunneling spectroscopy". *Journal of Vacuum Science & Technology A: Vacuum, Surfaces, and Films* **1988**, *6*, 319–322 (cit. on p. 39).

(102) Chen, C. J. "Tunneling matrix elements in three-dimensional space: The derivative rule and the sum rule". *Physical Review B* **1990**, *42*, 8841–8857 (cit. on p. 39).

(103) Chen, C. J. "Origin of atomic resolution on metal surfaces in scanning tunneling microscopy". *Physical Review Letters* **1990**, *65*, 448–451 (cit. on p. 39).

(104) Wachowiak, A. *Development of a 300mK Ultra High Vacuum Scanning Tunneling Microscope with 14 Tesla Magnet and Spin Polarized Scanning Tunneling Spectroscopy on Ferromagnetic Fe-Islands*, Ph.D. Thesis, Institute of Applied Physics, University of Hamburg, 2003 (cit. on p. 42).

(105) Muckel, F. *Sub 1K UHV Scanning tunneling microscope made of shapal and mapping of magnetic skyrmion collapse rates*, Ph.D. Thesis, RWTH Aachen University, 2020 (cit. on pp. 43, 44, 46).

(106) Jacobs, T. *Programmierung einer automatisierten Steuerung eines Helium-3 Gas-Handling-System*, 2022 (cit. on p. 44).

(107) Perdereau, J.; Biberian, J. P.; Rhead, G. E. "Adsorption and surface alloying of lead monolayers on (111) and (110) faces of gold". *Journal of Physics F: Metal Physics* **1974**, *4*, 798 (cit. on p. 44).

(108) Hove, M. V.; Koestner, R.; Stair, P.; Bibèrian, J.; Kesmodel, L.; BartoŠ, I.; Somorjai, G. "The surface reconstructions of the (100) crystal faces of iridium, platinum and gold". *Surface Science* **1981**, *103*, 189–217 (cit. on p. 44).

(109) Yagi, K.; Kobayashi, K.; Tanishiro, Y.; Takayanagi, K. "In situ electron microscope study of the initial stage of metal growth on metals". *Thin Solid Films* **1985**, *126*, 95–105 (cit. on p. 44).

(110) Wöll, C.; Chiang, S.; Wilson, R. J.; Lippel, P. H. "Determination of atom positions at stacking-fault dislocations on Au(111) by scanning tunneling microscopy". *Phys. Rev. B* **1989**, *39*, 7988–7991 (cit. on p. 44).

(111) Sadeddine, S.; Enriquez, H.; Bendounan, A.; Das, P. K.; Vobornik, I.; Kara, A.; Mayne, A. J.; Sirotti, F.; Dujardin, G.; Oughaddou, H. "Compelling experimental evidence of a Dirac cone in the electronic structure of a 2D Silicon layer". *Scientific Reports* **2017**, *7* (cit. on p. 44).

(112) Chen, W.; Madhavan, V.; Jamneala, T.; Crommie, M. F. "Scanning Tunneling Microscopy Observation of an Electronic Superlattice at the Surface of Clean Gold". *Phys. Rev. Lett.* **1998**, *80*, 1469–1472 (cit. on p. 45).

(113) Bode, M.; Pascal, R.; Wiesendanger, R. "STM study of carbon-induced reconstructions on W(110): strong evidence for a surface lattice deformation". *Surface Science* **1995**, *344*, 185–191 (cit. on p. 45).

(114) Dagata, J. A.; Schneir, J.; Harary, H. H.; Evans, C. J.; Postek, M. T.; Bennett, J. "Modification of hydrogen-passivated silicon by a scanning tunneling microscope operating in air". *Applied Physics Letters* **1990**, *56*, 2001–2003 (cit. on p. 49).

(115) Garcia, R.; Martinez, R. V.; Martinez, J. "Nanochemistry and scanning probe nanolithographies". *Chem. Soc. Rev.* **2006**, *35*, 29–38 (cit. on p. 49).

(116) Fuhrer, A.; Lüscher, S.; Ihn, T.; Heinzel, T.; Ensslin, K.; Wegscheider, W.; Bichler, M. "Energy spectra of quantum rings". *Nature* **2001**, *413*, 822–825 (cit. on p. 49).

(117) Puddy, R. K.; Chua, C. J.; Buitelaar, M. R. "Transport spectroscopy of a graphene quantum dot fabricated by atomic force microscope nanolithography". *Applied Physics Letters* **2013**, *103*, 183117 (cit. on p. 49).

(118) Magda, G. Z.; Jin, X.; Hagymási, I.; Vancsó, P.; Osváth, Z.; Nemes-Incze, P.; Hwang, C.; Biró, L. P.; Tapasztó, L. "Room temperature magnetic order on zigzag edges of narrow graphene nanoribbons". *Nature* **2014**, *514*, 608–611 (cit. on p. 49).

(119) Lee, J.; Wong, D.; Jr, J. V.; Rodriguez-Nieva, J. F.; Kahn, S.; Tsai, H.-Z.; Taniguchi, T.; Watanabe, K.; Zettl, A.; Wang, F.; Levitov, L. S.; Crommie, M. F. "Imaging electrostatically confined Dirac fermions in graphene quantum dots". *Nature Physics* **2016**, *12*, 1032–1036 (cit. on p. 49).

(120) Ghahari, F.; Walkup, D.; Gutiérrez, C.; Rodriguez-Nieva, J. F.; Zhao, Y.; Wyrick, J.; Natterer, F. D.; Cullen, W. G.; Watanabe, K.; Taniguchi, T.; Levitov, L. S.; Zhitenev, N. B.; Stroscio, J. A. "An on/off Berry phase switch in circular graphene resonators". *Science* **2017**, *356*, 845–849 (cit. on p. 49).

(121) Lyo, I.-W.; Avouris, P. "Field Induced Nanometer to Atomic Scale Manipulation of Silicon Surfaces with the STM". *Science* **1991**, *253*, 173–176 (cit. on p. 49).

(122) Eigler, D. M.; Schweizer, E. K. "Positioning single atoms with a scanning tunnelling microscope". *Nature* **1990**, *344*, 524–526 (cit. on p. 49).

(123) Custance, O.; Perez, R.; Morita, S. "Atomic force microscopy as a tool for atom manipulation". *Nature Nanotechnology* **2009**, *4*, 803–810 (cit. on p. 49).

(124) Crommie, M. F.; Lutz, C. P.; Eigler, D. M. "Confinement of Electrons to Quantum Corrals on a Metal Surface". *Science* **1993**, *262*, 218–220 (cit. on p. 49).

(125) Celotta, R. J.; Balakirsky, S. B.; Fein, A. P.; Hess, F. M.; Rutter, G. M.; Stroscio, J. A. "Invited Article: Autonomous assembly of atomically perfect nanostructures using a scanning tunneling microscope". *Review of Scientific Instruments* **2014**, *85*, 121301 (cit. on p. 49).

(126) Kalff, F. E.; Rebergen, M. P.; Fahrenfort, E.; Girovsky, J.; Toskovic, R.; Lado, J. L.; Fernández-Rossier, J.; Otte, A. F. "A kilobyte rewritable atomic memory". *Nature Nanotechnology* **2016**, *11*, 926–929 (cit. on p. 49).

(127) Vasko, S. E.; Kapetanovic, A.; Talla, V.; Brasino, M. D.; Zhu, Z.; Scholl, A.; Torrey, J. D.; Rolandi, M. "Serial and Parallel Si, Ge, and SiGe Direct Write with Scanning Probes and Conducting Stamps". *Nano Letters* **2011**, *11*, 2386–2389 (cit. on p. 49).

(128) Fuechsle, M.; Miwa, J. A.; Mahapatra, S.; Ryu, H.; Lee, S.; Warschkow, O.; Hollenberg, L. C. L.; Klimeck, G.; Simmons, M. Y. "A single-atom transistor". *Nat. Nanotechnol.* **2012**, *7*, 242–246 (cit. on p. 49).

(129) Loth, S.; Baumann, S.; Lutz, C. P.; Eigler, D. M.; Heinrich, A. J. "Bistability in Atomic-Scale Antiferromagnets". *Science* **2012**, *335*, 196–199 (cit. on p. 49).

(130) Khajetoorians, A. A.; Baxevanis, B.; Hubner, C.; Schlenk, T.; Krause, S.; Wehling, T. O.; Lounis, S.; Lichtenstein, A.; Pfannkuche, D.; Wiebe, J.; Wiesendanger, R. "Current-Driven Spin Dynamics of Artificially Constructed Quantum Magnets". *Science* **2013**, *339*, 55–59 (cit. on p. 49).

(131) Choi, T.; Paul, W.; Rolf-Pissarczyk, S.; Macdonald, A. J.; Natterer, F. D.; Yang, K.; Willke, P.; Lutz, C. P.; Heinrich, A. J. "Atomic-scale sensing of the magnetic dipolar field from single atoms". *Nat. Nanotechnol.* **2017**, *12*, 420–424 (cit. on p. 49).

(132) Ono, K.; Shimada, H.; Kobayashi, S.-i.; Ootuka, Y. "A New Fabrication Method for Ultra Small Tunnel Junctions". *Japanese Journal of Applied Physics* **1996**, *35*, 2369–2371 (cit. on p. 50).

(133) Matsui, S.; Ochiai, Y. "Focused ion beam applications to solid state devices". *Nanotechnology* **1996**, *7*, 247–258 (cit. on p. 50).

(134) Deshmukh, M. M.; Ralph, D. C.; Thomas, M.; Silcox, J. "Nanofabrication using a stencil mask". *Applied Physics Letters* **1999**, *75*, 1631–1633 (cit. on p. 50).

(135) Van den Boogaart, M. A. F.; Kim, G. M.; Pellens, R.; van den Heuvel, J.-P.; Brugger, J. "Deep-ultraviolet–microelectromechanical systems stencils for high-throughput resistless patterning of mesoscopic structures". *Journal of Vacuum Science & Technology B: Microelectronics and Nanometer Structures* **2004**, *22*, 3174 (cit. on p. 50).

(136) Gärtner, C.; Hoffman, R.; Pérez-Willard, F.; Sauter, M.; Sürgers, C.; v. Löhneysen, H. "Fully ultrahigh vacuum compatible fabrication of submicrometer spaced electrical contacts". *Rev. Sci. Instr.* **2006**, *77*, 026101 (cit. on p. 50).

(137) Staley, N.; Wang, H.; Puls, C.; Forster, J.; Jackson, T. N.; McCarthy, K.; Clouser, B.; Liu, Y. "Lithography free fabrication of graphene devices". *Applied Physics Letters* **2007**, *90*, 143518 (cit. on p. 50).

(138) Tien, D. H.; Park, J.-Y.; Kim, K. B.; Lee, N.; Seo, Y. "Characterization of Graphene-based FET Fabricated using a Shadow Mask". *Scientific Reports* **2016**, *6*, 25050 (cit. on p. 50).

(139) Linklater, A.; Nogami, J. "Defining nanoscale metal features on an atomically clean silicon surface with a stencil". *Nanotechnol.* **2008**, *19*, 285302 (cit. on pp. 50, 51, 77, 78).

(140) Stöffler, D.; Hoffmann-Vogel, R. "Enhanced positioning precision and in situ macroscopic contacts for shadow evaporated nanostructures". *J. Vac. Sci. Technol. B* **2015**, *33*, 013201 (cit. on p. 50).

(141) Lüthi, R.; Schlittler, R. R.; Brugger, J.; Vettiger, P.; Welland, M. E.; Gimzewski, J. K. "Parallel nanodevice fabrication using a combination of shadow mask and scanning probe methods". *Appl. Phys. Lett.* **1999**, *75*, 1314–1316 (cit. on p. 50).

(142) Egger, S.; Ilie, A.; Fu, Y.; Chongsathien, J.; Kang, D.-J.; Welland, M. E. "Dynamic Shadow Mask Technique: A Universal Tool for Nanoscience". *Nano Letters* **2005**, *5*, 15–20 (cit. on p. 50).

(143) Garcia, R.; Knoll, A. W.; Riedo, E. "Advanced scanning probe lithography". *Nature Nanotechnology* **2014**, *9*, 577–587 (cit. on p. 50).

(144) Li, L.; Bayn, I.; Lu, M.; Nam, C.-Y.; Schröder, T.; Stein, A.; Harris, N. C.; Englund, D. "Nanofabrication on unconventional substrates using transferred hard masks". *Scientific Reports* **2015**, *5* (cit. on p. 50).

(145) Shin, H.-J.; Choi, J. H.; Yang, H. J.; Park, Y. D.; Kuk, Y.; Kang, C.-J. "Patterning of ferroelectric nanodot arrays using a silicon nitride shadow mask". *Applied Physics Letters* **2005**, *87*, 113114 (cit. on p. 51).

(146) Zahl, P.; Bammerlin, M.; Meyer, G.; Schlittler, R. R. "All-in-one static and dynamic nanostencil atomic force microscopy/scanning tunneling microscopy system". *Rev. Sci. Instr.* **2005**, *76*, 023707 (cit. on p. 51).

(147) Savu, V.; van den Boogaart, M. A. F.; Brugger, J.; Arcamone, J.; Sansa, M.; Perez-Murano, F. "Dynamic stencil lithography on full wafer scale". *J. Vac. Sci. Technol. B* **2008**, *26*, 2054–2058 (cit. on p. 51).

(148) Steurer, W.; Gross, L.; Schlittler, R. R.; Meyer, G. "A variable-temperature nanostencil compatible with a low-temperature scanning tunnelling microscope/atomic force microscope". *Rev. Sci. Instr.* **2014**, *85*, 023706 (cit. on p. 51).

(149) Tun, T. N.; Lwin, M. H. T.; Kim, H. H.; Chandrasekhar, N.; Joachim, C. "Wetting studies on Au nanowires deposited through nanostencil masks". *Nanotechnol.* **2007**, *18*, 335301 (cit. on p. 51).

(150) Pan, S. H.; Behler, S.; Bernasconi, M.; Güntherodt, H.-J. *Bull. Am. Phys. Soc.* **1990**, *37*, 167 (cit. on pp. 51, 67).

(151) Bhaskar, P.; Mathioudakis, S.; Olschewski, T.; Muckel, F.; Bindel, J. R.; Pratzer, M.; Liebmann, M.; Morgenstern, M. "Mask aligner for ultrahigh vacuum with capacitive distance control". *Applied Physics Letters* **2018**, *112*, 161602 (cit. on p. 52).

(152) Pan, S. H., International Patent Publication Number WO 93/19494, 1993 (cit. on p. 67).

(153) Du, K.; Ding, J.; Liu, Y.; Wathuthanthri, I.; Choi, C.-H. "Stencil Lithography for Scalable Micro- and Nanomanufacturing". *Micromachines* **2017**, *8*, 131 (cit. on p. 68).

(154) Mathioudakis, S. *Inbetriebnahme und Test eines Mask Aligners für Ultrahochvakuum*, MA thesis, RWTH Aachen Univeristy, 2015 (cit. on pp. 70, 71).

(155) Beeker, J. *Growth of Pb islands with the help of an ultrahigh vacuum mask alinger*, MA thesis, RWTH Aachen Univeristy, 2022 (cit. on pp. 72, 74, 75, 77, 79, 80, 128–130).

(156) Reichl, L. E., *A modern course in statistical physics*; University of Texas Press: Austin, 1980 (cit. on p. 77).

(157) Farrow, R. F. C., *Molecular beam epitaxy: applications to key materials*; Noyes Publications: Park Ridge, N.J, 1995 (cit. on p. 77).

(158) Horcas, I.; Fernández, R.; Gómez-Rodríguez, J. M.; Colchero, J.; Gómez-Herrero, J.; Baro, A. M. "WSXM: A software for scanning probe microscopy and a tool for nanotechnology". *Review of Scientific Instruments* **2007**, *78*, 013705 (cit. on p. 78).

(159) Slezak, J.; Chab, V.; Chvoj, Z.; Mutombo, P. "Study of Pb diffusion on Si(111)-(7×7) with scanning tunneling microscopy: Low coverage". *Journal of Vacuum Science & Technology B: Microelectronics and Nanometer Structures* **2000**, *18*, 1151 (cit. on p. 79).

(160) Alicea, J. "Majorana fermions in a tunable semiconductor device". *Phys. Rev. B* **2010**, *81*, 125318 (cit. on p. 83).

(161) Mao, L.; Zhang, C. "Robustness of Majorana modes and minigaps in a spin-orbit-coupled semiconductor-superconductor heterostructure". *Phys. Rev. B* **2010**, *82*, 174506 (cit. on p. 83).

(162) Mao, L.; Shi, J.; Niu, Q.; Zhang, C. "Superconducting Phase with a Chiral f-Wave Pairing Symmetry and Majorana Fermions Induced in a Hole-Doped Semiconductor". *Phys. Rev. Lett.* **2011**, *106*, 157003 (cit. on p. 83).

(163) Linder, J.; Tanaka, Y.; Yokoyama, T.; Sudbø, A.; Nagaosa, N. "Interplay between superconductivity and ferromagnetism on a topological insulator". *Phys. Rev. B* **2010**, *81*, 184525 (cit. on p. 83).

(164) Sacépé, B.; Oostinga, J. B.; Li, J.; Ubaldini, A.; Couto, N. J.; Giannini, E.; Morpurgo, A. F. "Gate-tuned normal and superconducting transport at the surface of a topological insulator". *Nature Communications* **2011**, *2* (cit. on p. 83).

(165) Li, Y.; Xu, Z.-A. "Exploring Topological Superconductivity in Topological Materials". *Advanced Quantum Technologies* **2019**, *2*, 1800112 (cit. on p. 83).

(166) Muenks, M. *Probing the superconducting proximity effect in topological insulators*, Ph.D. Thesis, Michigan State University, 2013 (cit. on p. 83).

(167) Li, H.; Zhou, T.; He, J.; Wang, H.-W.; Zhang, H.; Liu, H.-C.; Yi, Y.; Wu, C.; Law, K. T.; He, H.; Wang, J. "Origin of bias-independent conductance plateaus and zero-bias conductance peaks in $Bi_2Se_3/NbSe_2$ hybrid structures". *Physical Review B* **2017**, *96*, DOI: 10.1103/physrevb.96.075107 (cit. on p. 83).

(168) Zhang, D.; Wang, J.; DaSilva, A. M.; Lee, J. S.; Gutierrez, H. R.; Chan, M. H. W.; Jain, J.; Samarth, N. "Superconducting proximity effect and possible evidence for Pearl vortices in a candidate topological insulator". *Phys. Rev. B* **2011**, *84*, 165120 (cit. on p. 83).

(169) Zareapour, P.; Hayat, A.; Zhao, S. Y. F.; Kreshchuk, M.; Jain, A.; Kwok, D. C.; Lee, N.; Cheong, S.-W.; Xu, Z.; Yang, A.; Gu, G.; Jia, S.; Cava, R. J.; Burch, K. S. "Proximity-induced high-temperature superconductivity in the topological insulators Bi2Se3 and Bi2Te3". *Nature Communications* **2012**, *3* (cit. on p. 83).

(170) Wang, E. et al. "Fully gapped topological surface states in Bi2Se3 films induced by a d-wave high-temperature superconductor". *Nature Physics* **2013**, *9*, 621–625 (cit. on p. 83).

(171) Xu, J.-P.; Wang, M.-X.; Liu, Z. L.; Ge, J.-F.; Yang, X.; Liu, C.; Xu, Z. A.; Guan, D.; Gao, C. L.; Qian, D.; Liu, Y.; Wang, Q.-H.; Zhang, F.-C.; Xue, Q.-K.; Jia, J.-F. "Experimental Detection of a Majorana Mode in the core of a Magnetic Vortex inside a Topological Insulator-Superconductor $Bi_2Te_3/NbSe_2$ Heterostructure". *Phys. Rev. Lett.* **2015**, *114*, 017001 (cit. on pp. 83, 84).

(172) Chen, Y. L.; Analytis, J. G.; Chu, J.-H.; Liu, Z. K.; Mo, S.-K.; Qi, X. L.; Zhang, H. J.; Lu, D. H.; Dai, X.; Fang, Z.; Zhang, S. C.; Fisher, I. R.; Hussain, Z.; Shen, Z.-X. "Experimental Realization of a Three-Dimensional Topological Insulator, Bi_2Te_3". *Science* **2009**, *325*, 178–181 (cit. on p. 84).

(173) Xia, Y.; Qian, D.; Hsieh, D.; Wray, L.; Pal, A.; Lin, H.; Bansil, A.; Grauer, D.; Hor, Y. S.; Cava, R. J.; Hasan, M. Z. "Observation of a large-gap topological-insulator class with a single Dirac cone on the surface". *Nature Physics* **2009**, *5*, 398–402 (cit. on p. 84).

(174) Hsieh, D. et al. "A tunable topological insulator in the spin helical Dirac transport regime". *Nature* **2009**, *460*, 1101–1105 (cit. on p. 84).

(175) Hanaguri, T.; Igarashi, K.; Kawamura, M.; Takagi, H.; Sasagawa, T. "Momentum-resolved Landau-level spectroscopy of Dirac surface state in Bi_2Se_3". *Phys. Rev. B* **2010**, *82*, 081305 (cit. on p. 84).

(176) Cheng, P. et al. "Landau Quantization of Topological Surface States in Bi_2Se_3". *Phys. Rev. Lett.* **2010**, *105*, 076801 (cit. on p. 84).

(177) Beidenkopf, H.; Roushan, P.; Seo, J.; Gorman, L.; Drozdov, I.; Hor, Y. S.; Cava, R. J.; Yazdani, A. "Spatial fluctuations of helical Dirac fermions on the surface of topological insulators". *Nature Physics* **2011**, *7*, 939 (cit. on pp. 84, 108).

(178) Okada, Y.; Dhital, C.; Zhou, W.; Huemiller, E. D.; Lin, H.; Basak, S.; Bansil, A.; Huang, Y.-B.; Ding, H.; Wang, Z.; Wilson, S. D.; Madhavan, V. "Direct Observation of Broken Time-Reversal Symmetry on the Surface of a Magnetically Doped Topological Insulator". *Phys. Rev. Lett.* **2011**, *106*, 206805 (cit. on p. 84).

(179) Scanlon, D. O.; King, P. D. C.; Singh, R. P.; de la Torre, A.; Walker, S. M.; Balakrishnan, G.; Baumberger, F.; Catlow, C. R. A. "Controlling Bulk Conductivity in Topological Insulators: Key Role of Anti-Site Defects". *Advanced Materials* **2012**, *24*, 2154–2158 (cit. on pp. 84, 93).

(180) Jiang, Y.; Sun, Y. Y.; Chen, M.; Wang, Y.; Li, Z.; Song, C.; He, K.; Wang, L.; Chen, X.; Xue, Q.-K.; Ma, X.; Zhang, S. B. "Fermi-Level Tuning of Epitaxial Sb_2Te_3 Thin Films on Graphene by Regulating Intrinsic Defects and Substrate Transfer Doping". *Phys. Rev. Lett.* **2012**, *108*, 066809 (cit. on p. 84).

(181) He, X.; Guan, T.; Wang, X.; Feng, B.; Cheng, P.; Chen, L.; Li, Y.; Wu, K. "Highly tunable electron transport in epitaxial topological insulator $(Bi_{1-x}Sb_x)_2Te_3$ thin films". *Applied Physics Letters* **2012**, *101*, 123111 (cit. on p. 84).

(182) He, X.; Li, H.; Chen, L.; Wu, K. "Substitution-induced spin-splitted surface states in topological insulator $(Bi_{1-x}Sb_x)_2Te_3$". *Scientific Reports* **2015**, *5*, 8830 (cit. on pp. 84, 108, 111).

(183) He, L.; Kou, X.; Lang, M.; Choi, E. S.; Jiang, Y.; Nie, T.; Jiang, W.; Fan, Y.; Wang, Y.; Xiu, F.; Wang, K. L. "Evidence of the two surface states of $(Bi_{0.53}Sb_{0.47})_2Te_3$ films grown by van der Waals epitaxy". *Scientific Reports* **2013**, *3* (cit. on p. 84).

(184) Kong, D.; Chen, Y.; Cha, J. J.; Zhang, Q.; Analytis, J. G.; Lai, K.; Liu, Z.; Hong, S. S.; Koski, K. J.; Mo, S.-K.; Hussain, Z.; Fisher, I. R.; Shen, Z.-X.; Cui, Y. "Ambipolar field effect in the ternary topological insulator $(Bi_xSb_{1-x})_2Te_3$ by composition tuning". *Nature Nanotechnology* **2011**, *6*, 705–709 (cit. on pp. 84, 108, 111).

(185) Zhang, H.; Ma, X.; Li, L.; Langenberg, D.; Zeng, C. G.; Miao, G. X. "Two-step growth of high-quality $Nb/(Bi_{0.5}Sb_{0.5})_2Te_3/Nb$ heterostructures for topological Josephson junctions". *Journal of Materials Research* **2018**, *33*, 2423–2433 (cit. on p. 84).

(186) Rosenbach, D. *Quantum transport and induced superconductivity in selectively deposited topological insulator devices*, Ph.D. Thesis, RWTH Aachen Univeristy, 2021 (cit. on pp. 85, 89, 90).

(187) Schüffelgen, P. et al. "Selective area growth and stencil lithography for in situ fabricated quantum devices". *Nature Nanotechnology* **2019**, *14*, 825–831 (cit. on pp. 85, 89).

(188) Schmitt, T. W. et al. "Integration of Topological Insulator Josephson Junctions in Superconducting Qubit Circuits". *Nano Letters* **2022**, *22*, 2595–2602 (cit. on p. 85).

(189) Volykhov, A. A.; Sánchez-Barriga, J.; Sirotina, A. P.; Neudachina, V. S.; Frolov, A. S.; Gerber, E. A.; Kataev, E. Y.; Senkovsky, B.; Khmelevsky, N. O.; Aksenenko, A. Y.; Korobova, N. V.; Knop-Gericke, A.; Rader, O.; Yashina, L. V. "Rapid Surface Oxidation of Sb_2Te_3 as Indication for a Universal Trend in the Chemical Reactivity of Tetradymite Topological Insulators". *Chemistry of Materials* **2016**, *28*, 8916–8923 (cit. on p. 88).

(190) Virwani, K.; Harrison, S. E.; Pushp, A.; Topuria, T.; Delenia, E.; Rice, P.; Kellock, A.; Collins-McIntyre, L.; Harris, J.; Hesjedal, T.; Parkin, S. "Controlled removal of amorphous Se capping layer from a topological insulator". *Applied Physics Letters* **2014**, *105*, 241605 (cit. on pp. 90, 92, 95).

(191) Dai, J.; Wang, W.; Brahlek, M.; Koirala, N.; Salehi, M.; Oh, S.; Wu, W. "Restoring pristine Bi2Se3 surfaces with an effective Se decapping process". *Nano Research* **2014**, *8*, 1222–1228 (cit. on p. 90).

(192) Fornari, C. I.; Rappl, P. H. O.; Morelhão, S. L.; Peixoto, T. R. F.; Bentmann, H.; Reinert, F.; Abramof, E. "Preservation of pristine Bi_2Te_3 thin film topological insulator surface after ex situ mechanical removal of Te capping layer". *APL Materials* **2016**, *4*, 106107 (cit. on pp. 90, 95).

(193) Krumrain, J.; Mussler, G.; Borisova, S.; Stoica, T.; Plucinski, L.; Schneider, C.; Grützmacher, D. "MBE growth optimization of topological insulator Bi2Te3 films". *Journal of Crystal Growth* **2011**, *324*, 115–118 (cit. on p. 90).

(194) Plucinski, L.; Mussler, G.; Krumrain, J.; Herdt, A.; Suga, S.; Grützmacher, D.; Schneider, C. M. "Robust surface electronic properties of topological insulators: Bi2Te3 films grown by molecular beam epitaxy". *Applied Physics Letters* **2011**, *98*, 222503 (cit. on p. 90).

(195) Maaß, H.; Schreyeck, S.; Schatz, S.; Fiedler, S.; Seibel, C.; Lutz, P.; Karczewski, G.; Bentmann, H.; Gould, C.; Brunner, K.; Molenkamp, L. W.; Reinert, F. "Electronic structure and morphology of epitaxial Bi_2Te_2Se topological insulator films". *Journal of Applied Physics* **2014**, *116*, 193708 (cit. on pp. 92, 95).

(196) Nellist, P.; Pennycook, S. In *Advances in Imaging and Electron Physics*; Elsevier: 2000, pp 147–203 (cit. on p. 93).

(197) Cheng, F.; Ding, Z.; Xu, H.; Tan, S. J. R.; Abdelwahab, I.; Su, J.; Zhou, P.; Martin, J.; Loh, K. P. "Epitaxial Growth of Single-Layer Niobium Selenides with Controlled Stoichiometric Phases". *Advanced Materials Interfaces* **2018**, *5*, 1800429 (cit. on p. 93).

(198) Revolinsky, E.; Spiering, G.; Beerntsen, D. "Superconductivity in the niobium-selenium system". *Journal of Physics and Chemistry of Solids* **1965**, *26*, 1029–1034 (cit. on p. 93).

(199) Kremer, G.; Zhu, K.; Pierron, T.; Fournee, V.; Ledieu, J.; Andrieu, S.; Kierren, B.; Moreau, L.; Malterre, D.; He, K.; Xue, Q.-K.; Fagot-Revurat, Y.; Lu, Y. "Recovery of surface state bands after desorption of Te capping layer on $(Bi_{1-x}Sbx)_2Te_3$ ternary topological insulators". *Journal of Physics D: Applied Physics* **2019**, *52*, 494002 (cit. on p. 95).

(200) Kagerer, P. et al. "Two-dimensional ferromagnetic extension of a topological insulator". *Phys. Rev. Res.* **2023**, *5*, L022019 (cit. on p. 95).

(201) Kellner, J. *A surface science based window to transport properties: The electronic structure of Te-based chalcogenides close to the Fermi level*, Ph.D. Thesis, RWTH Aachen University, 2018 (cit. on p. 97).

(202) Paniago, R.; Matzdorf, R.; Meister, G.; Goldmann, A. "Temperature dependence of Shockley-type surface energy bands on Cu(111), Ag(111) and Au(111)". *Surface Science* **1995**, *336*, 113–122 (cit. on p. 97).

(203) Pan, Z.-H.; Fedorov, A. V.; Gardner, D.; Lee, Y. S.; Chu, S.; Valla, T. "Measurement of an Exceptionally Weak Electron-Phonon Coupling on the Surface of the Topological Insulator Bi_2Se_3 Using Angle-Resolved Photoemission Spectroscopy". *Physical Review Letters* **2012**, *108* (cit. on p. 99).

(204) De Jong, N.; Frantzeskakis, E.; Zwartsenberg, B.; Huang, Y. K.; Wu, D.; Hlawenka, P.; Sańchez-Barriga, J.; Varykhalov, A.; van Heumen, E.; Golden, M. S. "Angle-resolved and core-level photoemission study of interfacing the topological insulator $Bi_{1.5}Sb_{0.5}Te_{1.7}Se_{1.3}$ with Ag, Nb, and Fe". *Physical Review B* **2015**, *92* (cit. on p. 101).

(205) King, P. D. C. et al. "Large Tunable Rashba Spin Splitting of a Two-Dimensional Electron Gas in Bi_2Se_3". *Phys. Rev. Lett.* **2011**, *107*, 096802 (cit. on p. 104).

(206) Bianchi, M.; Hatch, R. C.; Li, Z.; Hofmann, P.; Song, F.; Mi, J.; Iversen, B. B.; El-Fattah, Z. M. A.; Löptien, P.; Zhou, L.; Khajetoorians, A. A.; Wiebe, J.; Wiesendanger, R.; Wells, J. W. "Robust Surface Doping of Bi_2Se_3 by Rubidium Intercalation". *ACS Nano* **2012**, *6*, 7009–7015 (cit. on p. 104).

(207) Frantzeskakis, E. et al. "Dirac states with knobs on: Interplay of external parameters and the surface electronic properties of three-dimensional topological insulators". *Phys. Rev. B* **2015**, *91*, 205134 (cit. on p. 104).

(208) Mu, X.; Zhou, H.; He, D.; Zhao, W.; Wei, P.; Zhu, W.; Nie, X.; Liu, H.; Zhang, Q. "Enhanced electrical properties of stoichiometric Bi0.5Sb1.5Te3 film with high-crystallinity via layer-by-layer in-situ Growth". *Nano Energy* **2017**, *33*, 55–64 (cit. on p. 106).

(209) Lukyanova, L. N.; Makarenko, I. V.; Usov, O. A.; Dementev, P. A. "Scanning tunneling spectroscopy of the surface states of Dirac fermions in thermoelectrics based on bismuth telluride". *Semiconductor Science and Technology* **2018**, *33*, 055001 (cit. on p. 107).

(210) Xue-Dong, L.; Park, Y.-H. "Structure and Transport Properties of $(Bi_{1-x}Sb_x)_2Te_3$ Thermoelectric Materials Prepared by Mechanical Alloying and Pulse Discharge Sintering". *Materials Transactions* **2002**, *43*, 681–687 (cit. on p. 107).

(211) Abou El Soud, A. M.; Farag, B. S.; Farag, I. S. A.; Gad, S. A.; Zayed, H. A. "Crystal Structure and Optical Properties of Quaternary Systems of Bi-Sb-Te-Se". *Fizika A* **2008**, *17*, 15 (cit. on p. 107).

(212) Jia, S.; Beidenkopf, H.; Drozdov, I.; Fuccillo, M. K.; Seo, J.; Xiong, J.; Ong, N. P.; Yazdani, A.; Cava, R. J. "Defects and high bulk resistivities in the Bi-rich tetradymite topological insulator $Bi_{2+x}Te_{2-x}Se$". *Phys. Rev. B* **2012**, *86*, 165119 (cit. on p. 108).

(213) Ko, W.; Jeon, I.; Kim, H. W.; Kwon, H.; Kahng, S.-J.; Park, J.; Kim, J. S.; Hwang, S. W.; Suh, H. "Atomic and electronic structure of an alloyed topological insulator, $Bi_{1.5}Sb_{0.5}Te_{1.7}Se_{1.3}$". *Scientific Reports* **2013**, *3*, 2656 (cit. on p. 108).

(214) Scipioni, K. L.; Wang, Z.; Maximenko, Y.; Katmis, F.; Steiner, C.; Madhavan, V. "Role of defects in the carrier-tunable topological-insulator $(Bi_{1-x}Sb_x)_2Te_3$ thin films". *Phys. Rev. B* **2018**, *97*, 125150 (cit. on pp. 108, 112).

(215) Pauly, C.; Bihlmayer, G.; Liebmann, M.; Grob, M.; Georgi, A.; Subramaniam, D.; Scholz, M. R.; Sánchez-Barriga, J.; Varykhalov, A.; Blügel, S.; Rader, O.; Morgenstern, M. "Probing two topological surface bands of Sb_2Te_3 by spin-polarized photoemission spectroscopy". *Physical Review B* **2012**, *86* (cit. on p. 111).

(216) Zhang, Z.; Feng, X.; Guo, M.; Li, K.; Zhang, J.; Ou, Y.; Feng, Y.; Wang, L.; Chen, X.; He, K.; Ma, X.; Xue, Q.; Wang, Y. "Electrically tuned magnetic order and magnetoresistance in a topological insulator". *Nature Communications* **2014**, *5*, 4915 (cit. on p. 111).

(217) Mogi, M.; Yoshimi, R.; Tsukazaki, A.; Yasuda, K.; Kozuka, Y.; Takahashi, K. S.; Kawasaki, M.; Tokura, Y. "Magnetic modulation doping in topological insulators toward higher-temperature quantum anomalous Hall effect". *Applied Physics Letters* **2015**, *107*, 182401 (cit. on p. 111).

(218) Assig, M.; Etzkorn, M.; Enders, A.; Stiepany, W.; Ast, C. R.; Kern, K. "A 10 mK scanning tunneling microscope operating in ultra high vacuum and high magnetic fields". *Review of Scientific Instruments* **2013**, *84*, 033903 (cit. on p. 112).

(219) Bonnet, D.; Erlenkämper, S.; Germer, H.; Rabenhorst, H. "A new measurement of the energy gap in superconducting niobium". *Physics Letters A* **1967**, *25*, 452–453 (cit. on p. 112).

(220) Rezvani, S.; Perali, A.; Fretto, M.; Leo, N. D.; Flammia, L.; Milošević, M.; Nannarone, S.; Pinto, N. "Substrate-Induced Proximity Effect in Superconducting Niobium Nanofilms". *Condensed Matter* **2018**, *4*, 4 (cit. on p. 112).

(221) Pinto, N.; Rezvani, S. J.; Perali, A.; Flammia, L.; Milošević, M. V.; Fretto, M.; Cassiago, C.; Leo, N. D. "Dimensional crossover and incipient quantum size effects in superconducting niobium nanofilms". *Scientific Reports* **2018**, *8* (cit. on p. 112).

(222) Guo, Y.; Zhang, Y.-F.; Bao, X.-Y.; Han, T.-Z.; Tang, Z.; Zhang, L.-X.; Zhu, W.-G.; Wang, E. G.; Niu, Q.; Qiu, Z. Q.; Jia, J.-F.; Zhao, Z.-X.; Xue, Q.-K. "Superconductivity Modulated by Quantum Size Effects". *Science* **2004**, *306*, 1915–1917 (cit. on p. 114).

(223) Bose, S.; Raychaudhuri, P.; Banerjee, R.; Vasa, P.; Ayyub, P. "Mechanism of the Size Dependence of the Superconducting Transition of Nanostructured Nb". *Phys. Rev. Lett.* **2005**, *95*, 147003 (cit. on p. 114).

(224) Ternes, M.; Schneider, W.-D.; Cuevas, J.-C.; Lutz, C. P.; Hirjibehedin, C. F.; Heinrich, A. J. "Subgap structure in asymmetric superconducting tunnel junctions". *Phys. Rev. B* **2006**, *74*, 132501 (cit. on pp. 114–116).

(225) Hurd, M.; Datta, S.; Bagwell, P. F. "Current-voltage relation for asymmetric ballistic superconducting junctions". *Phys. Rev. B* **1996**, *54*, 6557–6567 (cit. on pp. 115, 116).

(226) Hurd, M.; Datta, S.; Bagwell, P. F. "ac Josephson effect for asymmetric superconducting junctions". *Phys. Rev. B* **1997**, *56*, 11232–11245 (cit. on pp. 115, 116).

(227) Ast, C. R.; Jäck, B.; Senkpiel, J.; Eltschka, M.; Etzkorn, M.; Ankerhold, J.; Kern, K. "Sensing the quantum limit in scanning tunnelling spectroscopy". *Nature Communications* **2016**, *7* (cit. on p. 116).

Publications

Publications described within this thesis

1. P. Bhaskar, S. Mathioudakis, T. Olschewski, F. Muckel, J. R. Bindel, M. Pratzer, M. Liebmann, and M. Morgenstern. Mask aligner for ultrahigh vacuum with capacitive distance control. *Appl. Phys. Lett.*, 112 161602, 2018. doi: 10.1063/1.5022462.

Further publications

1. J. Kellner, G. Bihlmayer, M. Liebmann, S. Otto, C. Pauly, J. E. Boschker, V. Bragaglia, S. Cecchi, R. N. Wang, V. L. Deringer, P. Küppers, P. Bhaskar, E. Golias, J. Sánchez-Barriga, R. Dronskowski, T. Fauster, O. Rader, R. Calarco, and M. Morgenstern. Mapping the band structure of GeSbTe phase change alloys around the Fermi level. *Communications Physics*, 1 5, 2018. doi: 10.1038/s42005-018-0005-8

Acknowledgements

I would like to express my gratitude to everyone who has been a part of my journey toward this thesis. The continuous support, invigorating discussions, and uplifting environment within and outside of the workplace have been indispensable.

My sincere gratitude to *Prof. Markus Morgenstern* for his constant guidance over the years. His enthusiasm and dedication to science have been an inspiration to many of us. His profound knowledge of physics makes for a demanding standard that has kept me incessantly learning.

I thank *Dr. Marcus Liebmann* for the many insightful discussions and support through all the struggles and unexpected challenges faced during this project. Thanks to *Dr. Marco Pratzer* for his expertise and advice in building the mask aligner chamber and *Jeff Strasdas* for his Igor skills.

Thanks to the PGI-9 team, especially *Prof. Detlev Grützmacher*, *Dr. Gregor Mussler* and *Dr. Peter Schüffelgen*, for providing the samples. A particular mention to *Michael Schleenvoigt* for sharing the struggles of the fabrication and the enormous time he dedicated to this project.

Thanks to *Dr. Lukasz Plucinski* for the opportunity to measure in his ARPES lab and *Tristan Heider* for his assistance during these measurements.

Special thanks to *Dr. Sayanti Samaddar* for the many inspiring talks over coffee. They served as the highlight of many hardship-filled days. Thanks to *Dr. Florian Muckel*, the most fun office mate and lab partner through the Covid isolation. His support through the late-night measurements and thesis writing has been invaluable. A mandatory shoutout to *Benjamin Pestka* for digging me out of roof collapses and being annoyingly funny. Thanks to *Marcus Esser*, who still owes me ice cream for the Vennbahn tour, and *Jonas Duffhaus* for their help in building the mask aligner chamber. Thanks to *Dr. Christian Holl*, *Dr. Tjorven Johnsen*, *Dr. Frank Volmer*, *Dr. Raphael Bindel*, *Simon Mathioudakis*, *Jonas Beeker*, *Felix Jekat*, *Dr. Philipp Küppers*, *Dr. Jens Kellner* and the rest of the group over the years for being wonderful colleagues.

Thanks to *Frank Neubauer*, *Raoul Sous*, *Helmut Hammers*, *Robert Feron* and the whole team of the mechanical workshop for their support in building the mask aligner system and creating my technical german vocabulary. The support in the institute administration to deal with the infamous german bureaucracy was always found thanks to *Beate Nagel*, *Margarete Betger*, *Ina Kürten* and *Beatrix Dangela*. A big thank you to the liquefication team, *Jörg Schirra* and *Sascha Mohr* to supply LHe and LN_2. I also want to express gratitude to the team of the electronic workshop *Uwe Wichmann*, *Lars van Hove* and *Guido Geulen* for the friendly support.

A special thanks to my family and friends for their prolonged support over the decades to arrive here. I thank my parents *Vasumathi Bhaskar* and *Bhaskar Krishnaswamy* for their encouragement to pursue my dreams; *Keroleine Derstappen–Weidmann* and *Bernd Weidmann* for always reminding me to balance my busy work life. To my closest friends, *Aislynn Lambrigts*, *Anurag Ranjan*, *József Bereczki*, *Ksenia Volkova*, *Mathias Jansson Pessi*, *Martin Johansson*, *Niels Lambrigts*, and *Sanyam Jain*, for helping me in trying to find that balance.

Most importantly, my partner-in-crime *Jan-Michael Mol* for being an unwavering rock during adversities and for infinite patience and understanding during the chaotic last year. Our discussions in physics and shared ideas and opinions have kept my intellect alive through laborious lab days. You are an inspiration to never stop learning. Also, a special thanks for making the best coffee in the world to keep me functioning through the many night shifts!

A note of gratitude to all the obstacles, hardships and failures – without these, I could not have learned and evolved.

Eidesstattliche Erklärung

Priyamvada Bhaskar erklärt hiermit, dass diese Dissertation und die darin dargelegten Inhalte die eigenen sind und selbstständig, als Ergebnis der eigenen originären Forschung, generiert wurden.
Hiermit erkläre ich an Eides statt

1. Diese Arbeit wurde vollständig oder größtenteils in der Phase als Doktorand dieser Fakultät und Universität angefertigt;

2. Sofern irgendein Bestandteil dieser Dissertation zuvor für einen akademischen Abschluss oder eine andere Qualifikation an dieser oder einer anderen Institution verwendet wurde, wurde dies klar angezeigt;

3. Wenn immer andere eigene- oder Veröffentlichungen Dritter herangezogen wurden, wurden diese klar benannt;

4. Wenn aus anderen eigenen- oder Veröffentlichungen Dritter zitiert wurde, wurde stets die Quelle hierfür angegeben. Diese Dissertation ist vollständig meine eigene Arbeit, mit der Ausnahme solcher Zitate;

5. Alle wesentlichen Quellen von Unterstützung wurden benannt;

6. Wenn immer ein Teil dieser Dissertation auf der Zusammenarbeit mit anderen basiert, wurde von mir klar gekennzeichnet, was von anderen und was von mir selbst erarbeitet wurde;

7. Ein Teil oder Teile dieser Arbeit wurden zuvor veröffentlicht und zwar in:
   P. Bhaskar, S. Mathioudakis, T. Olschewski, F. Muckel, J. R. Bindel, M. Pratzer, M. Liebmann, and M. Morgenstern. Mask aligner for ultrahigh vacuum with capacitive distance control. *Appl. Phys. Lett.*, 112 161602, 2018. doi: 10.1063/1.5022462.